A N N U A L R E P O R T

2003

and list of publications

Bayerisches Forschungsinstitut
für Experimentelle Geochemie und Geophysik
Universität Bayreuth

Bayerisches Geoinstitut
Universität Bayreuth
D-95440 Bayreuth
Germany

Telephone: +49-(0)921-55-3700
Telefax: +49-(0)921-55-3769
e-mail: bayerisches.geoinstitut@uni-bayreuth.de
www: http://www.bgi.uni-bayreuth.de

Editorial compilation by: Stefan Keyssner and Petra Ständner
Section editors: Tiziana Boffa Ballaran, Natalia Dubrovinskaia, Leonid Dubrovinsky, Dan Frost, Fabrice Gaillard, Florian Heidelbach, Falko Langenhorst, Catherine McCammon, David Rubie, Friedrich Seifert, Gerd Steinle-Neumann, Michael Terry

Staff and guests of the Bayerisches Geoinstitut in **July 2003**:

Die Mitarbeiter und Gäste des Bayerischen Geoinstituts im **Juli 2003**:

First row, from left (1. Reihe, v. links) Hélène Couvy, Nadège Hilairet, Giada Iacono Marziano, Stefan Keyssner

Second row, from left (2. Reihe, v. links) Hidenori Terasaki, Geoffrey Bromiley, Petra Ständner, Catherine McCammon, Diego Gatta, Fiona Bromiley, Natalia Dubrovinskaia, Wolfgang Böss

Third/fourth row, from left (3./4. Reihe, v. links) Ulrich Faul, Thilo Herrmann, Guoyin Shen, Gerti Gollner, Leonid Dubrovinsky, Tiziana Boffa Ballaran, Florian Heidelbach, Dan Frost, Kai Neufeld, Lydia Kison-Herzing, Ulrich Bläß, Sven Linhardt, Oskar Leitner, Hubert Schulze, Georg Herrmannsdörfer, Christian Liebske, Dave Rubie, Fred Marton, Gianluca Iezzi

Fifth/sixth row, from left (5./6. Reihe, v. links) Oliver Rausch, Paul Schofield, Roman Skála, Friedrich Seifert, Burkhard Schmidt, Steven Jacobsen, Fabrice Gaillard, Ulrich Böhm, Matthias Bechmann, Kurt Klasinski, Detlef Krauße, Gerd Ramming, Gerd Steinle-Neumann

Absent (Es fehlten) Sylvie Demouchy, Heinz Fischer, Christian Holzapfel, Falko Langenhorst, Jie Yuan Ning, Bettina Schmickler, Angelika Sebald, Iona Stretton, Mike Terry

Contents

Foreword

The research aims of the Bayerisches Geoinstitut are centred primarily on investigations of the structure, composition and dynamics of the Earth's interior. The approach to such studies involves experiments at high pressures and temperatures to determine the stability and the physical and chemical properties of Earth materials (minerals, melts and fluids) at depth in the Earth. In addition, computational mineral physics is playing an increasingly important role, and is especially crucial for understanding material properties at conditions that are difficult or impossible to attain experimentally. As the results presented in this Annual Report demonstrate, considerable progress has been achieved during 2003. The results of a wide variety of studies are presented, pertaining, for example, to the early evolution of the Earth, the mineralogy and properties of the Earth's lower mantle, effects of large meteorite impacts on climate, and processes involved in volcanic eruptions. As in previous years, $(Mg,Fe)SiO_3$ silicate perovskite, being the most abundant mineral in the Earth, is the subject of a significant number of studies. A particularly important achievement involves the development of a technique for growing large single crystals of this mineral at high pressure and temperature. The resulting high-quality crystals will enable a greatly improved understanding of its physical and chemical properties to be obtained. This in turn will result in a better understanding of the nature of the Earth's lower mantle in the depth range 660 to 2900 km.

An essential aspect of maintaining progress in experimental studies is the development of new experimental technologies and strategies. In the last year, major progress has been made in two areas. First, the diamond anvil cell laboratory has been further developed through the installation of an ultra-high intensity X-ray system for *in situ* studies to megabar pressures. This facility enables conditions of 150 GPa and 4000 K to be achieved, corresponding to a depth of about 3000 km in the Earth. Second, there have been further important developments in the use of gigahertz ultrasonic interferometry at high pressure in the diamond anvil cell. The aim of this technique is to determine the elastic properties of minerals under conditions of the Earth's interior. Such experimental data are fundamental for interpreting seismic velocity profiles in terms of mineralogical models of the Earth.

Late in 2002, the Professorship for *Experimental Geophysics of the Solid Earth* became vacant due to the move of Prof. Stephen Mackwell, to the Lunar and Planetary Institute (Houston, USA). The process of refilling this position has been an important event of 2003 and the results of the search have produced several highly qualified and excellent candidates. It is anticipated that the position will be refilled in the course of 2004.

As in previous years, and also on behalf of my colleagues, I would like to thank the *Free State of Bavaria* as represented by the *Bayerisches Staatsministerium für Wissenschaft, Forschung und Kunst* as well as the *Kommission für Geowissenschaftliche Hochdruckforschung* for their

continuing support and strong commitment to the Bayerisches Geoinstitut. We also gratefully acknowledge generous support from external funding agencies, in particular the *Alexander von Humboldt Foundation*, the *European Union*, and the *German Science Foundation*, which have also contributed greatly to the development and success of the Institute.

Bayreuth, February 2004 David C. Rubie

Vorwort

Informationen zur Struktur, Zusammensetzung und Dynamik des Erdinneren stellen die zentralen Forschungsziele des Bayerischen Geoinstituts dar. Um die gesteckten Ziele zu erreichen, werden Laborexperimente bei hohen Drücken und Temperaturen durchgeführt, mit denen die Stabilität sowie die physikalischen und chemischen Eigenschaften der Erdmaterie (Minerale, Schmelzen und Fluide) in entsprechender Tiefe in der Erde bestimmt werden. Zusätzlich spielt die rechnergestützte Mineralphysik eine stetig wachsende Rolle; sie ist von besonderer Bedeutung für das Verständnis von Materialeigenschaften, die experimentell nur schwer oder gar nicht zu bestimmen sind. Wie den Ergebnissen dieses Jahresberichts zu entnehmen ist, konnten auch im Jahr 2003 bedeutende wissenschaftliche Fortschritte erzielt werden. Die Resultate eines weiten Spektrums von Forschungsarbeiten werden in diesem Jahresbericht vorgestellt; sie betreffen zum Beispiel die frühe Entwicklung der Erde, die Mineralogie und die Eigenschaften des unteren Erdmantels, die Auswirkungen großer Meteoriteneinschläge auf die Klimageschichte, sowie Prozesse, die zu Vulkanausbrüchen führen. Wie in vorangegangenen Jahren ist Silikat-Perowskit $(Mg, Fe)SiO_3$, das häufigste Mineral im Erdinneren, das Thema einer großen Zahl von Untersuchungen. Ein besonderer Erfolg besteht in der Entwicklung einer Technik zum Züchten großer Einkristalle dieses Minerals unter hohen Drücken und Temperaturen. Mit den künstlichen Kristallen hoher Qualität lassen sich die physikalischen und chemischen Eigenschaften dieses Minerals sehr viel besser verstehen, was wiederum zu vertieften Erkenntnissen über die Natur des unteren Erdmantels im Tiefenbereich zwischen 660 und 2900 km führen wird.

Die Entwicklung neuer Experimentiertechniken und -strategien ist eine wesentliche Voraussetzung für anhaltende Erfolge bei Forschungsarbeiten im Labor. Im vergangenen Jahr konnten auf zwei Fachgebieten bedeutende Fortschritte erzielt werden. Einerseits wurde die Diamantstempel-Technologie durch ein neues ultra-intensives Röntgensystem für *in situ*-Untersuchungen unter Drücken im Megabereich erweitert. Dieses Gerät ermöglicht in Druck- und Temperaturbereiche von 150 GPa und 4000 K vorzudringen und damit die Bedingungen in der Erde in ungefähr 3000 km Tiefe experimentell nachzustellen. Weiterhin gab es bedeutende Fortschritte in der Entwicklung der Ultraschall-Interferometrie im GHz-Frequenzbereich für den Einsatz bei hohen Drücken in der Diamantstempelzelle. Mit dieser Technik sollen elastische Eigenschaften von Mineralen unter Bedingungen des Erdinneren erforscht werden. Derartige experimentell gewonnene Daten sind eine Voraussetzung für die Interpretation von Profildarstellungen der seismischen Geschwindigkeiten hinsichtlich mineralogischer Modelle für den Erdkörper.

Durch den Wechsel von Prof. Stephen Mackwell auf die Leitungsposition am *Lunar and Planetary Institute* der NASA in Houston, USA zum Ausklang des Jahres 2002 wurde der Lehrstuhl *Experimentelle Geophysik der Festen Erde* vakant. Das Wiederbesetzungs-verfahren, in dessen Verlauf einige hoch qualifizierte, exzellente Kandidaten gefunden werden konnten, war eines der Hauptanliegen des Jahres 2003. Mit einer Wiederbesetzung der Professur wird im Laufe des Jahres 2004 gerechnet.

Wie in den vorangegangenen Jahren möchte ich auch im Namen meiner Kollegen dem *Freistaat Bayern*, vertreten durch das *Bayerische Staatsministerium für Wissenschaft, Forschung und Kunst*, als auch der *Kommission für Geowissenschaftliche Hochdruckforschung* der *Bayerischen Akademie der Wissenschaften* meinen Dank für ihre fortwährende Unterstützung und ihre enge Verbundenheit mit dem Bayerischen Geoinstitut aussprechen. Wir sind auch für die großzügige Förderung durch externe Geldgeber, insbesondere durch die *Alexander von Humboldt-Stiftung*, die *Europäische Union* und die *Deutsche Forschungsgemeinschaft*, die ebenfalls wesentlich zur Entwicklung und zum Erfolg des Bayerischen Geoinstituts beigetragen hat, sehr dankbar.

Bayreuth, im Februar 2004 David C. Rubie

1. Advisory Board and Directorship

1.1 Advisory Board

The *Kommission für Geowissenschaftliche Hochdruckforschung* der *Bayerischen Akademie der Wissenschaften* advises on the organisation and scientific activities of the Institute. Members of this board are:

Prof. Dr. Drs. h. c. E. ALTHAUS	Emeritus, Mineralogisches Institut der Universität Karlsruhe
Prof. Dr. U. CHRISTENSEN	Max-Planck-Institut für Aeronomie, Katlenburg-Lindau
Prof. Dr. Drs. h. c. E. U. FRANCK	Emeritus, Institut für Physikalische Chemie der Universität Karlsruhe
Prof. Dr. Dr. h. c. G. NEUWEILER[1]	Department Biologie II der Universität München
Prof. Dr. H. PALME	Institut für Mineralogie und Geochemie der Universität zu Köln
Prof. Dr. R. RUMMEL	Institut für Astronomische und Physikalische Geodäsie der TU München
Prof. Dr.-Ing. G. SACHS (Chairman)	Lehrstuhl für Flugmechanik und Flugregelung der Technischen Universität München
Prof. Dr. E. SALJE	Department of Earth Sciences, University of Cambridge
Prof. Dr. Drs. h. c. W. SCHREYER	Emeritus, Institut für Mineralogie der Ruhr-Universität Bochum
Prof. Dr. H. SOFFEL	Emeritus, Institut für Allgemeine und Angewandte Geophysik der Universität München

[1] resigned from the *Kommission* in 2003

The Advisory Board held meetings in Bayreuth (14.-15.04.2003) and in Munich (14.11.2003).

1.2 Leadership

Prof. Dr. David C. RUBIE (Director)
Prof. Dr. Friedrich SEIFERT
N.N.

2. Staff, Funding and Facilities

2.1 Staff

At the end of 2003 the following staff positions existed in the Institute:

- Scientific staff: **11**
- Technical staff: **12**
- Administrative staff: **2**
- Administrative officer: **1**

During 2003, 12 scientific (111 months) and 1 technical (2,5 months) positions were funded by grants raised externally by staff members of the institute.

In addition 13 long-term scientific positions (94,5 months) were funded by the resources of the BGI Visiting Scientists' Program (see Sect. 5) which also supported short-term visits for discussing future projects or presenting research results (see Sect. 4.6). Fourteen scientists (62 months) were funded by personal grants (stipends).

2.2 Funding

In 2003, the following financial resources were available from the Free State of Bavaria:

- Investment Funding: 219.000 €
- Visiting Scientists' Program: 323.000 €
- Consumables: 281.000 €

The total amount of national/international external funding („*Drittmittel*") used for ongoing research projects in 2003 was 1.029.000 € (Positions: 409.000 €; equipment, consumables and travel grants: 620.000 €).

	positions	**equipment, consumables, travel grants**	**total**
• AvH	239.000 €	24.000 €	263.000 €
• DAAD	2.800 €		2.800 €
• DFG	90.000.€	488.000 €	578.000 €
• EU	72.000 €	95.000 €	167.000 €
• Others	5.500 €	13.000 €	18.500 €
			1.029.300 €

(AvH = Alexander von Humboldt Foundation; DAAD = German Academic Exchange Program; DFG = German Science Foundation; EU = European Union; "Others" in 2003: Aventis, France; Funds of the Chemical Industry; University of Bayreuth)

In the following list only the BGI part of the funding is listed in cases where joint projects involved other research institutions. Principal investigators and duration of the grants are listed in brackets.

Funding institution	**Project, Funding**	**Total Project Funding**
DFG	DU 393/1-1 (L.S. Dubrovinsky – 5.02 - 4.05) Investment money	555.000 €
DFG	Fr 1555/1-1 (D.J. Frost, D.C. Rubie – 9.01 - 8.03) Positions: BAT IIa/2, 24 months Consumables and travel funding:	11.800 €
DFG	Fr 1555/1-2 (D.J. Frost, D.C. Rubie – 9.03 - 8.04) Positions: BAT IIa/2, 12 months Consumables and travel funding:	6.125 €
DFG	La 830/4-5 (F. Langenhorst – 1.03 - 12.03) Positions: studentische Hilfskraft, 12 months Consumables and travel funding:	11.000 €
DFG	La 830/5-2 (F. Langenhorst – 1.03 - 12.03) Consumable and travel funding:	1.534 €
DFG	Ma 801/7-1 (A. Magerl and M. Göbbels/Erlangen, F. Seifert/ Bayreuth) Positions: BAT IIa, 24 months Consumables and travel funding: 18.400 € (Erlangen)	
DFG	Ru 437/6-1 (D.C. Rubie, D.J. Frost, F. Langenhorst, A. Holzheid – 4.02 - 3.04) Positions: BAT IIa/2, 24 months Consumables and travel funding:	13.800 €
DFG	Ru 437/7-1 (D.C. Rubie, B.T. Poe – 2.02 - 1.04) Positions: BAT IIa/2, 24 months Consumables and travel funding:	22.500 €
DFG	Schm 1622/1-1 (B.C. Schmidt – 10.01 - 9.03) Consumables and travel funding:	14.900 €
DFG	Se 301/24-1 and -2 (F. Seifert, D. Frost, F. Langenhorst, C. McCammon – 1.01 - 12.03) Positions: BAT IIa/2, 36 months Consumables and travel funding:	18.000 €
DFG	Wr15/20-2 (A. Sebald, B. Wrackmeyer/Bayreuth, joint project – 7.02 - 5.04) Positions: BAT IIa, 12 months, BAT IIa/2, 12 months Consumables and travel funding:	4.000 €

Funding institution	Project, Funding	Total Project Funding
DFG	Wr15/20-2 and Wr15/20-3 (A. Sebald, B. Wrackmeyer/ Bayreuth, joint project – 7.02 - 6.03) Positions: BAT IIa, 12 months, BAT IIa/2, 12 months Consumables and travel funding:	3.400 €
DFG	Travel funding (C.A. McCammon)	1.475 €
DFG	Travel funding (G. Steinle-Neumann)	985 €
EU	Hydrospec-Network (H. Keppler – 9.00 - 8.04) Positions/Consumables:	181.000 €
EU	"Access to Research Infrastructures" Programme (D.C. Rubie – 5.00 - 4.03) Positions, consumables, equipment, travel:	825.000 €
EU	Marie Curie Fellowships (Training Center) (S. Mackwell – 01.02. - 01.06) Positions, consumables, equipment, travel:	150.000 €
AvH	Sofia-Kovalevskaja-Programm (T. Boffa Ballaran – 8.01 - 7.04) Positions, consumables, equipment, travel:	843.740 €
FCI	(F. Seifert – 1997 - 2003) Consumables: Equipment:	23.500 € 51.100 €
	Collaboration with Fa. Anzaplan, Hirschau (F. Heidelbach)	1.440 €

2.3 Laboratory and office facilities

The institute occupies an area of

ca. 1200 m^2 laboratory space
ca. 480 m^2 infrastructural areas (machine shops, computer facilities, seminar room, library)
ca. 460 m^2 office space
in a building which was completed in 1994.

2.4 Experimental equipment

The following major equipment is available at Bayerisches Geoinstitut:

I. High-pressure apparatus

5000 tonne multianvil press (25 GPa, 3000 K)
1200 tonne multianvil press (25 GPa, 3000 K)
1000 tonne multianvil press (25 GPa, 3000 K)
500 tonne multianvil press (20 GPa, 3000 K)
3 piston-cylinders (0.5" and 0.75"; 4 GPa, 2100 K)
1 piston cylinder D-DIA (5 GPa, 2000 K)
Cold-seal vessels (700 MPa, 1000 K, H_2O), TZM vessels (300 MPa, 1400 K, gas), rapid-quench equipment
Internally-heated autoclave (1 GPa, 1600 K)

II. Structural and chemical analysis

2 X-ray powder diffractometers
1 X-ray powder diffractometer with furnace and cryostat
X-ray powder microdiffractometer
Single-crystal X-ray cameras
2 automated single-crystal X-ray diffractometers
2 Mössbauer spectrometers (1.5 - 1300 K)
Mössbauer microspectrometer
FTIR spectrometer with IR microscope
FEG transmission electron microscope, 200 kV analytical, with EDS and PEELS
FEG scanning electron microscope with BSE detector, EDS, EBSD and CL
3 high-resolution solid-state NMR spectrometers (100, 200, 300 MHz)
2 Micro-Raman spectrometers
JEOL JXA-8200 electron microprobe; fully-automated with 14 crystals, 5 spectrometer configuration, EDX, capability for light elements
Cameca SX-50 electron microprobe
ICP-AES sequential spectrometer
Water content determination by Karl-Fischer titration

III. *In situ* determination of properties

1 calorimeter (77 - 1000 K) scanning
1 dilatometer (to 1800 K)

Diamond anvil cells for powder and single crystal X-ray diffraction, Mössbauer, IR, Raman, optical spectroscopy and electrical resistivity measurements up to at least 100 GPa

Facility for *in situ* hydrothermal studies in DAC

Externally electrically heated DACs for *in situ* studies at pressures to 100 GPa and 1200 K

1-atm furnace (to 1873 K, gas mixing) equipped with zirconia fO_2 probes

Paterson HP/HT deformation apparatus

1-atm high-temperature creep apparatus

2 high frequency ultrasonic interferometers (crystalline and molten materials)

Gigahertz ultrasonic interferometer with interface to resistance-heated diamond-anvil cells

Heating stage for fluid inclusion studies

Impedance/gain-phase analyser for electrical conductivity studies

Apparatus for *in situ* measurements of thermal diffusivity at high P and T

The Geoinstitut is provided with well equipped machine shops, electronic workshop and sample preparation laboratories. It has also access to the university computer centre.

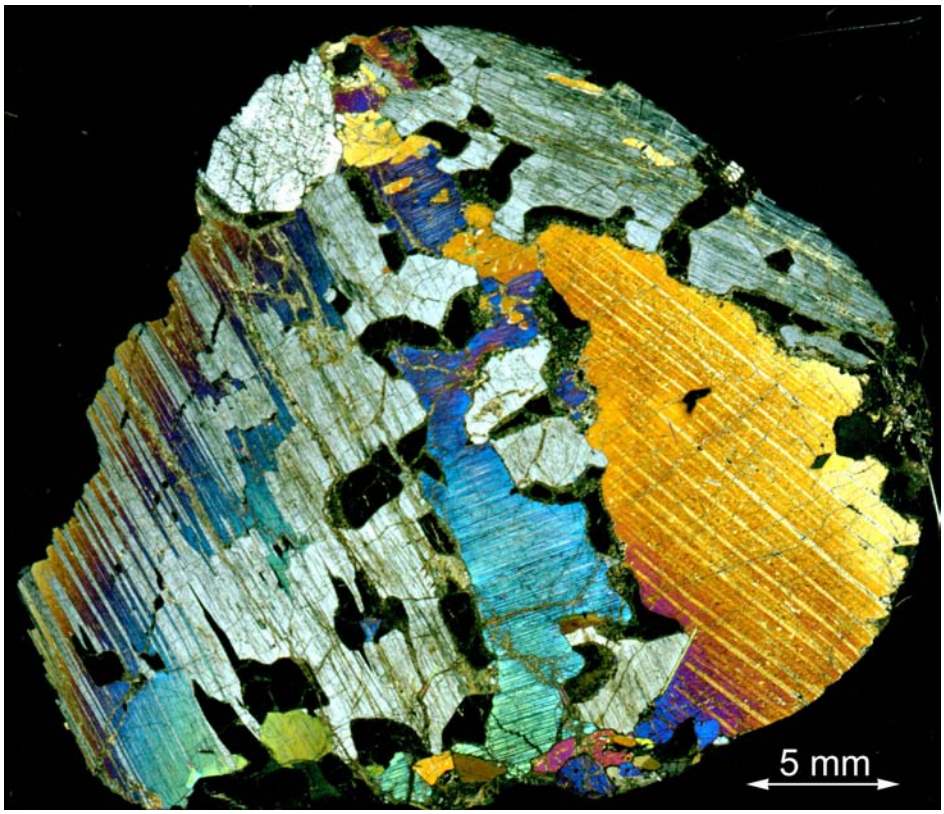

Inverted majorite (J.R. Smyth). This crossed-polars thin section photograph shows a garnet pyroxenite nodule from the Bellsbank Kimberlite, South Africa. The brightly-colored (birefringent) mineral is clinopyroxene, the gray, low-birefringent mineral is orthopyroxene, and the black (isotropic) mineral is garnet. The exsolution texture on the left indicates that the orthopyroxene, clinopyroxene, and garnet were once a single phase, which is only possible in the majorite garnet stability field at pressures above about 17 GPa (~ 500 km depth). A plausible explanation might be that the nodule originally crystallized as a single phase garnet in the transition zone at depths of 500 km or more, and subsequently re-equilibrated to pressures of 3 to 5 GPa before being transported to the surface in the kimberlite. Interestingly, the nodule also contains small K-rich sulfide inclusions consistent with the chalcophile nature of naturally radioactive K at high pressures.

Retrograd umgewandelter Majorit-Granat (J.R. Smyth). Das Dünnschliff-Foto zeigt einen Granat-Pyroxen-Einschluss aus dem Bellsbank-Kimberlit/Südafrika unter gekreuzten Polarisatoren. Das leuchtend gefärbte (doppelbrechende) Mineral ist Klinopyroxen, das graue mit niedriger Doppelbrechung ist Orthopyroxen, das schwarze (isotrope) ist Granat. Die Entmischungstextur links deutet darauf hin, dass Orthopyroxen, Klinopyroxen und Granat ursprünglich als eine einzige Phase vorlagen, was lediglich im Stabilitätsfeld des Majorit-Granats bei Drücken oberhalb 17 GPa, entsprechend einer Erdtiefe von ca. 500 km, möglich ist. Der Einschluss war also ursprünglich ein einzelner Granatkristall in der Übergangszone zwischen oberem und unterem Erdmantel in einer Tiefe von mindestens 500 km und wandelte sich später bei Drücken von 3 bis 5 GPa in die abgebildete Mineralvergesellschaftung um, bevor er in dem Kimberlitschlot an die Erdoberfläche transportiert wurde. Interessanterweise enthält dieses Aggregat auch kleine kaliumreiche Sulfideinschlüsse, was mit der chalkophilen Natur des natürlichen radioaktiven Kaliums unter hohen Drücken übereinstimmen würde.

3. Forschungsprojekte

Es wird an dieser Stelle nur über die wichtigsten, derzeit laufenden Projekte berichtet. Informationen über abgeschlossene Teilprojekte sind in den Abschnitten 4.1 und 4.2 in Form von Literaturzitaten angegeben. Die Beiträge des Kapitels 3 sollen nicht zitiert werden.

3.1 Rheologie

Die Erde ist ein dynamischer Planet, in dem Deformation in allen Tiefenbereichen von der oberen Kruste bis zum inneren Kern auftritt. Geologische Prozesse wie die Bewegung der Lithosphärenplatten, die Bildung von Gebirgsketten oder die Konvektion im Erdmantel werden direkt durch das Verformungsverhalten von verschiedenen Gesteinen bestimmt. Für ein vollständiges Verständnis des Erdinneren ist es daher nicht ausreichend, nur die Stabilität verschiedener Mineralphasen zu kennen, sondern wir müssen auch ihr rheologisches Verhalten untersuchen, d. h. ihr Verhalten bei mechanischer Spannung und Verformung. Die Rheologie eines Materials wird generell durch Fließgesetze beschrieben, die für ein bestimmtes Material die angewandte Spannung zu der Verformungsrate in Beziehung setzen und experimentell durch mechanische Testverfahren bestimmt werden können. Externe Faktoren wie die Temperatur, der Druck oder die Sauerstofffugazität müssen dabei ebenso in den Fließgesetzen ihren Ausdruck finden wie interne (probenspezifische) Faktoren wie die Korngröße, die kristallographische Vorzugsorientierung oder intrakristalline Defekte.

Plastische Verformungsprozesse, die im Erdinneren vorherrschen, verursachen oft Veränderungen der gesteinsphysikalischen Eigenschaften polykristalliner Gesteine, die sich am deutlichsten in dem Auftreten von Anisotropie ausdrücken. Die Anisotropie von gesteinsphysikalischen Parametern wie seismische Wellengeschwindigkeiten oder elektrische Leitfähigkeit wird in den unterschiedlichsten Bereichen des Erdinneren beobachtet, und die plastische Verformung von Mineralen und Gesteinen bietet eine plausible Erklärung für ihr Auftreten. Die Stärke und die Orientierung des anisotropen Verhaltens, die mit geophysikalischen Methoden bestimmt werden, können dann im Hinblick auf die Verformungsgeometrie und den Deformationsmechanismus interpretiert werden.

Am Bayerischen Geoinstitut versuchen wir, die Rheologie verschiedener Mineralphasen zu bestimmen, die die wichtigsten Bestandteile des Erdinneren ausmachen. Insbesondere Ausweitung von Deformationsversuchen zu hohen (Mantel-) Drücken ist hier von großem Interesse, da die Deformationsmechanismen der Minerale sich bei hohen Drücken drastisch ändern können. Die Rheologie von Aggregaten aus mehreren Phasen ist wichtig, da die meisten Gesteine mehrphasig sind und ihr Verformungsverhalten nicht durch einfache Interpolation zwischen den Endgliedern beschrieben werden kann. Die Änderung der intrakristallinen Struktur von Mineralen bei der Deformation ist der Hauptgrund für die physikalischen Unterschiede zwischen verformten und unverformten Gesteinen. Es ist daher wichtig, diese Veränderungen (Gitterdefekte) an Einkristallen oder Proben mit geringer Deformation zu untersuchen, da sie hier am deutlichsten hervortreten (z. B. intrakristalline Gleitsysteme). Entwässerungsreaktionen, die während der Deformation auftreten, können zu einer drastischen Veränderung des Verformungsverhaltens führen, z. B. von duktilem zu

bruchhaftem Verhalten. Physikalische Gesteinsparameter wie die elektrische Leitfähigkeit können dazu benutzt werden, die Entwicklung der Mikrostruktur während eines Deformationsexperiments zu verfolgen. Dabei muss allerdings genau bestimmt werden, welche mikrostrukturelle Eigenschaft tatsächlich für die Änderung des physikalischen Verhaltens verantwortlich ist.

3.2 Physikalische Eigenschaften von Mineralen

Zahlreiche geologische und geophysikalische Merkmale an oder nahe der Erdoberfläche sind Folge dynamischer Prozesse im Erdinneren. Dazu zählen sowohl die sicht- und spürbaren Auswirkungen der Plattentektonik, wie z. B. Vulkanismus, Erdbeben, Gebirgsbildung, sowie die langfristige chemische Evolution der Erde und das magnetische Feld unseres Planeten. Wir können uns ganz allgemein vorstellen, dass diese Prozesse eine Folge des anhaltenden Wärmetransports vom Inneren zur Oberfläche der Erde sind und dass sie durch die Konvektion im Erdmantel und im flüssigen äußeren Kern bestimmt werden. Die Aufklärung weiterer Details über die Prozesse und die auslösenden Kräfte stellt eines der zentralen Ziele der wissenschaftlichen Erforschung des Erdinneren dar.

Inverse geophysikalische Methoden wie die Seismologie und Magnetotellurik sorgen für ein immer klareres Bild über die interne Struktur der Erde, indem sie Momentaufnahmen der erdinneren Prozesse liefern. Zur Interpretation dieser Aufnahmen, und zum Vergleich geophysikalischer Beobachtungen mit geodynamischen Prozessen in der Erde, müssen die physikalischen Eigenschaften der Erdmaterie aus großen Tiefen, von den elastischen und elektromagnetischen Eigenschaften bis zur Viskosität, bekannt sein. Da die tiefere Erdmaterie für direkte Messungen nicht zugänglich ist, versuchen Mineralphysiker, die Drücke und Temperaturen des tieferen Erdinneren in Experimenten zu simulieren. Damit kann die entscheidende Beziehung zwischen geophysikalischen Prozessen in der Erde und geophysikalischen Beobachtungen hergestellt werden. Außerdem versucht die Mineralphysik, makroskopische Phänomene von einem atomistischen Ansatz aus zu verstehen.

Das Bayerische Geoinstitut liefert wichtige Beiträge zu diesen Fragestellungen, und physikalische Schlüsseleigenschaften von Mineralen werden sowohl bei Umgebungsbedingungen als auch unter hohen Drücken bestimmt. Die folgenden Beiträge decken mit der Analyse der elastischen und magnetischen Eigenschaften und des Kompressionsverhaltens sowie mit der Bestimmung der thermischen Ausdehnung bei erhöhten Drücken eine große Auswahl physikalischer Phänomene ab.

Das Kompressionsverhalten und die elastischen Eigenschaften von Einkristallen stellen die physikalischen Grundlagen für die seismische Abbildung des Erdinneren dar. Der erste Beitrag dieses Kapitels befasst sich mit der Untersuchung des Einflusses von Phasenverteilung auf die Elastizität von Aggregaten und nimmt so die wichtige Frage der Verformungsverteilung zwischen Mineralphase und Umgebungsgestein auf. Zwei Beiträge zur Bestimmung von Zustandsgleichungen befassen sich mit recht unterschiedlicher silikatischer Materie. Die Bestimmung der Kosmochlor-Diopsid-Konjugationslinie in Pyroxenen soll das Verständnis über Druck- und Temperaturbedingungen bei der Bildung

Kosmochlor-führender Meteorite verbessern. Edingtonit, ein Ba-führender Zeolith, wird komprimiert, um die Reaktion von mikroporösem Material auf Druck zu bestimmen. Eine neue, sehr intensive Röntgenquelle am Bayerischen Geoinstitut ermöglicht genauere Messungen der thermischen Ausdehnung von unter hohen Drücken synthetisierten Mineralen (Ringwoodit und der α-PbO_2-Phase von TiO_2). Derartige Messungen erlauben noch genauere Bestimmungen von thermodynamischen Eigenschaften von Mineralen bei hohen Drücken und Temperaturen.

Erste Bestimmungen der elastischen Konstanten von Einkristallen wurden mit dem GHz-Ultraschall-Interferometer am Bayerischen Geoinstitut durchgeführt. Zwei Beiträge finden sich in diesem Kapitel: Messungen der elastischen Konstanten von Magnetit (Fe_3O_4) als Funktion des Drucks und von einem Wüstit-Periklas-Mischkristall als Funktion von Komposition und Druck.

Der Einfluss des Magnetismus auf die Phasenstabilität und Thermodynamik von Mineralen, speziell des Verlustes des Magnetismus bei Kompression, wurde erst in den letzten Jahren erkannt. Das Geoinstitut trägt mit seiner Forschung auf diesem Gebiet erheblich zu einem besseren Verständnis der Zusammenhänge bei. Es werden hier Untersuchungen über die magnetischen Eigenschaften zweier prototypischer magnetischer Materialien (Eisen und FeO-Wüstit) vorgestellt, die von zentralem Interesse für Geo- und Materialwissenschaftler sind.

Dieses Kapitel schließt mit einem Beitrag ab, der sich mit der Analyse von lamellarem Magnetismus in der Ilmenit-Hämatit-Reihe befasst. Das Verständnis der ungewöhnlich starken magnetischen Suszeptibilität ist für paläomagnetische Betrachtungen, wie der Bestimmung von Plattenbewegungen sehr wichtig. Diese wiederum sind Teil der dynamischen Prozesse in und auf der Erde, mit denen dieses Kapitel eingeleitet wird.

3.3 Mineralogie, Kristallchemie und Phasenübergänge

Phasenumwandlungen treten in den meisten Materialien, einschließlich Keramiken, Metallen, Polymeren, organischen und anorganischen Komponenten und natürlich in Mineralen auf. Die Untersuchung von Umwandlungsprozessen in Mineralen entwickelte sich aus der Notwendigkeit, die physikalischen und thermodynamischen Eigenschaften der Bestandteile an der Oberfläche und im Innern der Erde zu verstehen. Tatsächlich sind nur wenige Minerale bekannt, die keine Umwandlungen bei den in der Erde herrschenden Drücken und Temperaturen zeigen. Daher ist es nicht überraschend, dass sich die meisten Beiträge dieses Kapitels mit Phasenübergängen befassen; auch überrascht nicht die Vielfalt der untersuchten Minerale, wenn man die große Zahl von Phasen bedenkt, die in den Gesteinen unseres Planeten präsent sind.

Fast jede Änderung in der Kristallstruktur aufgrund kleiner Verschiebungen der Atompositionen, Ordnungsvorgängen von Atomen und rekonstruktiven Phasenübergängen wird gewöhnlich von Veränderungen in den Gitterparametern begleitet. Derartige Variationen können quantitativ als eine Kombination von Linear- und Scher-Deformation beschrieben werden, wenn zuvor geeignete Referenz-Zustände definiert wurden. Sie ermöglichen

Einblicke in recht komplizierte Systeme wie inkommensurate Phasenübergänge, wie sie in Nephelin auftreten. Röntgendiffraktometrische Methoden werden in großem Maßstab eingesetzt, um Umwandlungsprozesse auch unter hohen Drücken und Temperaturen zu untersuchen; die Qualität dieser Technik ermöglicht heutzutage nicht nur eine Identifizierung neuer Hochdruck-Modifikationen, sondern auch ihre genaue Charakterisierung.

Auch Phononen sprechen auf jede Veränderung in der Kristallstruktur von Materie an. Die Raman- und die Infrarot-Spektroskopie werden als analytisches Hauptwerkzeug zur Beschreibung von Phasenübergängen eingesetzt. Die Diffraktometrie und andere spektroskopische Methoden werden komplementär verwendet; ihr kombinierter Einsatz führt zu einem besseren Verständnis einer Kristallstruktur und ihrer Veränderungen sowohl im makroskopischen als auch im sehr lokalen Maßstab.

Der Einsatz von Analogmaterialien spielt in Hochdruck-/Hochtemperatur-Untersuchungen eine wichtige Rolle, da für sie die experimentellen Randbedingungen leichter zu realisieren sind. Es kommt öfter vor, dass das eingesetzte Analogmaterial nicht nur zu einer Wissensvermehrung über gesteinsbildende Minerale führt, sondern einzigartige Eigenschaften darlegt, die von breiterem wissenschaftlichen Interesse sein können.

Wir dürfen auch nicht übersehen, dass unterschiedliche Zusammensetzungen kristalliner Materie tiefgreifende Abweichungen hinsichtlich thermodynamischer Stabilität und dem physikalischen Verhalten in diesem Material bewirkt. Die unterschiedliche Zusammensetzung kann auf der Substitution verschiedener Atome, oder einfach durch das Vorhandensein des gleichen Atoms in verschiedenen Wertigkeiten beruhen. Daher erscheint es wichtig, mögliche strukturelle Variationen aufgrund von Kationensubstitutionen zu erforschen, oder Methoden für die empirische Bestimmung von Valenzzuständen und Koordinationen von Übergangsmetallen in Festkörpern zu entwickeln.

3.4 Geochemie

Chemische Wechselwirkungen zwischen den die Erde aufbauenden Elementen beeinflussen nahezu jeden Prozess, der im Erdinnern und an der Oberfläche auftritt. Ein für uns besonders relevantes, an der Erdoberfläche angesiedeltes Phänomen stellt der Chemismus von Kohlenstoff und Sauerstoff dar, aus denen sich unsere Atmosphäre aufbaut. Der Zyklus von Einbau und Freisetzung dieser Elemente über geologische Zeiträume hängt sehr stark von der Geochemie des Erdmantels ab, wobei Kohlenstoff-Löslichkeit und Sauerstofffugazität nur zwei von zahlreichen ausschlaggebenden Parametern sind. Die Abfolge von Mantelprozessen kann oftmals aus geochemischen Signaturen in Mineralen entschlüsselt werden, wie zum Beispiel aus Elementverteilungsmustern oder aus Diffusionsprofilen, wobei sich Laborexperimente als sehr aufschlussreich erweisen. Mit einem weiteren Werkzeug der Geochemie, der theoretischen Modellierung, lassen sich Faktoren untersuchen, die sich auch im Labor nicht simulieren lassen, wie z. B. der Einfluss variabler thermischer Leitfähigkeit auf die Umwandlung des Olivin in Wadsleyit und somit die Mechanismen von tiefen Erdbeben. Die mit der Übergangszone von 410 bis 660 km Tiefe im Zusammenhang stehenden Strukturänderungen, z. B. von Olivin nach Wadsleyit, verlaufen nicht streng isochemisch, da

Elemente zwischen den Phasen nicht gleich verteilt vorliegen. Daten zur Elementverteilung, die in Hochdruck-Experimenten gewonnen werden, lassen sich mit Ergebnissen korrelieren, die mit geophysikalischen Methoden erfasst wurden, wie z. B. die Mächtigkeit der Diskontinuität in 410 km Tiefe. Auf diese Art können auch schwieriger zu messende Parameter des Erdmantels (z. B. die Temperatur) bewertet werden. Komplementäre Untersuchungen der vertikalen Ausdehnung der 410 km-Diskontinuität verwenden theoretische kinetische Modelle, um Eigenschaften des Mantels wie Konvektionsdynamik, das Geoid oder Viskosität einzugrenzen.

Die Bildung des Erdkerns stellte wahrscheinlich das gravierendste geochemische Ereignis in der gesamten Erdgeschichte dar. Obwohl ein allgemeiner Konsens bisher nicht besteht, beschreiben die meisten Modelle ein Aufschmelzen des eisenreichen Materials des Erdkörpers, gefolgt von einem Absinken der Schmelze und der daraus folgenden Bildung des Erdkerns. Diese kernbildenden Vorgänge prägten typische geochemische Muster im Erdmantel aus. Eine der Herausforderungen bei derartigen Untersuchungen ist der Mangel an natürlichen Proben aus dem unteren Erdmantel, an denen die verschiedenen Theorien getestet werden könnten. Mineraleinschlüsse in natürlichen Diamanten stellen derzeit die einzige Quelle natürlicher Proben dar; und während sie wichtige Informationen zur Eingrenzung der Diamantbildung und der Dynamik des Erdmantels liefern, bleibt jedoch die Frage offen, inwieweit diese Mineraleinschlüsse für die Gesamtzusammensetzung des unteren Mantels repräsentativ sind. Ein komplementärer Ansatz basiert auf Hochdruck-Experimenten, mit denen der Bedarf an dreiwertigem Eisen im Perowskit des unteren Erdmantels untersucht werden kann; daraus können Schlussfolgerungen über die Verteilung von siderophilen und lithophilen Elementen bei der Kern/Mantel-Differentiation gezogen werden. Modelle zur Erdkernbildung, die von der Perkolation einer Schmelze durch kristallines Material ausgehen, machen das Vorhandensein einer bestimmten Mikrostruktur erforderlich, bei der die Schmelzanteile über die Komponenten miteinander verbunden sind. Experimentelle Untersuchungen helfen die Bedingungen zu identifizieren, bei denen dieses Kriterium gegeben ist; sie zeigen daher auch, welche Randbedingungen für den Prozess der Kernbildung sowohl auf der Erde als auch auf anderen Planeten (wie dem Mars) gelten. Die Ergebnisse dieser Untersuchungen heben die Rolle anderer Elemente neben dem Eisen bei der Bildung des Erdkerns hervor; sie haben dazu geführt, dass auch Elemente wie Kohlenstoff und Magnesium im Zusammenhang mit der Erdkernbildung erforscht werden, die bisher nicht in derartige Untersuchungen einbezogen waren.

3.5 Metamorphose

Ähnlich wie das Jahr dem Zyklus der Jahreszeiten unterliegt, so beeinflusst ein Zyklus geologischer Prozesse die Mineralogie und Zusammensetzung natürlicher Gesteine. Die Metamorphose ist ein wichtiger geologischer Prozess dieses Zyklus; sie steht allgemein im Zusammenhang mit großen Temperatur- und/oder Druckveränderungen. Grundsätzlich existieren zwei metamorphe Prozesse, die in unterschiedlichem geologischen Kontext und auf sehr verschiedenen Zeitachsen ablaufen: 1) die (endogene) Regionalmetamorphose und 2) die (exogene) Schockmetamorphose.

Regionalmetamorphe Vorgänge können Millionen von Jahren andauern und treten in Verbindung mit Gebirgsbildungen auf; sie führen z. B. zur Subduktion von Gesteinen in große Tiefen, wo höhere Temperaturen und Drücke vorherrschen. Diese Veränderungen in den physikalischen Bedingungen bewirken eine Rekristallisation der Gesteine, die Bildung neuer Mineralvergesellschaftungen und können sogar eine Aufschmelzung einleiten. Form und Größe der Mineralkörner in metamorphen Wirtsgesteinen und die Art ihrer Verwachsung (d. h. ihre Texturen und Gefüge) liefern Schlüsselinformationen zur metamorphen Entwicklungsgeschichte der Wirtsgesteine. Zur Bestimmung des Gesteinsgefüges hat sich die Rasterelektronenmikroskopie (REM), kombiniert mit der Methode der Elektronenbeugung von rückgestreuten Elektronen (EBSD = electron back scattered diffraction) zu einem quantitativ einsetzbaren Werkzeug und zum Bestandteil in zahlreichen Untersuchungen am Bayerischen Geoinstitut entwickelt. In diesem Kapitel befassen sich zwei Beiträge mit extremen Bedingungen endogener Metamorphose, mit in der oberen Kruste auftretender Kontakt-Metamorphose und mit der plastischen Verformung von metamorphen Gesteinen an der Krustenbasis.

Die Schockmetamorphose ist ein exogener, extrem kurzzeitiger Prozess, der beim Impakt größerer Himmelskörper abläuft. Der Einschlag eines Projektils mit kosmischer Geschwindigkeit erzeugt lokal Drücke von bis zu mehreren Megabar und Temperaturen bis zu einigen 10.000 °C, die zur Verdampfung und Aufschmelzung sowie zur thermischen Zersetzung von Mineralen führt. Die durch einen Impakt freigesetzten Klimagase (z. B. CO_2 und SO_x aus Karbonaten und Sulfaten) werden als bedeutender Faktor für das Massensterben an der Kreide/Tertiär-Grenze angesehen. Um in diesem Aussterbe-Szenario die Rolle des SO_x abzuschätzen, wurde eine Serie von Schockexperimenten mit Anhydrit durchgeführt sowie das Phasendiagramm für Anhydrit in dem relevanten Hochdruck/Hochtemperatur-Bereich modelliert.

Weiter vom Einschlagsort entfernt liegende Gesteine werden von geringeren Druck- und Temperatureinflüssen betroffen und bleiben daher fest; sie erleiden jedoch eine starke kataklastische Zertrümmerung. Die Minerale entwickeln ganz spezielle Deformationsmerkmale; z. B. können sich planare Deformationsstrukturen in Hochdruckphasen umwandeln, die sonst lediglich in größerer Tiefe im Erdinneren erwartet werden. In diesem Jahr waren wir bezüglich des Nachweises derartiger Hochdruck-Modifikationen in natürlichen Impakt-Gesteinen recht erfolgreich. Die beiden letzten Beiträge dieses Kapitels berichten über die Entdeckung einer neuen Hochdruck-Modifikation des Kohlenstoffs und über Silikat-Hollandit, die Hochdruck-Modifikation von Feldspat.

3.6 Fluide und ihre Wechselwirkung mit Schmelzen und Mineralen

Es gibt kaum eine physikalische oder chemische Eigenschaft von Silikatsystemen, die nicht von Wasser beeinflusst wird. Darum sind Untersuchungen zur Verteilung des Wassers zwischen den unterschiedlichen geochemischen Reservoirs der Erde von fundamentaler Bedeutung. Das Erdinnere ist das bei weitem größte irdische Wasserreservoir, und es gibt eine Reihe von Indizien, dass Wasser im Erdmantel eine maßgebliche Rolle spielt. Wasser erniedrigt die Schmelztemperaturen von Silikatgesteinen; es ermöglicht die Mobilisation von

Elementen in Fluiden und Schmelzen, wodurch Variationen im geochemischen Muster des Erdmantels erzeugt werden. Die geochemische Anreicherung von Elementen durch sogenannte „metasomatische“ Fluide und Schmelzen kann in Gesteinsproben aus dem Erdmantel nachgewiesen werden, die durch vulkanische Aktivitäten bis an die Erdoberfläche gelangt sind. Der ursprüngliche Wassergehalt dieser Mantelgesteine ist jedoch ungleich schwieriger zu bestimmen, da Minerale dazu neigen, bei ihrem Transport an die Erdoberfläche Wasser an die Dampfphase abzugeben. Ebenso mögen die Mantelgesteine, die in Vulkanausbrüchen zu Tage gefördert werden, nicht die „typische“ Gesteinszusammensetzung des Erdmantels repräsentieren. Ihr Wassergehalt wird wahrscheinlich durch magmatische Aktivitäten beim Aufstieg beeinflusst.

Die Ungewissheit in Hinsicht auf das Wasserbudget des Erdmantels hat zahlreiche Forschungsarbeiten inspiriert, die häufig auf experimentell abgesicherten Daten aufbauen. Untersuchungen zur Diffusionsgeschwindigkeit von Wasser bzw. des strukturell gebundenen Wasserstoffs in Mantelmineralen ermöglichen Abschätzungen zur Wasserabgabe dieser Minerale beim Aufstieg an die Erdoberfläche. Umgekehrt ermöglichen Experimente zur Bestimmung der maximalen Speicherkapazität von bestimmten Mineralen eine bessere Abschätzung der Mengen an Wasser, die in Subduktionszonen in den Erdmantel zurückgeführt werden. Weitere geophysikalische Methoden, die eine unabhängige Abschätzung des Wassergehalts im Erdmantel ermöglichen, sind ebenfalls als sehr hilfreich anzusehen. So können z. B. Messungen der elektrischen Leitfähigkeiten des oberen Erdmantels durch den Wassergehalt des Hauptminerals Olivin beeinflusst werden. Wenn es gelingt, die elektrische Leitfähigkeit von Olivin als Funktion des Drucks und des Wassers bzw. des OH^--Gehaltes genau zu bestimmen, dann könnte eine derartige geophysikalische Fernerkundungsmethode verwendet werden, um den Wassergehalt des oberen Mantels zu „kartieren“. Wasser beeinflusst auch das Volumen und die elastischen Eigenschaften der Minerale, in denen es gelöst ist. Wadsleyit, ein Hauptmineral der Übergangszone in 400 - 660 km Tiefe kann große Wassermengen in Form von OH^- in seiner Struktur aufnehmen. Könnten die Auswirkungen von Wasser auf die Struktur des Wadsleyits genau beschrieben werden, so wäre es wohl möglich, Hinweise auf eine eventuelle Hydratisierung des Erdmantels durch seismologische Untersuchungen der Übergangszone zu finden, da die seismischen Wellengeschwindigkeiten wiederum von den physikalischen Eigenschaften der Minerale abhängen.

3.7 Physikalische und chemische Eigenschaften von Schmelzen und Magmen

Aufschmelzung und Migration von Magmen im Erdinnern sind für umfangreichen Massentransport und eine weiträumige chemische Differentiation in den vergangenen 4,6 Mrd. Jahren verantwortlich. Zu den Folgen des Aufschmelzens während der Evolution der Erde gehören 1) die Bildung des Erdkerns durch eine Trennung von (dichterem) metallischem und silikatischem Material, 2) die Bildung von kontinentaler und ozeanischer Kruste an Subduktionszonen bzw. Mittelozeanischen Rücken und 3) die Entwicklung der Atmosphäre durch Freisetzung von leichtflüchtigen (gasförmigen) Bestandteilen aus Lava oder Magmen nahe der Erdoberfläche. Das Verständnis des Magmentransports während der Differentiation der Erde erfordert vielschichtige experimentelle Ansätze, um Transporteigenschaften von Schmelzen und deren Abhängigkeit vom Druck zu bestimmen. Daher sind experimentelle

Messungen in einem weitgespannten Druck- und Temperaturbereich, einschließlich unter extremen Bedingungen, erforderlich.

Eine direkte Folge magmatischer Aktivität sind die Bedrohungen, die von explosiven Vulkanausbrüchen ausgehen. Der potenziell explosive Charakter eines Ausbruchs hängt entscheidend vom Anteil der Volatilen (im wesentlichen vom Wassergehalt) ab, die vor dem Ausbruch im Magma gelöst und beim Ausbruch freigesetzt werden. Fundamentale wissenschaftliche Fragestellungen lauten derzeit: Wieviel Wasser kann in Magmen gelöst werden? Wie ist es in die molekulare Struktur von Schmelzen eingebaut? Durch welche Prozesse wird dieses Wasser beim Aufstieg der Schmelzen freigesetzt? Diese Themen sind von ganz besonderem Interesse für Bevölkerungen, die in vulkanischen Risikogebieten leben.

Ein erheblicher Anteil der hier vorgestellten Forschungsarbeiten befasst sich mit Untersuchungen über Transporteigenschaften von Schmelzen unter niedrigen bis zu sehr hohen Drücken. Es werden wichtige neue Ergebnisse zu Diffusion und viskosem Fließen in Peridotitschmelzen bei Drücken des oberen Erdmantels vorgestellt. Die Resultate beschreiben den Einfluss der Schmelzzusammensetzung auf die Viskosität und verdeutlichen die Wichtigkeit des Drucks auf viskoses Fließen in einem tiefen Magma-Ozean, der sich mit großer Wahrscheinlichkeit während der frühen Erdgeschichte bildete. Die Ergebnisse haben Auswirkungen auf weiträumige globale Prozesse, wie z. B. auf die Bildung des Erdkerns und die frühe Differentiation der Erde durch Kristallisationsprozesse in einem Magma-Ozean. Transporteigenschaften von Magmen bei Drücken in der Erdkruste sind ebenfalls Teil der Untersuchungen. Die Rate von Wasserentgasung aus einem phonolitischen Magma des Vesuvs als Funktion der Aufstiegsgeschwindigkeit wird erläutert. Während des schnellen Magmenaufstiegs besteht ein deutliches Ungleichgewicht, was eine starke Übersättigung des Magmas an leichtflüchtigen Bestandteilen in flachen Tiefen zur Folge hat. Explosive Eruptionen können sich daher durch eine verzögerte und schlagartige Freisetzung von Volatilen aus dem Magma in der Nähe der Erdoberfläche ereignen. Die elektrische Leitfähigkeit von Schmelzen wurde im Zusammenhang mit dem Einfluss von Wasser und dem Anteil an Kristallen bestimmt; die Ergebnisse ermöglichen die mit anderen geophysikalischen Methoden kartierten elektrischen Signaturen von Schmelzkörpern in der Erde in Hinsicht auf ihren Wassergehalt und das Ausmaß ihrer Kristallisation zu interpretieren. Um Eigenschaften von Silikatschmelzen im makroskopischen Maßstab deuten zu können, ist auch ein Verständnis der molekularen Struktur von Schmelzen und der Strukturwechsel mit veränderten Druck- und Temperaturbedingungen erforderlich. Strukturbestimmungen machen den Einsatz von vibrationsspektroskopischen Methoden notwendig, die normalerweise an Gläsern als Strukturanalogon von Schmelzen angewandt werden. Die in diesem Kapitel beschriebenen Untersuchungen zur Speziation von Wasser und Bor in Silikatschmelzen tragen zum Verständnis von Produkten aus granitischem Magmatismus bei, insbesondere für die im spät-magmatischen Stadium gebildeten Erzlagerstätten. In den zwei letzten Beiträgen dieses Kapitels werden Abschätzungen zur Strukturanpassung im molekularen Maßstab als Reaktion auf Druckerhöhungen vorgestellt. Bei Si und Al, den dominierenden Netzwerk-Bildnern einer Silikatschmelze, wird bei zunehmendem Druck eine Erhöhung der Koordinationszahl registriert. Derartige Beobach-

tungen stellen die Basis dar, um Auswirkungen des Drucks auf Dichte und Viskosität von Schmelzen zu deuten.

3.8 Materialwissenschaften

Die moderne Mineralogie und Petrologie haben mit den Materialwissenschaften nicht nur gemeinsame methodische Ansätze wie z. B. physikalische und chemische Syntheseverfahren, Materialcharakterisierung, die Untersuchung von Struktur-/Eigenschaftsbeziehungen, sowie die Reaktion auf veränderte thermodynamische Parameter. Übereinstimmung besteht auch hinsichtlich vieler Untersuchungsgegenstände. Das bekannteste Beispiel ist Diamant. Während sich Geowissenschaften mit der Genese und den Lagerstätten unterschiedlicher Diamantvorkommen befassen, erforschen Materialwissenschaftler günstigere Methoden zur Herstellung synthetischer Diamanten. Auch neuartige Experimente zu Wachstumsmechanismen und zum katalytischen Effekt von Metallen am Bayerischen Geoinstitut können die Bedingungen für die Diamantsynthese optimieren.

Obwohl Diamant seit langem als das härteste Material gilt, gibt es ständige Bemühungen, noch härtere Substanzen herzustellen. Besonders vielversprechend waren bisher Experimente mit C_{60}-Fullerenen, die eine Polymerisation unter hohen Druck- und Temperaturbedingungen erfahren. Man nimmt sogar an, dass dreidimensional polymerisiertes Fulleren härter als Diamant ist. Allerdings ist die Reproduzierbarkeit bei der Synthese der 3D-Polymere problematisch. Das hängt teilweise mit dem nur vage festgelegten Phasendiagramm für metastabile C_{60}-Polymere zusammen. *In situ*-Experimente zeigen jetzt zum ersten Mal, dass abhängig vom Bildungspfad (Druckzunahme gefolgt von Aufheizung oder umgekehrt) unterschiedliche C_{60}-Polymere synthetisiert werden können.

Modifikationen von Titandioxyd (TiO_2) stellen aufgrund ihrer besonderen Eigenschaften ein äußerst vielseitiges Material für zahlreiche experimentelle und theoretische Untersuchungen dar. Hochdruck-Modifikationen von TiO_2 sind unter kristallchemischen Gesichtspunkten ein enges Analogon zu SiO_2, der wichtigsten Komponente der festen Erde. Es wurde eine neue TiO_2-Phase mit der Struktur des Fluorit-Typs entdeckt, die bei hohen Drücken und Temperaturen stabil ist. Unter der Bedingung, dass diese Phase bei Umgebungsbedingungen stabilisiert werden kann, könnte sie große Bedeutung als Material für Fotoelektroden bei der fotochemischen Energieumwandlung erlangen.

Druckinduzierte Phasenübergänge in nano-kristalliner Materie, die von Strukturänderungen begleitet werden, dienen als Modell für kinetisch kontrollierte Prozesse und atomistische Mechanismen bei Phasenübergängen erster Ordnung im festen Zustand. Sie verdienen auch wegen der möglichen Rolle nano-kristalliner Phasen im Inneren der Planeten Aufmerksamkeit. Eventuell können dichte nano-kristalline Phasen, die in geschockter Materie in der Erdkruste, in Meteoriten und möglicherweise in der Umgebung von präsolaren Sternen zu finden sind, zur Klärung der Bildungs- und Entwicklungsbedingungen beitragen. Untersuchungen über das Verhalten von Titandioxid und Cuprit (Cu_2O) unter Druck machen deutlich, dass die Kristallstruktur und die chemische Stabilität nano-kristalliner Materie von derjenigen der grobkristallinen Materie stark abweichen kann.

Die Struktur-/Eigenschaftsbeziehungen spielen in den Materialwissenschaften eine große Rolle. Sie werden einmal mehr durch neue Untersuchungen zu druckabhängigen Hochspin-Tiefspin-Umwandlungen in metall-organischen Verbindungen und von Zirkon-Phosphaten aufgezeigt, deren Struktur mit der Chemie variiert.

3.9 Methodische Entwicklungen

Moderne experimentelle Geowissenschaften sind untrennbar mit kontinuierlicher methodischer Weiterentwicklung verknüpft. Felddaten aus geophysikalischen und geochemischen Geländekampagnen (z. B. tiefenabhängige Darstellungen von Dichte, Elastizität, elektrischer Leitfähigkeit, Elementverteilung usw.) lassen sich nur dann erfolgreich interpretieren, wenn vergleichbare, hochwertige (möglichst *in situ* gewonnene) Vergleichsdaten für die Erdmaterie aus entsprechenden Experimenten vorliegen, in denen die dem Erdinneren entsprechenden hohen Druck- und Temperaturbedingungen nachgestellt werden. Das am Geoinstitut neu installierte Laser-Heizsystem ermöglicht die Erzeugung von Temperaturen über 4000 K in Diamantstempelzellen (DACs). Die DAC ist derzeit die einzige Hochdruck-Apparatur, die es ermöglicht, statische Drücke zu erzeugen, die den Bedingungen im Erdmittelpunkt entsprechen. Allerdings ist der bei der Messung der Materialeigenschaften aufgebrachte Druck oft nicht hydrostatisch. Die Theorie der winkeldispersiven Beugung befasst sich mit diesem Problem und zeigt Wege auf, wie sich präzisere Daten unter ultrahohen Drücken gewinnen lassen.

Die Gigahertz-Ultraschall-Interferometrie stellt eine neue hochfrequente akustische Methode dar, die in gemeinsamem Bestreben von Bayerischem Geoinstitut und der Universität von Colorado in Boulder/USA entwickelt wurde. Durch den Einsatz der schnellen Pikosekunden-Elektronik wurden traditionelle Ultraschall-Laufzeit-Verfahren auf den GHz-Frequenzbereich ausgedehnt, wodurch Elastizitätsmessungen an Probenkörpern in Mikrometer-Größe (µm) ermöglicht werden. Während bei der Entwicklung dieser Methode noch die Anwendung auf Einkristalle unter hohen Druckbedingungen im Vordergrund stand, werden hier neue Ergebnisse vorgestellt, die demonstrieren, dass die Gigahertz-Ultraschall-Methode auch auf verzwillingte Kristalle, auf Gläser und auf nano-kristalline Materie angewandt werden kann.

Mit der Beschreibung neuer analytischer Fortschritte in der Festkörper-NMR (Nuclear Magnetic Resonance Spectroscopy) schließt dieses Kapitel ab.

3. Research Projects

In this section an overview of the most important ongoing projects is given. Information concerning recently-completed projects can be obtained from the publication lists of sections 4.1 and 4.2. Please note that the following contributions should not be cited.

3.1 Rheology

The Earth is a dynamic planet where deformation takes place at all levels from the upper crust to the inner core. Geological processes like the movement of lithospheric plates, the formation of mountain chains and convection in the Earth's mantle are all directly governed by the deformation behaviour of rocks. For a complete understanding of the Earth's interior it is therefore not only sufficient to know the mineral phases present at various depths but also their rheological behaviour, *i.e.*, their response to mechanical stresses and strains. The rheology of a material is generally described by flow laws, which relate the applied stress to the strain rate for a given material and can be determined experimentally by mechanical testing. External factors such as temperature, pressure or oxygen fugacity have to be included in flow laws as well as material properties such as grain size, crystallographic preferred orientation and crystalline defects.

Plastic deformation processes which are predominant in the Earth's interior often also result in a change of physical properties of a polycrystalline material, most notably in the development of anisotropy. Anisotropy of physical parameters such as seismic wave velocity or electrical conductivity is observed in numerous regions inside the Earth, and deformation of minerals and rocks is a very likely explanation for its occurrence. The strength and orientation of the anisotropic behaviour determined by geophysical methods can then be interpreted in terms of deformation mechanism and geometry.

At the Bayerisches Geoinstitut an aim is to determine the rheology of the various phases that represent the most important components of the Earth's interior. In particular, the extension of deformation experiments to high (mantle) pressures is important, because deformation mechanisms may change drastically at the high pressures of the deep Earth. The rheology of two-phase mixtures is important because most rocks consist of two or more phases and their behaviour cannot simply be described by interpolating between the end members. The change of the intracrystalline structure of deforming grains is the principal reason why deformed rocks may show different physical properties than undeformed rocks. Therefore, deformed single crystals or samples with very little strain are investigated because they show most clearly the active deformation mechanisms (*e.g.* slip systems). Dehydration reactions occurring during deformation may cause a drastic change in deformation mode, *e.g.*, from ductile to brittle behaviour. Physical properties such as electrical conductivity can be used to monitor the development of microstructure during experimental high strain deformation. However attention has to be given in this approach to which microstructural parameter is actually governing the change of physical behaviour.

a. *Experimental deformation of clinopyroxene-plagioclase aggregates (M. Bystricky/Zürich, in collaboration with F. Heidelbach)*

Clinopyroxene and plagioclase are essential constituents of the oceanic and lower continental crust, yet little is known of the mechanical properties of aggregates composed of these two phases. We have performed an experimental study on the high-temperature high-pressure deformation of two-phase aggregates of clinopyroxene and plagioclase. The rocks were synthesized from powders with homogeneous grain sizes prepared from crystals or monomineralic aggregates. Clinopyroxene powders were ground from pieces of Sleaford Bay diopsidite, while plagioclase powders were prepared from clean inclusion-free labradorite crystals. Powders of the minerals were intimately mixed in fixed ratios (25-75, 50-50, 75-25 vol.%), cold pressed and hot pressed at 300 MPa confining pressure for 6 to 10 h at 1100-1150 ºC.

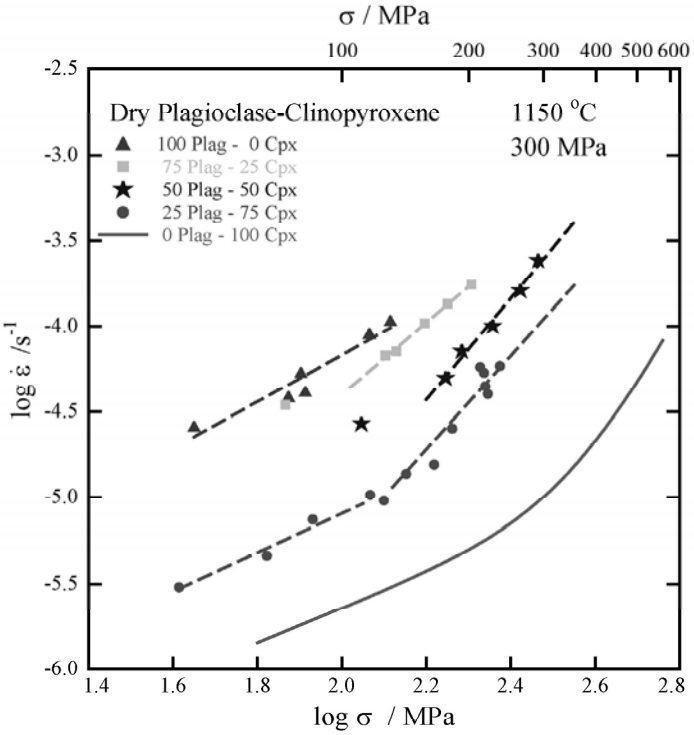

Fig. 3.1-1: Strain rate versus stress plot of creep data from experiments on dry plagioclase-clinopyroxene mixtures at 1150 °C and 300 MPa.

Essentially single-phase samples composed of diopside or labradorite with only about 1-2 % of a second phase (to buffer the activities of component oxides) were also prepared. All samples were deformed dry at constant stress in a Paterson deformation apparatus at a confining pressure of 300-400 MPa, 1050º to 1175ºC, with the oxygen fugacity buffered by Ni plus NiO powders. Differential stresses were maintained below 400 MPa to limit microcrack formation.

Mixed-mode deformation behaviour was observed in the pure end-members, with diffusional creep (n ~ 1) at lower stresses and a combination of diffusional and dislocation creep at high

stresses (n = 2-5) (Fig. 3.1-1). We determined activation energies for dislocation creep in diopside (760 kJ/mol) and an overall activation energy for plagioclase (480 kJ/mol). Two-phase samples had strengths that were intermediate between values determined for the end-members and fall within the bounds provided by the theoretical treatment of two-phase aggregates. Light and scanning electron microscopy analyses indicate intracrystalline deformation features in both phases. Electron backscattering diffraction analysis of the two-phase aggregates show the development of crystallographic preferred orientations (CPO): in diopside, a fiber texture develops with the pole to {110} in the fiber direction and a girdle of <001> perpendicular to it; anorthite has a pronounced maximum of <111> in the compression direction and a girdle of <100> perpendicular to it. These CPOs are consistent with the main slip systems in both phases and consistent with deformation in dislocation creep.

b. *Deformation texture in wadsleyite: implications for the seismic anisotropy of the upper transition zone (H. Couvy, A. Tommasi and D. Mainprice/Montpellier, P. Cordier/Lille and D.J. Frost)*

Seismic anisotropy in the Earth's mantle is generally believed to result from preferred orientations of crystals induced by plastic deformation related to mantle flow. The lack of information on the deformation of high-pressure minerals, however, has prevented modeling of seismic anisotropy in the transition zone. This study presents textures obtained from wadsleyite deformed in a multianvil apparatus at mantle pressures and temperatures as well as textures calculated using a viscoplastic self-consistent (VPSC) model. Based on these textures, the anisotropic seismic properties for the upper transition zone have been calculated.

Deformation experiments were performed in the 6-8 multianvil apparatus using a shear assembly. In this special assembly, a thin slice of synthesized polycrystalline wadsleyite (Mg_2SiO_4) with a platinum coating used as strain marker is sandwiched between two hard alumina pistons cut at 45°. Elastic strain stored in the sample column during compression is converted at high temperature to plastic shear strain in the sample. The samples were deformed at 16 GPa and 1400 °C for one and eight hours. Our approach is to combine two techniques to characterise the deformation. Electron backscattering diffraction (EBSD) in the scanning electron microscope (SEM) is used to characterise the crystallographic preferred orientation (CPO) of the recovered specimens and transmission electron microscopy (TEM) gives access to the dislocation microstructure and hence to the elementary mechanisms responsible for plastic strain.

The shear strain recorded by the strain marker is generally less than γ=0.4. The CPO produced in both one and eight hour experiments shows a concentration of the <100> axes close to the shear direction (X_0) and the <001> axes aligned toward the normal of the shear plane (Y_0) (Fig. 3.1-2). TEM analysis show that the deformation microstructure is dominated by [100] screw dislocations, but 1/2<111> dislocations are also common.

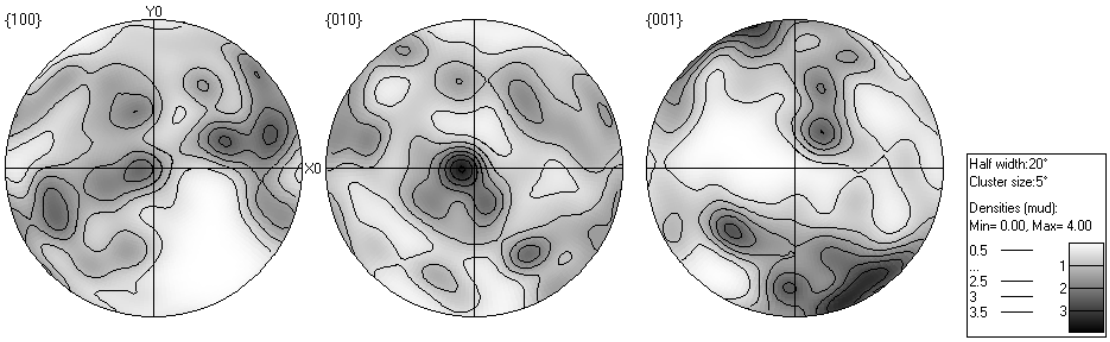

Fig. 3.1-2: Pole figures of crystal axis after eight hours of heating. X_0 is the shear direction and Y_0 is the normal of the shear plane; dextral shear.

Experimentally produced wadsleyite CPO is compared to the CPO evolution in VPSC simulations for simple shear and transpression. Several models are considered in which the relative critical resolved shear stresses (CRSS) for 1/2<111> and [100] slip systems varied. Experimental CPOs are best reproduced by transpression simulations. This agrees with EBSD measurements and microstructural characteristics, that indicate the best model for the CPO involves easy glide on [100](001) and 1/2<111>{101}.

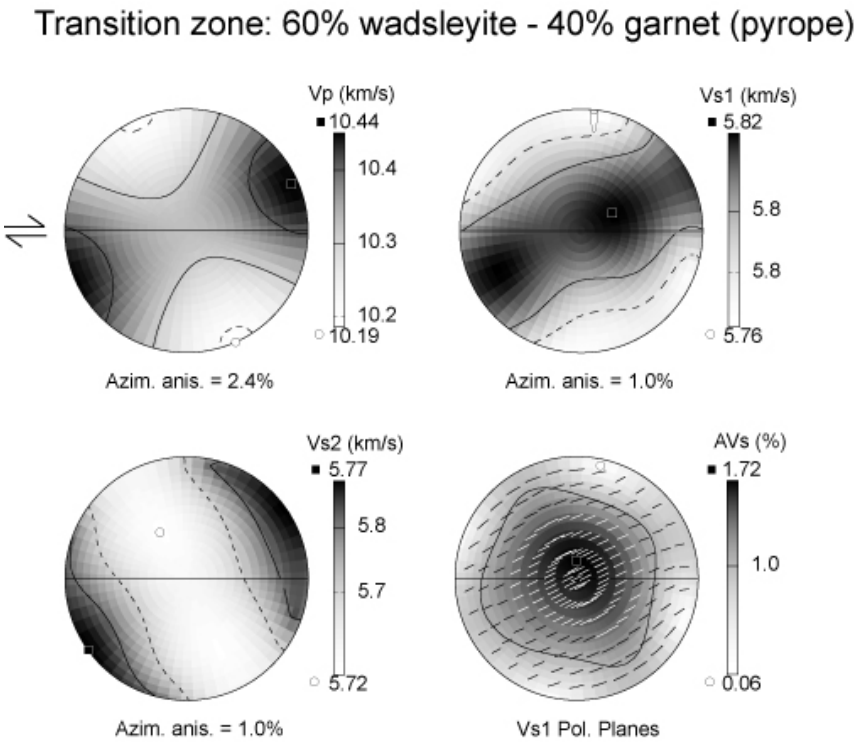

Fig. 3.1-3: Modeled three-dimensional compressional and shear waves velocity distributions, and shear wave polarization anisotropy (intensity and polarization direction of the fast shear wave). Lower hemisphere equal-area projections, contours at 0.1 km/s intervals for compressional waves, 0.02 km/s intervals for shear waves, and 0.5 % anisotropy intervals for shear waves polarization anisotropy.

The anisotropic seismic properties are calculated from the CPO simulated for a simple shear flow. Seismic anisotropy is weak even for the 100 % wadsleyite aggregates; azimuthal anisotropies are 4 % for P-waves and < 2 % for S-waves. Additionally, the anisotropic seismic properties of the upper transition zone are calculated for a 60 % wadsleyite-40 % garnet polycrystalline aggregate (Fig. 3.1-3). Addition of garnet leads to still weaker anisotropies (2.4 % for P-waves and ~ 1 % for S-waves). This seismic anisotropy is consistent with seismological observations of anisotropy in the transition zone on a global scale, if a tangential component dominates flow in the upper transition zone.

c. *Microstructure development during creep of MgO single crystals (E. Mariani and D. Prior/Liverpool, in collaboration with J. Mecklenburgh)*

Recrystallization processes and nucleation of new, strain-free grains during the deformation of rocks play an important role in controlling the rheology in the Earth's crust and upper mantle. Current kinematical models, aimed at understanding dynamic recrystallization and recovery in natural materials, are mainly based on two mechanisms: 1) sub-grain rotation recrystallization, and 2) grain boundary migration recrystallization. However, EBSD analyses of naturally deformed rocks have shown that the misorientation relationship observed between parent and recrystallized grains cannot be explained by the mechanisms of sub-grain rotation and grain boundary migration recrystallization alone. Thus, other processes that may exert an important control on the misorientation between host and recrystallized grains must be invoked.

In order to gain a better understanding of these processes we are carrying out a systematic experimental program involving the deformation of periclase single crystals and, ultimately, bicrystals (as analogues for parent grains) at different conditions of pressure, temperature, differential stress and strain rate. The study focuses on in-depth observation of the microstructures that develop during the experiments by means of powerful tools such as EBSD and TEM analyses.

MgO was chosen as the starting material because its simple NaCl structure and high melting temperature (2800 °C) allow a wide range of experimental conditions to be investigated. Also, with due caution, MgO may be used as an analogue for geological materials such as olivine and magnesiowüstite, which are abundant phases in the upper and lower mantle respectively.

As part of the preliminary stages of this study, two MgO single crystals (ps1 and ps2) were deformed in axial compression along ⟨100⟩ in a 1 atmosphere creep rig. Both specimens were tested at a temperature of 1400 °C, stress of 30 MPa and up to 20 % and 14 % strain respectively. Quasi steady state strain rates of 2.8×10^{-7} s^{-1} were measured. Both specimens deformed non-homogeneously. The microstructures of the two samples were investigated using automated electron backscatter diffraction mapping (EBSD). Orientation maps of sections cut parallel to the specimens axes, *i.e.* the loading direction, show continuous misorientation across the crystals from a reference orientation (Fig. 3.1-4a).

The maximum deviation angles measured are 22° and 27° for ps2 and ps1 respectively. While in ps2 (14 % strain) very little substructure can be observed, sample ps1 (20 % strain) shows higher substructure density and low angle boundaries (1° to 5°). These are likely to have formed by climb assisted dislocation glide of dislocations. In both specimens continuous small circle dispersion of the poles to {111}, {110} and {100}, with a rational crystallographic axis as the rotation axis (Fig. 3.1-4b), suggests that the {111}[110], {110}[110] and {100}[110] slip systems might have been concurrently active during deformation. Strain and temperature dependence of the microstructure in MgO single crystals will be investigated further by means of more creep and confined experiments, EBSD and TEM work.

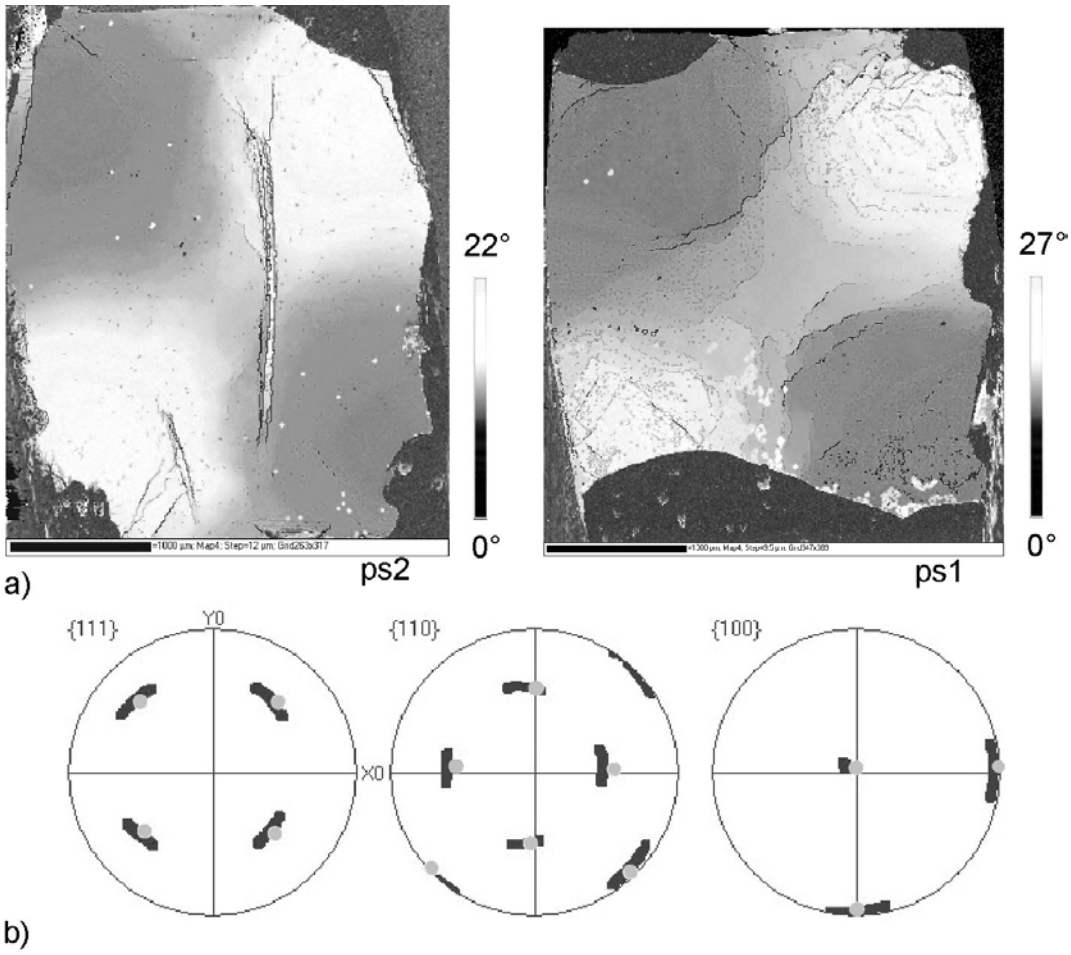

Fig. 3.1-4: a) Texture component maps, obtained from orientation maps of samples ps2 (left) and ps1 (right). The gray scale gradient shows the deviation of orientations measured across the samples from a reference orientation. Gray and black lines represent low angle boundaries between 1° and 2° and 2° and 5° respectively. The loading direction is vertical. The scale bar is 1 mm. b) Pole figures of the crystallographic planes {111}, {110} and {100} obtained from the orientation map of sample ps1 (black squares). The gray dots represent the orientation of the same planes measured in the starting material before deformation. The loading direction is parallel to Y0.

d. *Intracrystalline deformation microstructures in experimentally sheared magnesiowüstite (F. Heidelbach and F. Langenhorst)*

Magnesiowüstite presumably comprises 15 to 20 % of the lower mantle and is very likely the weakest material in this vast region of the Earth. The rheology of this material is therefore of great interest if we try to understand deformation and convection in the deep Earth. We investigated the microstructures in a series of polycrystalline samples of (Mg,Fe)O that were deformed to up high shear strains ($\gamma \leq 15$) in torsion. The temperature was 1400 K, the confining pressure was 300 MPa and the strain rate was 2×10^{-3} s^{-1}. The Fe-content was varied from 20 to 50 at.%. Mechanical and textural data from these samples were described in last year's annual report.

Analysis with electron backscattering diffraction (EBSD) in the SEM revealed that a crystallographic preferred orientation (texture) developed in all the samples indicating that dislocation creep contributes significantly to the deformation. At higher strains (> 3) deformation is also accompanied in all samples by grain size reduction. At low strains the interiors of grains show a continuous bending of the crystallographic lattice with changes in orientation of less than 1° per 1µm step. Orientation gradients are more pronounced towards the rim of deformed grains (Fig. 3.1-5) where also the formation of discrete subgrain boundaries appears first. The overall orientation change due to the bending can be described

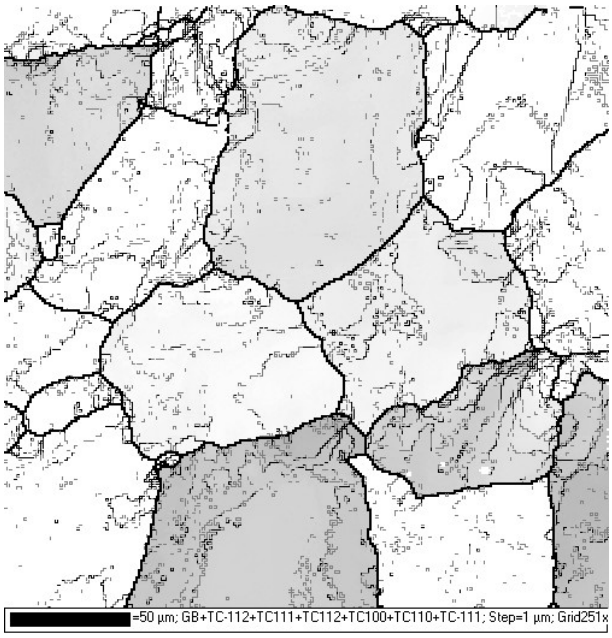

Fig. 3.1-5: Map of the subgrain structure in $Mg_{0.5}Fe_{0.5}O$ deformed to γ=1 generated with SEM-EBSD; shear is dextral and thick black lines indicate grain boundaries with misorientation angles > 10°; thin black lines mark misorientations > 0.7°; gray shading of selected grains shows orientation gradients.

by a rotation about the intermediate axis of the kinematic reference frame, *i.e.*, an axis in the shear plane and perpendicular to the shear direction. The rotation axes for the small misorientations do not show any preferred orientation relative to the crystal axes indicating that bending of the lattice is determined by the external kinematic frame. This is probably

facilitated by the large number of slip systems available in this material. With higher shear strains the continuous lattice bending is replaced by discrete subgrain boundaries which form a network and ultimately lead to a reduction in grain size. Transmission Electron Microscopy (TEM) of magnesiowüstite reveals relatively low dislocation densities in samples with higher Fe content as well as subgrain walls with very low misorientation angles (Fig. 3.1-6a, b). The direction of the Burgers vector for all dislocations is <110>. In high resolution a spotty contrast becomes visible in all samples independent of iron content, which is interpreted to be due to clusters of point defects (Fig. 3.1-6c). The Fe^{3+} content was determined by energy loss spectroscopy (ELNES) to lie between 2 and 4 % for all samples, yielding a sufficient number of point defects to cause the spotty contrast in high resolution.

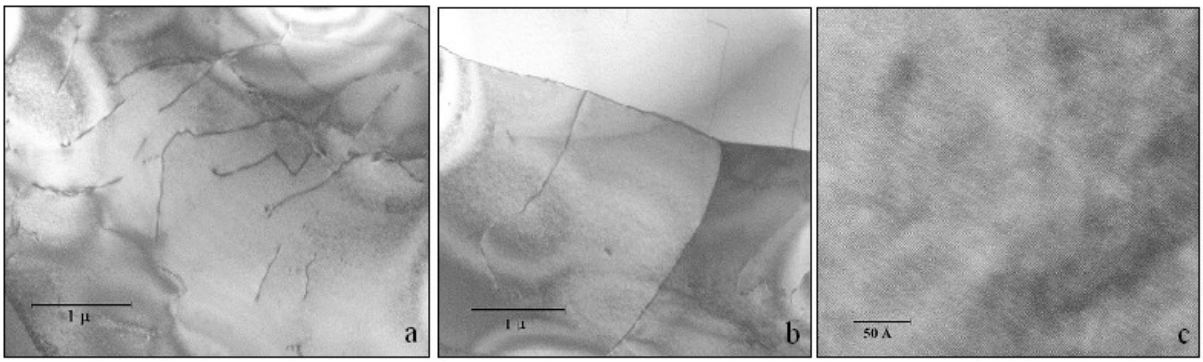

Fig. 3.1-6: TEM micrographs of $Mg_{0.5}Fe_{0.5}O$ deformed to γ=1; a) dislocation lines in bright field contrast; b) subgrain wall with low misorientation angle; c) high resolution image showing spotty contrast due to point defect clusters.

Increasing the iron content of magnesiowüstite at constant temperature causes enhanced grain boundary mobility (as reflected in the larger grain size), lower dislocation densities and slower texture development. The relative increase of the point defect density is likely to support deformation by diffusional processes relative to dislocation creep.

e. *Crystal-plastic deformation of quartz around the freezing point? (M. Bestmann, H. Rice and B. Grasemann/Vienna, in collaboration with F. Heidelbach)*

The microstructures of a quartzitic sandstone deformed under a Neoproterozoic glacier, Northern Norway, was studied by electron backscatter diffraction (EBSD) and cathodoluminescence (CL) in the scanning electron microscope. The overall aim of the project is the investigation and characterisation of possible deformation mechanisms for the formation of low-temperature microstructures in quartz, similar to crystal-plastic deformation features. Crystal-plasticity, where strain is accommodated by the activity of dislocation systems, is usually associated with high-temperature (*i.e.* $T/T_M > 0.3$) deformation. However,

dislocations can be active at lower temperatures, particular at the slow strain rate rates expected during geological deformation, resulting in such ubiquitous intracrystalline microstructures as undulose extinction and deformation lamellae. However, there is general agreement that crystal-plastic deformation of quartz does not occur at low temperatures around the freezing point.

The analysed microstructure is characterised in optical microscopy by a fine-grained quartz cataclastic zone (lower part of Fig. 3.1-7a) and by pronounced undulatory extinction, accompanied with patchy grain segmentation. Orientation maps constrained by EBSD data reveal lattice banding, subgrain boundaries, dauphine twin boundaries and the development of new small grains (Fig. 3.1-7c).

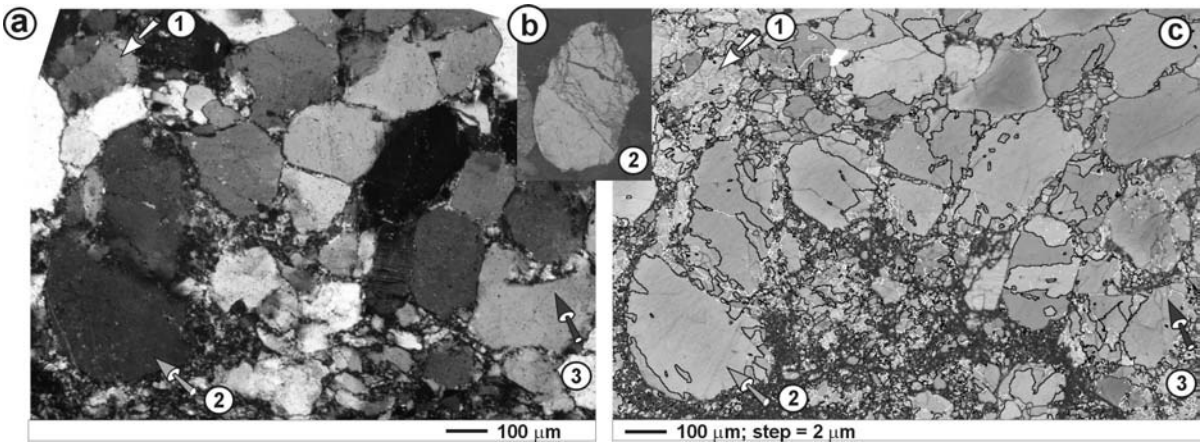

Fig. 3.1-7: (a) Optical micrograph of low-temperature deformation microstructure. (b) SEM-CL image of grain (2). (c) EBSD orientation map (band contrast mode; white lines indicate subgrains boundaries with misorientation angle 2-15°, thin black lines grain boundaries > 15° and thick black lines Dauphine twin boundaries). Arrows and number indicate individual analysed grains presented in Fig. 3.1-8.

New small grains have a similar crystallographic orientation as their host grain (Fig. 3.1-8b). The SEM-CL image shows that some of the deformation microstructures are related to microcracks (Fig. 3.1-7b). However, analysis of misorientation axes indicate, at least for some of the deformed quartz grains, a preferred orientation of misorientation axes (POMA) of subgrain boundaries with respect to the crystal reference frame (Fig. 3.1-8a).

These intracrystalline POMA features are characteristic for crystal-plastic deformation. However, it can not be ruled out that microcracks are related to specific crystallographic orientations and caused a crystallographically controlled block rotation on the microscale. Further investigation by transmission electron microscopy (TEM) should provide information about the possibility of crystal plastic deformation in quartz during glacial freezing condition.

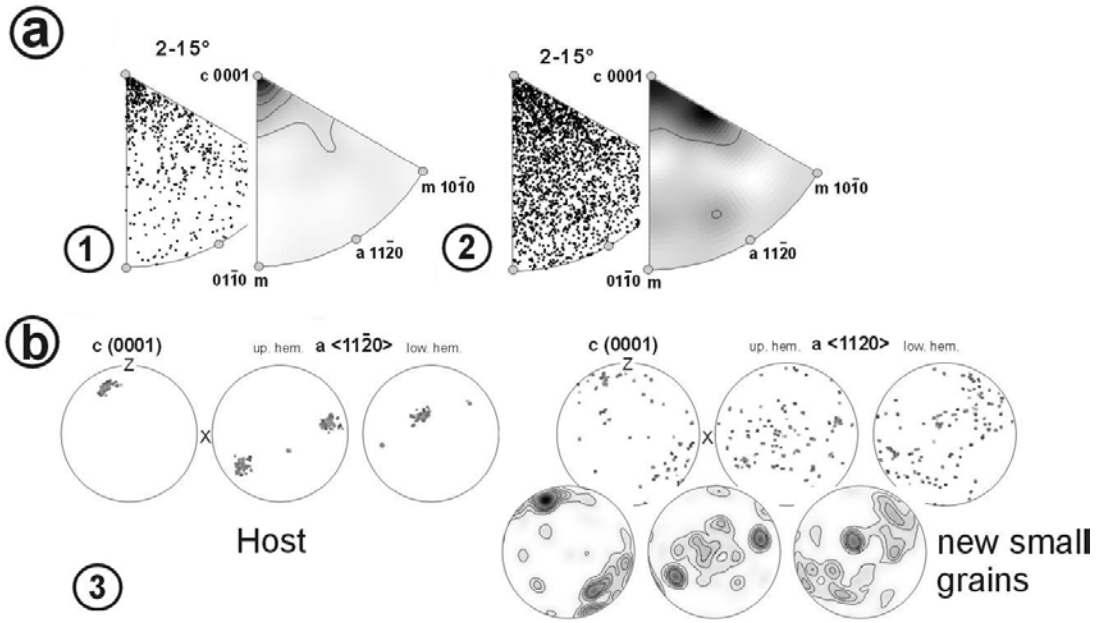

Fig. 3.1-8: (a) Distribution of misorientation axes of subgrain boundaries within grain 1 and 2, as marked in Fig. 3.1-7. Inverse pole figures are plotted with respect to the crystal reference frame. (b) Crystallographic orientation of grain 3. Host and new small grains are presented.

f. *Deformation and dehydration interactions in serpentinite under orogenic conditions (K. Neufeld and I.C. Stretton, in collaboration with S.J. Mackwell/Houston)*

Serpentinite rocks are very common in subduction and orogenic environments. The physical and mechanical properties of such rocks depend strongly on their degree of dehydration which can lead to remarkable changes in the deformation behaviour of the involved rock masses. This study is focused on the interplay between deformation and dehydration processes in serpentinite rocks in an orogenic environment, a research area that has been neglected up to now in serpentinte deformation studies, a field in which previous studies were focused mainly on subduction conditions.

The starting material for all experiments was an approximately 95 % pure serpentinite from the Bergell/Val Malenco area in the Swiss and Italian Alps. The rock is composed primarily of antigorite which occurs as fine laths approx 20 µm by 5 µm with a random shape preferred orientation. Also small amounts of chrysotile, spinel and magnetite were observed. This rock is part of the Val Malenco serpentinite complex, in which ultramafic rocks are connected with the mainly granitic Bergell intrusion. For this reason the studied material can be seen as a characteristic example for the combined influence of deformation and dehydration in a contact metamorphic environment (orogenic conditions).

Experiments in a Paterson deformation apparatus were performed up to a maximum of 300 MPa confining pressure (P_c) and temperatures (T) between 700 and 1200 K to produce

dehydration in a measurable period of time (see BGI annual report 2001 and 2002). Strain rates down to 6 x 10^{-7} s^{-1} were applied. For all experiments small cylinders of 25 mm in length and 10 mm in diameter were prepared. The water content was measured after the experiments by Karl-Fischer-Titration of small areas of the samples which were separately ground into powders.

Deformation experiments so far indicate a strong interaction between deformation and dehydration in the brittle deformation regime. Intense fracturing of the samples causes strong gradients of the water content inside partly dehydrated samples, suggesting fluid flow induced by deformation (Fig. 3.1-9).

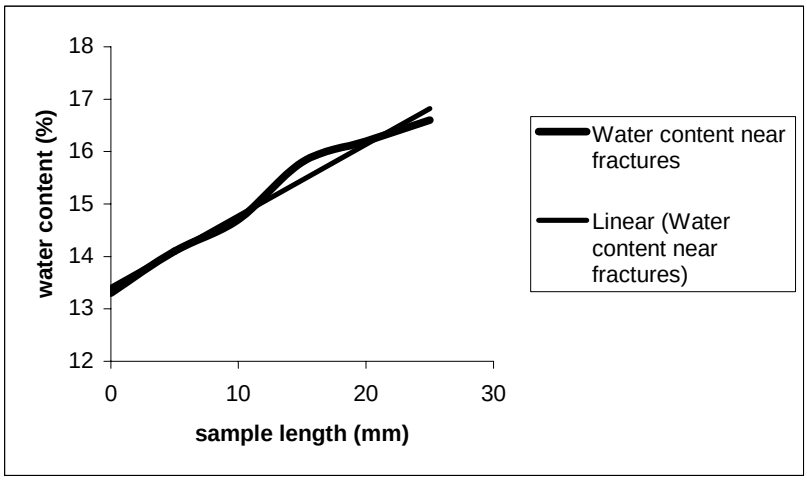

Fig. 3.1-9: Average of the water content along brittle fractures in a cross section of a deformed cylinder suggesting water flow along fracture zones (black line); the sample size was 25 mm in length and 10 mm in diameter; experimental conditions were P_c: 300 MPa, T: 930 K, heating time: 1 h, strain rate: 6 x 10^{-6} s^{-1}, undrained conditions.

This clear effect was observed in samples dehydrated under drained conditions just as much as under undrained conditions independently of temperature or pressure variations. Further experiments have to be carried out at varying temperatures above 1000 K, constant applied stress under drained and undrained conditions and a stepwise reduction of the effective pressure, controlled by pore water pressure. The aim is to obtain an overall picture of contact metamorphic process during serpentinite deformation and dehydration.

g. *Electrical conductivity of marbles during torsion (J. Mecklenburgh, F. Heidelbach and F. Gaillard)*

During high strain plastic deformation the microstructure of materials is generally affected by grain size reduction (dynamic recrystallisation), the generation of a crystallographic preferred orientation (CPO) and a drastic change of the grain boundary structure. This evolution of the

microstructure may have a strong effect on the strength of the material, but it is commonly not possible to analyze the microstructure of deformed materials *in situ, i.e.* during the deformation experiment. However, by measuring some physical property that is sensitive to the microstructure one can indirectly probe the microstructure during deformation. Electrical conductivity is a second rank tensor so consequently there is anisotropy in all but cubic materials. Hence the creation of a CPO in non-cubic materials results in a change in the bulk electrical conductivity tensor of a polycrystalline material. In addition, if the grain boundary and lattice conductivity are very different a change in the grain size or grain boundary structure could affect the bulk conductivity of a polycrystalline rock. In order to test the applicability of such an approach, preliminary experiments have been carried out to measure the electrical conductivity of marbles during high strain deformation in torsion.

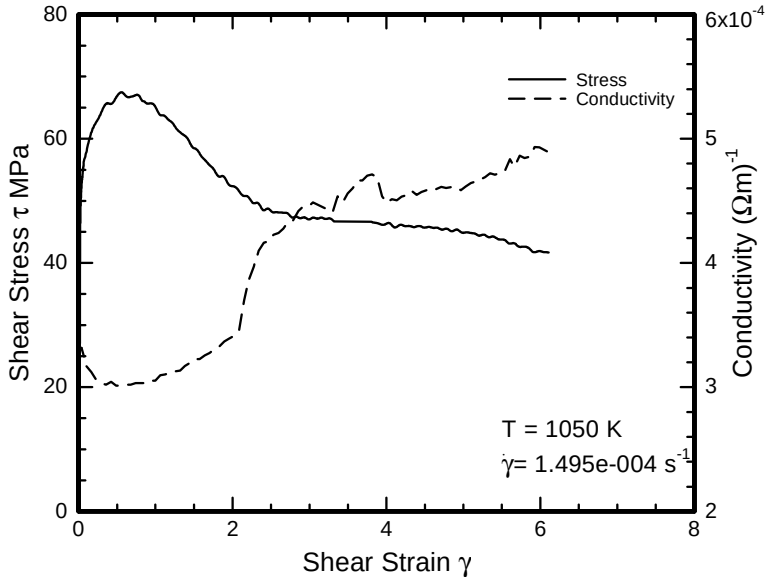

Fig. 3.1-10: Graph showing the evolution of strength and electrical conductivity with strain of a Carrara marble sample deformed to high strain.

Carrara marble was chosen as the starting material as it has been used extensively for deformation studies and a large amount of data on the microstructural evolution of this material during deformation is available. Hollow cylindrical samples were prepared and iron cylinders were made to fit inside the hollow samples. The sample was jacketed inside an iron sleeve and placed into the Paterson gas medium deformation apparatus. During torsion deformation the sample was twisted about its vertical axis hence the shear direction lies parallel to the circumference and perpendicular to the axis of the sample and the shear plane is perpendicular to the axis of the sample. The electrical conductivity was measured between the sample jacket and the inner iron core of the sample assembly. Thus the measurement was made parallel to the shear plane and perpendicular to the shear direction. Experiments have been performed at 1050 K to a shear strain of 6.5 at a strain rate of 10^{-4} s^{-1}.

During deformation the marble sample showed a dramatic drop in strength with a concurrent increase in the electrical conductivity (Fig. 3.1-10). Analysis of the starting and final microstructure shows the initially weakly textured marble develops a strong CPO aligning the $\{2\bar{1}\bar{1}0\}$ poles (=<a>) parallel to the shear direction (Fig. 3.1-11a). Using published data for

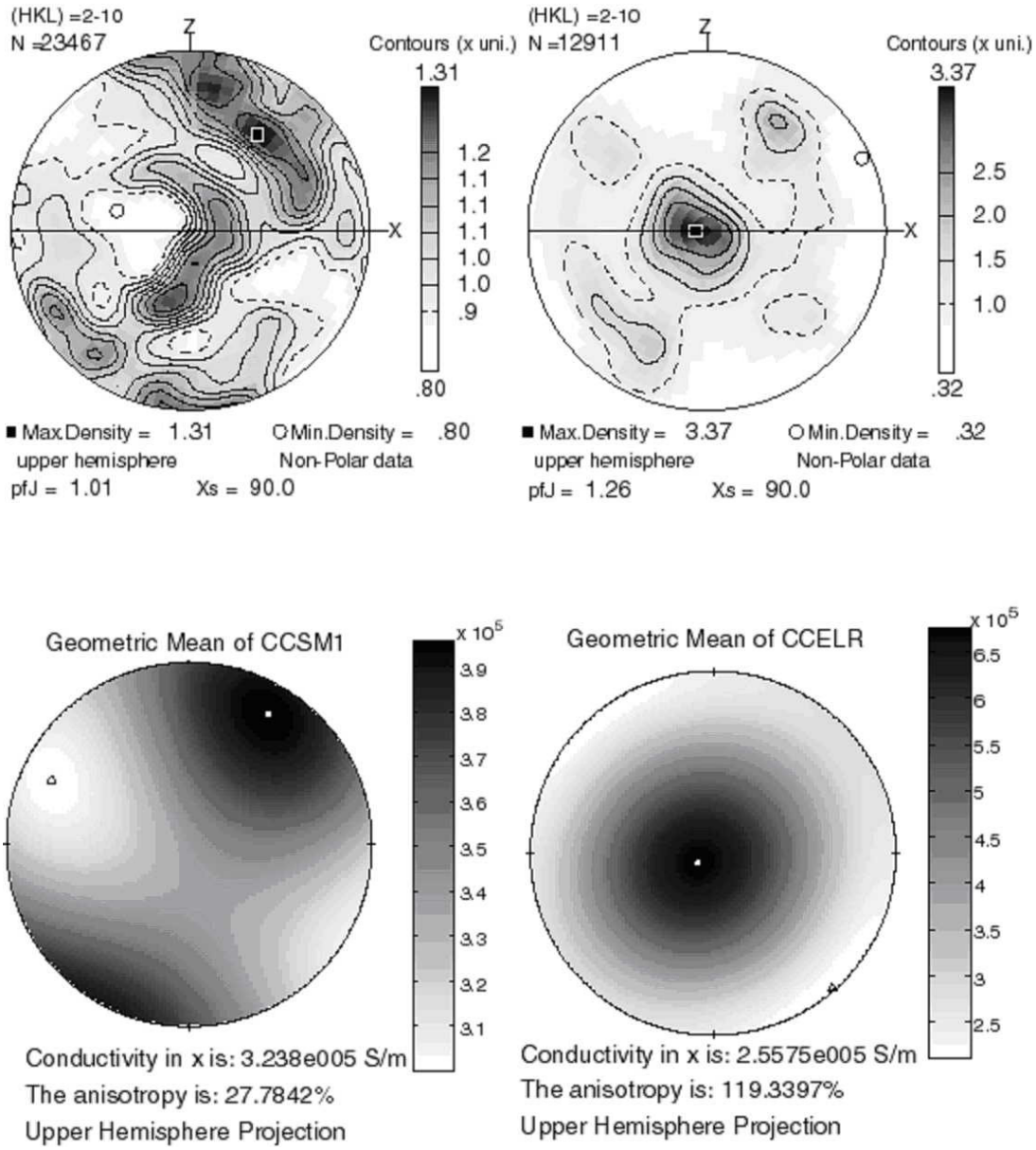

Fig. 3.1-11: Top: $\{2\bar{1}\bar{1}0\}$ pole figures of undeformed Carrara marble (left) and Carrara marble deformed to a shear strain of ~ 6 (right); the shear plane is marked by the horizontal line and the shear direction is coming out of the page; electrical conductivity was measured in the x direction. Bottom: Stereographic projections of the calculated bulk electrical conductivity of undeformed (left) and deformed (right) Carrara marble; the triangle and circle mark the minimum and maximum conductivity respectively.

the conductivity tensor of single crystal calcite and the CPO, the bulk conductivity tensor of the starting material and the deformed sample were calculated. Since the <a> is the most conductive direction for the calcite structure, the maxima of $\{2\bar{1}\bar{1}0\}$ poles parallel to the shear direction corresponds to the maximum in the conductivity (Fig. 3.1-11b). However, in the direction of the conductivity measurement (x) the electrical conductivity is predicted to decrease from 0.32 to 0.26 MSm^{-1} due to the deformation. This is inconsistent with the observed data in which the conductivity goes up as a result of the deformation. Hence the development of a LPO cannot explain the observed change in conductivity.

Along with the creation of a CPO the sample undergoes dynamic recrystallisation, dramatically reducing the grain size from ~ 150 µm to 10 µm. If the electrical conductivity in the grain boundaries is greater than through the crystal lattice, then reducing the grain size (and increasing the number of grain boundaries) will yield an increase in the electrical conductivity assuming that the grain boundary thickness remains constant.

3.2 Physical Properties of Minerals

Many geological and geophysical surface or near surface features are the result of dynamic processes in the Earth's interior. These include consequences of plate tectonics, like volcanism, earthquakes, or mountain building, the long term chemical evolution of the Earth, as well as our planet's magnetic field. While we understand in general terms that these processes are a consequence of the ongoing heat transport from the interior to the surface of the Earth, and are governed by convection in the Earth's mantle and the liquid outer core, elucidating further details of the underlying causes and forces is one of the central goals in deep Earth sciences.

Geophysical inverse methods, such as seismology and magnetotellurics, provide an ever clearer picture of the internal structure of the Earth, providing a snapshot of these deep Earth processes. In order to interpret such pictures, and to relate geophysical observations and geodynamical processes in the Earth in general, physical properties of relevant deep Earth materials must be known, ranging from elastic and electromagnetic properties, to viscosity. Since the material in the Earth's interior is not accessible to direct measurements, mineral physics is utilized by performing experiments and simulations at conditions of pressure and temperature approaching those in the Earth's deep interior, providing a critical link between physical processes in the Earth and geophysical observations. In addition, mineral physics is used to analyze and understand macroscopic phenomena from an atomistic point of view.

The Bayerisches Geoinstitut has and will continue to contribute significantly to these efforts, determining key physical properties for minerals at ambient conditions as well as high pressure. Contributions in this section cover a wide range of physical phenomena, analyzing elastic, compressive, and magnetic properties, as well as thermal expansion at elevated pressure.

Compressive behaviour and single crystal elastic properties of minerals are the main physical properties necessary in understanding the seismic images of the Earth's interior. The first contribution examines the influence of phase distribution on aggregate elasticity, addressing the important question of strain partitioning between the mineral phases composing a rock. Two equation of state measurements deal with quite different silicate materials: The kosmochlor-diopside pyroxene join is studied to understand pressure-temperature conditions of formation of kosmochlor-containing meteorites. Edingtonite, a Ba-containing zeolite, is compressed to understand the response of microporous media to pressure. Accurate measurement of thermal expansivity of ringwoodite and phase equilibria of the α-PbO_2 phase of TiO_2 allow to determine more accurately thermodynamic properties of minerals at high pressure and temperature. The first measurements of single crystal elastic constants with the GHz ultrasonic setup in the diamond anvil cell at the Bayerisches Geoinstitut have now been performed. In this yearbook two studies are presented: elastic constant measurements of

magnetite (Fe_3O_4) as a function of pressure, and on the wüstite-periclase solid solution, both as a function of composition and pressure.

The importance of magnetism on phase stability and the thermodynamics of minerals, in particular the effect of its loss under compression, has only been recognized in the past few years. Research at the Bayerisches Geoinstitut is contributing significantly to its understanding. Here, the magnetic properties of two prototypical magnetic materials are studied that are of central importance in the Earth and material sciences, iron and FeO wüstite. The section concludes with a contribution that analyzes the lamellar magnetism in the ilmenite-hematite series. An understanding of the unusually strong magnetic susceptibility is very important for paleomagnetism, a central tool in determining plate motions, coming back to the theme of dynamic processes in and on the Earth, raised in the first paragraph above.

a. *The influence of phase distribution on the elastic properties of polymineralic aggregates (P.F. Schofield/London, S.J. Covey-Crump/Manchester, M.R. Daymond/Chilton, I.C. Stretton and K.S. Knight/Chilton)*

An understanding of the composition, structure, and ultimately, the dynamics of Earth's interior, is of fundamental importance in Earth sciences, because it is the dynamics of the Earth's interior which controls the majority of processes occurring at the Earth's surface. The primary source of information about its composition and structure comes from attempts to match the geophysically observed seismic velocity structure of the Earth with the velocities calculated from the experimentally determined elastic properties of the rock types which are likely to be present. The main uncertainty in this process lies in the experimental measurements because although the single crystal elastic properties of all the important rock-forming minerals are relatively well established, the influence of microstructural variables (*e.g.*, texture, grain size and shape) on those elastic properties, is less well constrained. We have been developing a method for examining the influence of microstructural variables on the elastic properties of polycrystalline materials by performing *in situ* neutron diffraction experiments on samples that are under an applied load. We have demonstrated the validity of the method by measuring the elastic strains in both phases of a randomly intermixed, microstructurally isotropic, two-phase sample of olivine (54 vol.%) and magnesiowüstite (46 vol.%), and verifying that they lay between the tightly defined Hashin-Shtrikman bounds for this material. Subsequently, we applied the technique to an olivine+orthopyroxene sample which contained a strong crystallographic texture but in which the two phases were randomly intermixed. These studies have been extended here to investigate how variations in the spatial distribution of the phases influence the elastic properties of materials in which none of the phases have a lattice preferred orientation.

Since a suite of samples which are compositionally and microstructurally identical apart from the spatial distributions of the phases cannot easily be found, we fabricated our own samples

by hot isostatically pressing powders of olivine (ol) and magnesiowüstite (mw). We made three samples containing 70 %, 80 %, and 90 % olivine respectively, in which both phases were fully intermixed. This was to establish how elastic strain partitioning between the phases changes as the connectivity of one of the phases is lost. Further samples were also made in layer and column form (see Fig. 3.2-1). Each layer or column was not single phase but was itself a two-phase mixture, *e.g.*, in one of the layered samples, one layer type was 30:70 ol:mw whereas the other layer type was 70:30 ol:mw. In this way, a further six samples, which each had a bulk composition of 50:50 ol:mw but which had very different spatial distributions of the phases, were made. The hot-isostatic pressing conditions were 300 MPa and 1500 K for 6 hours, and resulted in fully dense samples in which the mean grain size of both phases was 30 µm, and where there were no grain shape fabrics or lattice preferred orientations induced.

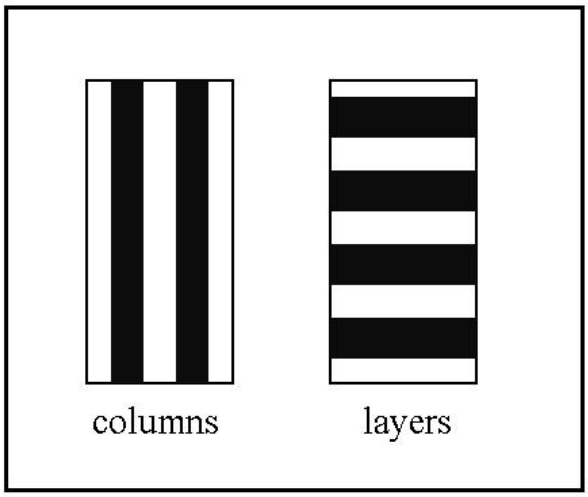

Fig. 3.2-1: Representation of the layer and column structure of six of the ol:mw samples (layer thickness much exaggerated).

In each neutron experiment a right circular cylindrical sample was loaded uniaxially in compression. Neutron diffraction patterns were collected at several different loads up to 15kN from a voxel 5x5x1.5mm in the centre of the sample. The geometry of the experimental set up was such that the diffraction patterns obtained from the two detectors yielded the lattice parameters parallel and normal to the loading direction respectively. Despite the large difference in spatial distributions of the phases in the samples, the strain partitioning between the phases was always close to, or within, the Hashin-Shtrikman bounds for an isotropic composite of the same bulk composition. The results for the three randomly intermixed samples of differing phase proportions are shown in Fig. 3.2-2. However, analysis of the strains in the different lattice directions of the olivine shows that the way in which this strain was accommodated within the olivine was very sensitive to phase distribution. Detailed microstructural analysis of the experimental samples is presently being performed to establish how the observed variation of ‘within olivine’ strain partitioning (*i.e.* strain partitioning

between olivine grains of different crystallographic orientation) correlates with phase connectivity.

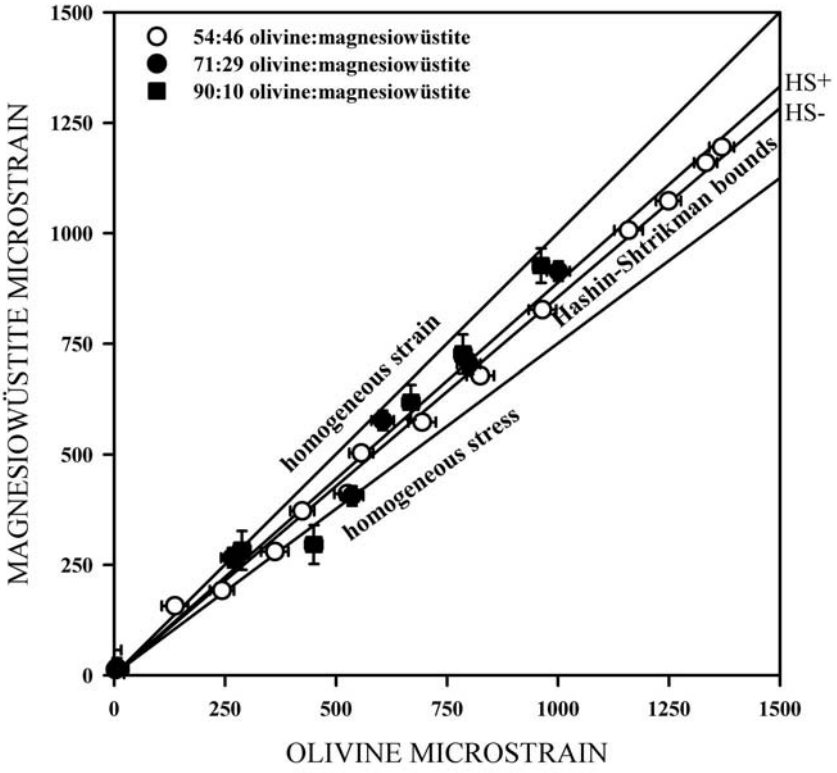

Fig. 3.2-2: Comparison of the ol and mw strains parallel to the loading direction. HS+ and HS- are the upper and lower limits on the phase average strain partitioning predicted by Hashin-Shtrikman. Open circles, filled circles and filled squares are 54:46, 71:29, and 90:10 ol:mw respectively.

b. *The compressional behaviour of kosmochlor-diopside solid solution (T. Boffa Ballaran, F. Nestola and M. Tribaudino/Torino)*

Great interest in kosmochlor ($NaCrSi_2O_6$)-bearing pyroxenes has arisen due to the possibility of using Cr^{3+} contents in natural samples to estimate the *P-T* conditions of formation of meteorites. A detailed analysis of the effect of Cr on the pressure-volume relationship in pyroxenes is, therefore, necessary to perform correct modelling of the thermodynamics at high pressure. The pyroxenes studied belong to the kosmochlor-diopside ($CaMgSi_2O_6$) system. The coupled substitution of Na for Ca and of Cr for Mg in the kosmochlor-diopside solid solution gives the opportunity to investigate the influence of $[M2]^{+}[M1]^{3+}$ cation substitution on the compressibility of a $[M2]^{2+}[M1]^{2+}$ pyroxene structure at high pressure.

A single crystal of pure $NaCrSi_2O_6$ [Ks_{100}] has been studied by *in situ* high-pressure X-ray diffraction up to 7.5 GPa. Single crystals belonging to the kosmochlor-diopside system with compositions $Na_{0.75}Ca_{0.25}Cr_{0.75}Mg_{0.25}Si_2O_6$ [$Ks_{25}Di_{75}$] and $Na_{0.25}Ca_{0.75}Cr_{0.25}Mg_{0.75}Si_2O_6$

[$Ks_{75}Di_{25}$] are at present under investigation and their unit-cell parameters have so far been measured up to 3 GPa. The compressibility of these pyroxenes decreases with increasing kosmochlor content (Fig. 3.2-3), with diopside having the smallest bulk modulus (K_0=104.1 GPa) and kosmochlor the largest (K_0=130.7 GPa). This is due to a change in compressibility of the *b*-axis which is the most compressible of the unit-cell axes in diopside, but becomes less compressible as Na and Cr contents increase. The coupled substitution of Na and Cr for Ca and Mg increases the structural stiffness; comparison with previous data on C2/c pyroxenes with transition metals in the M1 site suggests that this is related to Cr substitution.

The increase of the bulk modulus with pressure (as defined by *K*') is larger for diopside than for kosmochlor, and, extrapolated from our preliminary results, above 15 GPa and at 25 °C the diopside structure becomes stiffer than kosmochlor.

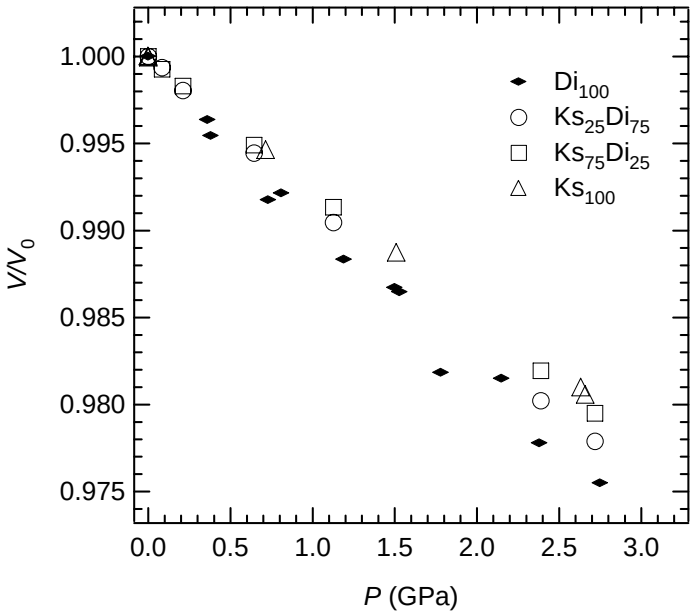

Fig. 3.2-3: Volume compressibility along the diopside-kosmochlor join. (Data for diopside are from Zhang *et al.*, Am. Min. 82, 245-258, 1997).

c. *Effect of Si/Al-ordering on the elastic behaviour of isomorphic framework silicates: pressure behaviour of orthorhombic and tetragonal edingtonite (G.D. Gatta and T. Boffa Ballaran, in collaboration with P. Comodi and P.F. Zanazzi/Perugia)*

Microporous and mesoporous materials are receiving increasing attention due to their applications in many industrial fields (*e.g.* radioactive waste isolation, agronomy, wastewater treatment, and petro-chemistry). There are many studies on thermal behaviour and catalytic activity of natural zeolites. However, studies of their behaviour with pressure are scarce. The presence of open cavities and channels make these materials very suitable for detailed investigations of phenomena concerning polyhedral tilt transitions. High-pressure (H*P*) studies can provide crucial information on the fundamental deformation mechanisms of framework microporous materials.

The behaviour with pressure of a natural Ba-containing zeolite, edingtonite ($Ba_2Al_4Si_6O_{20}\cdot 8H_2O$), was investigated by single-crystal X-ray diffraction up to 6 GPa. We have analysed the main deformation mechanisms and the different roles of the framework and extra-framework cations (and molecules) as well as the effects of the lattice microporosity on compressibility, using different pressure transmitting media: *a*) non-penetrating anhydrous media, in order to avoid super-hydration of the zeolite samples; *b*) hydrous media, to force water molecules to fill the channels.

Edingtonite is a fibrous zeolite with two isomorphic crystal structures: orthorhombic and tetragonal. The difference between the orthorhombic (O) and tetragonal (T) edingtonite is due to Si/Al-ordering into the tetrahedral sites. In both symmetries, the extra-framework content lies in the [001]-channels (Fig. 3.2-4). The crystal framework is based on a 4=1 Secondary Building Unit (SBU) consisting of four-member tetrahedral rings joined by a fifth tetrahedron to form [001]-chains. At room conditions, the Ba-extra-framework site is split into two sites ~ 0.3-0.4 Å apart.

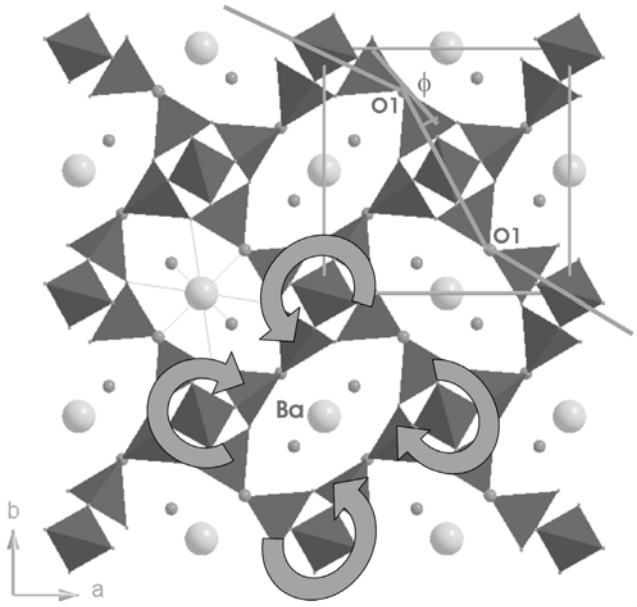

Fig. 3.2-4: Projection of the crystal structure of edingtonite viewed down [001]. The large spheres represent the extra-framework cation sites, whereas the small spheres represent the oxygen of the water molecules. High-pressures structural effects due to pressure increasing is shown (SBU-antirotation mechanism).

Glycerol, as a non-penetrating pressure medium, was used for the H*P*-experiment on the T-edingtonite. Cell volume data were fitted using a third-order Birch-Murnaghan equation of state (BM-EoS): V_0=601.6(3) $Å^3$, K_{T0}=59(2) GPa and K'=3.4(8). A second experiment was conducted using a methanol:ethanol:water (16:3:1) mixture, as a nominally penetrating

medium, for both T and O-specimens. No over-hydration effect has been observed within the pressure range investigated. Fitting the volume data of O and T-edingtonite with a third order BM-EoS we obtain: V_0 = 598.70(7) Å^3, K_{T0} = 59(1) GPa and K'= 3.9(4) for O-edingtonite and V_0=600.9(2) Å^3, K_{T0}=59(1)GPa and K'=4.2(5) for T-edingtonite. The EoS of T-edingtonite appears to be the same in the two different pressure media and also similar to the EoS obtained for the O-sample. As a first approximation, the lattice compressibilities of these two isomorphic silicates show that the Si/Al-distribution does not influence their elastic behaviour.

The evolution of the crystal structure was studied by comparing the results of refined data, collected at different pressures. The compressional behaviour of the tetrahedral framework in O- and T-edingtonite, represented by SBU bulk moduli, show that the different Si/Al-ordering slightly influences the elastic behaviour of the tetrahedral framework at H*P*-conditions, even though this effect is not evident in lattice compressibility. The different SBU-volume variations with pressure are probably due to the different tetrahedral tilting, leading to two different bulk modulus values (128(8) and 111(4) GPa for O- and T-edingtonite respectively.

The relevant structural variations are produced by cooperative rotation of the SBUs along [001]. The extra-framework content shows an interesting behaviour at H*P*-conditions: the occupancy of the split Ba2 site decreases with pressure and at P > 2.5 GPa the Ba2 site is completely empty, only the position Ba1 is occupied (Fig. 3.2-5).

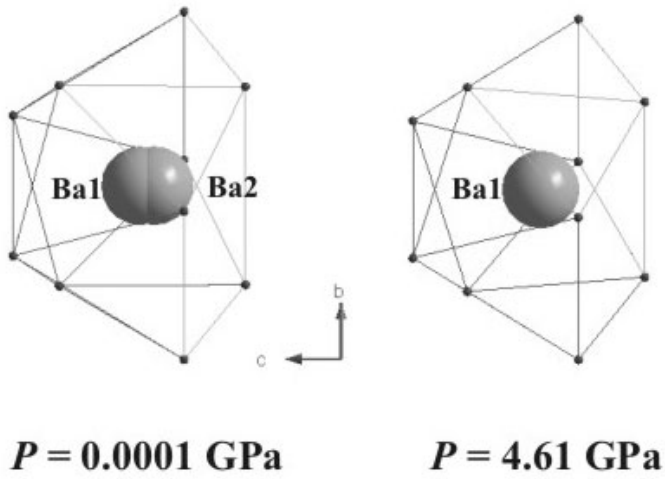

Fig. 3.2-5: Topological modification of Ba-polyhedron at high-pressure condition

Finally, our results show that the general bulk structure compression of the microporous silicates is a combination of "soft" behaviour of the channels and rigid behaviour of the tetrahedral framework and that the compressibility of these materials follows specific deformation mechanisms characterized by rotation of stiff tetrahedra and undistorted, but flexible, oxygen hinges.

d. *Thermal expansion of Mg_2SiO_4 ringwoodite (D.J. Frost and T. Boffa-Ballaran)*

Seismic discontinuities observed at 520 and 660 km depth likely arise from phase transformations involving the high-pressure phase $(Mg,Fe)_2SiO_4$ ringwoodite. If the stability field of ringwoodite can be accurately determined then information on the likely temperature and composition of the mantle can be extracted from seismic observations. A useful approach is to refine thermodynamic parameters using high-pressure experimental phase relations in order to calculate stability fields. This not only allows extrapolation of the phase boundaries to regions of pressure, temperature and composition outside of the experimental measurements but also allows multiple studies to be compared and uncertainties in pressure and temperature to be addressed. Such calculations benefit immensely if parameters used in the calculations, such as the bulk modulus and expansivity, can be accurately determined independently.

To calculate the effect of pressure on the Gibbs free energy of ringwoodite requires the molar volume at 1 bar and the temperature of interest. Mantle temperatures within the stability field of ringwoodite are approximately 1500 °C. A significant divergence occurs, however, between results of previous thermal expansion studies on ringwoodite when extrapolated to these temperatures. The large volume press and new Philips X-ray diffractometer at the BGI mean that expansivity data of high-pressure phases can now be measured with unprecedented accuracy.

Approximately 30 mg of ringwoodite were synthesised in the 5000 tonne press at 21 GPa and 1200 °C. The thermal expansion was measured using a furnace mounted on the Philips Xpert powder diffractometer. Monochromatic Mo-$K\alpha_1$ radiation was used. The sample was loaded into an Al_2O_3 sample holder with Si powder added as a standard. The temperature was raised in steps of 20 °C from 20 °C to 700 °C and then in steps of 50 °C to 800 °C. During this process the temperature was lowered to 20 °C from 400 °C, 500 °C and 600 °C in order to ensure that the sample remained unaltered. Diffraction patterns were collected from 20-120°2θ and each pattern took 2 hours. Lattice parameters were obtained from a full pattern refinement using the GSAS-program.

At 680 °C diffraction peaks for forsterite began to appear and by 750 °C, *i.e.* 6 hours later, all peaks for ringwoodite had disappeared. The refined mineral proportions imply that ringwoodite completely recrystallised to forsterite in this temperature range. The effect of temperature on the volume of ringwoodite between 20 and 700 °C is shown in Fig. 3.2-6. Several curves from previous studies on ringwoodite expansion are also shown for comparison. In order to fit and extrapolate these data we use an equation derived from Grüneisen theory with a Debye model to describe the energy of the lattice vibrations. With this approach the thermal expansion is related to three parameters, θ_D the Debye temperature, k a material constant related to K' the pressure derivative of the bulk modulus and Q_o a material constant related to the Grüneisen parameter and bulk modulus. By assuming K' is 4, in agreement with recent measurements, we refine a Debye temperature for ringwoodite of 865 K, which is in excellent agreement with the acoustic Debye temperature of 849 K.

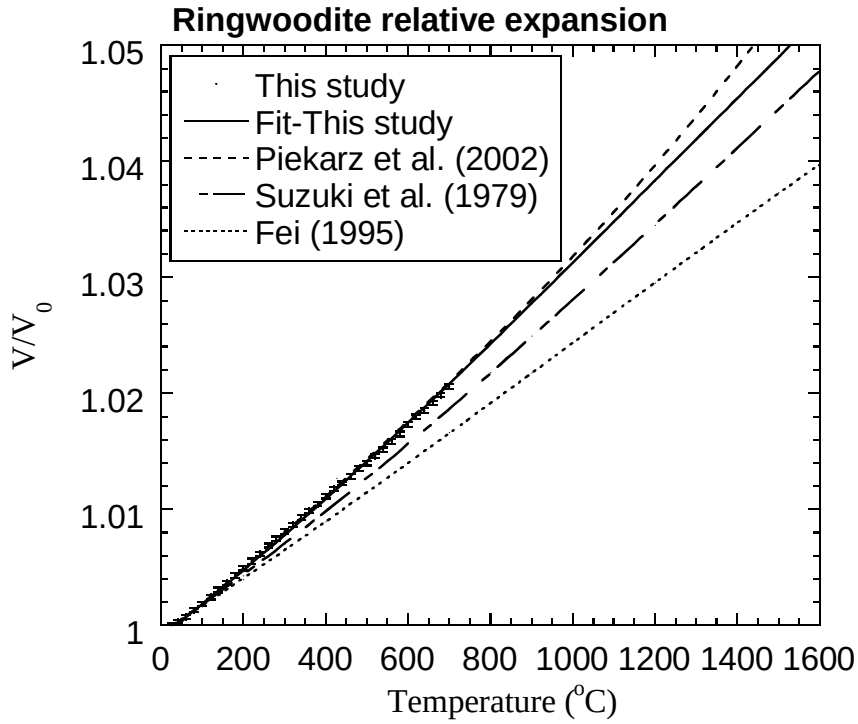

Fig. 3.2-6: The relative thermal expansion of ringwoodite determined in this study (shown as dots made visible by vertical error bars) is compared with similar measurements performed by Suzuki *et al.* (J. Phys. Earth 27, 53, 1979), results from a computer simulation of Piekarz *et al.* (J. Chem. Phys. 117, 3340, 2002) and a polynomial fit determined by Fei (AGU Handbook of Physical Constants 29, 1995) using previously published thermodynamic data. The extrapolation of our data using Grüneisen theory is shown by the solid curve.

e. *Thermodynamic properties of TiO_2 with the α-PbO_2 structure based on phase equilibria experiments (D.J. Frost, in collaboration with H.-J. Massonne, M. Burchard/Stuttgart and T. Theye/Bochum)*

Rutile is a common accessory mineral in metamorphic rocks such as eclogites. Recently a high-pressure polymorph of rutile with the α-PbO_2 structure (HP-TiO_2) has been characterised in ultrahigh pressure and impact rocks. If accurate laboratory determinations of the equilibrium phase boundary between the two polymorphs can be made, constraints can be placed on the pressures and temperatures experienced by these metamorphic rocks. There is considerable disagreement, however, between previous experimental determinations of this phase boundary, which may arise from the relatively sluggish reaction kinetics that occur close to the transformation boundary. We have bracketed this transformation using a piston cylinder apparatus between 400 and 1000 °C and a multianvil apparatus between 1000 and 1600 °C. Experiments performed below 1000 °C used a starting material comprised of a mixture of rutile and HP-TiO_2. Large amounts of the HP-TiO_2 were initially synthesised in the multianvil in order to assemble the starting material.

Our results are shown in Fig. 3.2-7. Data from both the piston cylinder and multianvil apparatus are consistent and can be reasonably fit to a single straight line. These data are in good agreement with an older study of Akaogi *et al.* (High Pressure Research 447, 1992) but have a much smaller gradient in comparison to the results of a more recent study (Withers *et al.*, Contrib. Min. Petrol. 145, 199, 2003). Thermodynamic properties of HP-TiO_2 were derived from the new experiments using existing data on rutile. The thermal expansivity and heat capacity of HP-TiO_2 were assumed to be identical to rutile. The compressibility of HP-TiO_2 was taken from the literature. We obtain an entropy and enthalpy of formation for HP-TiO_2 of 49.29 J/K and -943463 J, respectively, at standard conditions. These values differ only moderately from those of rutile. Independent measurements of the expansivity and heat capacity of the high-pressure phase would significantly improvement the accuracy of these thermodynamic data.

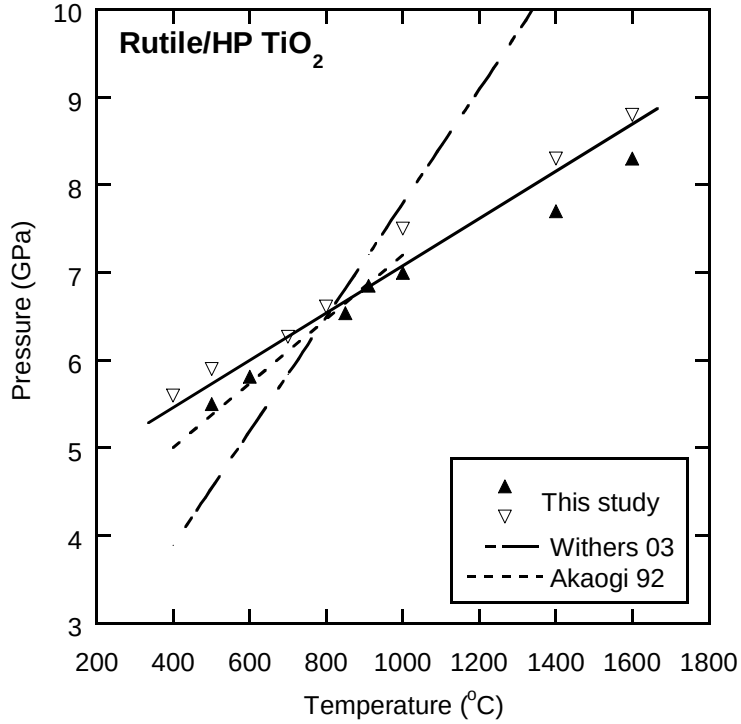

Fig. 3.2-7: The phase boundary between rutile (filled symbols) and HP-TiO_2 (open symbols) bracketed by piston cylinder (< 1000 °C) and multianvil (> 1000 °C) experiments. Only the experiments that constrain the curve are shown. Curves from two previous studies are shown for comparison.

f. *High-pressure elasticity of a natural magnetite (H.-J. Reichmann/Potsdam and S.D. Jacobsen)*

Magnetite (Fe_3O_4) is present throughout Earth's crust and uppermost mantle, where it forms spinel solid-solutions with magnesioferrite ($MgFe_2O_4$) and ulvöspinel (Fe_2TiO_4). Natural magnetites occur as primary or secondary mineralization products in nearly all major rock

types and the stony meteorites. Magnetite-spinel solid solutions are also among the most important ferrimagnetic materials for industrial applications such as data storage. Despite its ubiquity to both the Earth and material sciences, the pressure dependence of the elastic tensor (c_{ij}) of magnetite is not known.

Here we report the pressure dependence of the cubic elastic constants (c_{11}, c_{44}, c_{12}) and the adiabatic bulk (K_S) and shear (G) elastic moduli of magnetite to 9 GPa. The high-pressure elasticity of magnetite was determined *in situ* from measured compressional (P) and shear (S) elastic-wave travel times through a natural magnetite crystal compressed in the diamond anvil cell using gigahertz ultrasonic interferometry.

At ambient pressure, the single-crystal elastic constants are (in GPa); c_{11} = 260.5 ± 1.0, c_{44} = 63.3 ± 1.5, and c_{12} = 148.3 ± 0.3 GPa. The aggregate bulk modulus calculated from the elastic constants is 185.7 ± 3.0 GPa, and the shear modulus is 60.3 ± 3.0 GPa. The pressure dependence of the elastic tensor and aggregate elastic moduli for magnetite is shown in Fig. 3.2-8. The pressure derivatives of both c_{11} and c_{12} are similar and positive, with dc_{11}/dP = 5.14 ± 0.13 and dc_{12}/dP = 5.39 ± 0.07. However, the purely shear elastic mode (c_{44}) representing the cubic body-diagonal stiffness exhibits a negative pressure dependence over the experimental pressure range (corresponding to decreasing shear velocities with pressure), with dc_{44}/dP = -0.13 ± 0.04. This unusual shear mode-softening is direct evidence of a pressure-induced instability in the spinel structure of magnetite, which undergoes a first-order phase transformation at around 21 GPa.

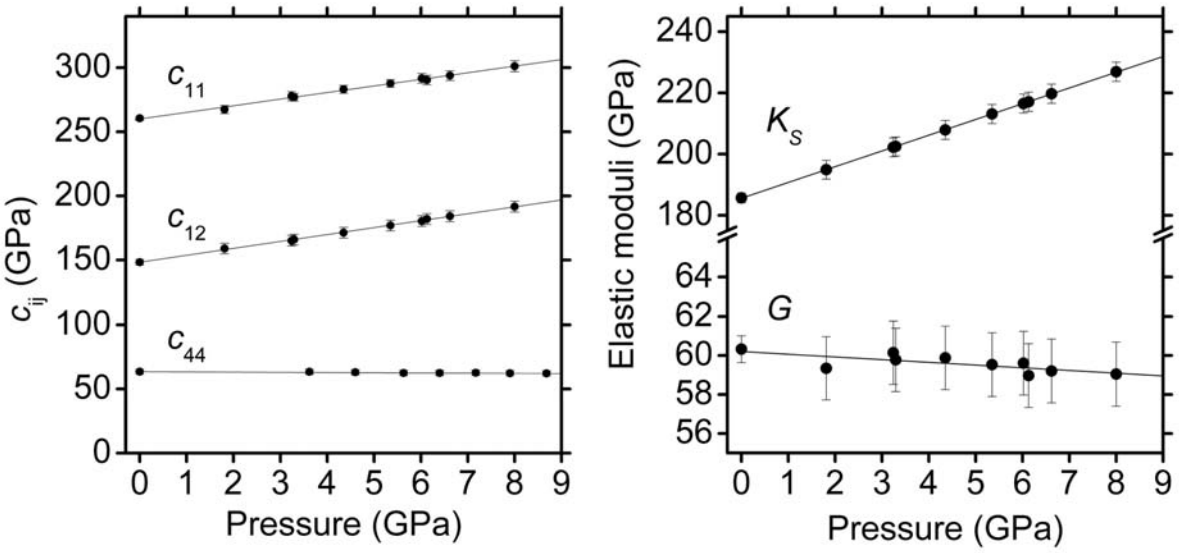

Fig. 3.2-8: Pressure-dependence of the single-crystal elastic tensor (c_{ij}) of magnetite (*left*) and the calculated aggregate bulk (K_S) and shear (G) moduli (*right*). The purely shear mode (c_{44}) representing the cubic body diagonal stiffness decreases with pressure, indicating a pressure-induced instability in the spinel structure of magnetite.

g. *High-pressure shear elasticity reveals structural instability in (Mg,Fe)O (S.D. Jacobsen)*

A dense oxide of iron and magnesium (Mg,Fe)O is expected to coexist with magnesium silicate perovskite (Mg,Fe)SiO_3 deep in Earth's lower mantle at 660-2900 km depth, but there remains considerable mystery surrounding the structure and behaviour of (Mg,Fe)O at high pressure. MgO (periclase) has the rocksalt (*B*1) structure to at least 230 GPa. On the other hand, FeO (wüstite) undergoes a displacive phase transition to a rhombohedral distorted *B*1 structure above 17 GPa, and subsequently to the NiAs-type (*B*8) structure above 100 GPa. Differences in the behaviour of MgO and FeO imply a change in topology of the high-pressure (Mg,Fe)O phase diagram, requiring there to be a two-phase field or exsolution gap, but just where in composition between ferropericlase (Mg-rich) and magnesiowüstite (Fe-rich) this should occur is not clear.

In order to address some of the questions surrounding (Mg,Fe)O stability in Earth's interior, elastic shear-wave travel times were measured ultrasonically in (Mg,Fe)O single crystals, from which the high-pressure behaviour of the c_{44} elastic constant ($=\rho V_{P[100]}^2$) was obtained as a function of composition. This pure-shear mode is the elastic parameter most sensitive to the rhombohedral distortion observed in FeO prior to the *B*1-*B*8 phase transition, and should therefore be a useful predictor of (Mg,Fe)O stability. Shear-mode softening (*i.e.* decreasing shear velocities with increasing pressure) in FeO is the result of strong magnetoelastic force coupling driving the *B*1 (paramagnetic) to rhombohedral (antiferromagnetic) phase transition. Therefore, increasing Mg-content should reduce this effect.

Measured shear-wave travel times and velocities for (Mg,Fe)O are plotted in Fig. 3.2-9. Sample nomenclature is Fe*X*, where *X* gives the atomic ratio Fe/(Fe+Mg). Indeed, [100] shear velocities are observed to decrease with increasing pressure for wüstite-FeO and magnesiowüstite samples Fe78 and Fe56, with $\partial V_S/\partial P$ = -42(1), -26.9(4), -15.2(2) $ms^{-1}GPa^{-1}$, respectively. However, for ferropericlase containing ~ 24 % iron component, the sign switches with $\partial V_S/\partial P$ = 11(1) $ms^{-1}GPa^{-1}$. The results reveal the rate at which increasing Mg-content in (Mg,Fe)O acts to stabilize the *B*1 structure at high pressures. The c_{44} elastic constants were calculated from the shear velocities as a function of composition and pressure. The results are plotted in Fig. 3.2-10, with the following polynomial fits,

Fe24: $c_{44} = 123.3(2) + 1.24(5)P$
Fe56: $c_{44} = 83.44(4) - 0.14(2)P - 0.003(2)P^2$
Fe78: $c_{44} = 63.42(6) - 0.91(3)P - 0.004(3)P^2$
FeO: $c_{44} = 46.09(7) - 0.86(4)P - 0.024(4)P^2$

This term of the elastic tensor provides an important proxy for the cubic body diagonal stiffness. The second-order displacive phase transition observed at room temperature for FeO is a rhombohedral distortion of the *B*1 structure, manifest by elongation of the body diagonal [111], and thus should be revealed by c_{44} mode softening. Over the experimental pressure

range, c_{44} is reduced in FeO and Fe78 by about 20 % and 13 %, respectively. Although the pressure derivative of c_{44} for Fe56 is still negative, it is reduced by less than 2 % at 10 GPa.

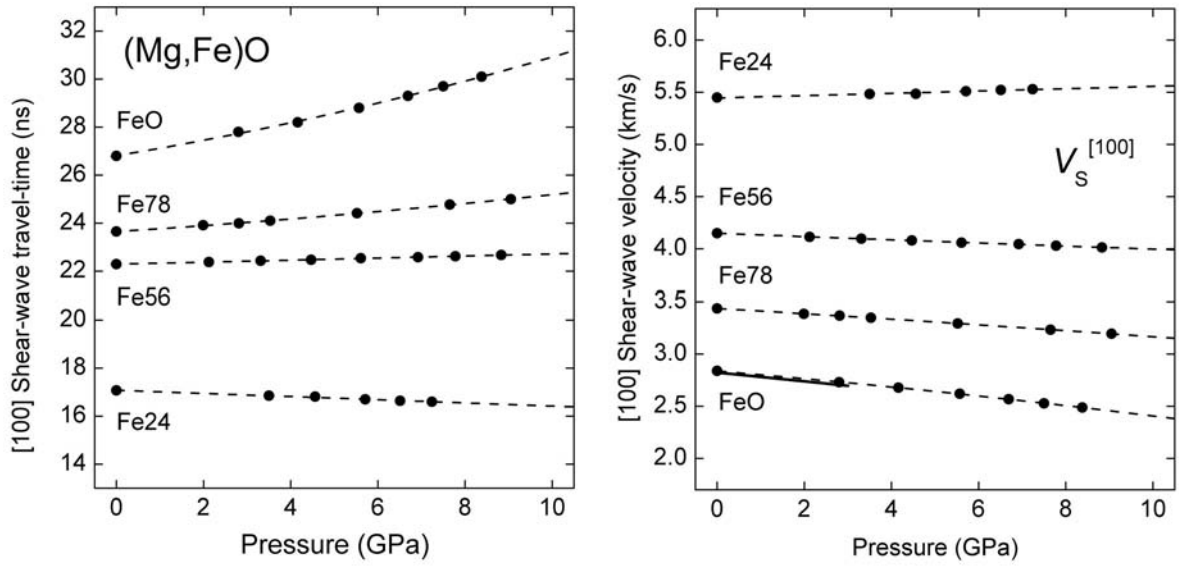

Fig. 3.2-9: Measured ultrasonic shear-wave travel times (*left*) and velocities (*right*) in (Mg,Fe)O single crystals. Previous results on FeO (to 3 GPa maximum) are shown by the solid curve (*right*). Compositions are given by Fe*X*, where *X* gives the atomic ratio Fe/(Fe+Mg). Decreasing shear velocities with increasing pressure indicates an elastic-mode softening related to pressure-induced instability in the rocksalt structure.

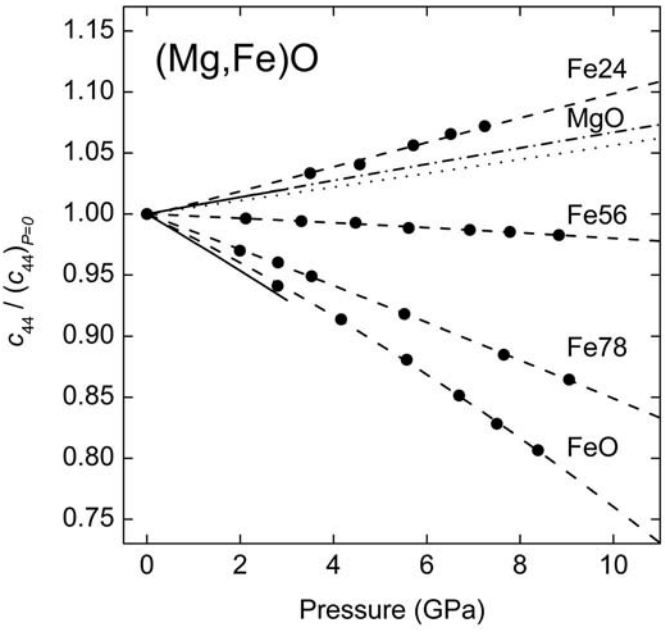

Fig. 3.2-10: Pressure and compositional dependence of the cubic c_{44} elastic constant, normalized to its initial (P_0) value. Previous results on FeO (solid line to 3 GPa) and MgO (dash-dot and dotted lines) are also shown. A complete switching in the sign of $\partial c_{44}/\partial P$ in the (Mg,Fe)O solid solution points to a change in the phase diagram topology at around 50 % iron. The results indicate that that rocksalt (*B*1) structure is favorable for potential lower mantle compositions (10-25 mol.% FeO) and that observed seismic scattering in Earth's lower mantle is more likely to be compositional heterogeneity than phase changes in (Mg,Fe)O.

h. *Mössbauer spectroscopic study of pressure induced magnetization in wüstite (FeO) (I.Yu. Kantor, C.A. McCammon and L.S. Dubrovinsky)*

Wüstite (hereafter referred to as FeO) is of great interest in solid state physics and chemistry because of its electrical, magnetic, structural and non-stoichiometric properties. Its high pressure and high temperature behaviour are important for Earth sciences, because FeO is considered to be one of the main iron-bearing phases in the lower mantle as a component of ferropericlase (Mg,Fe)O. FeO has a rather complex phase diagram with details unclear to date. A number of structural, magnetic, and electron transitions occur in FeO, and its nonstoichiometry ($Fe_{1-x}O$, where x varies up to 0.12) complicates the phase diagram significantly.

Under ambient conditions FeO crystallizes in the cubic rock-salt structure. As a result of antiferromagnetic ordering below the Néel temperature (~ 195 K), FeO transforms to a rhombohedral or monoclinic structure. On compression at room temperature, FeO transforms to a rhombohedral structure at approximately 15 GPa. This displacive transition appears to be similar to the rhombohedral distortion at low temperature, and since Mössbauer studies have demonstrated a magnetic transition in a similar pressure range, the two transitions have been generally assumed to coincide. *In situ* high-pressure Mössbauer study of FeO was carried out in nearly hydrostatic conditions up to a pressure of 13.5 GPa to verify this assumption.

The sample was a powder of a synthetic ^{57}Fe-enriched FeO with cubic cell dimension a = 4.307(7) Å, which corresponds to the composition $Fe_{0.945}O$. High-pressure experiments were performed using a diamond anvil cell (DAC) at room temperature (295 K). An ethanol-methanol mixture of 3:1 proportion was used as a pressure medium, which provides nearly hydrostatic conditions in the sample chamber to at least 10 GPa. Several ruby chips of ~ 1 μm diameter were also placed in the sample chamber for the purpose of pressure calibration. No detectable pressure gradients were observed up to the highest pressure of 13.5(1) GPa reached in this study.

We used several different approaches to determine the magnetic transition pressure. The first two are based on the observation of increasing broadening in the Mössbauer spectrum as a function of pressure due to magnetic ordering. We therefore chose a simple fitting model, in this case a singlet, and monitored the variation of line width as a function of pressure. There are two different trends: linear with a small slope for pressures less then 5 GPa, and linear with much higher slope for pressures higher than 6 GPa. The transition point is therefore calculated as the pressure where the two lines intersect, *i.e.* 5 ± 0.5 GPa. The second approach is based on a more realistic fitting model using a quadrupole doublet for FeO. The resulting fit gives nearly the same trend as before (Fig. 3.2-11, circles) with a similar Néel transition pressure (5 ± 0.5 GPa). The third approach adds a magnetic sextet to the fitting model. Linewidths associated with the magnetic subspectrum are extremely broad, likely due to the multiplicity of slightly different iron environments arising from non-stoichiometry. The relative area of the magnetic sextet increases with increasing pressure (Fig. 3.2-12), and the paramagnetic quadrupole doublet is estimated to disappear by ca. 15-16 GPa. The linewidth variation of the quadrupole doublet is essentially constant with pressure, indicating that the

overall spectral broadening is due to the appearance of the magnetic sextet (diamond symbols in Fig. 3.2-11). We note that the choice of fitting model does not affect determination of the pressure at which broadening is observed to occur.

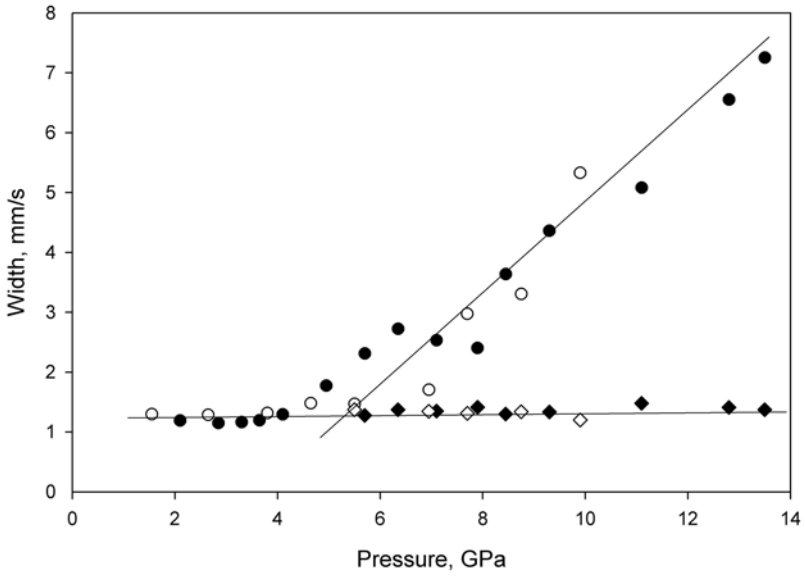

Fig. 3.2-11: Lorentzian linewidth variation with pressure for different fitting models of FeO Mössbauer spectra. Solid symbols indicate compression, while open symbols indicate decompression: circles - doublet linewidth from doublet-only model; diamonds - doublet linewidth from doublet-plus-sextet model.

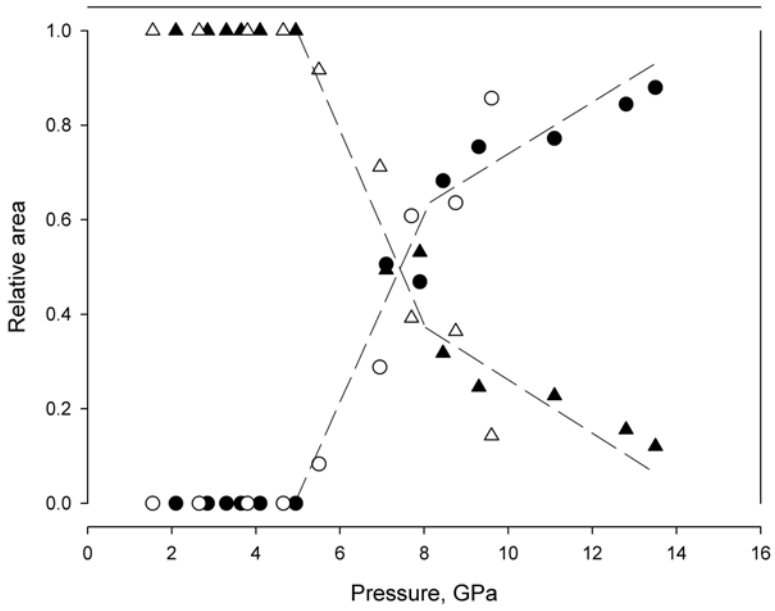

Fig. 3.2-12: Pressure variation of subspectral relative areas from the “doublet plus sextet” fitting model: circles - sextet, triangles - doublet. Solid symbols indicate compression, while open symbols indicate decompression. Lines are given as guides for the eye.

The co-existence of paramagnetic and antiferromagnetic states of FeO at pressures from 5 to ~ 15 GPa is likely related to the material itself. We have ruled out the presence of pressure gradients, and there is no evidence for hysteresis in the phase transition (Figs. 3.2-11 and 3.2-12). The presence of two magnetic states could be interpreted either as the co-existence of two separate phases, or as a single phase where magnetic exchange and/or its timescale between iron atoms varies depending on parameters such as defect clustering and the degree of magnetic coupling between clusters.

Our results show that the magnetic phase boundary between antiferromagnetic and paramagnetic phases does not coincide with the reported location of the structural phase boundary between cubic and rhombohedral phases of FeO, and that they differ from each other by at least 10 GPa at room temperature.

i. *Magnetism in dense hexagonal iron (G. Steinle-Neumann, in collaboration with R.E. Cohen/Washington, DC and L. Stixrude/Ann Arbor)*

Physical properties of iron (Fe) are of great importance to many fields in the sciences, as Fe is one of the most abundant and stable elements in the universe, and the very basis for the steel industry. Hexagonal close-packed (hcp) Fe, the form stable at high pressure, plays a central role in geophysics, as the Earth's inner core is thought to be primarily composed of this phase. The magnetic state of Fe has a major influence on the physics of Fe and Fe-alloys, including the relative stability of polymorphs. The phase stable around ambient conditions, body-centered cubic, owes its stability entirely to the presence of ferromagnetism. Heating above the Curie temperature causes the spins to disorder and the net magnetization to vanish, but the individual atomic moments are virtually unchanged in magnitude as temperature has little influence on the electronic structure. Pressure also has a large effect on the magnetic structure through the delicate balance between the potential energy, which stabilizes magnetism, and the kinetic energy, which stabilizes a non-magnetic state: potential energy is lowered by aligning spins since like spin electrons cannot occupy the same spatial orbital and therefore repel each other less than unlike spins. Because the magnetization energy is more favorable at larger volumes, magnetism tends to expand the lattice and to increase the compressibility as compared with the non-magnetic state.

The magnetic structure of hcp Fe has been the subject of a scientific debate for three decades, leading to contradictory results from experiments and theory: The absence of observable splitting in the Mössbauer signal in hcp iron to low temperature led to the conclusion that no significant magnetic moments are present. However, density functional theory based methods give a stable anti-ferromagnetic state for hcp Fe (afmII, Fig. 3.2-13) that is characterized by alternating spin up and down planes perpendicular to one of the basal planes in the hcp cell. Taking the afmII structure into account improves the agreement of computed and experimental equation of state for hcp Fe significantly.

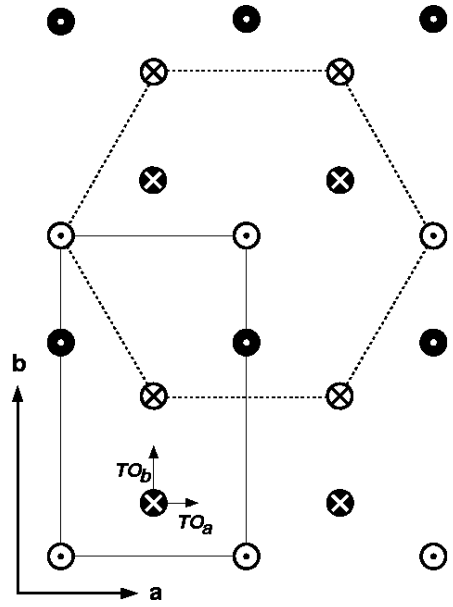

Fig. 3.2-13: Orthorhombic antiferromagnetic groundstate of hcp iron (afmII). Open circles show the atomic positions at z=1/4, filled circles at z=3/4 with arrows pointing in (crosses) and out of the plane (dots) indicating the direction of spin. The orthorhombic unit cell is given (solid lines, four atoms in the unit cell) and axes are labelled. The *a*- and *b*-axes define the eigenvectors for the *TO* modes (TO_a and TO_b). The *c*-axis is out of the plane. For reference a hexagonal base is outlined (dashed lines).

Recent experimental observations, including anomalous splitting of the Raman mode, shed some light on the apparent discrepancy between theory and experiment. The Raman active phonon in a monatomic hcp system is the doubly degenerate transverse optic (*TO*) mode. Consequently, only one peak is expected in Raman spectra of hcp Fe. However, experiments have revealed two peaks up to pressures of 40 GPa, suggesting a symmetry lower than that of the atomic arrangement. The afmII magnetic structure provides such a symmetry breaking mechanism, resulting in two *TO* modes, characterized by displacements of the close packed planes with respect to one another along the orthorhombic *a*- (TO_a) and *b*-axes (TO_b), respectively (Fig. 3.2-13). We have calculated the *TO* mode frequencies of the afmII structure using the accurate spin-polarized fully relativistic all-electron linearized-augmented plane-wave method (LAPW). We find that the two *TO* mode frequencies can quantitatively explain the splitting found in the Raman experiments (Fig. 3.2-14).

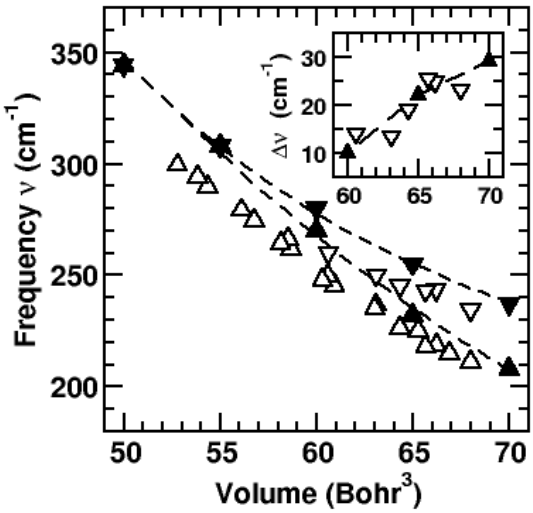

Fig. 3.2-14: Raman frequencies as a function of atomic volume. The afmII structure results in two frequencies (filled triangles) with TO_a being the lower (up) and TO_b (down) the upper branch. The dashed lines through TO_a and TO_b are third order polynomial fits in $V^{-2/3}$. Experiments identify two peaks in the Raman spectra up to 40 GPa in open symbols. The stronger peak is shown in the triangles up, and the weaker peak in triangles down. The inset compares the splitting in Raman frequencies from theory (filled) and experiment (open).

The inference of magnetism from the Raman splitting is in apparent conflict with the Mössbauer experiments that show no significant hyperfine field (HFF) for hcp Fe. To address the Mössbauer experiments we have calculated the HFF for afmII Fe, and find it to be only a few kG at all pressures. This is two orders of magnitude smaller than the HFF for bcc Fe. The separation of the outermost peaks in the Mössbauer spectrum (L1 and L6) is diagnostic of the HFF and a typical value for afmII would result in a separation of less than 0.2 mms^{-1}, within the resolution limit of Mössbauer experiments.

Other experimental investigations of magnetic states in hcp iron have been inconclusive and additional experiments probing for magnetism and magnetic correlations in iron under pressure, such as *in situ* susceptibility and neutron scattering, would be of great interest. They would help to elucidate the properties of this common element, help in understanding the equation of state for Fe, and shed important insight into extrapolations of physical properties to conditions of Earth's core. They will also help in understanding and refining theoretical methods for simulating and studying magnetism in materials.

j. *A fundamental problem of lamellar magnetism in the ilmenite-hematite series (P. Robinson and S. McEnroe/Trondheim, L. Brown/Sydney and R. Harrison/Cambridge, in collaboration with F. Heidelbach)*

The theory of "lamellar magnetism" has been developed to explain the unusually strong magnetic remanence and coercivity of natural finely exsolved members of the ilmenite-hematite series. Under room temperature conditions, ilmenite is a paramagnet and hematite is a spin-canted antiferromagnet with a very weak magnetic moment, and neither alone could account for these properties. These samples all contain exsolution lamellae parallel to (001) ranging in thickness from microns down to 1-2 nm, equivalent to the thickness of single unit cell, as shown by high-resolution transmission electron microscopy. According to this theory, "contact layers" form at the coherent (001) interfaces of fine exsolution lamellae of ilmenite in hematite or hematite in ilmenite. Based on Monte Carlo simulations, the contact layers consist predominantly of mixtures of Fe^{2+} ions as in ilmenite and Fe^{3+} ions as in hematite. Their formation reduces but does not eliminate charge imbalance along the interfaces.

In normal hematite the principal magnetic moments of alternate Fe^{3+}-rich layers are oriented at an angle about 179.96° apart and this minor deviation from 180° gives a weak spin-canted ferromagnetic moment, which is oriented at 90° to the principal magnetic moments. Detailed studies of hematite single crystals by others have shown that the principal magnetic moments are parallel to one of the *a*-crystallographic axes, and that the spin-canted magnetization lies normal to this direction. Because of Fe^{2+} substitution, the principal magnetic moments of contact layers on opposite sides of a lamella are lower than the principal magnetic moments of adjacent Fe^{3+}-rich hematite layers, but are magnetically locked to them and always parallel to each other. The principal magnetic moment of lamellar magnetism is produced by the

positive imbalance of the principal moments of these contact layers against the principal magnetic moment of a single oppositely magnetized hematite layer, after the self-cancelling effects of all even numbers of hematite layers are accounted for. According to this theory and the previous studies of hematite, the principal magnetic moment of lamellar magnetism should be oriented parallel to an *a*-crystallographic axis of ilmeno-hematite or hemo-ilmenite, whereas if the magnetism is caused by the spin-canted hematite, then the magnetic moment should be normal to an *a*-crystallographic axis.

The present study was designed to provide a test of the above theory using large natural crystals of exsolved rhombohedral oxide The sample chosen was from the Pramsknuten hemo-ilmenite deposit, a nearly mono-mineralic lens contained within the Åna Sira massif anorthosite containing single crystals of up to 2 cm size. For the magnetic measurements approximately 1 cm square prisms were cut from the slabs and oriented on both sides with Electron Backscattering Diffraction (EBSD) in the SEM which is capable of establishing absolute crystallographic axis directions with an accuracy of about 2°. The orientations of the *c*-axis and three *a*-axes from the front side and the back side were compared to see the degree of misorientation between front and back. Based on these observations crystals were graded as top (T) with little or no misorientation, intermediate (I) with a few degrees of misorientation, poor (P) with more disorientation, and very poor (VP) with the largest degree of misorientation. A single set of magnetic vectors and intensities for each was then measured on the Superconducting Cryogenic Magnetometer at University of Massachusetts.

Of the total of 34 crystal measurements, 10 are in a tight group with the magnetic vector within 5 degrees of the 001 plane and within 10° of an *a*-crystallographic axis (Fig. 3.2-15).These conform very closely to our theory. Another 8 also have magnetic vectors within 5° of the (001) plane but with magnetic vectors between 10° and 25° of an *a*-crystallographic axis, which could indicate a partial contribution from the spin-canted moment of hematite. Only 1 measurement has the magnetic vector within 5 degrees of the (001) plane and with an angle of 33.6 degrees to an *a*-crystallographic axis. This is the **only** measurement that could agree with the postulate that the magnetic moment of these materials is strictly parallel to the spin-

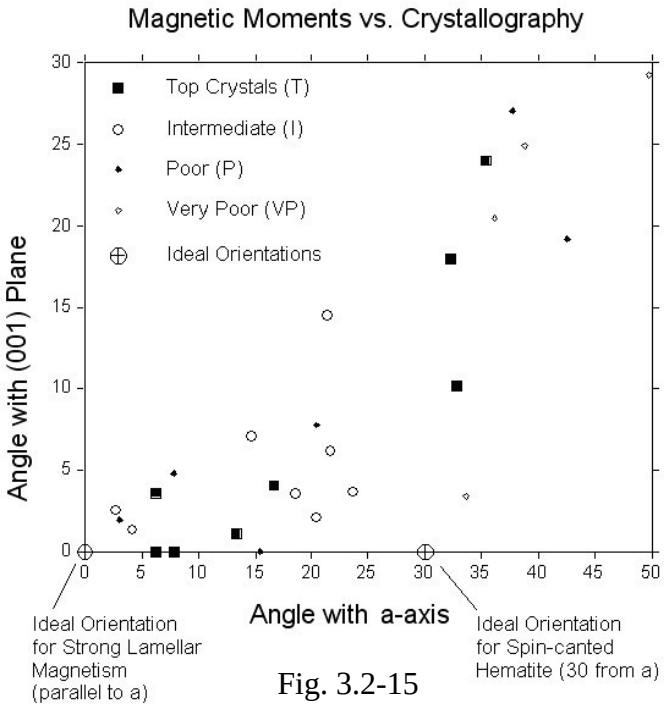

Fig. 3.2-15

canted moment of hematite. There are 3 more measurements with the magnetic vector within 10° of the 001 plane and 15-22° of an *a*-crystallographic axis. The remaining 12 measurements have magnetic moments with angles of greater than 10° from the (001) plane and with angles of greater than 20° to an *a*-crystallographic axis. A number of explanations are possible for these last results, including irregular shape of sawed prisms, multiple crystals not detected on top and bottom, and problems with the magnetometer. We expect some of these problems will be resolved with a new round of magnetic measurements.

The preliminary results summarized above show that 29 % conform very closely to our postulates for lamellar magnetism, another 23 % conform with modification for a contribution from a spin-canted component, and only 3 % (1 measurement) could possibly be interpreted as indicating that the magnetism of these materials is mainly due to spin-canted hematite. This study appears to be an example of successful convergence of instrumentally diverse approaches to a major mineral-magnetic problem.

3.3 Mineralogy, Crystal Chemistry and Phase Transformations

Phase transformations occur in most types of materials including ceramics, metals, polymers, organic and inorganic compounds and, of course, minerals. The study of transformation processes in minerals has evolved from the need to understand the physical and thermodynamic properties of the constituents of the Earth's surface and interior. There are, in fact, very few minerals which show no transformations in the critical range of pressures and temperatures relevant to the Earth. It is not surprising, therefore, that most of the contributions of this section concern phase transitions, and also not surprising is the variety of minerals studied, given the wide number of phases present in the rocks of our planet.

Almost any change in the structure of a crystal due to small atomic displacements, atomic ordering, reconstructive phase transformation etc. is usually accompanied by changes in lattice parameters. Such variations can be described quantitatively as combination of linear and shear strains, if suitable reference states are defined, and can give insight into quite complex systems, such as the incommensurate phase transition occurring in nepheline. Diffraction techniques are, therefore, largely used to investigate transformation processes, even at quite high pressures and temperature, and the quality of these techniques is nowadays such that new high pressure polymorphs are not only discovered, but also well characterised.

Phonons also respond to any change of the crystal structure of a material. Raman and IR spectroscopies have been used successfully as the primary analytical tools to describe phase transformations. Diffraction and spectroscopic methods are complementary and their combined use can give a better understanding of the crystal structure and its changes at both the macroscopic and local scale.

The use of analogue materials plays an important role in studies at high temperatures and pressures, because transformations occur at more accessible experimental conditions. It can often happen that such analogues are not only useful to better understand major rock forming minerals, but present unique characteristics which may be of interest to the broader scientific community.

Finally, we must not forget that compositional diversity can create profound differences in the thermodynamic stability and the physical behaviour of crystalline materials. Such diversity can be due to substitution of different atoms, or simply to the presence of the same atoms in different valence states. It is therefore important to explore the possible structural variation due to cation substitution or to develop empirical methods to determine the valence states and coordination of transition metals in solids.

a. *Formation of ordered oxygen-deficient perovskites: substitution of Si^{4+} by trivalent cations of Fe^{3+} and Al^{3+} in $CaSiO_3$-perovskite (U.W. Bläß, T. Boffa Ballaran, D.J. Frost, F. Langenhorst, C.A. McCammon, F. Seifert, in collaboration with P.A. van Aken/Darmstadt)*

Several studies indicate that calcium silicate perovskite is an important constituent of the Earth's transition zone and the lower mantle as a major host for calcium as well as for trace

elements. $CaSiO_3$-perovskite might reach an abundance of about 6 % in peridotitic compositions and probably up to 23 % in subducted slabs with MORB composition. In addition, the incorporation of Fe^{3+} or Al^{3+} by the defect mechanism could cause drastic changes in geophysically relevant properties due to the creation of oxygen vacancies. Relatively small amounts of trivalent cations and associated oxygen vacancies are probably disordered in the perovskite structure and may therefore strongly affect elastic or transport properties as is well known, for example, in iron- and aluminium-bearing magnesium silicate perovskite. Higher concentrations of trivalent cations in $CaSiO_3$ perovskite could lead to an ordering of cations and associated oxygen vacancies, which usually results in the formation of superstructures. For example, in the system $Ca(Ti_xFe_{1-x})O_{3-x/2}$ the ordering of oxygen vacancies into the pseudocubic (001) plane causes the formation of several brownmillerite-type structures with different stacking sequences.

Our previous multianvil experiments investigating the substitution of silicon by trivalent iron in $CaSiO_3$ perovskite resulted in the discovery of a completely ordered oxygen deficient perovskite with $Ca(Fe_{0.4}Si_{0.6})O_{2.8}$ stoichiometry (cf. Annual Report 2002). It is stable over a large *P* - *T* field ranging from about 11 GPa to about 20 GPa. Many observations with different techniques have indicated that its structural properties are characterised by a 10-fold superstructure along the pseudocubic [111] direction, consisting of alternating defect-rich layers with silicon in tetrahedral coordination and blocks of perovskite structure with silicon and iron in octahedral coordination and 3 oxygens per formula unit. More recent experiments performed at various P - T conditions and starting materials, in which silicon is exchanged by different amounts of aluminium, revealed the existence of two further oxygen deficient perovskites with $Ca(Al_{0.4}Si_{0.6})O_{2.8}$ and $Ca(Al_{0.5}Si_{0.5})O_{2.75}$ stoichiometries. Whereas the former has a similarly large stability field as the iron bearing defect perovskite as well as similar lattice constants and structural details, the latter differs in all these properties. In comparison to the iron-bearing defect perovskite, the stability field of the $Ca(Al_{0.4}Si_{0.6})O_{2.8}$ phase is shifted by 2 GPa to lower pressures, whereas the stability field of the $Ca(Al_{0.5}Si_{0.5})O_{2.75}$ phase is decreased by approximately 7 GPa. Lattice constants of the $Ca(Al_{0.5}Si_{0.5})O_{2.75}$ defect perovskite give evidence for an 8-fold superstructure, which is likely a polysome of the 10-fold superstructure with the number of octahedral layers reduced by two. The symmetry of all these three phases is monoclinic at ambient conditions, but probably rhombohedral at high temperature. Such a phase transition during quenching is indicated by needle shaped twin domains, which reflect the loss of a threefold axis by ferroelastic distortion. Examples of such needle shaped twins in the $Ca(Al_{0.5}Si_{0.5})O_{2.75}$ defect perovskite are illustrated in Fig. 3.3-1. The distortion of this ferroelastic transition is correlated to an elongation of the monoclinic *a* axis at room temperature of ~ 1.5 % in $Ca(Fe_{0.4}Si_{0.6})O_{2.8}$, ~ 0.6 % in $Ca(Al_{0.4}Si_{0.6})O_{2.8}$ and ~ 1.0 % in $Ca(Al_{0.5}Si_{0.5})O_{2.75}$. Therefore the associated spontaneous strain is maximum in the iron-bearing phase, and increases in the aluminium-bearing phases with decreasing number of superstructure layers. In addition, a second kind of twinning occurs in all three defect perovskites when synthesised at relatively high temperatures (above ca. 1200 °C for the iron-bearing compound). These features can be interpreted by growth of oxygen deficient layers along all pseudocubic {111} planes.

We also have addressed the potential occurrence of these defect perovskites in the Earth's interior. The existence of a $Ca(Al,Fe)_{0.4}Si_{0.6}O_{2.8}$ solid solution seems to be likely, due to the similar crystallographic properties of both phases possessing a 10-fold superstructure and the substantial overlap of their stability fields with P - T conditions of the Earth's transition zone. On the other hand, their high pressure stability is limited to about 20 GPa, which means that they would always coexist with majoritic garnet. Because trivalent cations are probably largely partitioned into majoritic garnet, the defect perovskites in the Earth's transition zone might not exist or might be restricted to particular P - T conditions or compositions. In downgoing slabs of MORB composition, where appropriate large amounts of calcium and trivalent cations could lead to a higher concentration of the defect perovskite, stishovite saturation at such high pressures might suppress the formation of silicon-undersaturated phases such as the defect perovskite.

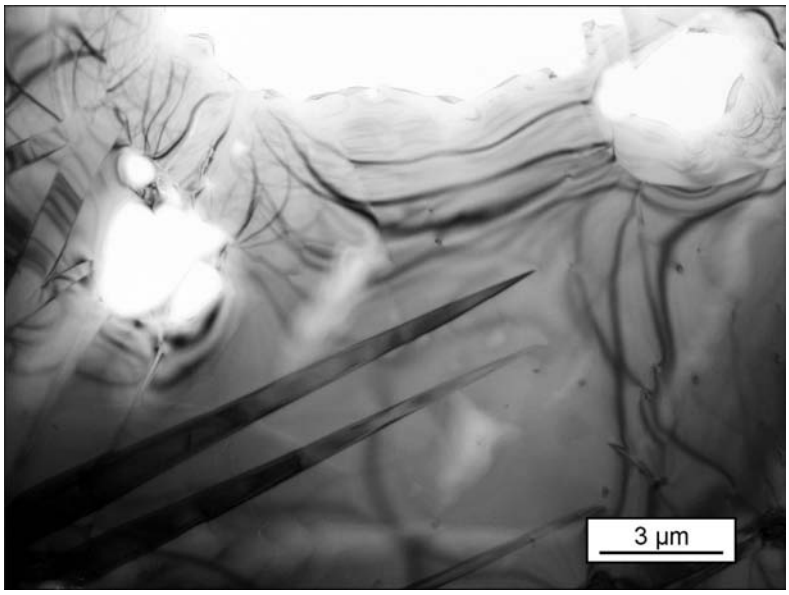

Fig. 3.3-1: Bright field TEM image of needle shaped twin domains in $Ca(Al_{0.5}Si_{0.5})O_{2.75}$ defect perovskite indicating a ferroelastic phase transition during quenching from rhombohedral to monoclinic symmetry.

b. *Towards an empirical determination of Fe^{3+} in (Mg,Fe)(Si,Al)O_3 perovskite and (Mg,Fe)O (C.A. McCammon, in collaboration with S. Lauterbach/Darmstadt, F. Seifert, F. Langenhorst and P.A van Aken/Darmstadt)*

The oxidation state of iron in lower mantle phases plays an important role in determining the chemical and physical properties of the lower mantle, which has motivated a continuing effort at Bayerisches Geoinstitut to study the crystal chemistry of iron-containing lower mantle phases including the determination of $Fe^{3+}/\Sigma Fe$. Methods that have been refined at Bayerisches Geoinstitut for these studies include Mössbauer spectroscopy using a point

source (Mössbauer milliprobe) and Electron Energy Loss Spectroscopy (EELS). Both of these methods were combined in a study of synthetic $(Mg,Fe)(Si,Al)O_3$ perovskite-$(Mg,Fe)(Si,Al)O_3$ majorite-(Mg,Fe)O assemblages (see also BGI Annual Report 2001). EELS was used to determine $Fe^{3+}/\Sigma Fe$ values for each phase in multiphase assemblages, and to calibrate a fitting method for Mössbauer spectra to determine $Fe^{3+}/\Sigma Fe$ of $(Mg,Fe)(Si,Al)O_3$ perovskite. Mössbauer spectroscopy was then used to determine $Fe^{3+}/\Sigma Fe$ in the perovskite phase occurring in natural assemblages where iron concentration was too low for EELS.

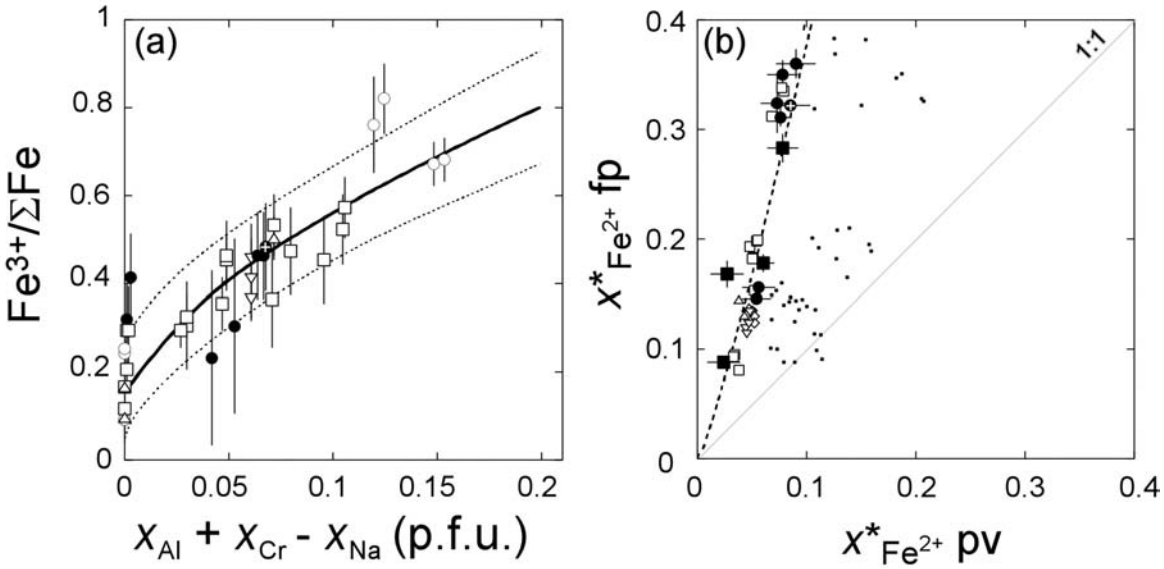

Fig. 3.3-2: (a) Variation of $Fe^{3+}/\Sigma Fe$ with adjusted Al concentration in $(Mg,Fe)(Si,Al)O_3$ perovskite. Solid circles correspond to Re capsule experiments, and the solid circle with white cross to a Fe capsule experiment. Open symbols are data from the literature. The solid line indicates the empirical relation with 90 % prediction limits given by the dashed lines. (b) Fe^{2+}-Mg partitioning between $(Mg,Fe)(Si,Al)O_3$ perovskite (pv) and (Mg,Fe)O ferropericlase (fp). Values are given as normalised Fe^{2+} concentration in each phase – $Fe^{2+}/(Fe^{2+} + Mg)$. Black symbols represent data corrected for Fe^{3+} determined by either EELS or Mössbauer spectroscopy, while open symbols are based on estimated values. The dashed line indicates the best fit of all Fe^{2+} data. For comparison, normalised Fe_{total} concentrations of all data are indicated as dots.

The $Fe^{3+}/\Sigma Fe$ ratio of $(Mg,Fe)(Si,Al)O_3$ perovskite increases with increasing Al concentration (Fig. 3.3-2a), consistent with previous work. Particularly notable is the negligible influence of oxygen fugacity on this trend – the white cross indicates a sample synthesised at Fe equilibrium, which gives the same results as other experiments buffered by Re-ReO_2. We derived an analytical expression to predict Fe^{3+} concentration of $(Mg,Fe)(Si,Al)O_3$ perovskite solely from the electron microprobe compositions, motivated by the difficulty of obtaining $Fe^{3+}/\Sigma Fe$ values from Mössbauer spectroscopy (due to small sample diameter) and EELS (due to instability in the electron beam). We applied the empirical formula, coupled with similar

systematic observations in (Mg,Fe)O, to data from the literature to calculate true Fe^{2+}/Mg partition coefficients based on the chemical composition data corrected for $Fe^{3+}/\Sigma Fe$. Results show that all data fall along the same trend, regardless of Al concentration (Fig. 3.3-2b), implying that there is little variation in Fe^{2+}/Mg partitioning between $(Mg,Fe)(Si,Al)O_3$ perovskite and (Mg,Fe)O over the conditions (temperature, pressure, composition, oxygen fugacity) represented by the experiments. Traditionally Fe^{3+} has been ignored in lower mantle assemblages partly due to the difficulties of measurements, but we suggest that the empirical relations derived from our work constitute a more realistic first approximation than ignoring it altogether.

c. *Modelling clinopyroxenes phase transitions at high pressure: role of site dimensions (G.D. Gatta, G. Iezzi and T. Boffa Ballaran)*

Clinopyroxenes (cpx) are one of the most experimentally investigated mineral families, given the wide range of cation substitutions which can occur in their structure and their use as geobarometers and geothermometers. The most common structure of clinopyroxenes has *C*2/*c* symmetry with two equivalent tetrahedral single-chains. Some clinopyroxenes such as, for example, those belonging to the clinoenstatite-clinoferrosilite solid solution have $P2_1/c$ symmetry, and are characterized by the tetrahedral chains being differently kinked. A displacive phase transitions from $P2_1/c$ to *C*2/*c* may occur both as a function of temperature and pressure. The H*T*-*C*2/*c* and the H*P*-*C*2/*c* structures are not the same, however. In fact the H*T*-*C*2/*c* phase has extended equivalent chains, whereas the H*P*-*C*2/c type polymorphs have extremely kinked chains. The lengthening and/or the kinking of the chains can be expressed in terms of the O3-O3-O3 angle.

Several studies have been carried out on the high-temperature and high-pressure behaviour of pyroxenes having different cations at the M1 and M2 sites. With respect to Li-cpx, the knowledge of their behaviour is limited to end-members compositions, *i.e.* ^{M2}Li and $^{M1}M^{3+}$, with M = Fe^{3+}, Sc, Al. It is well known, however, that cation substitution can have drastic effects on the thermodynamic behaviour of any mineral. Therefore, accurate site occupancies as well as study of mixed compositions are required to provide thermodynamic models. Synthetic samples are, therefore, very important since they give the opportunity of varying the composition of the investigated sample without having to deal with small amounts of impurities always present in natural systems.

The aim of this study is to investigate the effects of Mg substitution on the high-pressure behaviour of $LiFe^{3+}Si_2O_6$. It is demonstrated that such substitution increases the stability field of the $P2_1/c$ structure with respect to the end-member composition.

A crystal with composition $^{M2}(Li_{0.85}Mg_{0.09}Fe^{2+}_{0.06})^{M1}(Fe^{3+}_{0.85}Mg_{0.15})Si_2O_6$ with $P2_1/c$ symmetry was loaded in a diamond anvil cell with 16:3:1 methanol:ethanol:water as a

pressure medium, and a quartz crystal as an internal standard. Unit-cell lattice parameters have been collected up to 6 GPa. Their variations as a function of pressure, normalized to the respective room pressure values, are shown in Fig. 3.3-3. Unit-cell volume data were fitted with a third order Birch-Murnaghan Equation of State using the data weighted by the uncertainties in *P*-*V*. The resulting EoS parameters are: V_0= 415.67(2) Å^3, K_{T0}= 82.2(6) GPa and K'=10.6(3). No phase transition has been observed within the pressure range investigated. A careful inspection of the intensity of *b*-type reflections (*h*+*k* = 2*n*+1) confirms that up to 6 GPa the primitive lattice is maintained.

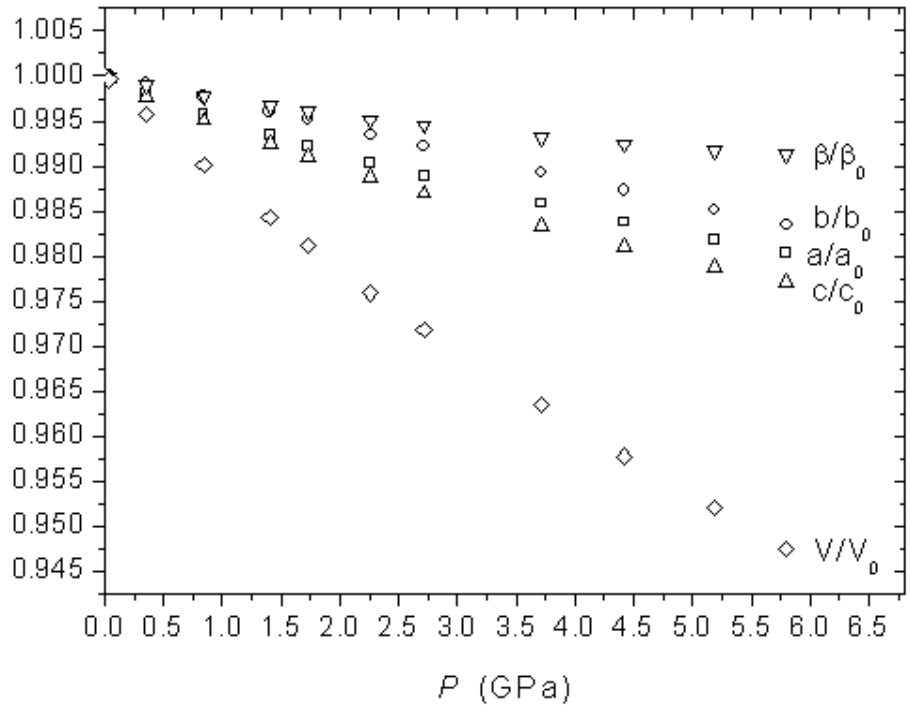

Fig. 3.3-3: Lattice parameters of $^{M2}(Li_{0.85}Mg_{0.09}Fe^{2+}_{0.06})^{M1}(Fe^{3+}_{0.85}Mg_{0.15})Si_2O_6$ pyroxene, normalized to the room condition values, *vs* pressure

d. *Structurally-incorporated hydrogen as an internal probe to phase transitions in minerals: an investigation of $MgSiO_3$ (enstatite) (G.D. Bromiley, F.A. Bromiley and S.D. Jacobsen)*

Many so-called nominally anhydrous minerals (NAMs) have been shown to contain small, but significant amounts of structurally-incorporated hydrogen, bound to oxygens in their mineral structures. The main method used to characterise such hydrogen is FTIR spectroscopy, where the vibrational mode of the OH dipole gives rise to absorption bands in IR spectra. The wavenumber of these bands depends on the strength and geometry of the OH bonds, but is also largely a function of the bond neighbourhood. Therefore, in theory, it should be possible to gain some information on the local structure of the host phase by careful examination and characterisation of the absorption bands in the IR spectra.

Enstatitic pyroxene is one of the most important phases in the upper mantle, existing in one of three main forms, orthoenstatite (Oen), low-temperature clinoenstatite (LCen) and high-pressure clinoenstatite (HCen). Previous work has demonstrated that Oen can contain several hundred ppm water as structurally-bound hydrogen. In this study, the effects of structural changes on the mode of hydrogen incorporation and on hydrogen solubility in enstatite have been investigated. Large enstatite crystals, doped with Al, have been synthesised over a range of pressures and temperatures, and samples were characterized using XRD, micro-Raman spectroscopy and polarised FTIR spectroscopy. Al doping has previously been shown to increase the number of absorption bands in IR spectra for enstatite, and the solubility of hydrogen. Data from IR spectra have been used to propose mechanisms for hydrogen incorporation in the different forms of enstatite.

IR spectra for all samples are characterized by a large number of O-H stretching absorption bands over the wavenumber range 4000 to 2000 cm^{-1}, implying the presence of structurally-incorporated hydrogen. IR spectra for Oen are clearly distinguishable from spectra for both forms of Cen, allowing the Oen stability field to be mapped out in P-T space (Fig. 3.3-4). Comparison of results with previous investigations suggests that differences in water solubility between the different forms of enstatite could have an influence on phase stability in the system.

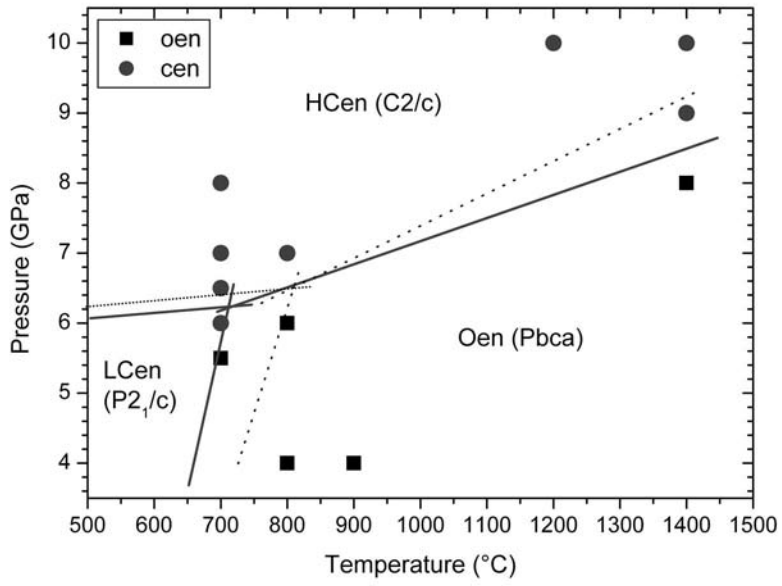

Fig. 3.3-4: The stability field of Oen mapped-out using differences in IR spectra (solid lines). Dotted black lines represent boundaries determined by Ulmer and Stadler (Am. Mineral. 86, 1267-1274, 2001), and are in broad agreement. Slight differences in phase boundaries could be the result of differences in water solubility between the different phases. The position of the LCen-HCen boundary is also shown, as determined from experiments at 700 °C (Fig. 3.3-5). The position of this boundary cannot be determined at lower temperatures due to the stability of the 10Å phase.

Previous investigations have demonstrated that HCen is non-quenchable, and that it reverts to LCen during decompression. In accordance with this observation, sample characterization by

micro-Raman spectroscopy reveals no differences between samples grown in the stability fields of LCen and HCen. However, for samples synthesized at 700 °C, differences between IR spectra are noted between the sample grown at 6.0 GPa and samples grown at higher pressure (Fig. 3.3-5). This coincides with the likely position of the LCen to HCen phase transition. Higher water solubility in the 6.0 GPa sample could imply that this sample grew in the LCen stability field, and that higher-pressure samples were originally HCen which have reverted to LCen during decompression. Therefore, characterization of H incorporation using FTIR spectroscopy provides a method for bracketing a supposedly non-quenchable phase transition from quenched samples. This technique could potentially be used to determine whether orthopyroxene in mantle xenoliths was originally HCen, and thus be of considerable use in UHP thermobarometry.

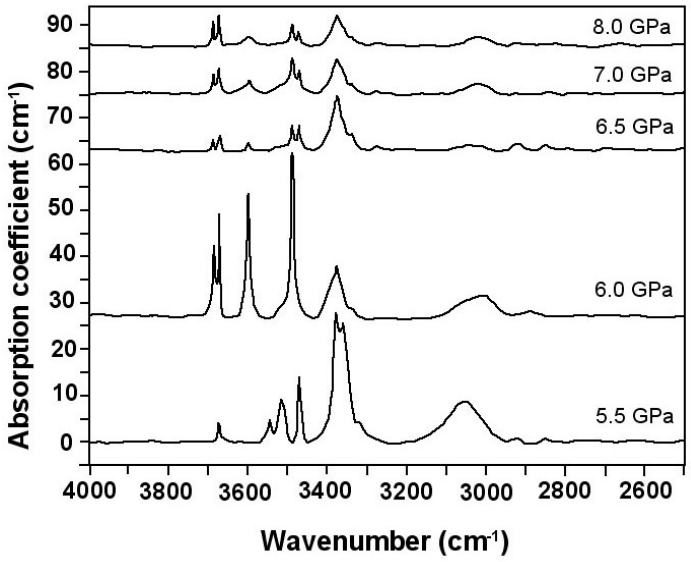

Fig. 3.3-5: Averaged polarised FTIR spectra for Al-doped enstatite grown under water saturated conditions at 700 °C, with increasing pressure (offset vertically). Sample synthesized at 5.5 GPa is Oen. All higher-pressure samples are LCen. However, a large difference in water solubility is noted between 6.0 and 6.5 GPa. In addition, the absorption band at approximately 3500 cm^{-1} in the 6.0 GPa sample is split into a doublet in higher-pressure samples. These differences probably indicate that samples synthesized at 6.5 GPa and higher were originally HCen which has reverted to LCen during decompression. In contrast, the sample at 6.0 GPa was grown in the LCen stability field.

e. *Amphibole crystal-chemistry, cation ordering and phase-transitions: new directions (G. Iezzi, in collaboration with G. Della Ventura/Roma, F. Càmara and R. Oberti/Pavia, G. Redhammer/Salzburg, G. Pedrazzi/Parma and J.L. Robert/Orléans)*

Due to its complexity and flexibility, the amphibole structure may incorporate a large number of different cations and anions. In fact, almost all the most abundant elements, except C and S, have been reported to be present in these minerals. Many studies have been devoted to understanding the particular aspects of the amphibole crystal-chemistry by using synthetic analogues. Synthetic amphiboles produced by hydrothermal synthesis, both in pressure-vessels and/or piston cylinder apparatus, allow the number of compositional parameters to be

reduced and the interpretation of data to be simplified. A comprehensive understanding of solid-solution behaviour, site-ordering (either long-range or short-range) and phase-transitions in amphiboles is a pre-requisite to formulating reasonable thermodynamic models that can be applied to petrogenetical modelling.

Recent studies, still in progress, show that the aggregate cation-charge arrangements in the structure have a more important role than previously believed. Li-bearing ferric-amphiboles represent an enlightening case, showing new and unexpected cation orderings. Some relevant points of the research recently done in Fe-bearing systems can be summarized as follows: a) the previous assumption of immiscibility between ^{B}Li- and ^{B}Na-amphibole groups is not observed in synthesis experiments (in agreement with very recent data on natural samples); b) the Mg, Mn, Fe, Li amphibole group is effectively connected with the alkali group through solid solution exchanges; c) due to its particular crystal-chemical behaviour, Li must be definitively regarded as an A-, B- and C-site cation in the amphibole structure; d) all Fe-rich Li-bearing synthetic amphiboles investigated by us have *C*2/*m* symmetry.

In the Na_2O-Li_2O-MgO-SiO_2-H_2O amphibole system there is complete solid-solution of Mg, Li and Na on the B-site, the A-, C- and T-sites being occupied only by Na, Mg and Si, respectively. In this system we have not found configurations involving ^{A}Li so far. This synthetic system, although not found in nature, is very interesting as all the studied compositions crystallize in the *P*2$_1$/*m* space group at room T. This finding suggests that the driving force for the P $\Rightarrow$ C phase-transition, is not only controlled by the aggregate cation radius at the B-sites. In the $(Mn^{2+},Fe^{2+},Mg)_7Si_8O_{22}(OH)_2$ amphibole system, with a virtually empty A-site, the *P*2$_1$/*m* space groups is restricted to the Mg-rich compositions, whereas with the introduction of $^{B}Fe^{2+}$ and/or $^{B}Mn^{2+}$, the structure transforms to *C*2/*m*. Notably, in the Na_2O-MgO-SiO_2-H_2O amphiboles, Na_1Mg_1 is the local environment on the B-site, implying an important increasing of the B-site dimension.

HT studies, still in progress, show that is possible to model the B-site dimensions versus the transition temperature. A *P*2$_1$/*m* synthetic amphibole with composition close to $NaNaMgMg_5Si_8O_{22}(OH)_2$, transform at 257 °C to the *C*2/*m* space group; this displacive phase-transition is second order in character (Fig. 3.3-6).

In this composition, OH-stretching modes of IR spectra show two higher-frequency bands, due to the local MgMgMg-OH-^{A}Na envinronments. The two bands can be assigned to two different O3-H groups in the *P*2$_1$/*m* structure; the band at 3667 cm^{-1} being assigned to local cummingtonitic arrangement (Fig. 3.3-7). *In situ* HT IR allows the phase transitions to be monitored, showing the merging of these two higher-frequency bands. Therefore HT-IR OH-stretching spectroscopy can be considered as a new and alternative tool to investigate displacive phase-transitions in hydrous minerals.

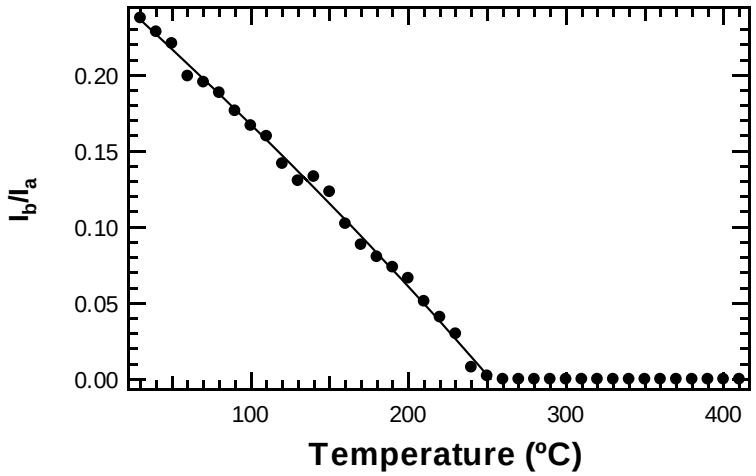

Fig. 3.3-6: Changes in the aggregate intensity ratio as a function of temperature for the synthetic amphibole $NaNaMgMg_5Si_8O_{22}(OH)_2$. The line is the polynomial fit of a *246* Landau potential to experimental data.

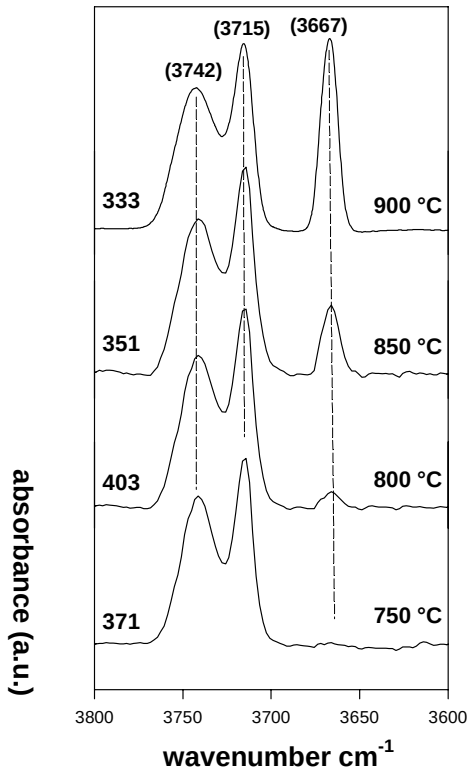

Fig. 3.3-7: IR OH-stretching data for nominal $NaNaMgMg_5Si_8O_{22}(OH)_2$ amphibole synthesized in the 750 °C (bottom) 900 °C (top) temperature range.

f. *High-pressure behaviour of $Ca_{0.2}Sr_{0.8}Al_2Si_2O_8$ feldspar (F. Nestola/Torino and T. Boffa Ballaran, in collaboration with P. Benna, M. Tribaudino and E. Bruno/Torino)*

The feldspar structure can accommodate in the cavities of its tetrahedral framework a wide range of cations that affect its behaviour as a function of pressure and temperature. The

highest symmetry possible for the feldspar structure is *C*2/*m*, and there are several transition pathways that can be traced from this structure down to the $P\bar{1}$ symmetry of anorthite ($CaAl_2Si_2O_8$). In particular, substitution of Ca by larger Sr cations gives rise to phase transformations from $P\bar{1}$ anorthite-rich samples to $I\bar{1}$ samples at intermediate compositions, and to $I2/c$ Sr-rich ordered feldspars. A phase transition from $P\bar{1}$ to $I\bar{1}$ occurs as a function of temperature in anorthite end-member. A phase transformation from $I\bar{1}$ to $I2/c$ has also been observed with increasing temperature for Sr-rich feldspars that are triclinic at room temperature. High-pressure investigations were undertaken only on pure end-members of the $(Ca,Sr)Al_2Si_2O_8$ solid solution. Anorthite transforms between 2.5 and 3.1 GPa to a $I\bar{1}$ structure which appears to be different from the high-temperature $I\bar{1}$ structure. A further phase transformation to a yet undefined structure has been observed at about 10 GPa by Raman spectroscopy. The behaviour of the Sr-feldspar end-member is less clear, since it appears to become triclinic as a function of pressure at 3.2 GPa, but the bulk modulus relative to the monoclinic phase is too high for a feldspar structure, suggesting that the volume data presented in the literature may be affected by some systematic errors. However, preliminary single-crystal investigation up to 5 GPa on Sr-feldspar did not show the onset of any transition. As yet, the high-pressure behaviour of intermediate compositions of the solid solution has not been investigated.

A single-crystal of $Ca_{0.2}Sr_{0.8}Al_2Si_2O_8$ having $I\bar{1}$ symmetry at room conditions has been loaded in a diamond anvil cell together with a quartz single-crystal as internal pressure standard and a 4:1 methanol:ethanol mixture as pressure medium. Unit-cell parameters were measured as a function of pressure up to 7.7 GPa. At pressure above 4 GPa a first-order transition from triclinic to monoclinic symmetry is observed, indicated by the a discontinuous change in α and γ unit-cell angles (Fig. 3.3-8). Careful cycling above and below the transition

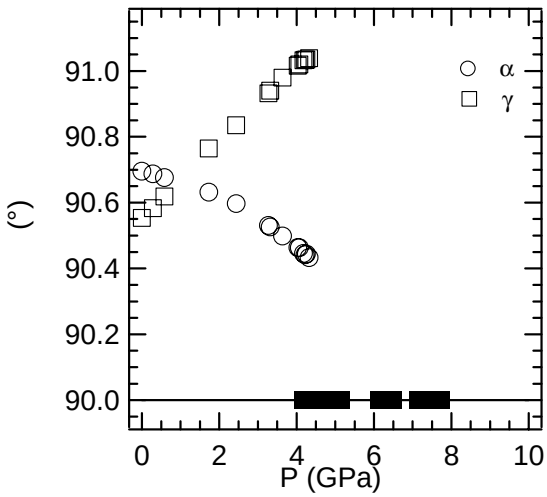

Fig. 3.3-8: Variations of α and γ unit-cell angles in $Ca_{0.2}Sr_{0.8}Al_2Si_2O_8$ feldspar as a function of temperature. The sudden changes to 90° are clearly indicating the phase transition from triclinic (open symbols) to monoclinic (filled symbols) symmetry.

has shown the presence of hysteresis between 4.0 and 4.3 GPa. This transition is likely to be the $I\bar{1}$ to $I2/c$ phase transformation observed for the same sample with increasing temperature. The H*P*-monoclinic structure is at present under investigation. EoS parameters for the triclinic phase calculated up to 4.1 GPa using a Birch-Murnaghan equation of state are V_0=1393.97(5) Å^3 K_0=88.7(7) GPa and K'=1.5(2). The bulk modulus of this feldspar is very similar to that reported for the anorthite end-member. A further first-order phase transformation from monoclinic to monoclinic symmetry (Fig. 3.3-9) has been observed at pressure above 7 GPa with a volume change of ~ 1.7 % and is at the moment under investigation.

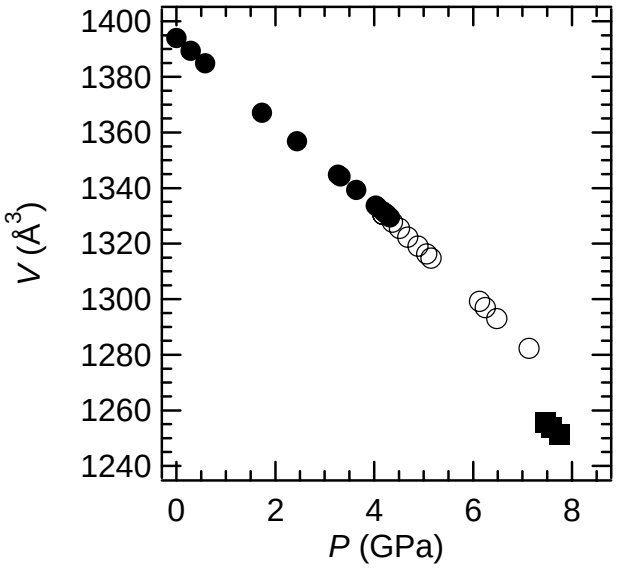

Fig. 3.3-9: Unit-cell volume variation in $Ca_{0.2}Sr_{0.8}Al_2Si_2O_8$ feldspar as a function of pressure. Note the discontinuity near 7 GPa, indicating an additional phase transition.

g. *Spontaneous strain and order parameter coupling associated with the incommensurate phase transition in nepheline (M.A. Carpenter/Cambridge, T. Boffa Ballaran, K.S. Knight/Didcot)*

The lattice parameters of a natural sample of nepheline (~ $Na_9[K_{2\ 1}]Al_{11}Si_{13}O_{48}$) have been determined from high resolution neutron powder diffraction patterns. Data were collected during heating from 4 to 650K and during cooling from 630 to 15 K. During the heating cycle disordering of potassium atoms and vacancies occurs, but during cooling the incommensurate structure returns by a largely displacive mechanism. As expected for incommensurate phase transitions, the changes in lattice parameters are small but, thanks to the exceptionally high resolution of the high-resolution powder diffraction at the ISIS facility, they are clearly resolved for the first time. The data are shown in Fig. 3.3-10, along with spontaneous strains extracted from them. Absolute values of the strains ($e_1=(a-a_o)/a_o$, $e_3=(c-c_o)/c_o$) are not well constrained because the baselines (a_o, c_o, V_o: dashed lines) depend on the slight curvature of

lattice parameters for the disordered structure above ~ 450 K. The pattern of variation of these strains is much less sensitive to the choice of baselines, however. K/vacancy ordering causes a shearing of the structure (contraction along c and expansion along a), while the displacive transition causes a small positive volume strain.

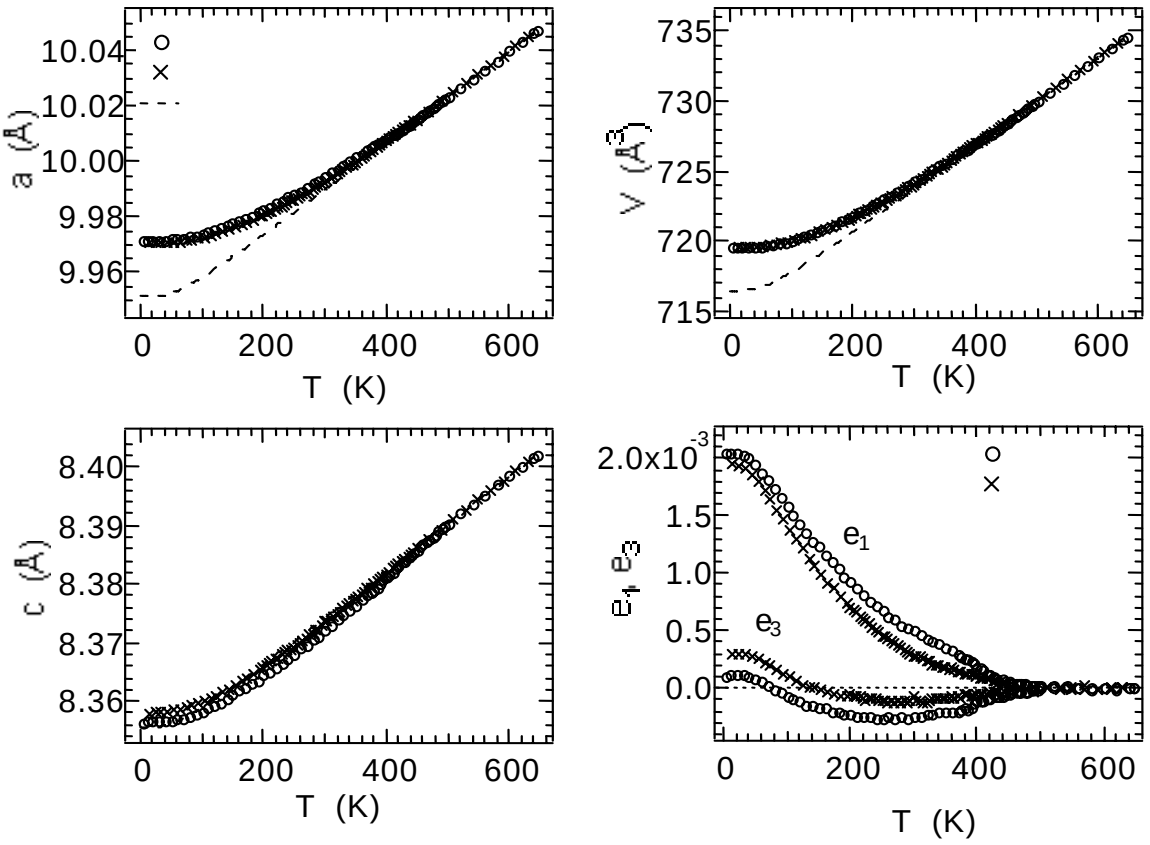

Fig. 3.3-10: Variation of the lattice parameters as a function of temperature and derived strain components associated to the incommensurate phase transition of nepheline.

Because displacive and order/disorder components of the incommensurate phase transition cause some strain, it is likely that they can couple by a common strain mechanism. The coupling will be bilinear, with the implication that the main effect will be to renormalise the transition temperature and to produce an unusual temperature dependence for the strains, similar to what is actually observed. The low temperature, displacive transition will occur at higher temperatures if cooling is slow enough to allow K/vacancy ordering to occur. This interpretation provides a basis for developing a Landau model of the phase transition, in which bilinear coupling occurs between incommensurate structures formed by a displacive mechanism and by an order/disorder mechanism. The same coupling mechanism is likely to be responsible for the incommensurate structure of plagioclase feldspars, and we predict that there might be a displacive incommensurate phase transition in intermediate plagioclases with high degrees of Al/Si disorder.

h. *Germanate garnets as an analog system of the mantle transition zone high-pressure garnets (G. Iezzi, T. Boffa Ballaran, C.A. McCammon, F. Langenhorst and F. Seifert)*

Germanate systems are often used in Earth and Material Sciences as analogues for silicate systems. The main advantage resides their lower temperature (*T*) and pressure (*P*) of crystallization, with respect to their corresponding silicate topological structure. Garnets are common phases in the Earth and, due to their crystal-structure and compositional variations, they are stable over a huge *T* and *P* range from high crustal levels down to the transition zone of the mantle (400-670 km). Majorite is the most stable garnet at high pressure and it was first discovered in meteorites. This garnet accounts for about 40 % (vol.) of the mantle transition zone phases. High-pressure experiments have demonstrated that there is a possible solid-solution between majorite ($^{VIII}Mg_3{}^{VI}Mg^{VI}Si^{IV}Si_3O_{12}$) and pyrope ($^{VIII}Mg_3{}^{VI}Al^{IV}Si_3O_{12}$). The principal difference between the two garnets is due to the ordering of Mg and Si in the octahedral sites of majorite, with consequent reduction of symmetry from cubic to tetragonal. This phase transition could account for a seismic discontinuity, revealed by geophysical studies. Study of majorite garnets and of their cation ordering is difficult, because of the very high *T* and *P* required, therefore Ge-garnets are an ideal analogue system.

The aim of this project is to explore the stability conditions of Ge-garnets in the system: CaO-FeO-Fe_2O_3-Al_2O_3-GeO_2 and the relation between composition and structural topologies. Calcium germanate ($^{VIII}Ca_3{}^{VI}Ca^{VI}Ge^{IV}Ge_3O_{12}$) garnet is the analogue of majorite, and is stable at a pressure and temperature range 1 to 6 GPa and 700 °C to 1500 °C. This composition is strongly affected by slow crystallization kinetics; thus the use of glass starting materials and hydrothermal syntheses are required. Dodecahedral (X) and tetrahedral (Z) sites in this garnet are occupied only by Ca and Ge respectively, whereas Ca and Ge can both substitute onto the octahedral (Y) sites. The difference between *a* and *c* axes of the tetragonal unit-cell decreases with increasing *T* of crystallization, as Ca and Ge disorder on the Y sites, with consequent reduction of the tetrahedral distortion (Fig. 3.3-11).

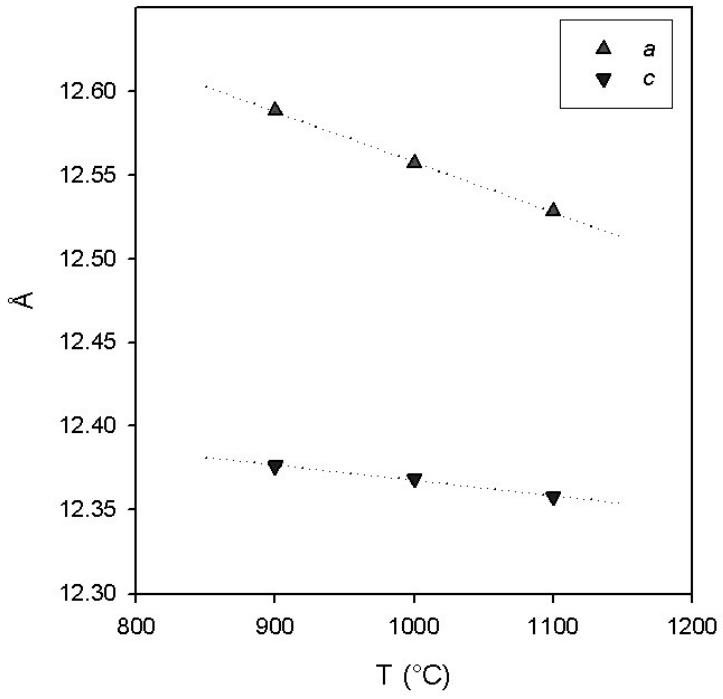

Fig. 3.3-11: Tetragonal unit cell edges as a function of temperature of crystallisation.

The introduction of iron into the $Ca_4Ge_4O_{12}$ structure causes a decrease of the tetragonal cell parameters (Fig. 3.3-12), as observed for the pyrope-majorite solid solution. However, despite the higher fO_2 imposed, a constant increase of Fe^{2+} is observed in $Ca_4Ge_4O_{12}$-rich samples as a function of the *T* of synthesis, as revealed by both Mössbauer and ELNES spectroscopy. The constant increase of Fe^{2+} in the run-products is coupled with a decrease of Ca at the Y site. It has also been found that at 3 GPa the solid solution between $Ca_4Ge_4O_{12}$ and $Ca_3Fe_2Ge_3O_{12}$ is not complete, as testified by the coexistence of both tetragonal and cubic garnets at intermediate compositions (Fig. 3.3-12).

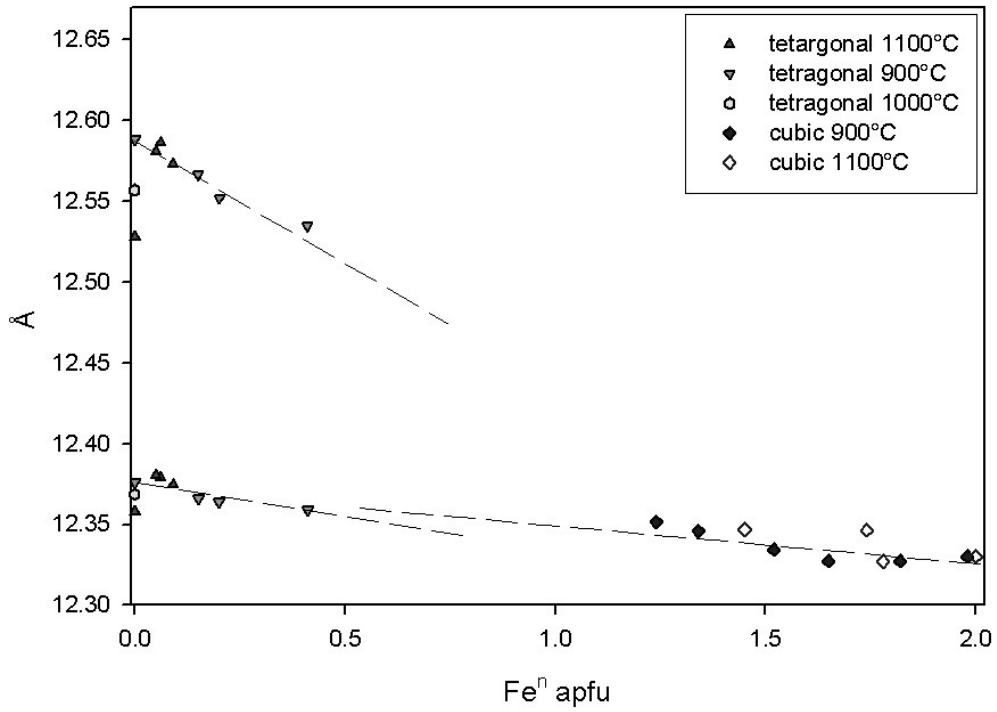

Fig. 3.3-12: Unit cell parameters as a function of garnet composition (as total Fe atoms per formula unit) and temperature of synthesis.

i. *A macroscopic and microscopic investigation of the magnesite-otavite solid solution (F.A. Bromiley, T. Boffa Ballaran, F. Langenhorst, in collaboration with M. Zhang/Cambridge)*

Knowledge of the calcite-magnesite system is fundamental to understanding the carbon cycle in the Earth's crust and mantle. In natural rocks, the calcite end-member, $CaCO_3$, and the intermediate ordered dolomite phase, $CaMg(CO_3)_2$, are the most important minerals belonging to this system. With increasing temperature, the two-phase region closes and simultaneously the intermediate phase (dolomite) disorders - a similar situation as in the diopside - jadeite system. The detailed configuration of the phase diagram is dependent on the nature of the order-disorder phase transition, but required experimental conditions make a precise analysis of this transition difficult. The binary join within the magnesite ($MgCO_3$) –

otavite ($CdCO_3$) system has, therefore, been investigated as an analogue for the magnesite – calcite system, because experiments can be carried out at significantly lower temperatures.

Solid-state syntheses were carried out at 500, 600, 650, 700 and 800 °C and 1 GPa in a piston cylinder press, using silver oxalate as a CO_2 source. An ordered structure of cadmium dolomite [$CdMg(CO_3)_2$] was observed by X-ray powder diffraction and Transmission Electron Microscopy (TEM) in the central region of the system at temperatures of 500, 600 and 650 °C. Towards Mg-rich compositions, a two-phase run product was confirmed, implying the presence of a miscibility gap between magnesite and cadmium dolomite. Run products at the cadmium-rich end of the system consisted of only one carbonate phase, suggesting that a miscibility gap between otavite and cadmium dolomite, if it exists, has a critical temperature below 500 °C.

Experiments run at 700 and 800 °C were found to be completely disordered across the entire solid solution, this result being significantly different from previous studies on the same system. It was also found that it was not possible to yield a completely ordered sample and equilibrium was reached at approximately 19 hours.

Infra-red analysis was carried out on the samples in order to determine the local structural response to cation substitution and order. The effect of cation substitution on the peak position across the solid solution may be seen evidently in Figure 3.3-13. It may be seen that with increasing substitution of cadmium, the peaks shift to lower wavenumbers.

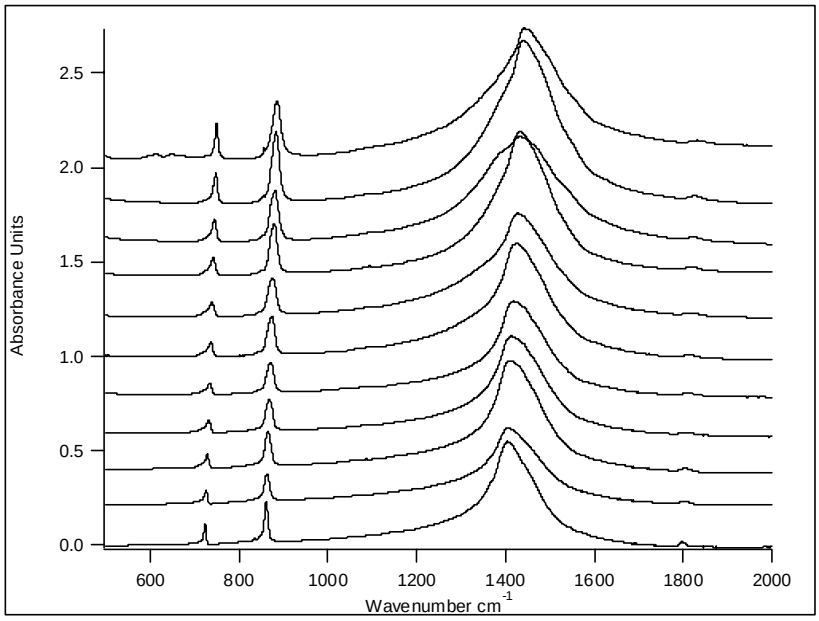

Figure 3.3-13: A section of the mid-infrared (MIR) spectra collected at room temperature for samples synthesised at 800 °C, showing the shift of peaks to lower wavenumbers with increasing substitution of cadmium. The three peaks can be assigned to three different forms of CO_3 bending and stretching. The peak at ~ 700cm^{-1}, ν_4, is due to doubly degenerate bending of the CO_3 groups. The peak at ~ 850cm^{-1}, ν_2, is due to the out of plane bending of the planar CO_3 groups. The large peak at between 1400-1500cm^{-1}, ν_3, is due to doubly degenerate asymmetric stretching of the CO_3 groups.

There is a clear linear correlation between substitution of cadmium and shift in wavenumber. It may also be seen that peaks for the two end-members are much sharper than those at intermediate compositions. Preliminary analysis of the line broadening suggests that the solid solution displays non-ideal behaviour. Further IR analysis will be carried out in order to quantify the effect of order-disorder on the local structure.

j. *In situ Raman spectroscopic studies of phase relations among TiO_2 polymorphs (N.A. Dubrovinskaia, L.S. Dubrovinsky, A. Kantor and I.Yu. Kantor)*

The group IV metal dioxides are known for their manifold polymorphs that form under varying chemical, temperature, and pressure conditions. Outstanding properties of some silica (SiO_2), germania (GeO_2), titania (TiO_2), and zirconia (ZrO_2) polymorphs have not only made those phases extremely useful in many applications, but also identified them as prime materials for experimental and theoretical studies. High-pressure transformations of SiO_2, the most abundant chemical component of the Earth's mantle, have attracted special attention, as well as low-pressure analogues of silica, *i.e.* GeO_2 and TiO_2.

A number of experimental and theoretical studies indicate that titanium dioxide could have a series of high-pressure phases with the hardness possibly approaching that of diamond. For example, the baddeleyite-type phase of TiO_2 has the high bulk modulus K_{300} of 290 GPa. The monoclinic baddeleyite-type structure (MI, space group $P2_1/c$) with its seven-fold coordination of the metal is known to transform, upon further compression, through an intermediate orthorhombic (OI, space group *Pbca*) structure to another orthorhombic (OII, space group *Pnma*) cotunnite-type phase. Cotunnite-structured ZrO_2 and HfO_2 possess extremely high bulk moduli of 444 and 340 GPa, respectively. TiO_2 with the cotunnite structure is proven to be among the most incompressible and hard oxides.

A series of experiments have been conducted in laser- or electrically-heated diamond anvil cells (DACs). Anatase or rutile (99.99 % TiO_2) was used as a starting material. At applied pressures of about 12 GPa or above, both rutile and anatase transform to the baddeleyite ($P2_1/c$) phase. On further compression, reflections due to the MI phase could be followed to over 60 GPa. At pressures above about 45 GPa, however, the quality of the diffraction pattern decreased drastically and at about 60 GPa, the material became translucent. We observed that at pressures above 50 GPa, TiO_2 absorbs Nd:YAG laser radiation and the laser-heated areas of the sample became black. After heating at 1600-1800 K by laser for 40 minutes at pressures between 60 and 65 GPa, the material transformed to a new phase as evident from X-ray diffraction spectra. All reflections of the new phase could be indexed in an orthorhombic cotunnite-type cell. Transformations observed by X-ray diffraction were confirmed by Raman spectroscopy (Fig. 3.3-14). Although *in situ* high pressure and temperature Raman spectroscopy in DACs does not provide direct structural information, this method is much faster and experimentally easier for realisation than X-ray powder diffraction. Raman signals

from all titania phases are strong and clearly distinguishable (Fig. 3.3-14) and we used Raman spectroscopy to follow some phase relations in TiO_2 at high-P,T conditions. Particularly, as shown in Fig. 3.3-15 we found that the slope of the phase boundary between α-PbO_2-type TiO_2 and MI phase (77(3) K/GPa) is significantly lower than 188 K/GPa earlier reported by Tang and Endo (*J. Am. Ceram. Soc.* **76** 796, 1993).

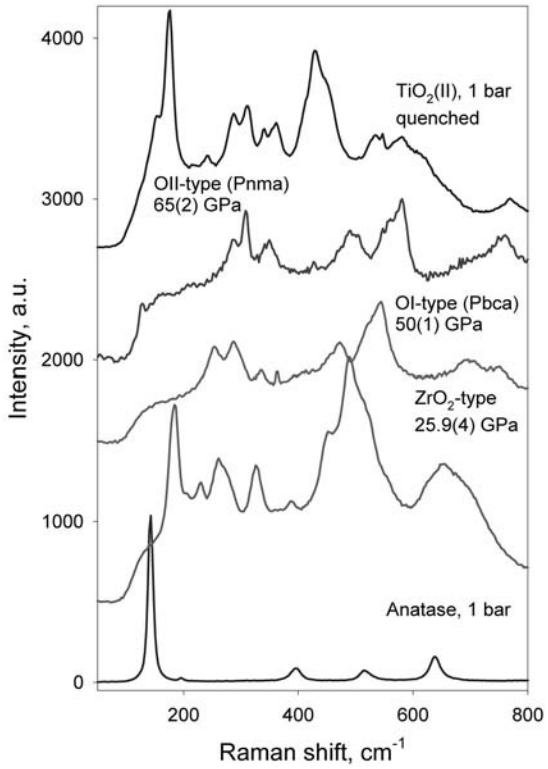

Fig. 3.3-14: Raman spectra of some TiO_2 polymorphs synthesized in electrically heated diamond anvil cells.

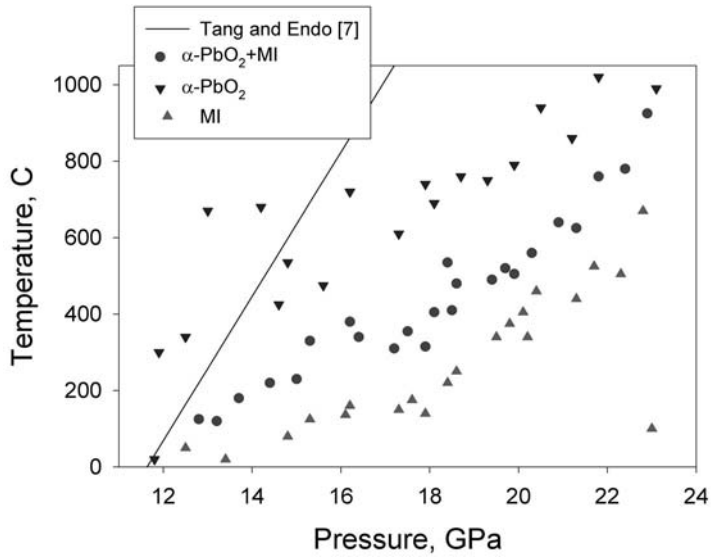

Fig. 3.3-15: Phase relations between α-PbO_2- and baddelyite- (MI) structured TiO_2 phases.

k. *A new α-PbO_2-type high-pressure polymorph of GeO_2 (L.S. Dubrovinsky, in collaboration with V. Prakapenka, G. Shen, M. Rivers and S. Sutton/Chicago)*

The great interest in the polymorphism of GeO_2 comes from both the fundamental point of a possible common sequence of high-pressure structural transformations of group IV element dioxides (SiO_2, GeO_2, SnO_2 and PbO_2), and practical application as a material with unique optical properties. There are two well established polymorphs of GeO_2 at ambient pressure: α–quartz and rutile-type structures with fourfold- and sixfold-coordinated germanium ions, respectively. The high-pressure behaviour of both the quartz and rutile phases of GeO_2 has been studied intensively for the last three decades because their structures are believed to display the high-pressure properties of geologically important silica at relatively moderate pressures. However, there are inconsistencies in the results of high-pressure phase transformations of GeO_2 reported by different groups.

A phase transition of α–quartz-type of GeO_2 above 6 GPa has been observed at room temperature with various techniques: X-ray diffraction, EXAFS, infrared and Raman spectroscopy. It has been established that transformation results in an increase of Ge coordination number with pressure from four to six. The amorphous structure of this high-pressure phase of α–quartz type GeO_2 above 6 GPa has been reported by several groups. Meanwhile, a crystalline high-pressure phase of α-quartz-type GeO_2 with monoclinic structure (space group $P2_1/c$, Z=6) was reported. The post α-quartz GeO_2 monoclinic-type phase was found to be metastable up to 50 GPa at room temperature. Recent *ab initio* calculations predict the following sequence of phase transformations of GeO_2: rutile ⇒ (19 GPa)$CaCl_2$ ⇒ (36 GPa) α-PbO_2 ⇒ (65.5 GPa)Pa3 (pyrite). Such phase transitions were either observed, or theoretically predicted for silica SiO_2. Despite extensive studies of GeO_2, a high-pressure polymorphism of GeO_2 remains unclear. No evidence of the theoretically predicted α–PbO_2 phase has been reported.

High resolution angle dispersive X-ray diffraction experiments were performed at the Advanced Photon Source (APS) at Argonne National Laboratory (GSECARS, sector 13, Chicago, USA) and the European Synchrotron Radiation Facility (ESRF, ID30 and SNBL beamlines, Grenoble, France) using on-line image plate or a CCD detector. At the APS the double-sided laser-heating technique with laser spot of 20-40 μm was used. The laser heating at ESRF was carried out using a Nd-YAG laser (λ=1064nm, 17 W).

Examples of diffraction spectra are shown in Fig. 3.3-16. The high-pressure induced phase transformation of α–quartz type structure of GeO_2 to a poorly crystalline monoclinic structure (space group $P2_1/c$) phase is detected above 6 GPa [Fig. 3.3-16(b)]. This crystalline phase was observed to at least 52 GPa. During laser heating, as temperature was increased to 1600±100 K, the gradual transformation of the monoclinic phase directly to the orthorhombic structure was observed at 36.4 GPa [Fig. 3.3-16(c)]. The high-pressure phase has the $CaCl_2$-type structure (space group *Pnnm*, Z=2).

On further compression to 41 GPa and laser heating at ~ 1600 K the reflections from a new high-pressure phase started to grow. The relative intensities of the reflections corresponding to the $CaCl_2$-structured phase decreased with increasing pressure. Above 44 GPa [Fig. 3.3-16(d)] the diffraction intensities from the new phase are greater than those from the $CaCl_2$-type phase, although coexistence of both phases was observed up to 60 GPa.

The structure of the new phase is an orthorhombic α–PbO_2-type (Fig. 3.3-17). The crystal structure of α–PbO_2 (*Pbcn* space group symmetry) can be described in terms of an *hcp* packing of oxygen with one-half of the available octahedral interstices occupied by germanium ions to form 2x2 zigzag chains of GeO_6 edge-sharing octahedra. In the case of the $CaCl_2$ (*Pnnm*) or rutile ($P4_2/mnm$) structures, germanium ions are arranged in such a way as to generate straight chains of edge-sharing octahedra, which are corner linked to form a 3D network with *hcp* or distorted *hcp* arrays of oxygen, respectively. The molar volume of the α–PbO_2-type is smaller than that of the $CaCl_2$-type: at 44.5 GPa the difference is 1.4 % (14.36(1) cm^3/mol and 14.56(5) cm^3/mol respectively) and at 60 GPa it is 1.6 % (13.89(0) cm^3/mol and 14.12(1) cm^3/mol respectively). The molar volume versus pressure data were fitted using a third-order Birch-Murnaghan equation of state with K' fixed to 4. The fit gave values of the bulk modulus for α–PbO_2 and rutile-type phases of 256(2) GPa and 247(3) GPa, respectively.

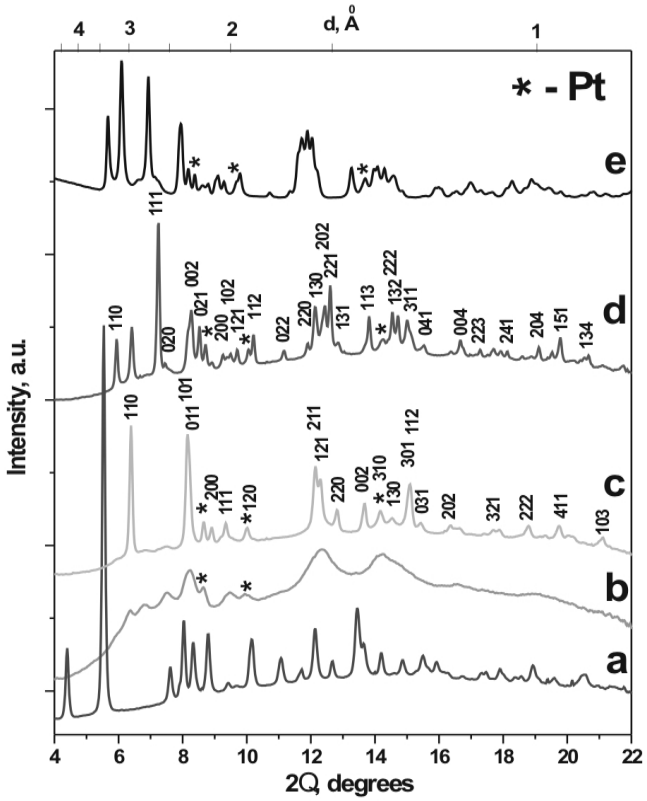

Fig. 3.3-16: Integrated X-ray diffraction spectra of various GeO_2 phases collected at different pressure-temperature conditions: (a) starting material α-quartz-type at ambient conditions after loading in DAC, (b) monoclinic-($P2_1/c$-type) structure at 34 GPa at room temperature, (c) $CaCl_2$-type structure at 36.4 GPa after laser heating at 1600±100 K, (d) mixture of α-PbO_2-type and $CaCl_2$-type structure at 44.6 GPa after laser heating at 1600±100 K, (e) – sample recovered from 60 GPa after laser heating at 1800±100 K.

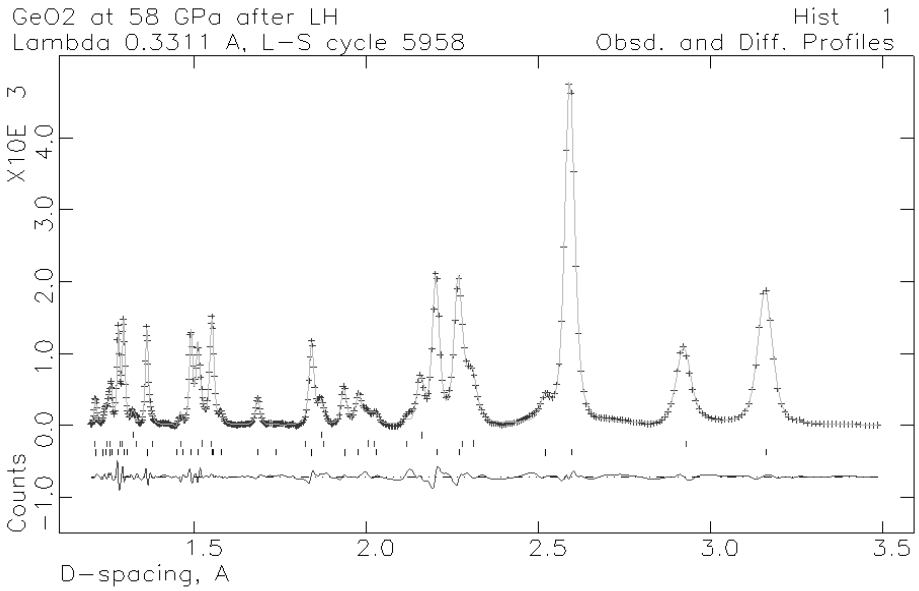

Fig. 3.3-17: Rietveld full profile refinement of α-PbO_2-type phase of GeO_2 at 60 GPa after annealing at 1800±100 K (upper markers – Pt, middle – $CaCl_2$-structured phase, and lower - α-PbO_2 structured phase).

l. *Effect of the titanium valence state on the O-K electron energy loss near-edge structure (E. Stoyanov, F. Langenhorst and G. Steinle-Neumann)*

Electron energy loss spectroscopy (EELS) is a powerful nanoscale technique for the detection of the valence state and coordination of transition metals in solids. Both the electron energy loss near-edge structure (ELNES) of the O K edge and transition metal *L* edge can serve as valuable fingerprints to the valence state. To exploit the potential of the ELNES technique, we have conducted a series of O *K* edge measurements on three titanium oxides (TiO, Ti_2O_3, TiO_2), all containing titanium in octahedral coordination. These compounds represent a set of standards for titanium in three different valence states (Ti^{2+}, Ti^{3+}, Ti^{4+}), and their characterization is essential for the identification of cation ordering and oxygen defect clustering in oxidic compounds.

In order to understand the signals in ELNES spectra and to derive crystal-chemical information from them, theoretical modeling is essential. There are basically two categories of modeling techniques: multiple scattering (MS) calculations and first principles calculations on the basis of density functional theory (DFT). We used DFT in the Linearized Augmented Plane Wave implementation (WIEN2k code) to compute the transition energies of the O *K* ELNES of the three titanium oxides for perfect crystals.

The results of O K ELNES measurements and computations for TiO_2 (rutile), Ti_2O_3 and TiO are summarized and compared in Fig. 3.3-18. Peaks in the O K edge spectra that are due to

the five degenerated Ti 3d orbitals (3 t_{2g} and 2 e_g levels) are labeled as 1 and 2, respectively. Major peaks in the higher energy region that originate from Ti 4s and 4p orbitals are labeled as 3, 4 and 5. Calculated O *K* spectra generally agree well with measured spectra. We note the following spectral changes as function of increasing valence state: *(i)* the crystal-field splitting (between peaks 1 and 2) and *(ii)* the energy separation between the Ti 3d and Ti 4s/4p orbitals become larger, and *(iii)* the Ti 4s/4p band-width decreases. The crystal-field splitting between peaks 1 and 2 depends on the magnitude of covalent bonding. As the number of d electrons increases from TiO_2 to TiO (Ti^{4+} - no d-electrons, Ti^{3+} - 1 d-electron and Ti^{2+} - 2 d-electrons), covalent bonding between Ti and O is weakened. The energy separation between the Ti 3d and O 2p orbitals increases from TiO to TiO_2 (each electron occupying the t_{2g} level reduces the energy by $2/5\Delta_o$), which results in the smaller band-width of Ti 3d. On the other hand, the band-width of Ti 4s/4p becomes larger with the increasing number of d-electrons (this leads to decreasing of the number of the unoccupied d-states and makes possible the transition 2p→4s and 2p→4p). In conclusion, our initial results demonstrate that EELS data combined with DFT computations provide fundamental insight into the detailed electronic structure of Ti compounds.

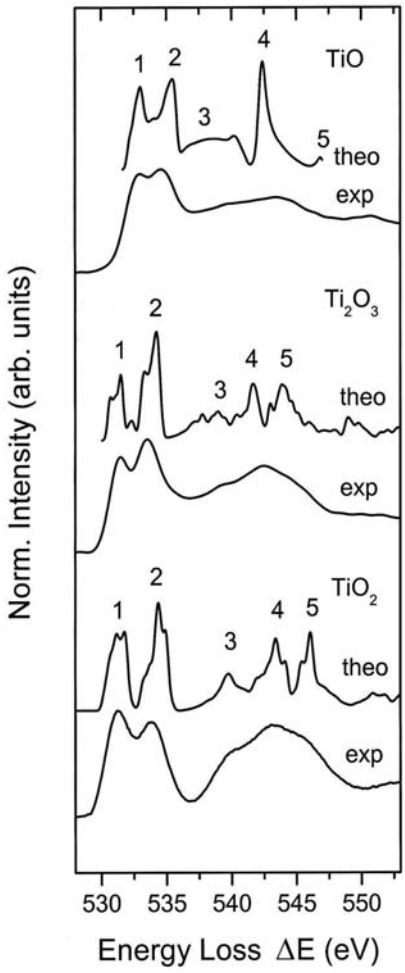

Fig. 3.3-18: Comparison between calculated and experimental O K edge ELNES for TiO_2, Ti_2O_3 and TiO.

3.4 Geochemistry

Chemical interactions between the elements that make up the Earth influence nearly every process that occurs inside and on its surface. Particularly relevant for us as surface dwelling creatures is the chemistry of carbon and oxygen which make up our atmosphere. The storage and cycling of these elements through geological time depends strongly on mantle geochemistry, where carbon solubility and oxygen fugacity are only two of many crucial parameters. The history of mantle processes can often be deciphered from geochemical markers in minerals, for example element partitioning patterns and diffusion profiles, where laboratory experiments are crucial for establishing the baseline behaviour. Theoretical modelling is also an important geochemical tool, and it allows scenarios to be investigated that would otherwise be impossible in the laboratory, such as the effect of variable thermal conductivity on the transition from olivine to wadsleyite, and hence the mechanism of deep-focus earthquakes. Structural transformations associated with the transition zone, *e.g.* from olivine to wadsleyite, are not strictly isochemical, because elements are not partitioned equally between phases. Partitioning data from high-pressure experiments can be correlated with geophysical observables such as the width of the 410 km seismic discontinuity in order to elucidate less easily measured parameters of the mantle, such as temperature. Complementary investigations of the width of the 410 km discontinuity using theoretical kinetic models provide constraints on mantle properties such as convection dynamics, the geoid and mantle viscosity.

The formation of the Earth's core was perhaps the most profound geochemical event to have occurred within the Earth's history. Although consensus is not universal, most models involve melting of iron-rich material and percolation to form the Earth's core, which then imprinted a signature of the core-forming process on mantle geochemistry. One of the challenges in such investigations is the paucity of natural samples from the lower mantle with which to test the various theories. Mineral inclusions in diamond provide our only source, and while they provide important constraints on diamond formation and mantle dynamics, questions remain open as to how closely they represent bulk lower mantle composition. A complementary approach involves high-pressure experiments, where aspects such as the ferric iron requirements of the lower mantle perovskite phase can be studied, with implications for the partitioning of siderophile and lithophile elements during core-mantle differentiation. Models of core formation involving percolation of melt through crystalline assemblages require a particular microstructure, *e.g.* dihedral angles of less than 60° between liquid iron-alloy and the solid silicate. Experimental investigations help to identify under which conditions this criterion is satisfied, and hence which constraints are relevant for the core-formation process, both on Earth and other planets such as Mars. The results from such studies emphasise the role of elements other than iron in core formation, and have motivated investigations of elements traditionally not included in experimental studies, such as carbon and magnesium.

a. *Carbon solubility in upper mantle minerals (S.S. Shcheka, H. Keppler/Tübingen, M. Wiedenbeck/Potsdam, in collaboration with D.J. Frost)*

The total amount of carbon stored in the mantle is several orders of magnitude larger than the mass of carbon in all near-surface reservoirs. However, the mode of carbon storage in the mantle is essentially unknown mainly due to the absence of reliable data on the solubility of carbon in ordinary mantle minerals. If carbon were significantly soluble (at least a few hundred parts per million by weight) in olivine, pyroxenes, spinel or garnet, the entire mantle carbon could be stored in these minerals, thereby making carbonates or carbon-rich fluids unstable throughout most of the mantle.

Previous attempts to measure carbon solubility in olivine were hampered by the slow diffusion of carbon in crystals and by contamination problems. Carbon solubility in other important mantle minerals such as pyroxenes, garnet and spinel was never investigated.

We synthesized carbon-saturated forsterite, enstatite, diopside, garnet, and spinel by growth from a carbonatite melt, which was isotopically enriched to contain more than 99 % of the isotope ^{13}C. The isotopic enrichment distinguishes any contamination (with normal isotopic composition) from carbon dissolved in the minerals. Experiments were carried out in a piston-cylinder apparatus (T = 900-1100 °C, P = 1.5-3.5 GPa), and a multianvil press (T = 1300 °C, P = 6 GPa). Run products were euhedral inclusion-free crystals (Fig. 3.4-1) embedded in a fine-grained matrix of carbonates.

Infrared spectra of carbonates recovered from the capsule confirmed that the carbon during experiments was mainly ^{13}C. Carbonates were removed by etching with hydrochloric acid. Carbon contents of the samples were measured with a Cameca ims 6 f ion probe specially tuned to suppress any carbon background. However, the measured carbon was dominated by the istotope ^{12}C. But unlike the samples with normal carbon isotope composition, the synthetic crystals yielded stable elevated ratios of $^{13}C/^{12}C$ up to 4 %. Assuming that any contamination had “normal” isotopic composition, we were able to quantify the carbon content of samples using appropriate reference materials. Synthetic forsterite, ion-implanted with a known dose of ^{13}C was used to calculate the carbon content of olivine. Data obtained for enstatite ($MgSiO_3$), diopside ($CaMgSi_2O_6$), pyrope ($Mg_3Al_2(SiO_4)_3$) and spinel ($MgAl_2O_4$) were calibrated against synthetic tholeiite glasses doped with ^{13}C and should be regarded as preliminary because secondary ion yields are matrix dependent. Nevertheless, the order of magnitude of C content in these minerals is certainly correct.

Carbon solubility in minerals of the upper mantle is exceedingly low (Fig. 3.4-2, Table 3.4-1). Even if data for forsterite were extrapolated to the pressures of the base of the upper mantle, the carbon content would not exceed 1 part per million by weight. Obviously, carbon must reside in separate carbon-rich phases, in particular carbonates, which can be easily mobilized

during even low degrees of partial melting. Carbonates decompose upon decompression below 2.5-3.5 GPa and release carbon dioxide, which can be rapidly transferred to the surface.

Table 3.4-1: Carbon concentrations in upper mantle minerals
(preliminary results)

Mineral	*T*, °C	*P*, GPa	Duration, hours	C, wt. ppm
Enstatite	900-1100	1.5	96-168	1.4-3.0
Diopside	900-1100	1.5	96-168	0.27-0.5
Pyrope	1300	6-9	10	1.9-2.2
Spinel	1100	1.5	168	Not detected

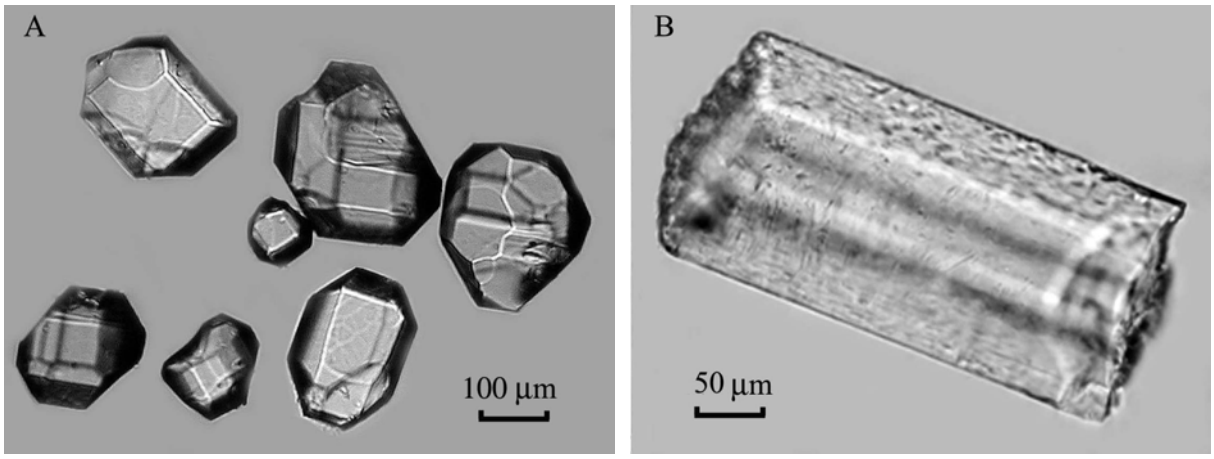

Fig. 3.4-1: Optical micrograph of run products after removal of carbonates. A: olivine, B: enstatite.

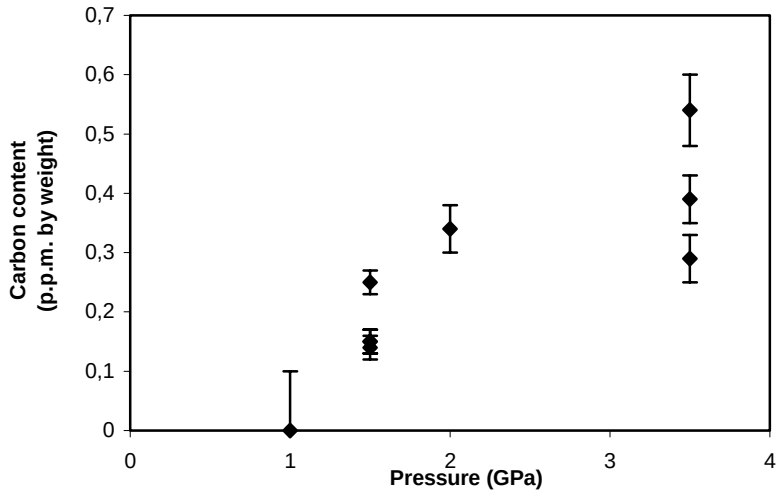

Fig. 3.4-2: Carbon solubility in forsterite as a function of pressure.

b. *Oxygen fugacity control in the cratonic mantle (C.A. McCammon, in collaboration with M. Kopylova/Vancouver)*

Oxygen fugacity exerts a major influence on chemical and physical properties of the mantle, particularly with regard to the composition and speciation of fluids, and thereby the melting behaviour of the mantle. A major question that remains to be answered concerns the nature of oxygen fugacity control within the mantle. If the mantle is assumed to be a closed system with no oxygen exchange with external sources, then oxygen fugacity is an intrinsic quantity that is completely determined by the bulk composition at a given pressure and temperature. The degree to which the system preserves this oxygen fugacity in the event of fluid infiltration or other influx of oxygen reflects the buffering capacity of the different equilibria, which depends in part on the concentration of oxidised species. Discussion regarding the nature of oxygen fugacity control within the mantle has been ongoing for more than two decades, where the current consensus seems to be that no single component dominates, and that factors likely vary in different parts of the mantle.

To investigate the control of oxygen fugacity in the cratonic mantle, we investigated a suite of mantle xenoliths from the Slave Province (northwestern Canada). The sample set comprised single grains of garnet and spinel chosen from peridotites, harzburgites, pyroxenites and megacrysts. Major element analysis was performed using the electron microprobe and the relative Fe^{3+} concentration was determined using the Mössbauer milliprobe. Pressures and temperatures were determined using various mineral thermobarometers, and oxygen fugacities were calculated using the olivine-orthopyroxene-spinel and olivine-orthopyroxene-garnet oxybarometers. There is a significant decrease in relative oxygen fugacity with depth through the cratonic mantle (Fig. 3.4-3). The variation of relative oxygen fugacity with depth

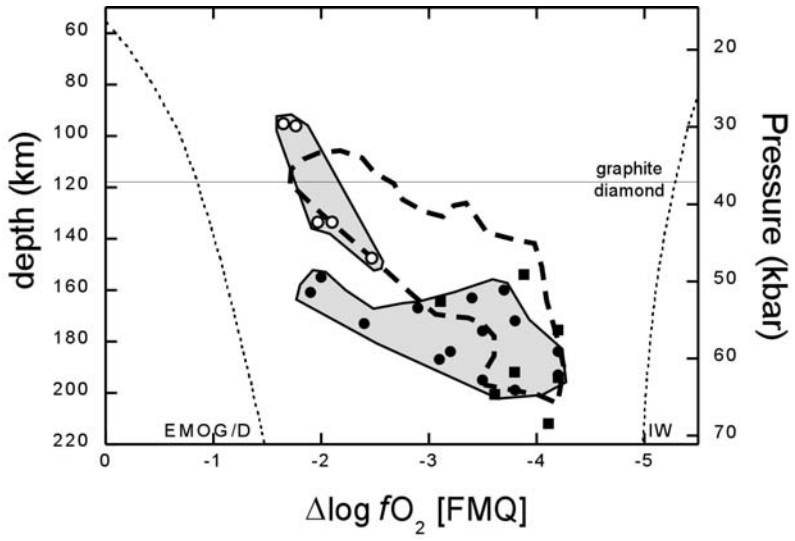

Fig. 3.4-3: Oxygen fugacity (relative to FMQ) of spinel-garnet and garnet peridotites as a function of depth. Open circles: N Slave spinel-garnet peridotite; solid circles: N Slave garnet peridotite; solid squares: SE garnet peridotite. Grey fields enclose values for the N Slave craton. The dashed field indicates literature data for the Kaapvaal craton (Woodland and Koch, 2003, Earth Planet. Sci. Lett., 214, 295) and Fennoscandia (Woodland and Peltonen, 1999, Proc. VII Inter. Kimb. Conf., 904). EMOG/D and IW indicate buffer curves according to the inferred geotherm for the Slave craton.

for N Slave spinel-garnet peridotite (grey field with open circles) is significantly steeper than for N Slave garnet peridotite (grey field with solid circles), which is consistent with the different ΔV terms of the reactions. Relative oxygen fugacity decreases with depth within the garnet peridotite facies also in the Kaapvaal craton (South Africa) and Fennoscandia (Fig. 3.4-3). This general trend is a consequence of the large negative ΔV (relative to ΔV of FMQ) describing the incorporation of Fe^{3+} into garnet, and together with the change in slope between spinel-garnet and garnet peridotite, implies that iron equilibria provide the dominant control on oxygen fugacity for this type of mantle.

c. *The effect of water on trace element partitioning in komatiitic melts (L.A. Gilpin, D.J. Frost, in collaboration with J.D. Blundy/Bristol)*

The origin of komatiites is quite controversial, and at the forefront of this debate is the issue of the water content in komatiites. Some models propose that komatiite melts had low to negligible water contents but high temperatures ("dry"), while others advocate moderate to high amounts of water with lower temperatures ("wet"). In this study we are investigating the effects of water on trace element partitioning in komatiitic liquids to see if certain trace elements can be used as indicators for the presence of water. Certainly this would have implications not only for the "wet/dry" komatiite debate, but could potentially be used as a tool to look for the presence of magmatic water in any system.

Starting compositions were calculated by combining a previously published experimental melt composition that was similar to Gorgona komatiite with the expected coexisting solid phase compositions. The water contents, added as hydroxides, varied in the range from 0-10 wt.%. Samples were placed in graphite sleeves in a Pt capsule, and run in the multianvil apparatus at 4 GPa and 1100-1600 °C. Chemical analyses were performed on crystals and liquids in the quenched samples at the University of Bristol, where major elements were measured using an electron microprobe and trace elements using a laser ablation ICP-MS.

All experiments produced an assemblage of garnet, orthopyroxene, and liquid (plus olivine in the dry experiments) and partitioning data were obtained for all phases. As shown in Fig. 3.4-4, the calculated mineral melt partition coefficients for certain elements (Ti, Zr, Sm, Hf, also Ga not shown for reasons of scale) show a robust correlation with water content. This effect seems to be much greater than that of temperature. For these elements, the partition coefficients decrease with increasing water content. Other elements (Yb, Lu) seem to be unaffected by the presence of H_2O. We have used the chondrite-normalised partitioning data in a simple batch-melting model in order to demonstrate how these data may be of use in identifying the role of H_2O in komatiite melt generation. Figure 3.4-5 shows a plot of how the Zr/Sm and Zr/Hf ratios in the melt would evolve for varying degrees of partial melting under dry and wet conditions. The trends for varying H_2O contents are compared with analyses of Gorgona komatiites. The model lends support to the idea that H_2O may have been present

during the partial melting event that produced the Gorgona komatiites. These results are preliminary, however, and a number of further factors and element ratios should be considered before firm conclusions on the origin of such melts can be made.

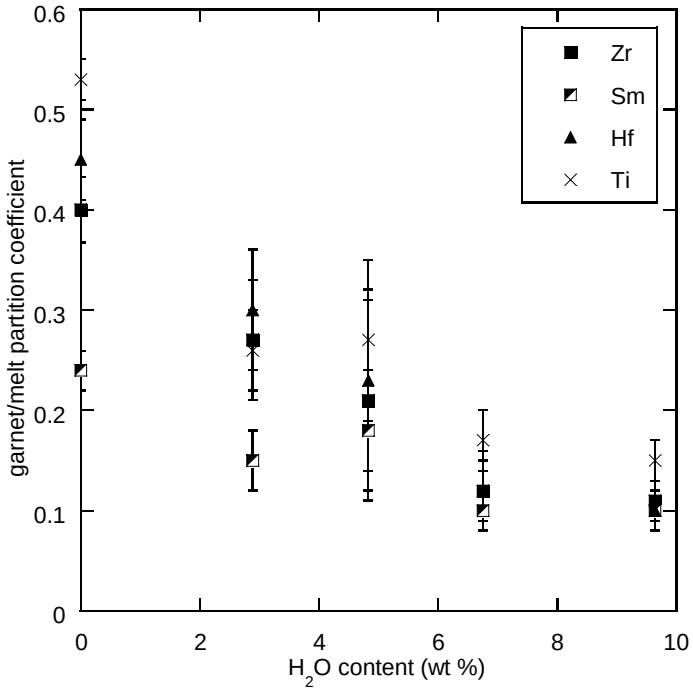

Fig. 3.4-4: Garnet/melt partition coefficients for four trace elements as a function of experimental bulk H_2O content.

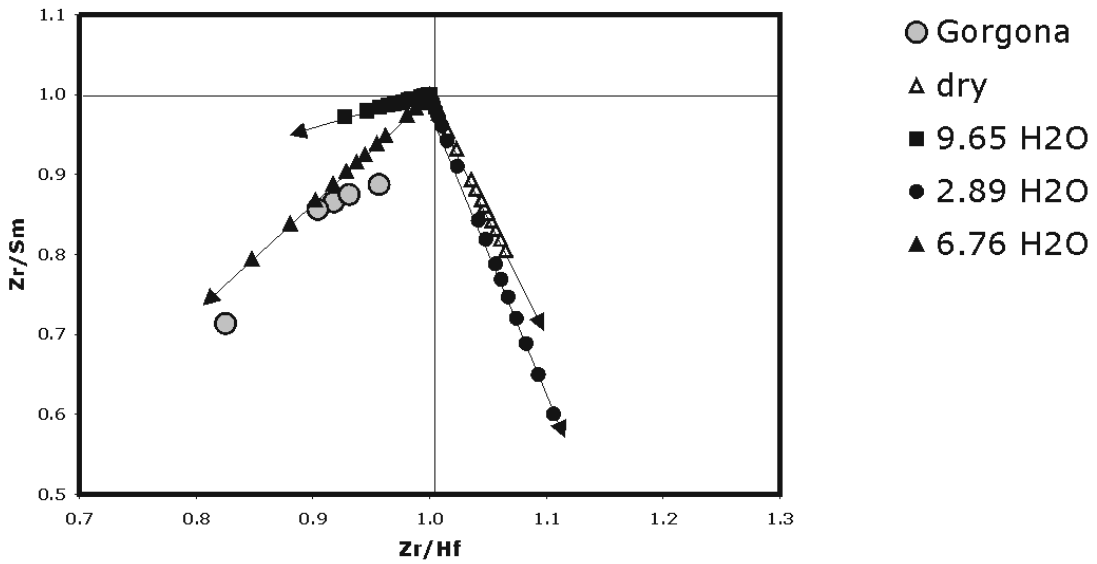

Fig. 3.4-5: A batch melting model shows how trace element ratios in a komatiite-like liquid evolve with increasing degrees of partial melting under wet and dry conditions. The ratios have been normalised to chondritic values.

d. *Experimental and TEM study of garnet-orthopyroxene composite diffusion couple: Simultaneous determination of Fe-Mg partition coefficient and diffusion coefficients in both phases (J. Ganguly and F. Langenhorst)*

Diffusion coefficients of major divalent cations in garnet (grt) are of extraordinary interest in the modelling of diffusion-induced or diffusion-modified compositional zoning to unravel the thermal history of the host rocks. In addition, diffusion-induced Fe-Mg compositional zoning in orthopyroxenes (opx) has been reported in high grade metamorphic rocks, mantle xenoliths and stony-iron meteorites. Thus, the time scales of wide ranging geological and planetary processes may be retrieved from modelling Fe-Mg zoning in opx if well constrained diffusion data are available for this mineral. In addition, the Fe-Mg distribution coefficient between orthopyroxene and garnet is a widely used geothermometric tool for high grade metamorphic rocks and mantle xenoliths.

Divalent cation diffusion in garnet has been extensively investigated over the past two decades. However, there are no directly measured diffusion data in Fe-bearing opxs; hence a theoretical prediction has usually been applied to model compositional zoning in ferromagnesian orthopyroxene samples. Fe-Mg partitioning between garnet and orthopyroxene has been previously experimentally determined, but there are significant differences between the various calibrations that are yet to be resolved. In this work, we have explored a new experimental technique using a composite diffusion couple of garnet and orthopyroxene with the hope of being able to simultaneously determine the diffusion coefficients in both phases along with their equilibrium Fe-Mg distribution coefficient.

Gem quality garnet and orthopyroxene crystals were cut into half-cylindrical shapes, polished to a mirror finish on the flat surfaces, and then joined together to form a cylinder. The sample was inserted into a graphite capsule and annealed at 23 kb, 1200 °C for 258 hours in a piston-cylinder apparatus. The sample was quenched, polished and analysed in an electron microprobe along line traverses normal to the interface. These data (Fig. 3.4-6) showed conspicuous diffusion zoning across the interface of the composite couple. However, the measured mineral compositions were continuous through the interface instead of showing a fractionation of the Fe/Mg ratio, which resulted from the spatial averaging or convolution effect in the microprobe analyses. We therefore carried out a study of the sample by analytical transmission electron microscopy (ATEM) to see if the diffusion profiles could be analysed by resolving the interface fractionation. The diffusion couple was successfully thinned to electron transparency near the interface, hence circumventing the problem of sample separation, and the compositional profiles were then measured quantitatively in scanning mode at different positions within the sample using an energy dispersive X-ray (EDX) system.

The TEM observations show the diffusion couple to be defect-free both near the interface and in the bulk sample, and the diffusion direction in the orthopyroxene sample to be

approximately parallel to the [120] direction in the *a*-*b* plane. The compositional profiles of Fe and Mg in garnet and orthopyroxene are shown in Fig. 3.4-7. The data show a clear difference in the composition of Mg between garnet and orthopyroxene at the interface, but rather surprisingly, do not show any difference in the interface composition of Fe. It should be noted, however, that there is no thermodynamic requirement to have discontinuities of both Mg and Fe profiles at the interface; it is only the Fe/Mg ratio that must be different from unity. The interface compositions of garnet and orthopyroxene yield a Fe-Mg distribution coefficient, K_D, of 1.80 ± 1.0, which is in excellent agreement with a previous calibration.

Work is currently in progress to model the diffusion profiles to retrieve the Fe and Mg self-diffusion coefficients in garnet and orthopyroxene. In the meantime, we note that the data in Fig. 3.4-7 show that Fe-Mg inter-diffusion in opx along the [120] direction is slower than that in garnet, where diffusion is isotropic. However, as previously predicted, the Fe-Mg diffusion in opx along the *c*-direction is expected to be significantly faster than that in the *a*-*b* plane. The results of this study open a new direction in the study of diffusion kinetics of minerals and equilibrium element fractionation in that we show that composite diffusion couple experiments and TEM analyses can be successfully carried out to yield a wealth of information on these mineralogical properties. Also, because of the spatial resolution of ATEM, it is possible to conduct experiments at temperatures corresponding to or close to those of high grade regional metamorphism, and still get adequate diffusion penetration that can be measured sufficiently accurately for modelling.

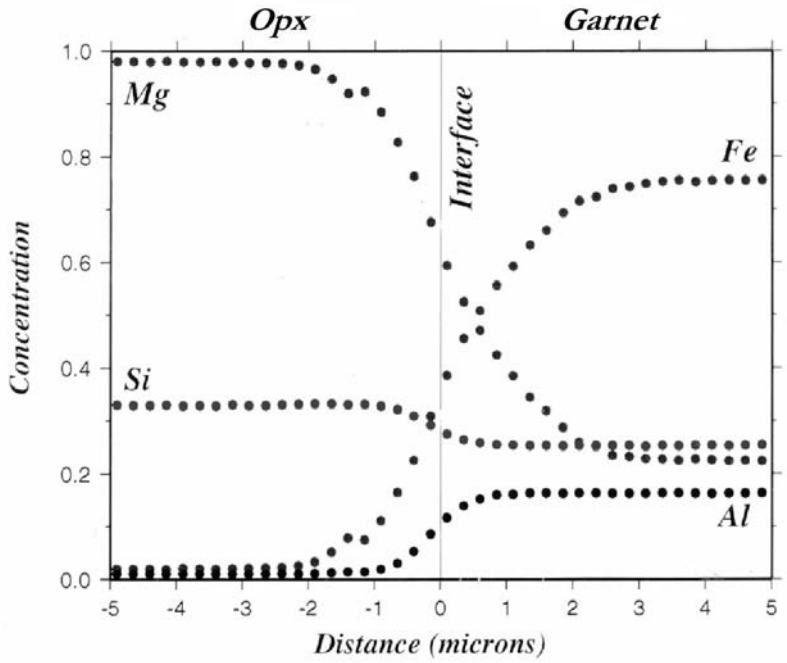

Fig. 3.4-6: Microprobe spot analyses of compositional profiles in a garnet-orthopyroxene diffusion couple annealed at 23 kb, 1200 °C for 258 hours in a piston-cylinder apparatus.

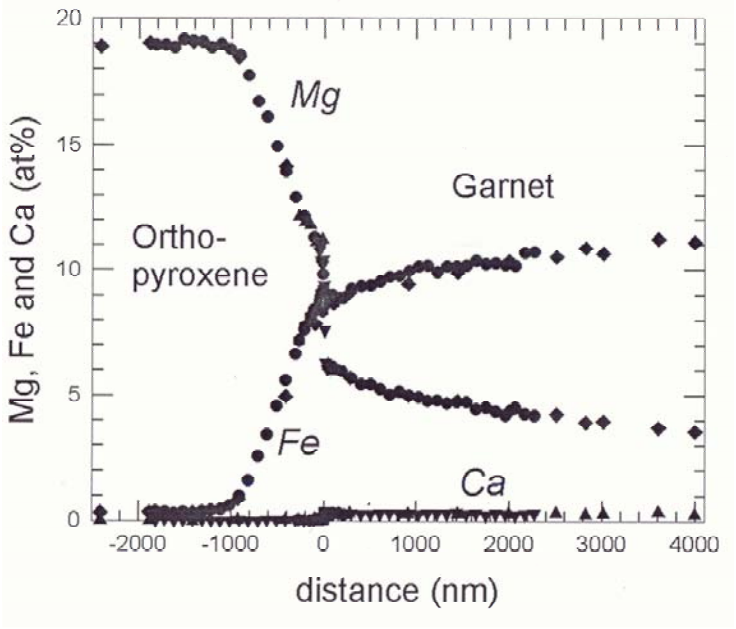

Fig. 3.4-7: TEM spot analyses of concentration profiles of the sample shown in Fig. 3.4-6. Several profiles were measured for each element. Note the discontinuity of the Mg profile at the interface.

e. *Effects of variable thermal conductivity on the mineralogy of subducting lithosphere and deep seismogenesis (F.C. Marton and D.C. Rubie, in collaboration with T.J. Shankland/Los Alamos and Y. Xu/New Haven)*

Thermal and thermo-kinetic models of subduction zones have been based, in general, on a fixed value of thermal conductivity (k), along with constant values of isobaric heat capacity (C_P) and density (ρ) for solving the heat flow equation. In order to make such models more realistic, we have used variable thermal conductivities that are functions of pressure (P), temperature (T), and mineralogy (X) as recently determined by high pressure and temperature experiments on San Carlos olivine, wadsleyite and ringwoodite. We have used these variable conductivities along with C_P and ρ that are also functions of P, T and X to model a variety of slabs with thermal parameters (vertical subduction rate × age of lithosphere at the trench) ranging between 3500-17000 km. Our results show that when only lattice k is used, metastable wedges of olivine are roughly the same size as those in model slabs run with a standard fixed value of k (3.138 W/m-K), within 10 %. When radiative transfer is included, however, k can increase by as much as 2 W/m-K relative to the fixed value, causing temperatures in the interiors of the slabs to increase by 50-100 °C. In turn, the volume of metastable olivine in the slabs is reduced by as much as 20-30 %, with the maximum depth of olivine metastability decreasing by 30-50 km (Fig. 3.4-8). In general, the maximum depths of olivine metastability are 160-230 km less than the depths of the deepest seismicity. Even in the extreme case of Tonga, with a thermal parameter of ~ 17000 km, metastable olivine falls short of the deepest earthquakes by 140 km in our model. Even taking various uncertainties

into account, these results indicate that deep-focus earthquakes occur in regions already transformed to wadsleyite or ringwoodite, and must therefore be caused by a mechanism other than transformational faulting such as shear or plastic instabilities, which does not require the survival of olivine to great depths and so is not affected by its absence.

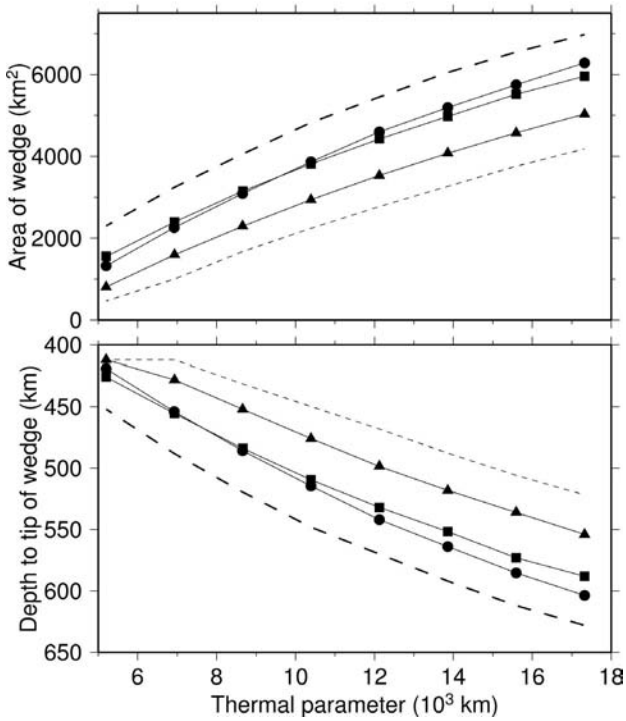

Fig. 3.4-8: Cross-sectional areas (top) and maximum depths (bottom) of metastable wedges of olivine in subducting slabs with thermal parameters 5200-17000 km; dip angle 60°, age 100 My, velocity 6-20 cm/yr. Circles: fixed *k*; squares: variable lattice *k* only; triangles: variable lattice plus radiative transfer *k*; long dashed line: lattice *k* –25 %; short dashed line: lattice plus radiative transfer *k* +25 %.

f. *The effect of temperature on partitioning between $(Mg,Fe)_2SiO_4$ olivine and wadsleyite solid solutions (D.J. Frost)*

The width of the 410 km (*d410*) seismic discontinuity can be determined by studying seismic waves that are reflected and converted at this boundary. Estimates from numerous studies vary, however, from less than 4 to greater than 20 km thick. While some of the very sharp observations may be an effect of topography of the discontinuity, there is increasing evidence that the thickness varies between regions of the mantle. *d410* is likely caused by the divariant transformation of $(Mg,Fe)_2SiO_4$ olivine to wadsleyite. Many factors may affect the width of this transformation, *e.g.* the partitioning of Fe^{2+}, Fe^{3+}, H_2O, temperature and the coexistence of other phases that partition Fe and Mg such as garnet and pyroxene. If these effects can be experimentally calibrated it may be possible to draw conclusions on the nature of the mantle

at 410 km depth from estimates of the discontinuity width. An even clearer picture of the mantle on a local scale could be gained if seismic estimates of the discontinuity width, depth and velocity contrast in specific regions could be interpreted using an accurate petrological and mineral physical model of mantle rocks.

Determining variations in the transformation interval using phase equilibria experiments is extremely challenging at these pressures (14 GPa), because the variations in width we are interested in (probably between 0.1 and 0.7 GPa) are for the main part likely to be below the precision of such high-pressure experiments (~ 0.5 GPa). Here the effect of temperature on the width of the dry olivine to wadsleyite phase transformation has been studied by deriving a thermodynamic model from the results of Fe-Mg partitioning experiments between olivine and magnesiowüstite and between wadsleyite and magnesiowüstite. Magnesiowüstite is basically used as a standard material with which to determine the partitioning between olivine and wadsleyite as a function of composition. Olivine and wadsleyite only coexist at a single composition at a given pressure, while magnesiowüstite coexists with both polymorphs over much wider ranges of composition and pressure. Experiments were performed in the presence of metallic Fe to buffer Fe^{3+} concentrations at the lowest level, as is probably applicable to the transition zone. In one experiment Re and ReO_2 were added in order to examine the effects of higher oxygen fugacity. Figure 3.4-9 shows three curves for the olivine-wadsleyite Fe/Mg K_D, (the Fe/Mg distribution coefficient $K_D = X_{Fe}^{Ol} X_{Mg}^{Wad} \big/ X_{Mg}^{Ol} X_{Fe}^{Wad}$), as a function of the olivine Fe/(Fe+Mg) ratio calculated from experiments involving magnesiowüstite and metallic Fe at 1200, 1400 and 1600 °C. Some results of partitioning between coexisting olivine and wadsleyite are also shown at 1400 °C, which match the model very well. At 1200 °C Fe-Mg diffusion kinetics are very slow such that experiments lasting at least 1 week are required for the equilibrium compositions to be properly bracketed. The gradient of the curves decreases with increasing temperature, indicating that Fe-Mg mixing in these solid solutions is becoming more ideal with increasing temperature. Previous studies have tended to underestimate K_D at a given temperature, which may be a result of temperature overestimation or the presence of Fe^{3+}. As all Fe is considered to be Fe^{2+} when analysed, the presence of Fe^{3+}, which most likely partitions more favourably into wadsleyite, will lower K_D. This is supported by the experiment performed in the presence of Re and ReO_2 at 1400 °C, which falls well below the curve determined from experiments performed in the presence of metallic Fe.

Figure 3.4-10 shows olivine-wadsleyite two-phase regions at various temperatures calculated from thermodynamic data that have been optimised using the Fe-Mg partitioning results. As the data are calibrated over a range of temperature, the model can be reliably extrapolated to even lower temperatures where slow diffusion kinetics would prevent experiments reaching equilibrium in practical times scales. For a mantle olivine composition, Fe/(Fe+Mg) = 0.1, the transformation interval narrows from 0.3 GPa at 1200 °C to 0.2 GPa at 1600 °C, *i.e.* from around 12 to 6 km. The effect is relatively small, implying that large variations in the observed width of *d410* are unlikely to be solely a result of temperature variations in the mantle.

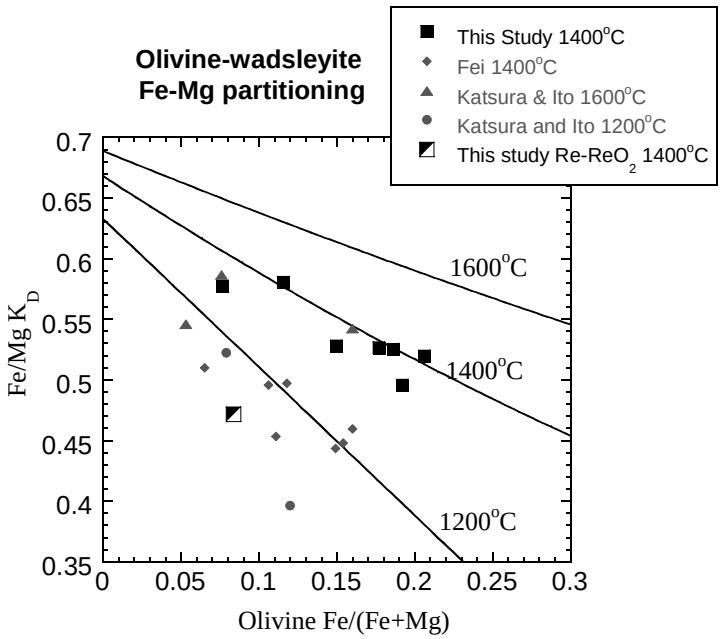

Fig. 3.4-9: Curves showing the olivine-wadsleyite Fe-Mg distribution coefficient are calculated at 1200, 1400 and 1600 °C from thermodynamic data optimised with results from Fe-Mg partitioning experiments between magnesiowüstite and the two $(Mg,Fe)_2SiO_4$ polymorphs. Data points from coexisting olivine and wadsleyite compositions at 1400 °C that were also encountered in this study are shown (solid squares). These data were not used in the optimisation but are in excellent agreement with the calculated curve. In general previous studies have reported lower values of K_D consistent with higher oxygen fugacitites.

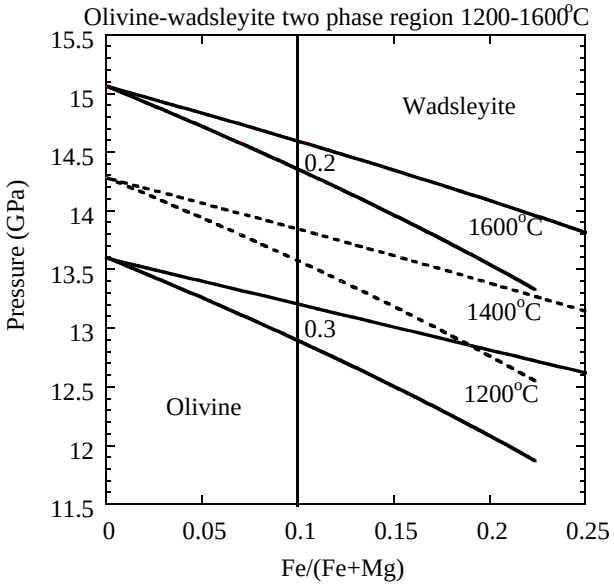

Fig. 3.4-10: Two-phase regions of coexisting olivine and wadsleyite in the Mg_2SiO_4-Fe_2SiO_4 system are calculated at 1200, 1400 and 1600 °C from optimised thermodynamic data. Transformation pressure intervals for a typical mantle composition (solid vertical line) are indicated for the 1200 and 1600 °C transformations in GPa.

g. *Phase transformation kinetics at the 410 km discontinuity (F.C. Marton and D.C. Rubie, in collaboration with B. Steinberger/Kanagawa)*

The 410 km seismic discontinuity is a feature of the Earth's mantle that is quite sharp (< 4 km thick), but shows some degree of topography (up to 20 km). It is believed to be caused by the transformation of α-$(Mg,Fe)_2SiO_4$ (olivine) to β-$(Mg,Fe)_2SiO_4$ (wadsleyite). This is supported by thermodynamic studies of the $(Mg,Fe)_2SiO_4$ system which show that at upper mantle bulk compositions ($Mg_{1.8}Fe_{0.2}SiO_2$) and temperatures, the $\alpha \rightarrow \beta$ divariant phase loop occurs at a narrow pressure range corresponding to a depth of ~ 410 km. The width of the isothermal two-phase field, however, while narrow, appears to be 5 to 15 km thicker than the discontinuity itself. The convection of the mantle may explain the topography of the discontinuity, as its depth would be influenced by variations in temperature due to the positive Clapeyron slope of the $\alpha \leftrightarrow \beta$ transitions. This, however, would not explain its narrowness. In a convecting mantle, material would be both upwelling and downwelling across the discontinuity. This material transport would influence both the width and depth of the discontinuity if the velocity of material across the two-phase region were faster than the rate of phase transformation. Such behaviour would have consequences for the dynamics of mantle convection, the geoid, and the Earth's dynamic topography. Kinetics at the 410 km discontinuity are also of great interest to geodynamicists because of the possible effects on rates of glacial rebound and therefore estimates of mantle viscosity. Experimental determinations of Fe-Mg interdiffusion coefficients for both olivine and wadsleyite are now available at conditions of the 410 km discontinuity, and it is noteworthy that the interdiffusion in wadsleyite is faster than in olivine by more than an order of magnitude. These data make it possible to model diffusion-controlled growth of olivine or wadsleyite in the two-phase field as the 410 km discontinuity becomes displaced from its equilibrium location (either upwards or downwards) by material transport. Our kinetic model will be based on a finite-difference solution to the diffusion-controlled, two-phase moving-interface problem. In particular, it will be tested whether the advection of phase boundaries due to latent heat and kinetic effects significantly reduces the amplitude of predicted dynamic surface topography and whether this improves agreement with observations.

h. *Iron oxidation state of inclusions in diamonds from the lower mantle, with implications for mantle structure and dynamics (C.A. McCammon, in collaboration with T. Stachel/Edmonton and J. Harris/Glasgow)*

Inclusions in diamonds are the only known source for natural samples from the deeper parts of the Earth. The lower mantle paragenesis, which includes the compositions $(Mg,Fe)(Si,Al)O_3$, $(Mg,Fe)O$ and $CaSiO_3$, provides an opportunity to study deep material that is essentially unaltered from the chemical composition existing at the time of diamond formation. While the extent to which such inclusions represent the bulk lower mantle is still

an open question, there is overwhelming evidence that points to their origin below the enigmatic 660 km discontinuity.

Diamonds from Kankan, Guinea and their inclusions represent a range of depths encompassing the lithosphere and asthenosphere, with parageneses from the transition zone and lower mantle. Mössbauer spectra were collected for nine (Mg,Fe)O inclusions and one (Fe,Mg)(Si,Al)O_3 inclusion, which complement the dataset collected several years ago for similar inclusions in diamonds from São Luiz, Brazil. There is a nearly linear variation of trivalent cation abundance with Na abundance for (Mg,Fe)O (Fig. 3.4-11a), which strongly suggests a substitution of the form $Na_{0.5}M^{3+}{}_{0.5}O$ (M = Fe^{3+}, Cr^{3+}, Al^{3+}). The majority of data points from Kankan lie close to the 1:1 correlation line, indicating that trivalent cations are stabilised primarily by coupled cation substitution, and not by vacancies. São Luiz inclusions show a greater excess of trivalent charge that is likely balanced by structural vacancies, and coupled with trends in Fe^{3+}-Fe_{total} concentrations (not shown), suggest that São Luiz inclusions generally formed at more oxidising conditions than those of Kankan. Considerations of likely redox conditions within the mantle coupled with geochemical evidence that supports a subducted protolith source for asthenospheric diamonds suggest a scenario of mixing between subducted material and more reduced primitive lower mantle to provide conditions favourable for diamond formation. Diamond is stable over a large range of oxygen fugacity; hence the more reduced conditions suggested by Kankan inclusions are equally compatible with the more oxidising conditions suggested by São Luiz inclusions.

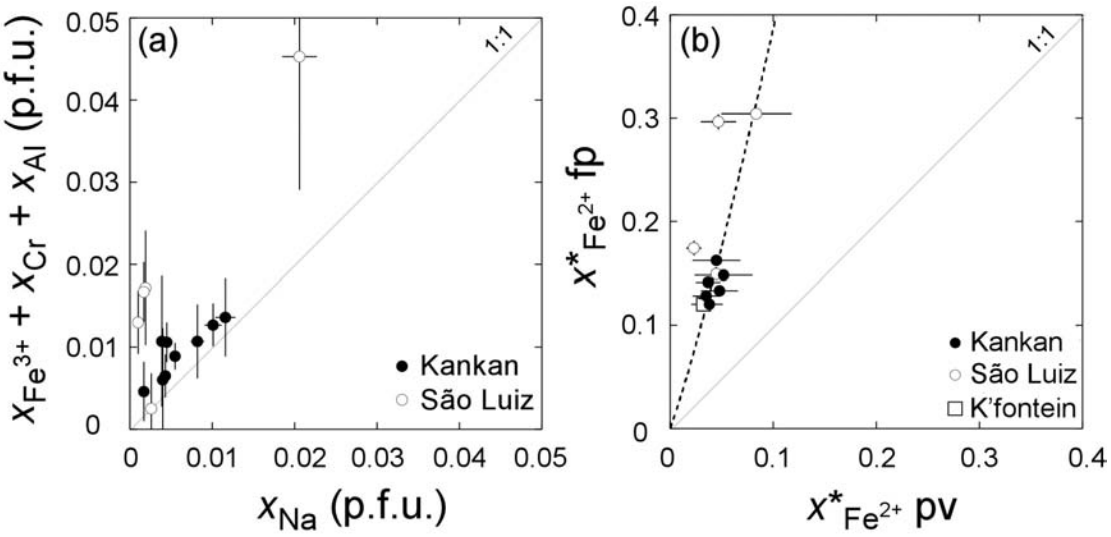

Fig. 3.4-11: (a) Variation of trivalent cation concentration with Na concentration in (Mg,Fe)O inclusions from lower mantle diamonds. Values for São Luiz diamonds are taken from the literature (McCammon *et al.*, Science, 278, 434, 1997). (b) Fe^{2+}-Mg partitioning between (Mg,Fe)(Si,Al)O_3 perovskite (pv) and (Mg,Fe)O (fp) from inclusions in lower mantle diamonds. Values are given as normalised Fe^{2+} concentration in each phase, $Fe^{2+}/(Fe^{2+} + Mg)$. The dashed line represents the trend for high-pressure experimental data.

The occurrence of (Fe,Mg)(Si,Al)O_3 and (Mg,Fe)O inclusions in the same diamond enables the calculation of cation partition coefficients in order to assess whether the inclusions were in equilibrium. Our Mössbauer data coupled with recently derived empirical systematics (Section 3.3, this Annual Report) enable the derivation of true Fe^{2+}/Mg partition data for a number of inclusion pairs (Fig. 3.4-11b). Many of the inclusions show equilibrium, but there are two exceptions, which might reflect significant changes in the source region during the crystallisation of individual diamonds. There are several possible scenarios that could lead to the observed values, and while further data is required, these results emphasise the potential heterogeneity of lower mantle diamond sources, and that compositions of lower mantle diamonds do not necessarily reflect those of the bulk mantle.

i. *The ferric iron content of aluminous silicate perovskite in equilibrium with metallic iron and above the silicate solidus (D.J. Frost, C. Liebske, F. Langenhorst, C.A. McCammon, D.C. Rubie, in collaboration with R.G. Trønnes/Reykjavík)*

Aluminous silicate perovskite can accommodate large amounts of ferric iron with some reported levels as high as 80 % of the total iron content. In previous experiments high levels of ferric iron have been reported in samples synthesised in both Re capsules with added ReO_2, and in Fe capsules, implying that the ferric iron solubility may be relatively independent of oxygen fugacity. However, to ensure equilibrium between perovskite and metallic iron most likely requires iron to be dispersed throughout the solid assemblage, and very long run times may be required as solid-state diffusion at these conditions is known to be very slow. During the accretion of the Earth, it is likely that large regions of what is now the lower mantle were close to, or above, the silicate solidus. It is, therefore, also important to study the likely speciation of ferric iron at these high temperatures in order to investigate if fractionation of silicate perovskite in an early magma ocean could have led to ferric iron being concentrated in the lower mantle.

In this study samples of aluminous enstatite and ferropericlase were combined with 20 wt.% metallic iron powder and equilibrated in iron capsules in a multianvil apparatus at 24-26 GPa and 1600 °C. Experiments were performed for durations of up to one week. A second series of experiments were performed in graphite capsules using a peridotite starting composition at conditions above the silicate solidus. Recovered experimental charges were analysed with Mössbauer and electron energy loss spectroscopy to determine the perovskite ferric/ferrous ratio. Figure 3.4-12 shows an iron capsule containing silicate perovskite, ferropericlase and metallic iron. Capsules were prepared by melting iron inside an alumina tube of 0.8 mm inner diameter. The composite tube was then sliced into 0.5 mm sections and the iron was spark eroded to produce a sample chamber. Alumina instead of MgO must surround the iron capsule as the equilibrium between MgO and iron would impose a lower oxygen fugacity than is applicable to the mantle.

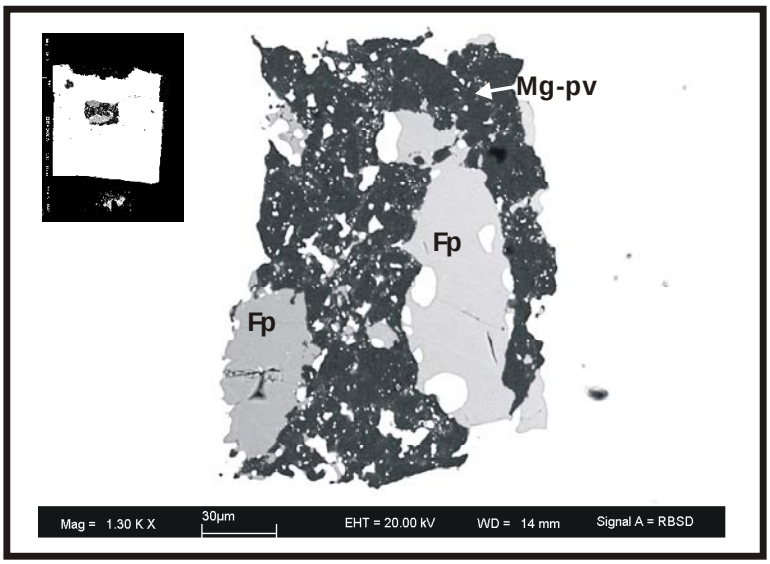

Fig. 3.4-12: Scanning electron miscoscope image of an iron capsule containing ferropericlase (Fp) and alumina-bearing magnesium-silicate perovskite (Mg-pv). Metallic Fe powder was added to the starting material. The entire capsule is shown in the top left corner.

Results are shown in Fig. 3.4-13 where ferric iron content is plotted against Al content. The shaded grey region encompasses results from experiments performed under more oxidising conditions in Re capsules and with added ReO_2. A non-linear trend is indicated by these data, which may be due to a change in the dominant substitution mechanism with increasing Al content. The results from experiments performed in the presence of metallic iron, however, also fall along this trend. This confirms the earlier suggestion that the high ferric iron concentrations in aluminous silicate perovskite are indeed independent of the oxygen fugacity. The dashed vertical line indicates the likely Al content of the lower mantle, which implies a perovskite ferric iron content of approximately 60 % and a bulk rock ferric iron content of approximately 50 %. Perovskites synthesised at and above the silicate solidus also have significant ferric iron contents (up to 46 % of total iron).

The ferric iron content of average upper mantle is believed to be on the order of 3 % of total iron. If the lower mantle has a ferric iron content of approximately 50 %, then this raises two possible scenarios depending on whether the oxygen content of the mantle is either heterogeneous or homogeneous. Either the lower mantle is enriched in ferric iron, possibly as a result of perovskite fractionation in a Hadean magma ocean, or perovskite sequesters oxygen by the reduction of some other species, either volatiles or FeO. The first possibility seems the more unlikely one. Seismic tomography shows slabs descending into the lower mantle, and if significant mixing has occurred between the upper and lower mantle, it is hard to explain why the ferric iron content of the upper mantle has remained so low. The second possibility would imply that volatile species such as CO_2 and H_2O are reduced in the lower mantle, but even assuming generous estimates for mantle volatile contents, such reduction

cannot produce the amount of ferric iron required. The most likely possibility, therefore, is that FeO disproportionates in the lower mantle to produce ferric and metallic Fe. About 1 wt.% of a metallic iron-rich phase would need to form to produce the required amount of ferric iron. This metallic phase would have to exsolve in the lower mantle as silicate perovskite formed, and it could not have significantly separated to the core without leaving behind a lower mantle enriched in oxygen. Small amounts of separation to the core may have occurred, however, and this may explain why the bulk oxygen content of today's upper mantle is higher than it was likely to have been during core segregation. The partitioning of siderophile elements during core-mantle differentiation may also have been influenced by the formation of a metallic phase that remained trapped in the lower mantle.

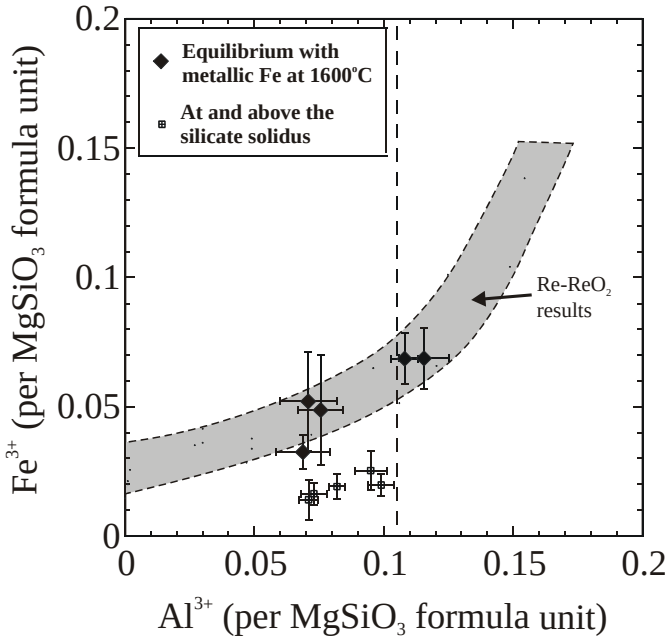

Fig. 3.4-13: Al and Fe^{3+} variation in silicate perovskite reported as atoms per $MgSiO_3$ formula unit. The grey field encompasses analyses from experiments performed at a higher oxygen fugacity (Re-ReO_2 buffer). Results of experiments performed in equilibrium with metallic Fe are shown as black diamonds. Perovskite analyses from samples formed at or close to the silicate solidus (~ 2200 °C) are shown as small squares. The vertical dashed line indicates the approximate Al content of silicate perovskite in the lower mantle.

j. *Trace element partitioning between Mg-silicate perovskite and silicate melt – geochemical constraints on a "hidden" perovskitic reservoir in the lower mantle (C. Liebske, D.J. Frost, D.C. Rubie, in collaboration with A. Corgne, B.J. Wood/Bristol)*

During the accretion of the Earth a magma ocean, possibly over 1000 km deep, may have existed. Fractionation of Mg-silicate perovskite (Mg-pv) at depths > 700 km in such a deep

magma ocean could be one explanation as to why the Si/Mg ratio of the Earth's upper mantle is low when compared to CI chondrites. Recent findings in seismology and geochemistry suggest a chemically heterogeneous lower mantle and raise again the question of a "hidden" perovskitic reservoir in the deep interior of the Earth. Here we present new trace element partitioning data between Mg-pv and silicate melt as a function of bulk composition, which puts tight constraints on likely geochemical effects of Mg-pv fractionation.

Melting experiments were performed in a multianvil apparatus at pressures of ~ 27 GPa and temperatures between 2250-2350 °C. A synthetic peridotite with varying Al_2O_3 concentrations and a synthetic CI-chondrite composition, both doped with a selection of trace elements, were used as starting materials. Trace element concentrations in Mg-pv and coexisting silicate melt were analysed by secondary ion mass spectrometry (SIMS) using an O^- primary ion beam. Measured elements were normalised against ^{30}Si after calibrating on a NIST 610 standard.

Mg-pv ($MgSiO_3$) has an orthorhombic (*Pbnm*) unit cell and can be regarded as a distorted $CaTiO_3$ perovskite structure. This structure has two cation sites: a 6-fold coordinated B-site, usually occupied by Si, and an 8(12)-fold coordinated A-site, occupied by Mg. Most trace elements, such as rare Earth elements (REEs) and large ion lithophile elements (LILEs), substitute onto the larger A-site. As suggested in previous studies, Al has a large effect on cation substitution mechanisms in Mg-pv. This is in agreement with our observations, in that the partition coefficients D_i ($C_i^{\text{Mg-pv}}/C_i^{\text{melt}}$) for some tri- and tetravalent refractory lithophile elements (RLEs) increase with increasing perovskite Al content (Fig. 3.4-14). The effect of Al concentration is very significant, to the point that some elements which are incompatible (partition more favourably into the melt) at low Al concentrations become compatible at high Al concentrations. This may involve substitution of Si^{4+} by Al^{3+} on the B-site charge balanced by M^{4+}/M^{3+} cations onto the Mg-site, such as:

$2\ Si^{4+} + Mg^{2+} = 2\ Al^{3+} + M^{4+}$
$Si^{4+} + Mg^{2+} = Al^{3+} + M^{3+}$.

Our new partitioning data can be used to put constraints on the maximum amount of Mg-pv fractionation that could have separated into a hidden reservoir in the lower mantle. As Mg-pv fractionates from a magma ocean, element ratios of the residual liquid will evolve. The upper mantle may then have formed from the residual melt. However, any fractionation of Mg-pv has to be reconciled with chondritic ratios of RLEs observable in the present day upper mantle. Therefore, crystal fractionation may have only occurred to an extent which does not drive ratios of RLEs outside their estimated uncertainties (Fig. 3.4-15). Our results show that a larger amount of Mg-pv may have fractionated from a more Fe-rich but Al-poor (chondritic) magma ocean than from a peridotitic bulk composition. A large scale separation of Mg-pv (> 10 %) seems to be precluded by our data, whereas around 60 % Mg-pv fractionation would be required to explain why the Si/Mg ratio of the upper mantle differs from CI chondrite.

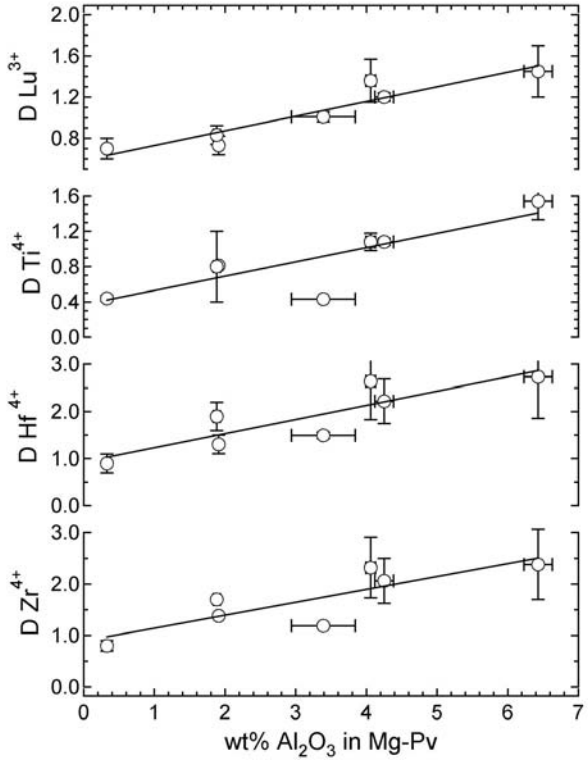

Fig. 3.4-14: Partition coefficients as a function of Al_2O_3 concentration in Mg-pv. Note that for some elements (Ti, Lu) the geochemical behaviour changes from incompatible ($D < 1$) to compatible ($D > 1$).

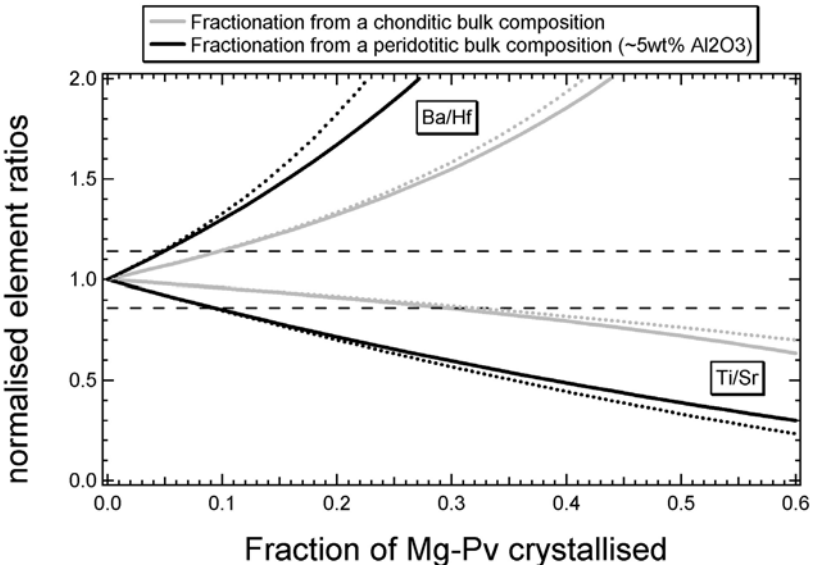

Fig. 3.4-15: Refractory lithophile element ratios in the residual magma ocean as a function of crystallised Mg-pv fraction. Horizontal black dashed lines indicate the present day upper mantle range. Black lines represent fractionation from a peridotitic bulk composition while grey lines indicate fractionation from chondritic material. Dotted black and grey lines show results for a fractional crystallisation model.

k. *Sulfide melt distribution in partially molten silicate aggregates (A. Holzheid/Münster, in collaboration with H. Terasaki, D.J. Frost, D.C. Rubie and P. Balog/Stuttgart)*

The dihedral angle, *i.e.* the angle formed by liquid in contact with two crystalline grains, determines whether a continuous interconnected melt network can be formed, and hence has a strong influence on mechanisms of core formation. Experiments to study the effect of silicate partial melting on the dihedral angle (and hence metallic liquid percolation) were performed within a pressure range of 1-11 GPa using the piston cylinder apparatus at Universität Münster and using a multianvil apparatus at Bayerisches Geoinstitut. The starting material in all experiments was a mixture of metal sulphide powder and finely-ground San Carlos olivine (Fo_{90}) coated with a basaltic silicate gel. Liquid metal sulphide and liquid basaltic silicate coexisted in a crystalline olivine matrix during the experiments. The two-phase dihedral and three-phase interfacial angles between sulphide melt, basaltic liquid, and olivine were measured in the recovered experimental charges with image processing software AnalySis from digital images acquired by backscattered electron detection on the secondary electron microscope JSM-840 A at Universität Münster.

Apparent dihedral angles between liquid metal sulphide and solid olivine, $\Theta_{FeS\text{-}Ol}$, are plotted in Fig. 3.4-16 as a function of pressure. All three data sets agree well, although the starting material used by Shannon & Agee (1996) was different to that used in the other studies, *i.e.* a natural Allende meteorite composition. The two-phase dihedral angles, $\Theta_{FeS\text{-}\beta}$ and $\Theta_{FeS\text{-}\gamma}$, result from the transformation of olivine at higher pressure into wadsleyite (β-phase) and ringwoodite (γ-phase). No simple pressure correlation of $\Theta_{FeS\text{-}Ol}$ seems to exist, however, even by including the dihedral angles of the high pressure olivine polymorphs. The three-phase interfacial angles between liquid metal sulfide (FeS), solid silicate (Ol) and liquid silicate (Sil), $\Theta_{FeS\text{-}Ol+Sil}$, plot within the range of the two-phase dihedral angles; hence silicate partial melts of up to 12.5 vol.% do not appear to enhance FeS melt segregation from olivine.

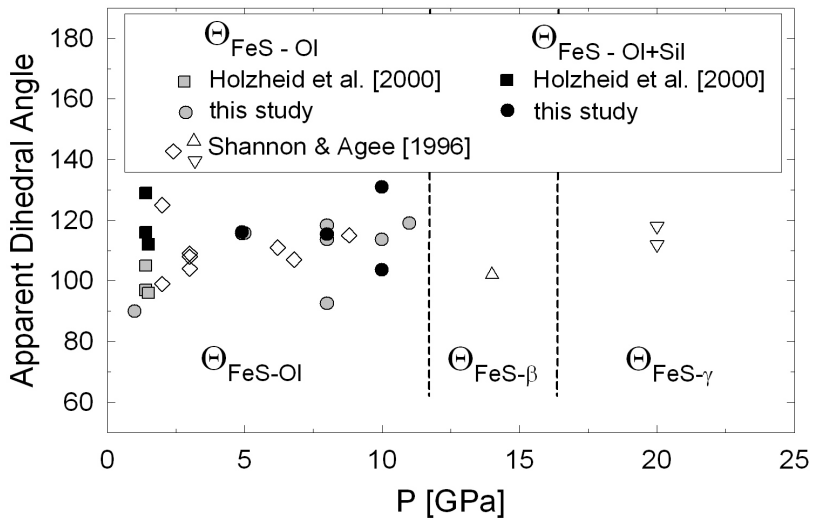

Fig. 3.4-16: Apparent two-phase dihedral angles, $\Theta_{FeS\text{-}Ol}$, and three-phase interfacial angles, $\Theta_{FeS\text{-}Ol+Sil}$, as function of pressure. Grey shaded symbols and open diamonds: two-phase metal sulfide - olivine dihedral angles; triangles: metal sulfide β- and γ-phase dihedral angles; closed symbols: three-phase metal sulfide-olivine + silicate interfacial angles. References: Holzheid *et al.* (2000, J. Geophys. Res., 105, 13555); Shannon and Agee (1996, Geophys. Res. Lett., 23, 2717).

In conclusion, the dihedral angle between metal sulphide melt and crystalline olivine is significantly greater than the critical 60° angle in all experimental charges, *i.e.* a significant portion of the metallic phase is trapped as melt pockets inside the crystalline olivine matrix. This wetting behaviour does not change even by the coexistence of two liquid phases (metallic and basaltic melt) in the olivine matrix, as shown by the three-phase interfacial angle values that are well above 100°, indicating again a trapped metallic melt phase inside the two-phase crystalline matrices.

I. *The effect of light elements on the dihedral angle between Fe-alloy melt and silicate grains at high pressure (H. Terasaki, D.C. Rubie, D.J. Frost and F. Langenhorst)*

In comparison to the Earth, the Martian mantle is richer in FeO (~ 18 wt.%) and the Martian core is believed to contain more sulphur (~ 14 wt.%). These compositional differences between Earth and Mars could have resulted in important differences in the core formation mechanism, *i.e.* the dihedral angle between liquid iron-alloy and solid silicate may change with composition allowing the percolation of liquid iron-alloy. A recent dihedral angle study reports that a liquid iron-alloy can wet an olivine matrix under high oxygen and sulphur fugacities at ambient pressure and should therefore be interconnected. However, in order to understand planetary core formation, it is important to systematically study the effects of the oxygen and sulphur content of iron-alloy on the dihedral angle behaviour under high pressure conditions. We have investigated the effects of sulphur and oxygen on the dihedral angle up to 20 GPa, which covers more than 80 % of the depth of the entire Martian mantle.

High pressure experiments were carried out using a MA8 type multianvil apparatus. Up to pressures of 8 GPa, a 25/15 type assembly was used and compressed in 1200 and 1000-tonne presses. Above 8 GPa, an 18/8 type assembly was used in a 5000-tonne press. These large assemblies were employed in order to obtain a large sample volume and to minimize thermal gradients across the sample. In both assemblies, graphite was used as a sample capsule. Starting materials were mixtures of powdered iron-sulphide (containing 31, 39 and 50 at.% sulphur) and synthetic olivine (FeO/(FeO+MgO) = Fe# = 0, 0.10, 0.24 and 0.50). Fe# = 0.10 and 0.24 are applicable to olivine compositions in the mantles of the Earth and Mars, respectively. All experiments were performed for 12 hours, which corresponds to the time scale required to reach textural steady state. Imaging and chemical analyses were carried out using a SEM/EDX and an electron microprobe. In order to observe the microstructure of the Fe-S melt pockets with high magnification, high-resolution imaging was also carried out using a TEM.

Texturally equilibrated dihedral angles decrease with increasing sulphur content and also decrease significantly with increasing FeO content of silicates (Fig. 3.4-17). This can be clearly seen in backscattered electron images where curvatures of the interfaces bounding iron-alloy melt pockets clearly change with the FeO content of olivine. Increasing the FeO

content of silicates results in an increase in both the oxygen fugacity and oxygen solubility in the Fe-S melt. Oxygen is found to be much more effective for reducing the dihedral angle than sulphur. No evidence of iron-alloy melt films could be found along the olivine grain boundaries from TEM observations (Fig. 3.4-18). The dihedral angle between liquid iron-alloy and a silicate matrix in the Martian mantle would have been much closer to the wetting boundary of 60° than in the Earth's interior, but it is still too large ($\theta > 60°$) to allow percolation to occur. Rather, higher temperatures would have been required such that the silicates were molten or partially molten to complete the core formation.

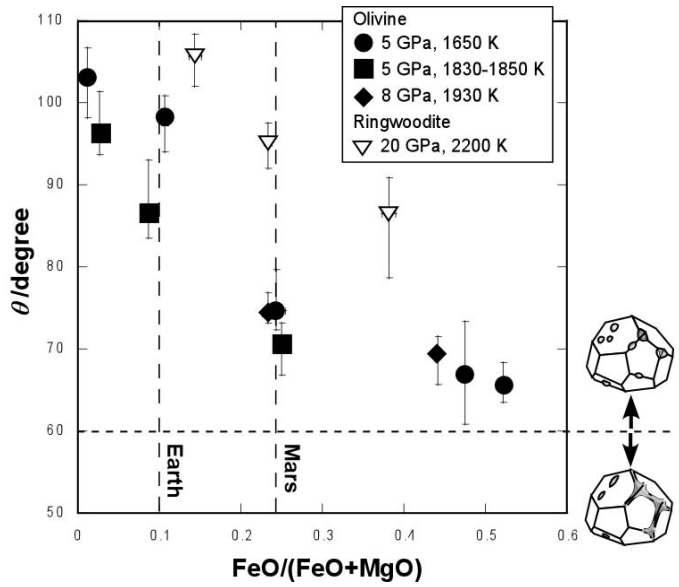

Fig. 3.4-17: Dihedral angle as a function of FeO/(FeO+MgO) in silicates (molar ratio). Closed circles, squares and diamonds show the results of experiments in the olivine stability field at 5 GPa and 1650 K, 5 GPa and 1830-1850 K and 8 GPa and 1930 K, respectively. Open triangles indicate the results of experiments in the ringwoodite stability field at 20 GPa and 2200 K. Vertical dashed lines represent the respective compositions of olivine in the mantles of the Earth and Mars.

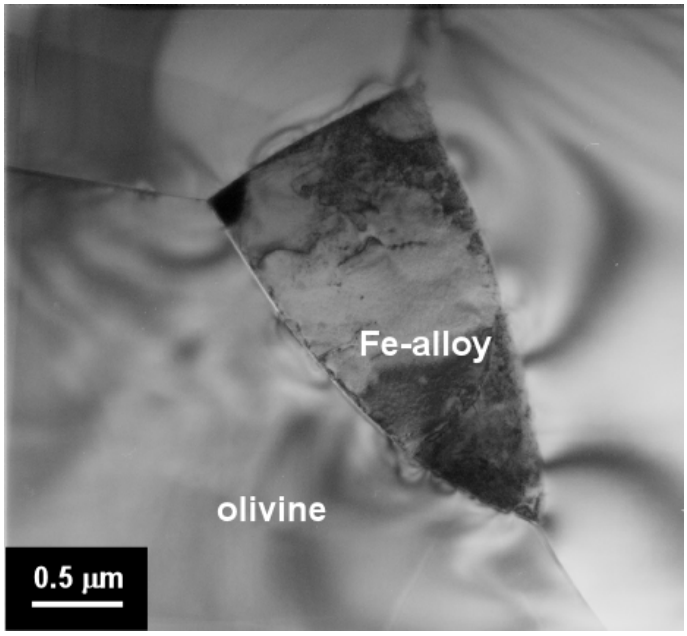

Fig. 3.4-18: TEM image of an Fe-S melt pocket showing that melt films are not present along olivine grain boundaries. The pressure and temperature conditions of the experiment were 4.6 GPa and 1960 K.

m. *Partitioning of oxygen during core formation on Earth and Mars (D.C. Rubie, C.K. Gessmann/Mainz and D.J. Frost)*

Knowledge of the solubility of oxygen in liquid iron alloy at high pressure is necessary for determining if oxygen is present as a major light element in the Earth's core. In addition, solubility measurements enable the partitioning of oxygen between metal and silicates and the oxidation state of residual silicates to be constrained during core formation in planetary bodies. We have determined oxygen solubility experimentally as a function of pressure (9-18 GPa), temperature (2173-2673 K) and oxygen fugacity (1.1 to 3.6 log units below the iron-wüstite buffer) in samples of liquid Ni-Fe alloy contained in magnesiowüstite capsules using a multianvil apparatus. Results show that solubility increases as a function of oxygen fugacity (fO_2) and temperature, with the maximum solubility determined in this study being 1.28 wt.% (Fig. 3.4-19). In order to determine the effect of pressure independently of oxygen fugacity, we calculate the distribution coefficient, K_D, for the partitioning of oxygen between liquid Fe-alloy and magnesiowüstite:

$$K_D = \frac{X_O^{met} X_{Fe}^{met}}{X_{FeO}^{mw}}$$

where X_O^{met}, X_{Fe}^{met}, and X_{FeO}^{mw} are the mole fractions of oxygen in metal, Fe in metal and FeO in magnesiowüstite, respectively. K_D includes the term $X_{Fe}^{met} / X_{FeO}^{mw}$ and is therefore independent of fO_2. The distribution coefficient, and therefore oxygen solubility at constant fO_2, decreases with increasing pressure. In order to extrapolate the oxygen solubility data to higher pressure (P) and temperature (T), we use the relationship

$$RT \ln K_D = -\Delta H + T\Delta S - P\Delta V,$$

where ΔH, ΔS and ΔV are the changes in enthalpy, entropy and volume, respectively, for the oxygen exchange reaction and R is the gas constant. The results of fitting this equation to data both from this study and an earlier study are shown in Fig. 3.4-19. Extrapolations of the solubility results show that at moderate pressures (*e.g.* 5-10 GPa) oxygen solubility reaches 5-15 wt.% at 3500-4000 K. However, as pressure exceeds ~ 40 GPa, O solubility becomes low, even at very high temperatures.

Using the extrapolation of the results to higher pressures and temperatures, we have modelled the geochemical consequences of metal-silicate separation in magma oceans and can thus explain why the FeO content of the Earth's mantle (~ 8 wt.%) is much lower than that of the Martian mantle (~ 18 wt.%) (Fig. 3.4-20). We assume that both Earth and Mars accreted originally from material with a chondritic composition, and because the initial oxidation state is uncertain, we vary this parameter by defining different initial oxygen contents. The geochemical consequences of metal-silicate separation are determined using a simple

fractionation model and we assume that the temperature at the base of a magma ocean is close to the peridotite liquidus. In the case of Earth, high temperatures in a magma ocean with a depth > 1200 km would have resulted in significant quantities of oxygen dissolving in the liquid metal with the consequent extraction of FeO from the residual silicate. In contrast, on Mars, even if the magma ocean extended to the depth of the current core-mantle boundary, temperatures would not have been sufficiently high for oxygen solubility in liquid metal to be significant. The results show that Earth and Mars could have accreted from similar material, with an initial FeO content around 18 wt.%. On Earth, oxygen was extracted from silicates by the segregating metal during core formation, leaving the mantle with its present FeO content of ~ 8 wt.%. On Mars, in contrast, the segregating metal extracted little or no oxygen and left the FeO content unaltered at ~ 18 wt.%. A consequence of this model is that oxygen could be an important light element in the Earth's core but not in the Martian core.

As metal migrates to greater depths below the base of the magma ocean, the solubility of O is predicted to decrease strongly, which could lead to precipitation of FeO and the enrichment of the lower part of the mantle in this component. Alternatively, if all or part of the dissolved oxygen is transported to the core (*e.g.* as a disequilibrium component), the consequences could include the presence of significant amounts of oxygen as a light element in the core and/or the formation of a FeO-rich layer at the core-mantle boundary due to exsolution of the excess oxygen.

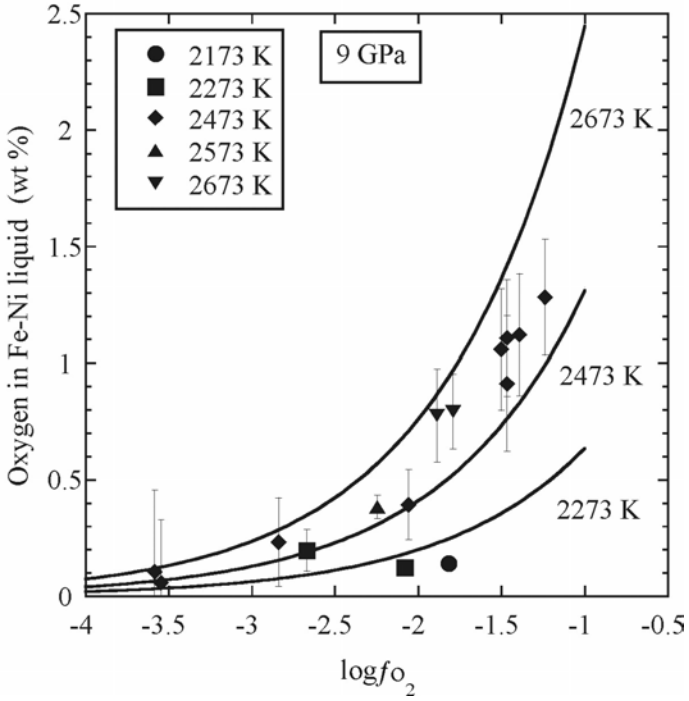

Fig. 3.4-19: Oxygen content in liquid Fe-alloy as a function of oxygen fugacity (fO_2) determined experimentally at 9 GPa and 2173-2673 K. The solid lines indicate fits to the present data as well as earlier data of O'Neill *et al.* (1998, J. Geophys. Res. 103, 12239).

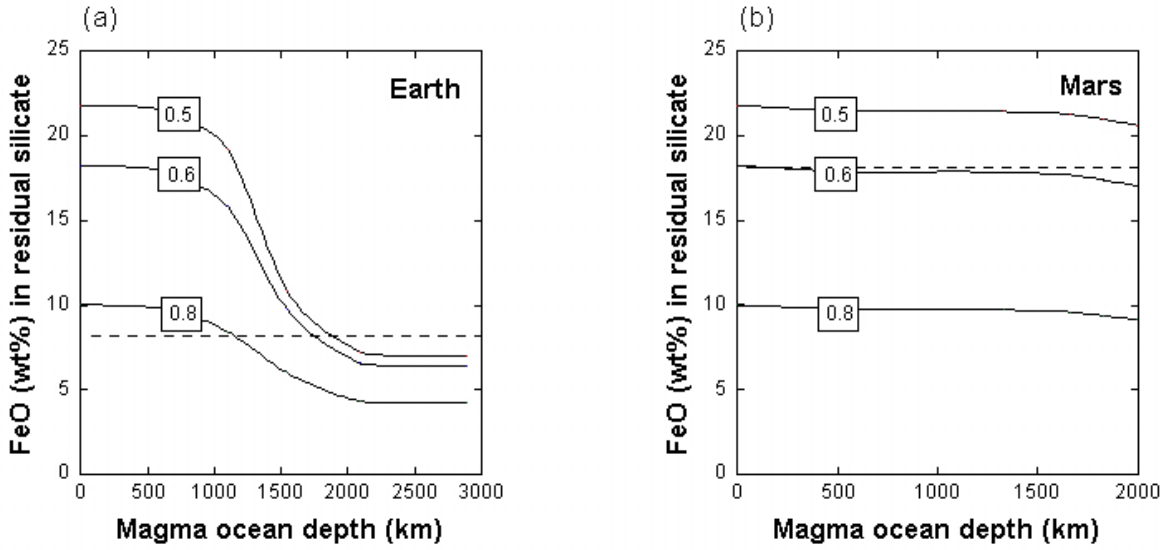

Fig. 3.4-20: Results of metal-silicate separation models for (a) Earth and (b) Mars. The FeO contents of the residual silicate mantles (after metal segregation) are shown as a function of magma ocean depth. In each case, the three curves correspond to different initial oxygen contents and are labelled with the weight fraction of Fe that is initially present as metal; the three values correspond to 22, 18 and 10 wt.% FeO, respectively, in the silicate fraction. Results show that metal-silicate separation in a deep magma ocean would strongly reduce the FeO content of the silicate mantle on Earth; whereas on Mars metal-silicate separation has little effect. The horizontal broken lines indicate the FeO contents of the mantles of Earth and Mars.

n. *Diamond formation in core segregation experiments (J. Siebert, V. Malavergne and R. Combes/Marne la Vallee, in collaboration with D.J. Frost)*

Heterogeneous accretion models propose that the initial stages of the Earth's accretion involved material that was relatively reduced, with iron mainly in the metallic state. Under such reducing conditions silicon would have likely been present in the metal that segregated to form the core. Siderophile element abundances in the present day mantle are consistent with a model where up to 90 % of the volume of the Earth was accreted from a mixture of reduced, volatile-free components along with minor amounts of oxidised, volatile-rich components (*e.g.* a mixture of EH and CI chondrites). In order to investigate the behaviour of carbon during such an accretion scenario we have performed experiments on mixtures of carbonate and silicon-rich alloys.

Multianvil press experiments were performed on mixtures of siderite ($FeCO_3$) and silicon-rich metal, between 10 and 25 GPa and up to 1800 °C. Varying the starting proportions of silicon in the metal allowed a variety of relatively reducing conditions to be applied. Run products in the recovered samples were consistent with the reaction (see Figs. 3.4-21 and 3.4-22):

2 $FeCO_3$ + 3 Si (in metal) = 2 Fe (in metal) + 3 SiO_2 (stishovite) + 2 C (in metal and diamond).

These experiments provide a plausible mechanism for the spontaneous growth of diamond in the Earth's primitive mantle. The redox conditions of our experiments are very reduced as a result of the high initial silicon content in metal, which causes diamond to form as a result of carbonate reduction by the Fe-Si liquid.

In order to explain the high Mg/Si ratio of the Earth's mantle with respect to many meteorite compositions, heterogeneous accretion models frequently call on high Si contents in the Earth's core. The higher Mg/Si ratio of the mantle with respect to CI chondrite, for example, could be explained if the core contained approximately 7 wt.% Si. Our results show that under the reducing conditions compatible with the stability of Fe-Si liquids, carbonates would be unstable. The temperature dependence of these buffering reactions is such, however, that carbonates could coexist with Si-rich Fe liquids at temperatures above 2000 °C.

The presence of diamond implies that the coexisting metal is saturated in carbon. We are therefore able to estimate the maximum carbon solubility in metal under these high-pressure conditions. The carbon content in the metal was measured by ion microprobe and found to be approximately 1.5 (±0.3) wt.% at 20 GPa and 1800 °C. This measurement is at odds with estimates made using thermodynamic calculations, which may arise from inaccuracies in the thermodynamic model or in the analytical technique. Further analyses and experiments will help to clarify this and lead to a more accurate understanding of carbon solubility as a function of pressure, temperature and oxygen fugacity. These preliminary results, however, suggest that the relatively low carbon solubility in metal could allow diamond saturation to occur during core segregation and result in the formation of a primitive diamond reservoir in the mantle.

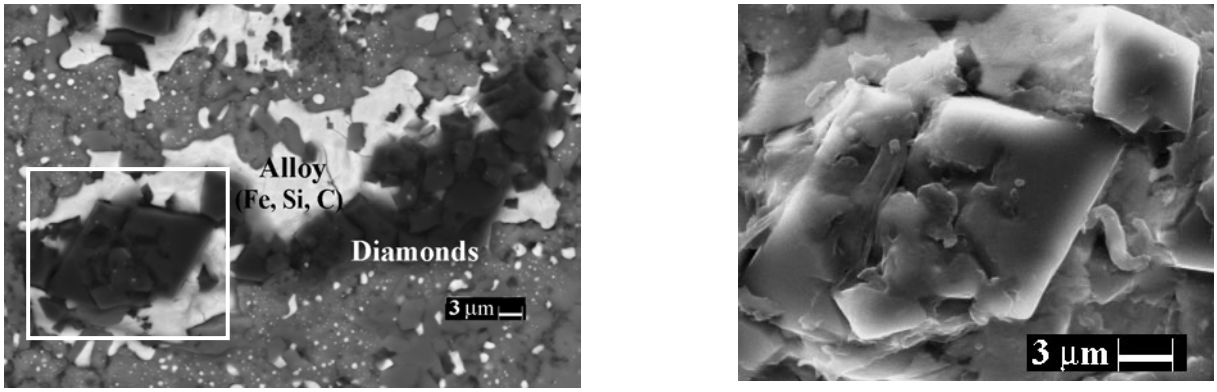

Fig. 3.4-21: Backscattered and secondary electron images of sample S3264 (20 GPa, 1700 °C) (left) and enlargement of the region containing diamond crystals enclosed by the white frame (right). The size of diamonds can reach up to 20 µm, and the octahedral diamond crystals have the same form as natural diamonds.

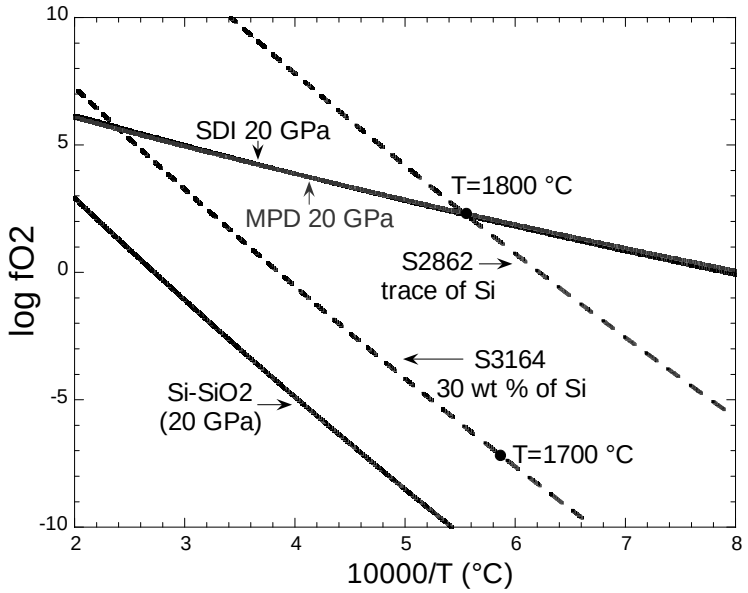

Fig. 3.4-22: Calculated oxygen fugacity of two experiments (S2862-1800 °C; S3164-1700 °C) at 20 GPa relative to the Si-SiO_2[(a)] buffer shown with their Si contents in the Fe-rich metal alloy. The stability of siderite is described by the position of the SDI[(b)] buffer determined at 20 GPa. The present fO_2 estimations are in very good agreement with experimental observations. In the range of temperature studied, the presence of silicon in the metal phase is not compatible with stable carbonates described by SDI and MPD[(c)] buffers.
[(a)] $Si + O_2 = SiO_2$
[(b)] $FeCO_3 = Fe + C_{diamond} + 3/2\ O_2$ (Siderite-Diamond-Iron)
[(c)] $MgCO_3 = MgO + C_{diamond} + O_2$ (Magnesite-Periclase-Diamond)

o. *Iron-magnesium alloying at high pressures and temperatures (N.A. Dubrovinskaia, L.S. Dubrovinsky and C.A. McCammon)*

The potential alloying of iron and magnesium at high pressures and temperatures could be important for Earth sciences, based on the high abundance of both elements and the fact that the molten Fe-dominated core is surrounded by Mg-containing mantle (in the form of complex oxides, where Mg-containing oxides are a primary component). The complete Mg-Fe phase diagram has not yet been determined. The maximum solid solubility of Fe in Mg is 0.00041 at.% Fe, and the Fe concentration at the eutectic point is estimated to be less than 0.008 at.%. Below 1000 °C the solubility of Mg in Fe is below the detection limit, while the maximum solid solubility of Mg in δ-Fe is approximately 0.25 at.% Mg at the monotectic temperature. There is clear evidence that magnesium and iron do not mix in the liquid state at ambient pressure. At the same time, two close chemical analogues of iron, namely nickel and cobalt, do form intermetallic compounds with magnesium, and at high temperatures they form solid solutions. Although the reason for such a dramatic difference in the behaviour of iron compared to cobalt and nickel is not clear, it raises the possibility that alloying of iron and magnesium may be more favourable under different conditions.

At 1 GPa and 1000 °C there was no detectable evidence of alloying between iron and magnesium. Similar to the results obtained at ambient pressure, after heating the Fe-Mg mixture (50:50 at.%) at 1 GPa and 1700 °C, the run products contained pure magnesium and iron with up to 0.3 at.% Mg (Fig. 3.4-23a). Figure 3.4-23b shows SEM images of the polished quenched product of the experiment on the Fe-Mg (50:50 at.%) mixture reacted for 10 minutes in a piston-cylinder apparatus at 3.5 GPa and 1700 °C. There are clear textural differences between the samples recovered from experiments at 1 GPa and at 3.5 GPa. Both MgO and iron-rich particles appear as spherical droplets in the material treated at 3.5 GPa. While there is no detectable amount of iron in magnesium, iron-rich droplets contain 1.7 to 2.7 at.% of Mg. The lattice parameter of this α-Fe-based alloy is 2.8686(5) Å, while the lattice parameter of pure α-Fe is 2.8665 Å.

Annealing the Fe-Mg (50:50 at.%) mixture for 20 min in the multianvil apparatus at 20 GPa and 2000 °C resulted in formation of a distinct texture in the quenched material (Fig. 3.4-23c).

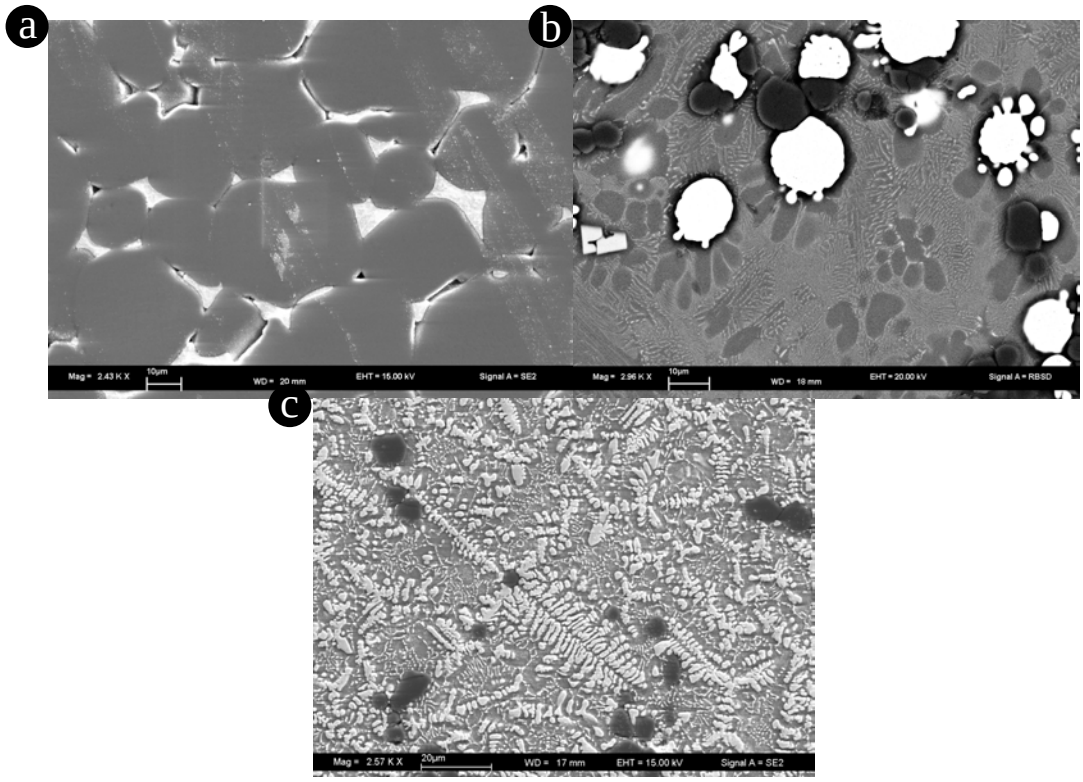

Fig. 3.4-23: SEM secondary electron images of the polished quenched product of the experiment on Fe-Mg (50:50 at.%) mixture treated (a) for 15 min in a piston-cylinder apparatus at 1 GPa and 1700 °C (white particles are Fe-0.3 at.% Mg alloy, and dark-grey particles are magnesium); (b) for 10 min in a piston-cylinder apparatus at 3.5 GPa and 1700 °C (white spherical particles are Fe-2.2(5) at.% Mg, dark-grey spherical particles are MgO, and the grey matrix is magnesium); (c) in the multianvil apparatus for 20 min at 20 GPa and 2000 °C (light-colored dendrites are Fe–4.5(5) at.% Mg alloy, dark-grey spherical particles are MgO, and the light-grey matrix with crystals is a Mg-rich alloy/compound).

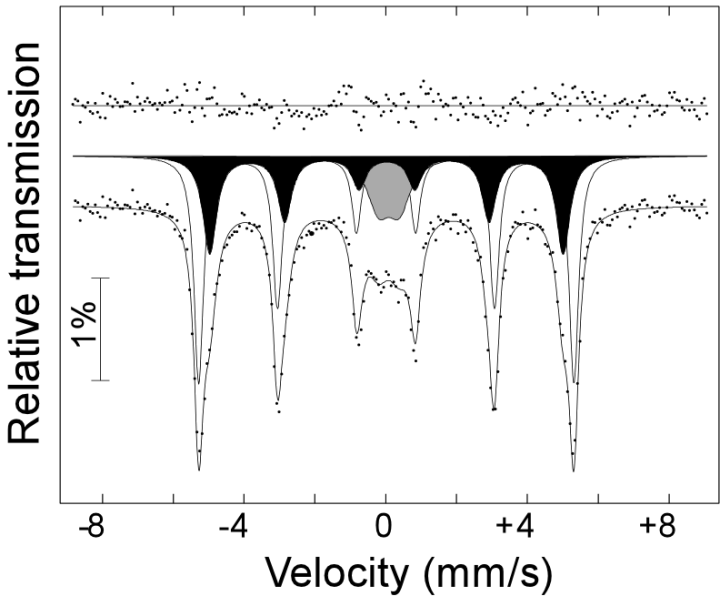

Fig. 3.4-24: Room temperature Mössbauer spectrum of the material recovered after treatment at 20 GPa and 2000 °C. Subspectra are assigned to a non-magnetic Mg-rich alloy/compound (grey doublet) and alloy (black sextet). The unshaded sextet shows hyperfine parameters close to those for pure iron, and may correspond to iron atoms in the Fe–4.5(5) at.% Mg alloy with no Mg next-nearest neighbours.

An iron-rich phase with 4 to 5 at.% Mg forms dendrites, while the matrix consists of a mixture of MgO plus a Mg-rich alloy or compound. Chemical analysis of the mixture is difficult due to submicron grain sizes. X-ray powder diffraction data shows the presence of non-reacted Mg and MgO in the sample, consistent with the Mg/MgO buffer controlling oxygen fugacity. The lattice parameter of the *bcc*-structured Fe-Mg alloy is 2.8733(4) Å, which is significantly higher (~ 2.4 %) than the lattice parameter of pure α-Fe. The Mössbauer spectrum of the sample can be fitted to two magnetic sextets plus a quadrupole doublet (Fig. 3.4-24). The doublet [CS=0.09(2) mm/s; QS=0.58(5) mm/s] is assigned to the non-magnetic Mg-rich alloy or compound, and while one magnetic sextet shows hyperfine parameters close to those for pure α-Fe, the other shows a magnetic hyperfine field that is distinctly different. The two magnetic sextets could correspond to a single phase Fe-rich alloy containing 4-5 at.% Mg, where the local magnetic environment of iron atoms differs depending on the number of Mg next-nearest neighbours.

It is usually assumed that the geometric factor, namely the large difference in the atomic sizes of iron and magnesium, is responsible for the immiscibility of these two metals (at ambient conditions the molar volume of α-Fe is 7.09 cm^3 compared to that for Mg of 14.00 cm^3). We have demonstrated, however, that at high temperatures and relatively moderate pressures (20 GPa), it is possible to synthesise a homogeneous iron-magnesium alloy with up to 4 at.% Mg.

3.5 Metamorphism at Different Time Scales

As the seasons change in a year, natural rocks undergo also a cycle of geologic processes, which steadily change their mineralogy and composition. Metamorphism is an important geologic process in this cycle and is commonly associated with large changes in temperatures and/or pressures. There are basically two metamorphic processes that occur in different geologic settings and at grossly different time scales: (1) Regional (endogenic) metamorphism and (2) shock (exogenic) metamorphism.

Regional metamorphism can last for millions of years and occurs in the context of orogeny, *e.g.* leading to subduction of rocks to great depths where higher temperatures and pressures prevail. These changes in physical conditions cause solid-state recrystallization, formation of new mineral assemblages and can even result in incipient melting. The shape and size of mineral grains and the way they are intergrown in metamorphic rocks (*i.e.* their textures and fabrics) provide key information on the metamorphic evolution of the hosts. The analysis of rock fabrics by scanning electron microscopy (SEM) combined with electron back-scattering diffraction (EBSD) has become a quantitative tool and an integral part in many studies at the Bayerisches Geoinstitut. This year, there are two contributions devoted to the extremes of endogenic metamorphism, *i.e.* they focus on *(a)* contact metamorphism occurring in the upper crust and *(b)* on plastic deformation of metamorphic rocks at the base of the crust.

Shock metamorphism is an exogenic, extremely short-lived process that is caused by bolide impacts. The impact of a projectile at cosmic velocity generates pressures and temperatures locally up to several megabars and 10,000 °C, resulting in vaporisation and melting of rocks as well as decomposition of minerals. The impact-induced release of climate gases (*e.g.*, CO_2 and SO_x) from carbonates and sulfates is considered to be an important factor in the mass extinction at the Cretaceous/Tertiary boundary. To assess the role of SO_x in the extinction scenario, we have carried out a series of shock experiments on anhydrite and attempted to model its phase diagram in the relevant high pressure – high temperature regime.

Further away from the point of impact, target rocks are affected by lower pressures and temperatures and remain solid but still suffer strong cataclastic destruction. The constituent minerals develop specific deformation features (*e.g.*, planar deformation features = PDFs) and can undergo transformations to high-pressure phases that are otherwise only expected to occur at great depth in Earth's interior. This year, we were successful in detecting such high-pressure polymorphs in natural impact rocks. The final two contributions report on the discovery of a new high-pressure carbon polymorph and on silicate hollandite, the high-pressure polymorph of feldspar.

a. *Formation of low pressure migmatites of Gennargentu Igneous Complex, central-eastern Sardinia (V. Misiti/Rome, in collaboration with F. Heidelbach)*

The Gennargentu Igneous Complex is one of the best examples of a contact aureole generated at low-P and high-T (780-820 °C, 100 MPa), where the temperature of the plutonic body (quartz diorite) was high enough to cause partial melting of the metapelitic rocks in the contact aureole. A crystal size distribution (CSD) study has been carried out on selected samples to clarify the crystallisation processes from a liquid in the quartz diorite and the migmatite leucosome. A series of quartz diorite and migmatite samples (24 in total) were analyzed with respect to the CSD of plagioclase. The quartz diorite samples were divided into three subfacies according to their modal composition: *(1)* fine grained facies, (*2)* dark inner portion and *(3)* light NE portion. The migmatites were subdivided according to their mesoscopic and microscopic features into folded and stromatic types.

For each sample a number of images were acquired with the scanning electron microscope (SEM) at different magnifications and the width and length of the plagioclase crystals were measured (Fig. 3.5-1). The two-dimensional data were converted into a three-dimensional CSD by assuming a grain shape ratio of 1:2:2 and a random orientation of the crystal shapes. CSDs were plotted on a Ln (population density) *vs* crystal size (length in mm) diagram. The slope and shape of the CSD can then be interpreted in terms of crystallization time and history.

The CSD diagrams for the quartz diorite samples show a variation in the curve from a linear trend (fine grained facies) to a slight bending of the curve (dark inner portion) up to a visible bell-shape curve (light NE portion). This trend can be explained in terms of the crystallisation processes: The fine grained facies reflects a magmatic system where the melt was always in contact with the forming crystals. Samples of the dark inner portion crystallised in an average time of 5000 years and show a bending curve that indicates the formation of partially resorbed nuclei; the most numerous population of crystals occurs at a size of 200-300 μm. Finally the presence of a strong bell-shaped curve in samples belonging to the light NE portion testifies a slow crystallization (average of 7300 years) with a complete resorption of nuclei and increase of the grain size.

Compared to the quartz diorite the plagioclases in the leucosomes of the migmatites show a more complicated behaviour. Both folded and stromatic migmatites show bell-shaped curves, which are centered at fine to medium crystal sizes. In the folded migmatites the CSD is concave upwards for crystals greater than 100 μm. This curve shape is typically found where an accumulation process takes place and it is also indicative of melt loss during the crystallization process. In contrast, the stromatic migmatites show a general flattening of the curve with a negative slope, indicating a decrease in population density with increasing grain size. In general, the CSD patterns found in the all migmatite samples are typical for a crystallization from a melt, suggesting that they are truly magmatic. The calculated

crystallization ages range from 800 years for the folded migmatites to about 4000 years for stromatic migmatites.

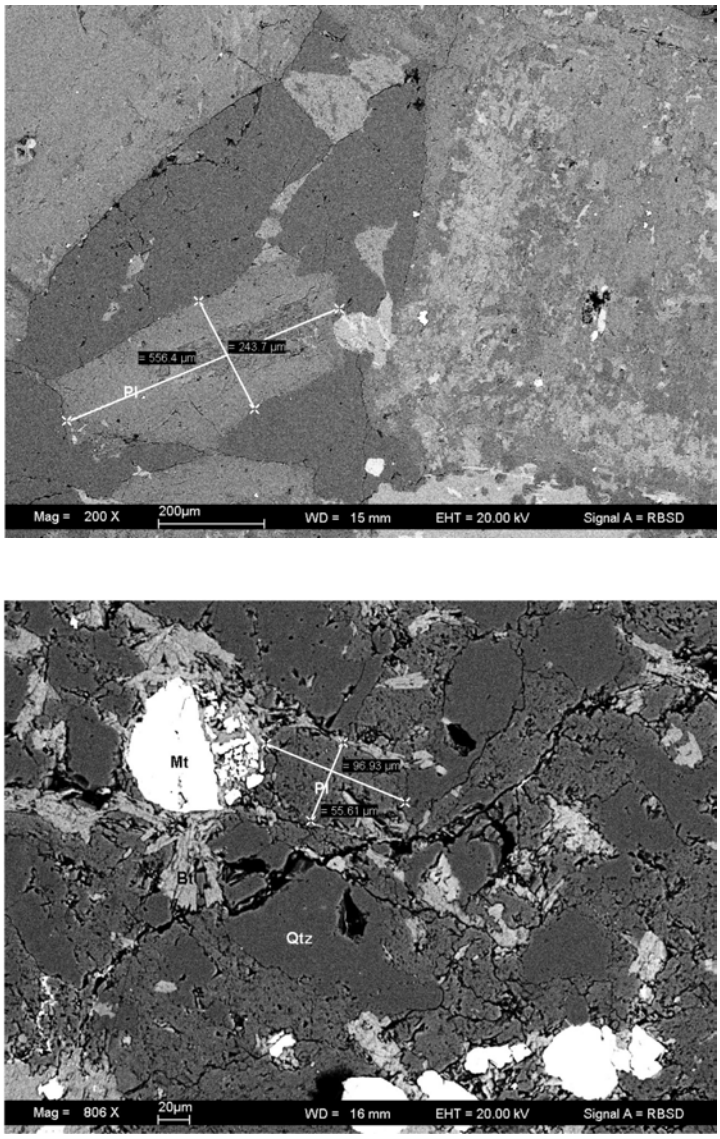

Fig. 3.5-1: SEM image of plagioclase crystals in the quartz diorite (top) and the migmatite (bottom). The lines represent the maximum and minimum length of the crystal.

b. *Microstructures and texture in olivine associated with continental subduction in the Kvalvika peridotite lens, Western Gneiss Region, Norway (M.P. Terry, F. Heidelbach, H. Couvy and G.D. Bromiley)*

Microstructures and textures in the Kvalvika peridotite lens were examined to provide an initial insight into the interaction between the crust and mantle and emplacement mechanisms

for these mantle-derived peridotites. The Kvalvika peridotite that has an exposed area ~ 5 m wide and ~ 40 m long and is composed of partially serpentinized dunite with layers of garnet-pyroxenite that is enclosed by dioritic gneiss. Dioritic gneiss at the contact with the peridotite lens is eclogite, and contains the assemblage garnet-omphacite-quartz-rutile. Both garnet and omphacite in this eclogite have a strong shape preferred orientation. Linear and planar structural elements, including fold axes, mineral lineation, and foliation in the eclogitized gneiss, have the same orientation as in the peridotite lens, indicating that both experienced the same deformation at eclogite-facies conditions. Detailed study of these structural fabrics indicate they have a U-Pb zircon age of 412 Ma and are kinematically and geometrically consistent with continental subduction associated with the Scandian Orogeny (425-385 Ma).

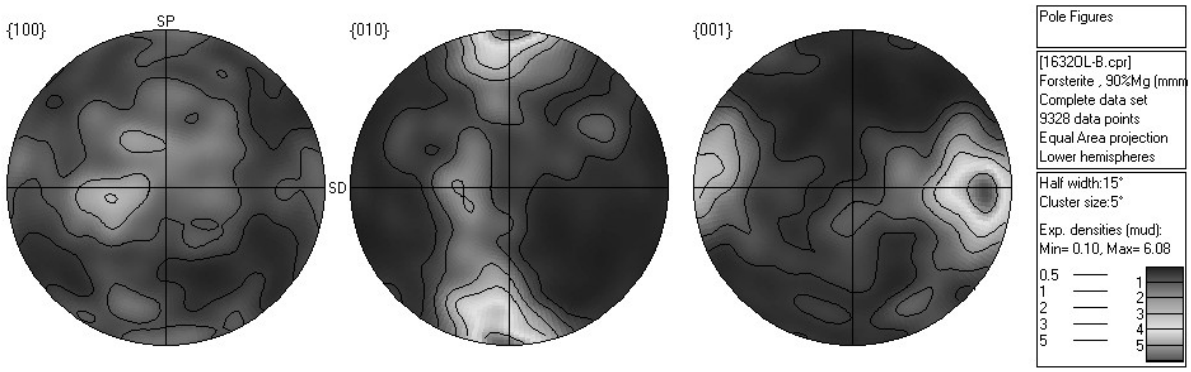

Fig. 3.5-2: Pole figures showing textures in olivine

Microstructures were studied using petrographic microscopy, electron backscattering diffraction (EBSD), and transmission electron microscopy (TEM). In thin sections, olivine in the dunite has a strong grain-shape preferred orientation and is cut by serpentinized fractures. Textural analysis using EBSD shows an alignment of {010} and <001> with foliation and lineation respectively, indicating intracrystalline deformation involved glide on the (010)[001] slip system. At the TEM scale, microstructures are heterogeneous and most olivine grains appear to be free of defects. However, two major groups of dislocations could be recognized in the other olivine grains. The first group of dislocations, seen in Figs. 3.5-3a and 3.5-3b, appear to have slipped considerably away from their sources. These dislocations are absolutely straight and are of screw character. The dislocation densities remain modest in the range: 5×10^{11} m^{-2} to 8×10^{12} m^{-2}. The activated slip systems are identified as either [001](100) and [001](010). There are not enough dislocations to estimate the relative frequencies of these two slip systems, but the EBSD results indicate that the latter type were more important during intracrystalline deformation. The second group of dislocations is associated with pervasive microcracks or fractures. Locally, these microcracks are found inside the grains but in most cases the fractures are filled with serpentine (Fig. 3.5-3c). The cracks are commonly associated with emission of dislocation loops (Fig. 3.5-3d) that did not move very far from the crack tip. The Burgers vector of these dislocations is also [001].

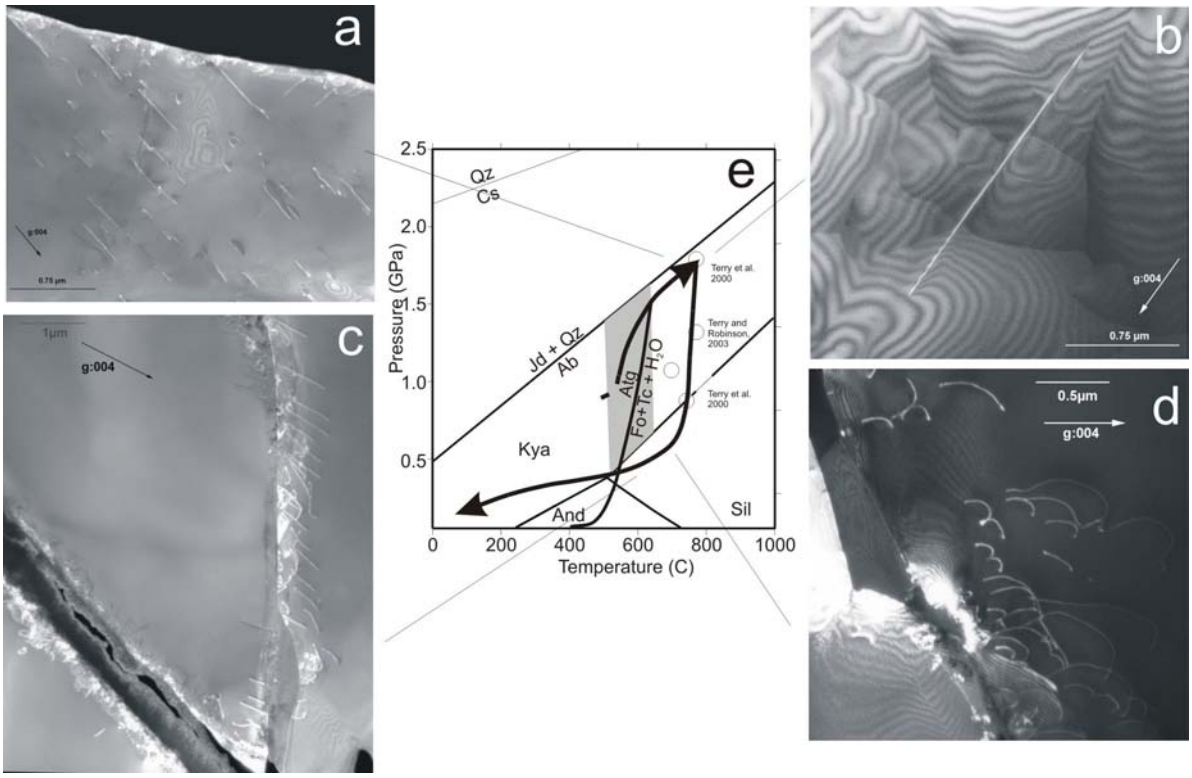

Fig. 3.5-3 a and b: TEM images of dislocations associated with higher temperature deformation. c and d: TEM images of dislocations of lower temperature and/or pressure deformation. PT path (e) for the lithotectonic unit containing the Kvalvika peridotite. Gray box shows constraints constraint on the prograde part of the PT path.

Infrared spectroscopy was used to estimate water content in the center of olivine grains that were free of fractures. Unpolarized spectra were obtained from 13 olivine crystals in a 200 µm thick section. Spectra show OH absorption bands at 3613 (small), 3570 (probably two bands at 3598 and 3579) and 3525 (small) cm^{-1}, with average water content of 12 ppm H_2O by weight. In contrast, previous workers determined the maximum water content in olivine to be 135 ppm H_2O at 2.5 GPa. Results are consistent with re-equilibriation of water contents in olivine during serpentinization.

Interpretations and implications include the following: (1) The straight [001] dislocations are interpreted to represent plastic deformation with mobile dislocations that occurred in eclogite-facies at ~ 780 °C and 1.8 GPa (Fig. 3.5-3e). (2) The combined EBSD and TEM results indicate deformation is predominantly associated with [001] glide on (010). (3) Dislocations associated with microcracks and fractures are interpreted to reflect the behaviour close to the brittle-ductile transition for olivine and likely occurred during decompression and/or cooling prior to serpentine growth (Fig. 3.5-3e). (4) Systematic absence of subgrain boundaries and activation of [001] glide are interpreted to represent a low temperature and possibly high-stress subduction environment. (5) Microstuctural and textural analysis may provide another method to identify low-temperature (700-800 °C) Scandian and younger deformation fabrics,

which can be used to elucidate mechanisms associated emplacement of mantle during HP and UHP metamorphism, from high-temperature (1250-1450 °C) Proterozoic deformation fabrics.

c. *Deformation phenomena in experimentally shock-loaded anhydrite (R. Skála, F. Langenhorst and F. Hörz/Houston)*

The Chicxulub impact is believed to have caused a worldwide mass extinction of biota at the Cretaceous/Tertiary (K/T) boundary. Various killing mechanisms are discussed to have contributed to this extinction, including global deterioration of the atmosphere and hydrosphere from the shock-induced release of SO_x from sulfate-bearing target rocks. The devolatilization of anhydrite is inferred mainly from thermodynamic models but no systematic study of the shock-induced effects in anhydrite exists so far.

Anhydrite has been experimentally shock-loaded using a 20-mm-caliber powder gun at the JSC-NASA, Houston, Texas, USA. Peak shock pressures range from 4 to 64 GPa. Recovered samples were examined by optical microscopy, micro-Raman spectroscopy, scanning (SEM) and transmission electron microscopy (TEM), and X-ray diffraction to detect the solid-state shock deformations.

Samples recovered after shock-loading are pervasively fractured and are white, opaque with a matt surface. Under the polarizing microscope, the samples display a strong internal fragmentation and undulatory extinction. Twinning appears to be more frequent in shocked samples compared to the starting material, which contains some needle-shaped twins. SEM observations corroborate the heavy comminution of anhydrite at even the lowest pressure of 4 GPa and reveal that the distribution of shock effects is not completely homogeneous throughout the sample volume.

All X-ray powder diffraction patterns yield anhydrite as a dominant phase together with trace amounts of dolomite and/or quartz. This agrees with chemical data acquired with SEM and TEM. The unit-cell dimensions, refined from the ten most prominent non-overlapping diffraction lines, do not display any systematic correlation with pressure; maximum differences are less than 0.15 rel.%. Line broadening, however, is prominent already at 4 GPa and increases systematically with pressure, albeit not linearly, up to 50 GPa. Above this limit the broadening decreases slightly (see Fig. 3.5-4). A similar tendency was observed with Raman spectroscopy, revealing a correlation between band broadening and pressure.

Transmission electron microscopy showed that the starting material is almost free of lattice defects. It contains, in addition to rare growth twins and cleavage fractures, only few straight dislocations. Contrary to that, the shocked anhydrite contains already at low pressures abundant deformation features; these are mainly dislocations and twins. So-called Rose channels due to a multiple mechanical twinning have been identified in the sample shock-

loaded to 20 GPa. Straight dislocations are typical for unshocked starting material and for samples shocked to less than 30 GPa, albeit the density of dislocations is markedly higher in shock-loaded material. At higher pressures, dislocations are polygonized and simultaneously some areas appear where the dislocations are completely wiped out. Both observations suggest rapid recovery of the microstructure in regions of elevated post-shock temperature. Samples shock-loaded to 60 GPa and above provide indications to melting (Fig. 3.5-5), which is localized in some shear zones and melt pockets. At the highest pressure of 64 GPa, we observe pervasive melting and the presence of some bubbles.

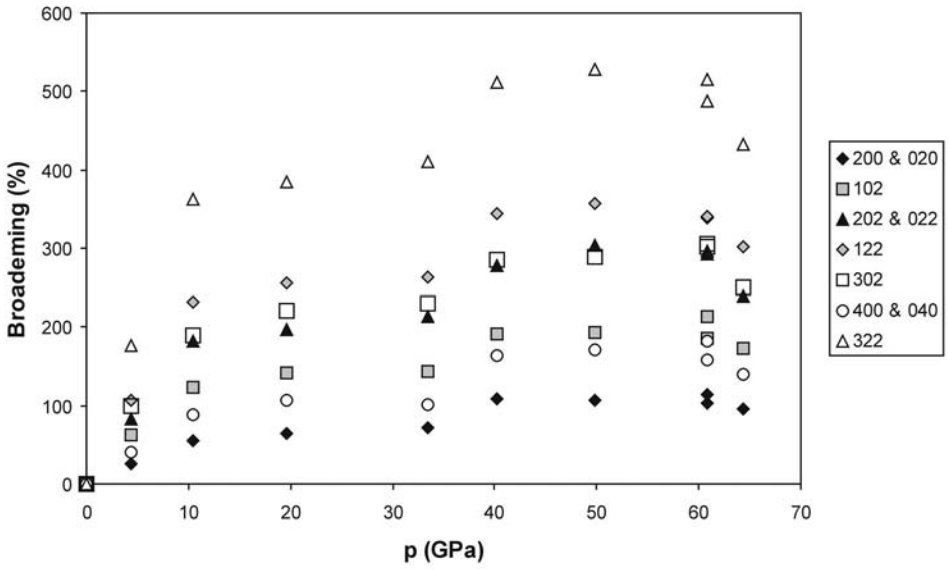

Fig. 3.5-4: Relative broadening of selected reflections (indexed in the Amma setting of the space group).

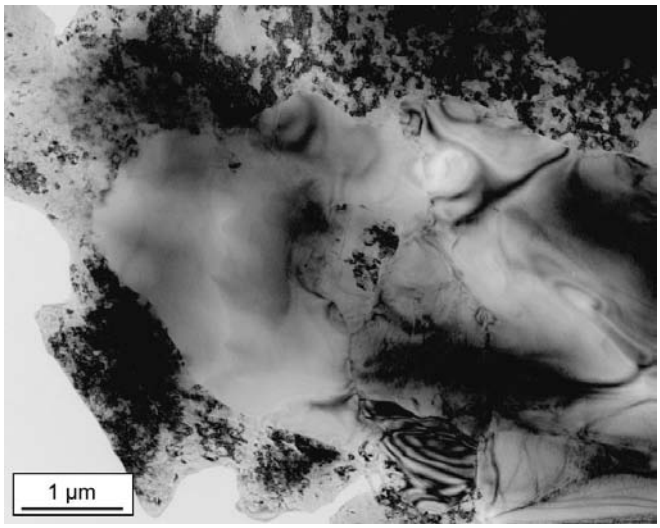

Fig. 3.5-5: Bright-field TEM image of highly (61 GPa) shocked anhydrite material showing defect-free grains that have crystallized from the quenched melts. Coexisting defect-rich grains show polygonization of dislocations.

In conclusion, the results show, contrary to literature data reporting incipient vaporization of anhydrite to require approximately 32 GPa, that anhydrite is a rather stable mineral under the conditions simulated by the experiments (up to almost 65 GPa). While a marked increase in the number of defects (dislocations, twinning) has been observed with increasing peak shock pressure, no phase changes (high-pressure polymorphs, decomposition products) have been found. At the pressures above 60 GPa, anhydrite starts to melt and at 64 GPa the melting is pervasive. Gradual narrowing of peaks in powder patterns above 50 GPa is consistent with find of defect-free grains that have grown from quenched melts.

d. *Theoretical constraints on shock melting and decomposition of anhydrite (B.A. Ivanov/ Moscow, F. Langenhorst, A. Deutsch/Münster and U. Hornemann/Efringen-Kirchen)*

In the context of the Chicxulub impact, it became recently obvious that experimental and theoretical research on the shock behaviour of sulfates is essential for an assessment of the role of shock-released gases in the K/T mass extinction. The Chicxulub crater is the only known impact structure where the bolide penetrated a sedimentary layer with large amounts of interbedded anhydrite. The sulfuric gas production by shock compression/decompression of anhydrite is an important issue for climatic changes, even if the size of Chicxulub crater is half of the so far assumed size.

The comparison of anhydrite experimentally shocked at various laboratories reveals large differences in the pressures for melting and decomposition. To gain insight into this issue, we have made a theoretical investigation of the thermodynamic properties of anhydrite. The project includes the review of data published in the last 40 years - reasons to study anhydrite cover a wide field of interests: from industrial problems of cement production to the analysis of nuclear underground explosions in salt domes, conducted in the USA and USSR in the 1970's.

The review of data presents anhydrite as a material with a complex behaviour in various aspects. Static and shock compression shows that anhydrite has two solid-solid polymorph phase transitions at high pressure. At least the second one is a martensitic transformation, which causes the double shock wave structure in the relevant pressure range. High temperature experiments at ambient pressure reveal a complex behaviour near to the melting point (T~1738 K). The melting point of anhydrite is very close to the temperature of the decomposition reaction $CaSO_4 \rightarrow CaO + SO_2 + ½\ O_2$. In case of a closed system, anhydrite may melt congruently, *i.e.* the SO_2 partial pressure suppresses the decomposition. However, in an open system from which SO_2 is removed, anhydrite melts incongruently. In the latter case, the eutectic melting of a resultant mixture with 75 % $CaSO_4$ and 25 % CaO (75 % + 25 %) may occur at T~1638 K. The kinetics of the decomposition reaction is very slow; degassing of a 0.5 g sample takes several hours.

To reconcile known experimental data, we made an attempt to construct the phase diagram and equation of state of anhydrite, which can then be used to numerically model shock experiments and natural impact events. The P-T phase diagram is compiled with a standard set of thermodynamic data for $CaSO_4$, CaO, SO_2, and O_2. A simple Fortran program allows us to vary the partial pressures for SO_2 and O_2 gases resulting in P-T curves for the decomposition of anhydrite under various SO_2 venting conditions (Fig. 3.5-6).

To model the pressures and temperatures of anhydrite under shock compression and decompression, we modified the Fortran hydrocode ANEOS (ANalytical Equation Of State, Los Alamos design), which allowed us to construct separate fields for three solid phases of $CaSO_4$. As ANEOS computes all thermodynamic properties for a material, we can estimate also phase boundaries. Due to the lack of high-pressure compressibility data for anhydrite, we used an ANEOS construction similar to that for the quartz-coesite-stishovite system. This provided first hints to the geometry of phase boundaries in the $CaSO_4$ system. Figure 3.5-7 shows multi-phase ANEOS estimates for the Hugoniot (shock front) and release temperatures. At pure hydrostatic conditions, anhydrite may melt when released from pressures between 80 to 90 GPa. Under real conditions, plastic work due to shear strain can readily dissipate additional heat in the sample and decrease the onset pressure for melting and degassing.

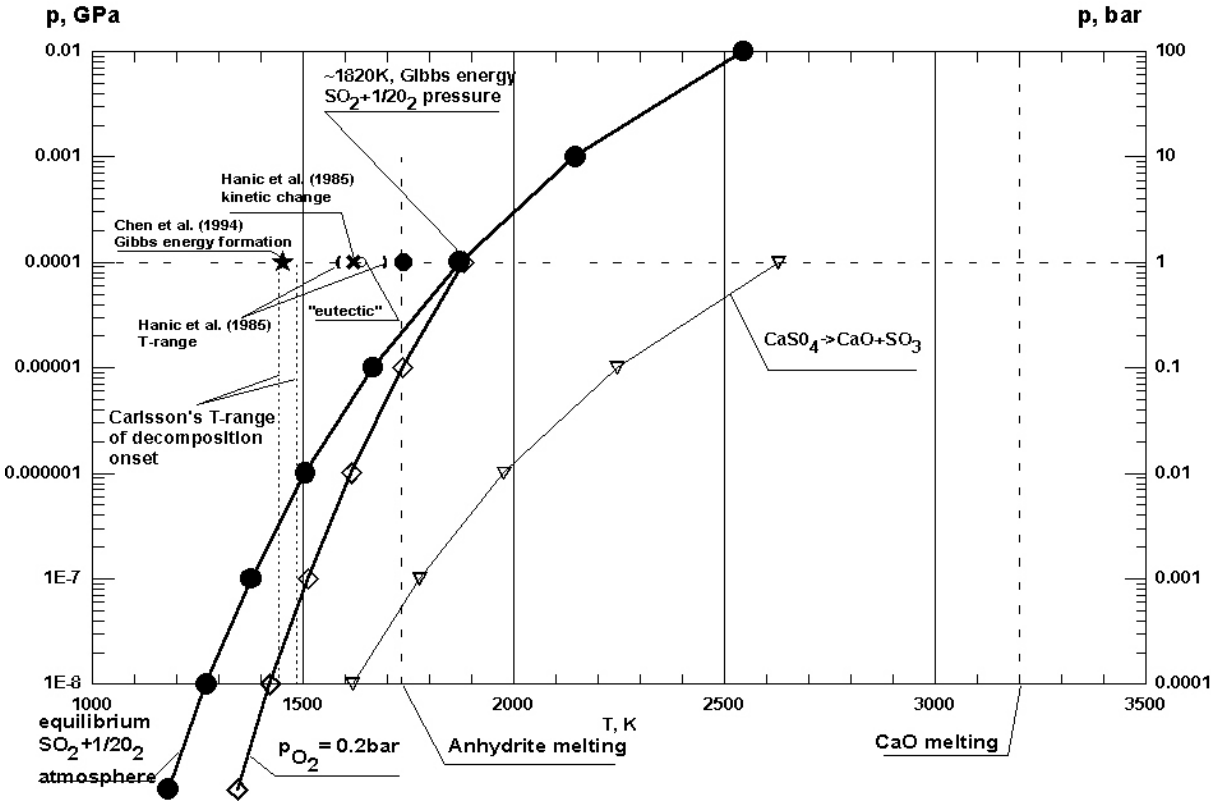

Fig. 3.5-6: P-T diagram for the decomposition of anhydrite under an equilibrium atmosphere of sulfur dioxide and oxygen and an atmosphere with 0.2 bar oxygen and variable pressure of SO_2. Decomposition equilibrium estimates for $CaSO_4$ → CaO + SO_3 reaction are shown for comparison.

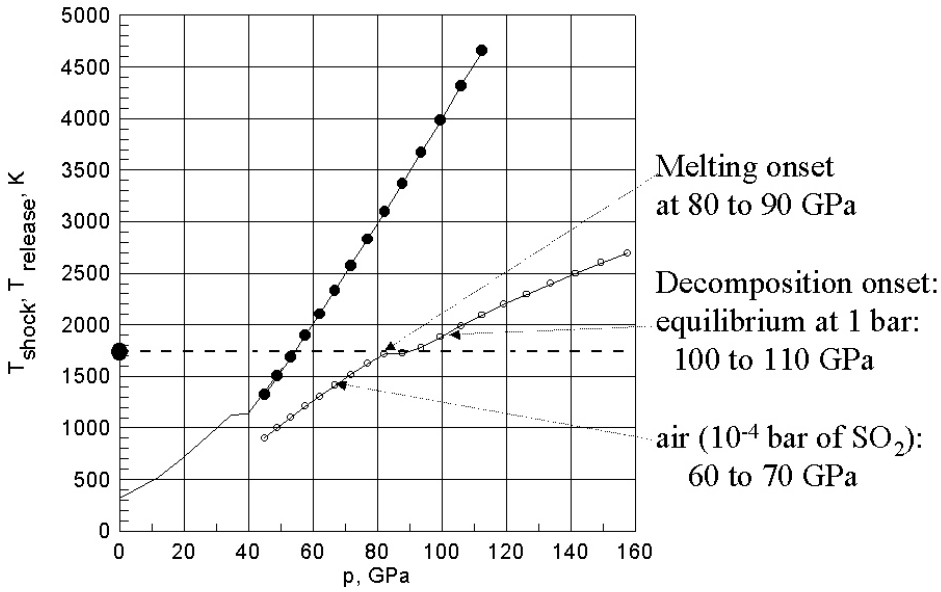

Fig. 3.5-7: Hugoniot and released temperatures estimated for anhydrite by the ANEOS code. In dependence of SO_2 partial pressure, the decomposition may start below or above the melting point.

e. *Experimentally shock-loaded quartz: Comparison of two different experimental setups through TEM and X-ray powder diffraction data (R. Skála, F. Langenhorst and F. Hörz/JSC-NASA, Houston)*

As the most widespread mineral in the Earth's crust, quartz has been subject to numerous experimental shock studies. Experiments enabled us to calibrate shock-induced effects at the laboratory scale and to apply the obtained data to naturally shocked quartz. Recently, however, some studies questioned the validity and plausibility of these calibrations, pointing out that the actual experimental setup may have a significant influence on the observed shock-induced phenomena. To assess the role of the experimental setup, we compare here new data on quartz shock-loaded at the JSC-NASA (Houston, TX, USA) with existing data on quartz shocked at the Ernst-Mach-Institut, Fraunhofer-Gesellschaft (Efringen-Kirchen, Germany). The former setup uses relatively subtle containers and flyer plates accelerated with a 20 mm-caliber powder propellant gun, whereas the latter design utilizes massive containers as well as driver plates, which are accelerated by a contact explosive.

Six quartz samples experimentally shock-loaded at JSC-NASA to peak shock pressures between 8 GPa and 33 GPa and a standard reference sample have been ion-thinned, carbon coated and observed in a transmission electron microscope (TEM). The samples were imaged using bright-field (BF), dark-field (DF) and diffuse-scattering DF techniques (Figs. 3.5-8 and 3.5-9). Selected area electron diffraction (SAED) patterns were used to decipher the crystallographic orientation of planar deformation features (PDFs), occurring in all shocked samples except those shocked to 8 GPa and 33 GPa. The 8 GPa sample displays only

ubiquitous fracturing, resulting in a mosaic structure. This is also documented in SAED as pronounced streaking of diffraction spots. The 33 GPa sample, on the other hand, shows almost complete transformation to glass with only rare remnants of crystalline materials occurring in small lamellar patches. The crystallographic orientation of most of the PDFs corresponds to that previously described in the literature (*e.g.*, {11.0}, {11.2}, {11.3}), however, some exotic orientations also appeared (*e.g.*, {12.5}, {13.5}, {001}).

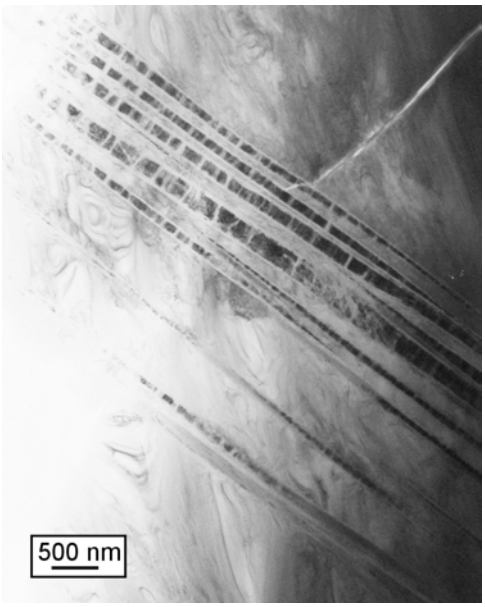

Fig. 3.5-8: Bright-field TEM image of quartz shock-loaded to 23 GPa containing abundant PDF lamellae with {11.2} orientation.

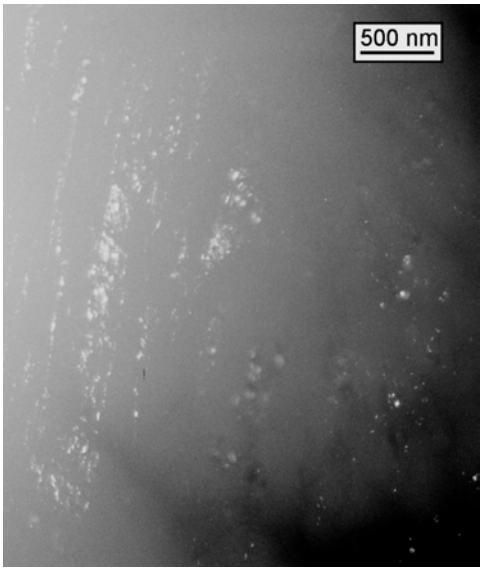

Fig. 3.5-9: Dark-field TEM image of quartz shock-loaded to 33 GPa. Sample contains rare patches of crystalline material (white) embedded in glass (gray).

Unit-cell dimensions determined from the powder data of the samples shock-loaded at the JSC-NASA remain invariant in a wide range of peak shock pressures up to about 22 GPa. At higher pressures the unit-cell expands proportionally to the pressure applied. The expansion observed is anisotropic – the lattice constant *a* increases more than the *c* parameter. Contrary to previously published data (increase in unit-cell volume: 3 rel.%), the maximum change of the unit-cell volume does not exceed ca. 0.5 rel.% at approximately 30 GPa.

The determination of the diaplectic glass content, which is due to the formation of the planar deformation features in quartz, has been carried out applying a quantitative X-ray diffraction (XRD) analysis. The integral intensity of the (10.1) diffraction line of quartz has been measured to calculate the absolute quartz content, with the remaining fraction reflecting the absolute diaplectic glass content. The powder XRD study confirmed the positive correlation between the glass content and peak shock pressure in experimentally shocked quartz. There is almost no amorphous material (below 5 %) up to the pressure of 16 GPa. At 18 GPa, the glass content increases abruptly reaching almost 25 %. From this point on, a relatively tight linear correlation between modal glass content and pressure occurs up to 33 GPa, where less than 5 % of material remains crystalline.

In conclusion, the general trends in all the observed properties (orientations and appearance of PDFs, unit-cell dimensions, and glass content variation) are independent of the technique used to shock-load quartz samples. The quantitative differences observed can be attributed to the quality of the precursor crystal and mainly to the variations in the temperature history of the samples.

f. *A novel cubic, transparent and super-hard polymorph of carbon from the Ries and Popigai craters (A. El Goresy/Mainz, L.S. Dubrovinsky, Ph. Gillet/Lyon, A.S. Simionovici/Grenoble, V.L. Masaitis/St. Petersburg)*

Cubic diamond (space group *Fd3m*) and lonsdaleite (space group *P63/mmc*) are so far the only known natural high-pressure polymorphs of carbon. We report the results of microbeam X-ray diffraction studies of transparent carbon materials found in shocked gneisses from Popigai and Ries impact craters using Synchrotron radiation at the ESRF Facility in Grenoble, France.

A large (70 µm of maximum dimension) transparent flat platelet with very high relief (height up to 12 µm above the section surface) that could be misidentified as diamond was selected for the synchrotron study. The grain displays uneven surface with rough gouges and particles of metallic lead scraped from the lead polishing disc. It shows a highly variable relief indicating the presence of different transparent materials with different polishing hardness. The transparent interior part of the platelet is covered with small flakes (up to 7 µm) of secondary graphite formed by back transformation. EDAX analysis at low voltage, without carbon coating and with a Field Emission SEM (FESEM) indicated that the grain is pure

carbon. The grain was then cored out using a high-precision micro-drilling instrument and mounted on a hole in a metal plate holder. X-ray diffraction, imaging and fluorescence studies were carried out at the ID22 beam line of the ESRF in Grenoble, France. The sample was mounted in a metallic holder and positioned in the image plane on a high precision XYZ remote-controlled stage. A 100 mm Ø CCD camera located behind the sample recorded diffraction images simultaneously with the fluorescence measurements. The X-ray microbeam (2 x 10 μm) was scanned over the whole grain and the surrounding silicate matrix. Diffraction and fluorescence data were collected for every beam spot. X-ray and fluorescence phase identification mapping was laid out on the microscopic photograph thus allowing fine-scale spatial phase separation and further delineation of the textural relations of the coexisting phases.

The platelet is encompassed by a 40 μm long cristobalite grain on the right side and a 15 μm long quartz grain on the left (Fig. 3.5-10). The carbon phases and the surrounding low-pressure silica phases are enclosed in quenched wavy plagioclase. X-ray diffraction mapping of the platelet indicated the presence of three distinct crystalline carbon phases in a remarkable setting (Fig. 3.5-10). The high relief portion of the interior of the grain (Fig. 3.5-10) revealed, in addition to the (111) and (200) reflections of metallic Pb, an X-ray pattern that is different from any known carbon modification (Fig. 3.5-11). The pattern is also different from that of cristobalite, quartz, plagioclase, garnet, rutile, ilmenite or zircon, minerals that are present in the gneiss. The diffraction lines are also different from those of nontronite. Contamination from the neighbouring phases can be entirely ruled out. Twenty-three diffraction lines obtained from the super-hard carbon could be unambiguously indexed in terms of a cubic cell with a = 14.6970 Å; cell volume V = 3174.58 Å^3 (space group: *Pm-3m*). The estimated density, based on the structural model, is ρ = 2.49 gm/cm^3. This phase is a novel natural super-hard, polymorph of carbon. The diffraction mapping indicates that the platelet has an onion-skin like structure. The new carbon phase is entirely surrounded by lonsdaleite (Figs. 3.5-10 and 3.5-11), followed by an outermost, 7 μm shell of secondary graphite, respectively (Fig. 3.5-10). Lonsdaleite occupies the portion of the interior of the grain with a lower relief than that of the new phase, thus manifesting its lower polishing hardness compared to the new phase (Fig. 3.5-10).

The petrographic setting of the three carbon phases is indicative of reconstructive phase transformation to the new dense phase and lonsdaleite, followed by partial back transformation of lonsdaleite to secondary polycrystalline graphite at high post-shock temperatures. The spatial arrangement of the new phase occupying the core of the dense carbon platelet with lonsdaleite completely surrounding it may reflect a sharp change in the peak-shock pressures from the interior outwards. We do not know at present if the new carbon phase is a primary species or a quench phase of an unknown metastable much denser carbon polymorph. Our estimated density (ρ= 2.49 gm/cm^3) of the new phase is subject to the validity of the computed atomic arrangements in the structural model. At any case, the polishing hardness of the new carbon phase is considerably higher than that of cubic diamond (Ries) and lonsdaleite (Popigai), respectively.

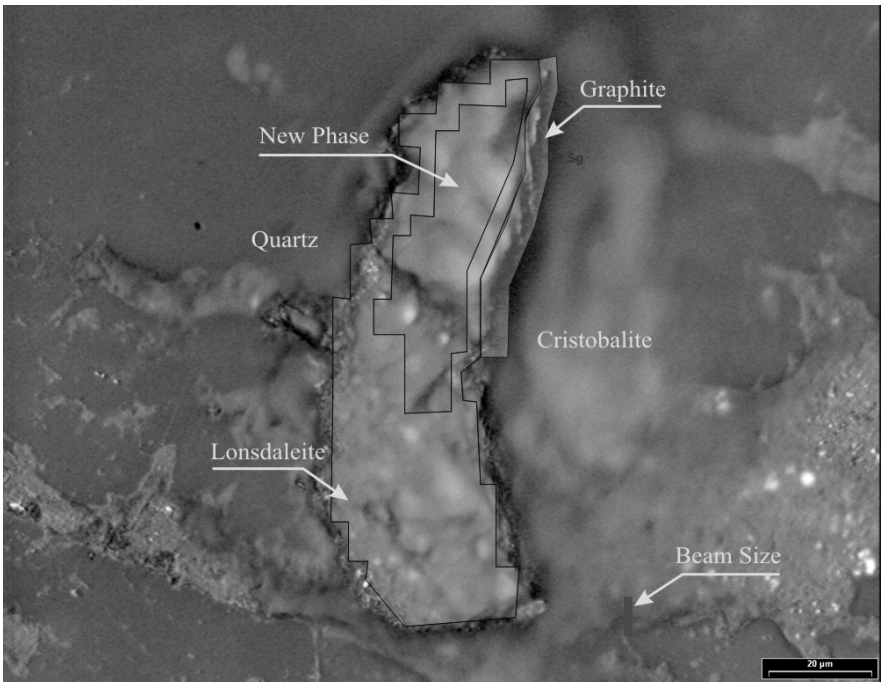

Fig. 3.5-10: Fine scale textural relations of the new polymorph of carbon, lonsdaleite and secondary graphite as obtained from Synchrotron micro-beam X-ray diffraction and fluorescence mapping studies. The length of black scale bar on the lower right corner is 20µm.

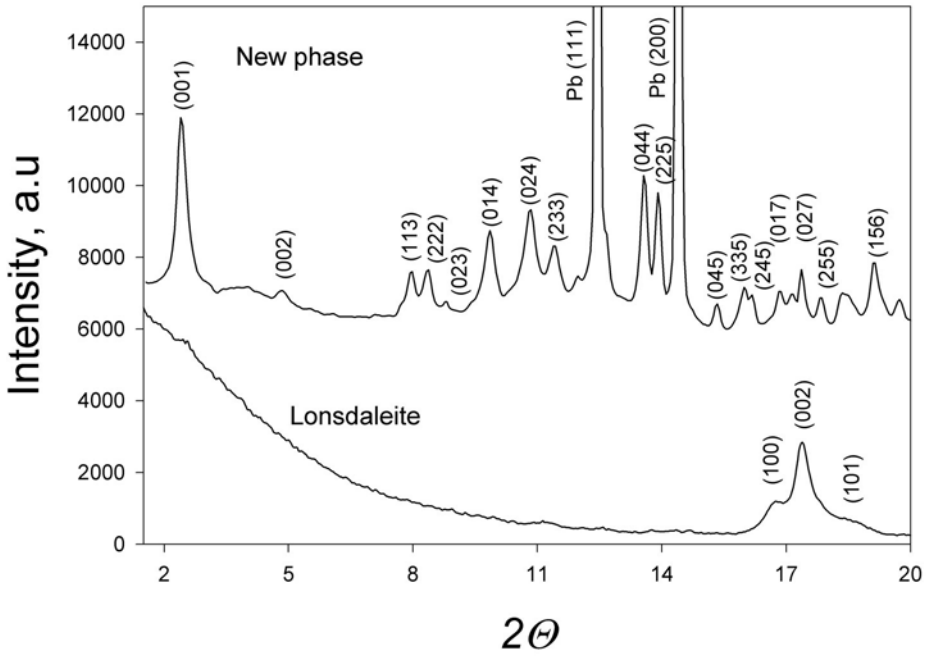

Fig. 3.5-11: X-ray diffraction patterns of the new super-hard carbon phase with the strongest reflections (111) and (200) of the polishing lead (upper pattern) and the pattern of lonsdaleite (lower pattern) obtained from the pertinent phases as shown in Figure 3.5-10.

g. *Discovery of silicate hollandite in a terrestrial rock (F. Langenhorst and B. Dressler/ Thornhill)*

Feldspars transform at high pressure to a hollandite-structured polymorph with silicon in octahedral coordination. Silicate hollandite is, for example, expected to occur at inaccessibly great depth in subduction zones. In nature, silicate hollandite has so far only been found in the context of impact events in heavily shocked meteorites such as L6 ordinary chondrites and SNC achondrites. In this transmission electron microscope (TEM) study we report the first find of silicate hollandite in a terrestrial rock, a strongly shocked anorthosite from the central uplift of the Manicouagan impact crater, Canada.

The shocked anorthosite contains plagioclase and K-feldspar as main phases. Both feldspars are almost completely converted into diaplectic glass with perlitic fissures. The feldspars retain only their crystalline state in the immediate vicinity of denser accessory phases such as garnet, titanite, scapolite, and orthopyroxene. These phases have a higher shock impedance and hence show less shock damage than feldspars, *i.e.* they exhibit only a strong internal fragmentation but retain their crystalline state. Additionally, titanite developed mechanical twins and scapolite contains planar deformation features. Besides these shock features in minerals, the “glassy” rock shows also traces of shock in form of several grayish to brownish shock veins, which pervade the rock in an irregular fashion. At the optical scale it is already obvious that the thin (< 100 µm) veins contain birefringent phases but identification is impossible due to the small grain size.

To identify the phases in shock veins, we therefore used analytical transmission electron microscopy (TEM). TEM observations and selected electron diffraction (SAED) experiments show that the veins are composed of polycrystalline aggregates of silicate hollandite with grain sizes ranging from a few nanometers up to 0.1 µm (Fig. 3.5-12a). The grains have spherical to lath-like shapes and are commonly surrounded by an amorphous silicate matrix. Due to the nanocrystalline nature of aggregates, SAED patterns show almost complete diffraction rings with interplanar spacings (Fig. 3.5-12b), which are fully compatible with the tetragonal hollandite structure. The cell parameters refined from SAED patterns are: a=8.94 Å and c=2.57 Å. Energy-dispersive X-ray (EDX) measurements reveal that silicate hollandite has a feldspar composition ($Ab_{41}An_{58}Or_1$), equivalent to that of the maskelynite in the bulk anorthosite.

In summary, we report here the discovery of silicate hollandite in a terrestrial impact rock. Similar to heavily shocked meteorites, the silicate hollandite formed in shock veins, which are regarded as quenched shear melts. The small grain size and embedding in an amorphous matrix suggest that silicate hollandite crystallized from this high-pressure melt. The isotropization of feldspars indicates that the host anorthosite has been shocked to pressures of approximately 35 to 40 GPa. Silicate hollandite has however crystallized at lower pressures during the decompression phase since the stable assemblage at 35 to 40 GPa would be Ca-ferrite + stishovite.

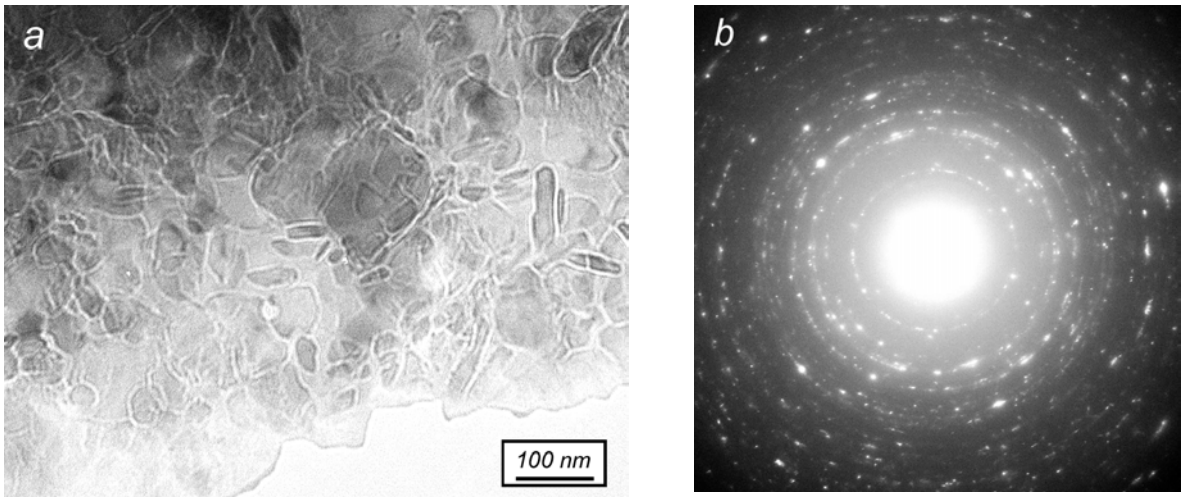

Fig. 3.5-12: (a) Bright-field TEM image and (b) corresponding selected area electron diffraction (SAED) pattern of a polycrystalline silicate hollandite aggregate found in a shocked anorthosite from the Manicouagan impact structure, Canada.

3.6 Fluids and their Interaction with Melts and Minerals

There are very few physical and chemical properties in silicate systems that are not modified in some way by the presence of water. The fact that water influences so many of the Earth's processes underscores the importance of determining how water is distributed between the Earth's various geochemical reservoirs. The Earth's interior has the potential to contain by far the largest terrestrial water reservoir and there is certainly a significant amount of evidence that water is an important agent in the Earth's mantle. Water lowers melting temperatures of silicate rocks and allows elements to be mobilised in fluids and melts creating variations in the geochemistry of the mantle. The geochemical enrichments created by so called "metasomatic" fluids and melts can be analysed in rock samples of the mantle brought to the surface in volcanic eruptions. Identifying the original water contents in these mantle rocks is much harder, however, because minerals tend to lose water to the vapour phase during ascent to the Earth's surface. Similarly, the mantle rocks that reach the surface in volcanic eruptions may not be typical of the bulk of the mantle and their water contents may have been influenced by the very magmatic activities that brought them to the surface.

The uncertainties in the mantle water budget have stimulated many research projects that often rely on corroborative data from laboratory experiments. Examining the rate at which water, or structurally bound hydrogen to be more accurate, diffuses through mantle minerals, for example, allows estimates to be made of the likely quantities of water lost from these minerals during their ascent to the surface. Conversely, experiments to measure the maximum amount of water that can be accommodated by particular mantle minerals allow constraints on the quantities of water that may be recycled back into the mantle at subduction zones. Geophysical methods that could give independent estimates of the mantle's water content are also potentially extremely useful. Electrical conductivity measurements of the upper mantle, for example, may be sensitive to the water content of the dominant mineral olivine. If the electrical conductivity of olivine can be precisely measured as a function of pressure and water (*i.e.* OH^-) content then such a geophysical remote sensing method could be used to map the water content of the upper mantle. Water also affects the volume and elastic properties of the minerals in which it dissolves. Wadsleyite, a dominant mineral in the Earth's transition zone (400-660 km deep), can accommodate large amounts of water in its structure as OH^-. By characterising the effects that water has on the wadsleyite structure it should be possible to look for evidence of mantle hydration in seismological studies of the transition zone because seismic wave velocities are sensitive to mineral physical properties.

a. *New insights into hydrous wadsleyite from polarized FTIR spectroscopy and X-ray diffraction (S.D. Jacobsen, S. Demouchy, D.J. Frost and T. Boffa Ballaran)*

Wadsleyite (β-Mg_2SiO_4) and ringwoodite (γ-Mg_2SiO_4), have the potential to store more "water" as hydroxyl $(OH)^-$ in Earth's transition zone (410-520 km) than is currently present in

the liquid oceans. Wadsleyite has an extraordinary affinity for H due to an unusual non-silicate oxygen (O1) in its structure. This oxygen site is coordinated to only five Mg atoms and has a Pauling bond strength about half-way between a normal oxygen and a hydroxyl group.

A systematic study of hydrogen incorporation into pure-Mg wadsleyite was made using polarized FTIR spectroscopy and X-ray diffraction on oriented single crystals. The new suite of well-ordered hydrous wadsleyite samples was synthesized in the 1200- and 5000-ton multianvil presses at 16 GPa and 1300ºC from mixed oxides (with water added as brucite), resulting in single crystals up to 1 mm in length. The hydrogen content of the samples, estimated from the infrared spectra, spans three orders of magnitude, with ~ 100, 2500, and 10,000 ppm wt. H_2O (using the Paterson calibration for polarized spectra). Our attempts to synthesize anhydrous wadsleyite from synthetic forsterite resulted in water contents of no less than 100 ppm wt. H_2O.

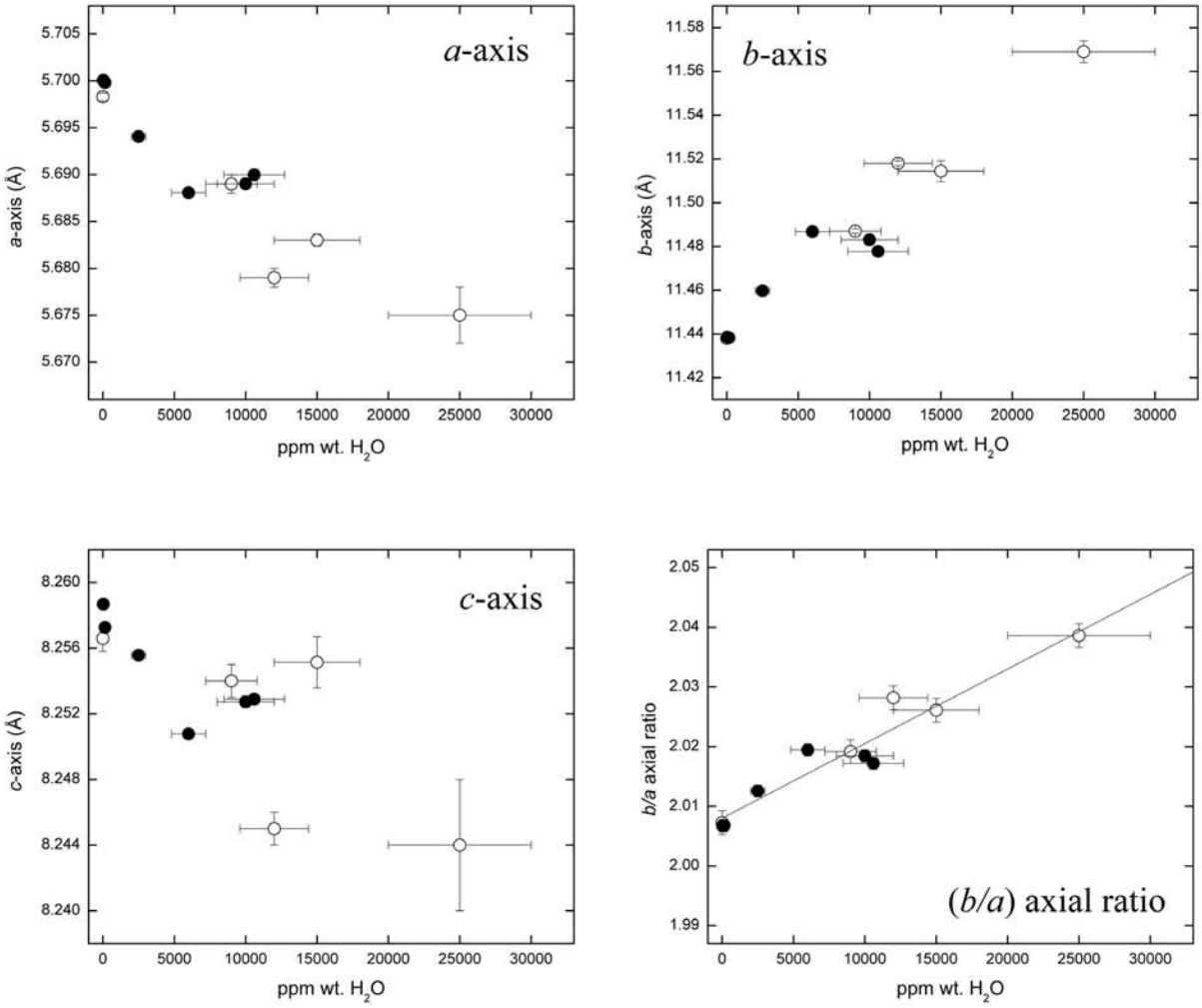

Fig. 3.6-1: Unit cell parameters of wadsleyite from this (solid symbols) and other studies (open symbols).

Figure 3.6-1 shows the cell parameters of wadsleyite from this and other studies. The volume of hydration for wadsleyite is surprisingly small, with ΔV ~ 0.1 % for 1 wt.% (10,000 ppm wt.) H_2O, and to date a reliable calibration for water (based on the cell parameters) has not been deduced due to an insufficient number of data points and the large absolute uncertainties associated with comparing cells from different single-crystal diffractometers (*i.e.* wavelengths). The systematic errors can be avoided by calibrating the IR-water content against the axial ratio *b/a*. This ratio was chosen because the *b*-axis is increasing while the *a*-axis is decreasing (and *c* shows the most scatter). Furthermore, the axial ratio should be independent of the local instrument. The resulting semi-quantitative calibration for water in wadsleyite is,

$$C_{\mathrm{H2O}} = \frac{(b/a) - 2.008(1)}{1.3(1)\times 10^{-6}}$$

where C_{H2O} is the water content in ppm H_2O by weight (Fig. 3.6-1).

The structure of wadsleyite containing about 100, 2500, and 10,000 ppm water by weight was refined from single-crystal X-ray diffraction data (Fig. 3.6-2). There are three different octahedral (M) sites occupied by magnesium, and one Si_2O_7 sorosilicate group. The non-silicate oxygen site, labeled O1, is coordinated to five M3 sites. We observe 3.5 % and 7.2 % cation vacancy at this site on hydration to 2500 and 10,000 ppm, respectively. The results confirm that the dominant hydration mechanism is protonation of O1, with one M3 vacancy for every 2 H introduced, or more generally, $Mg_{1-2x}H_{2x}SiO_3$.

Three crystals of each composition were oriented and double-polished to 15-50 μm thickness for polarized FTIR spectroscopy. The absorption spectra (Fig. 3.6-2) display at least five strongly pleochroic bands in the O-H stretching region. In the most hydrous samples, the pair at 3360 and 3326 cm^{-1} dominate when the dielectric vector (E) is parallel to [001] and [100], but with E// [010] a new peak at 3317 cm^{-1} replaces the one at 3326 cm^{-1}, while the band at 3360 cm^{-1} remains. In the least hydrous sample, the band at 3360 cm^{-1} is not present and the pleochroic pair is at 3324 and 3317 cm^{-1}. This group likely corresponds to protonation of O1, with the O-H dipole pointing either in the [001] direction, or along the oblique M3 octahedral edge.

The polarized absorption spectra for wadsleyite are also strongly pleochroic in the *a*-*b* plane. With E// [100], the spectra feature a band at 3614-3619 cm^{-1}, alternating with a band at 3579-3581 cm^{-1} when E// [010]. In summary, the results suggest that rather than H positions occupying the M-site cavities (as has been suggested), the hydrogen bonding is dominantly along M-site octahedral edges (as in ringwoodite) running parallel or perpendicular to *a* and *b*. While FTIR provides important information on O-H stretching directions, ultimately, only a single-crystal neutron diffraction study of hydrous wadsleyite will confirm the protonation sites in this important mantle phase.

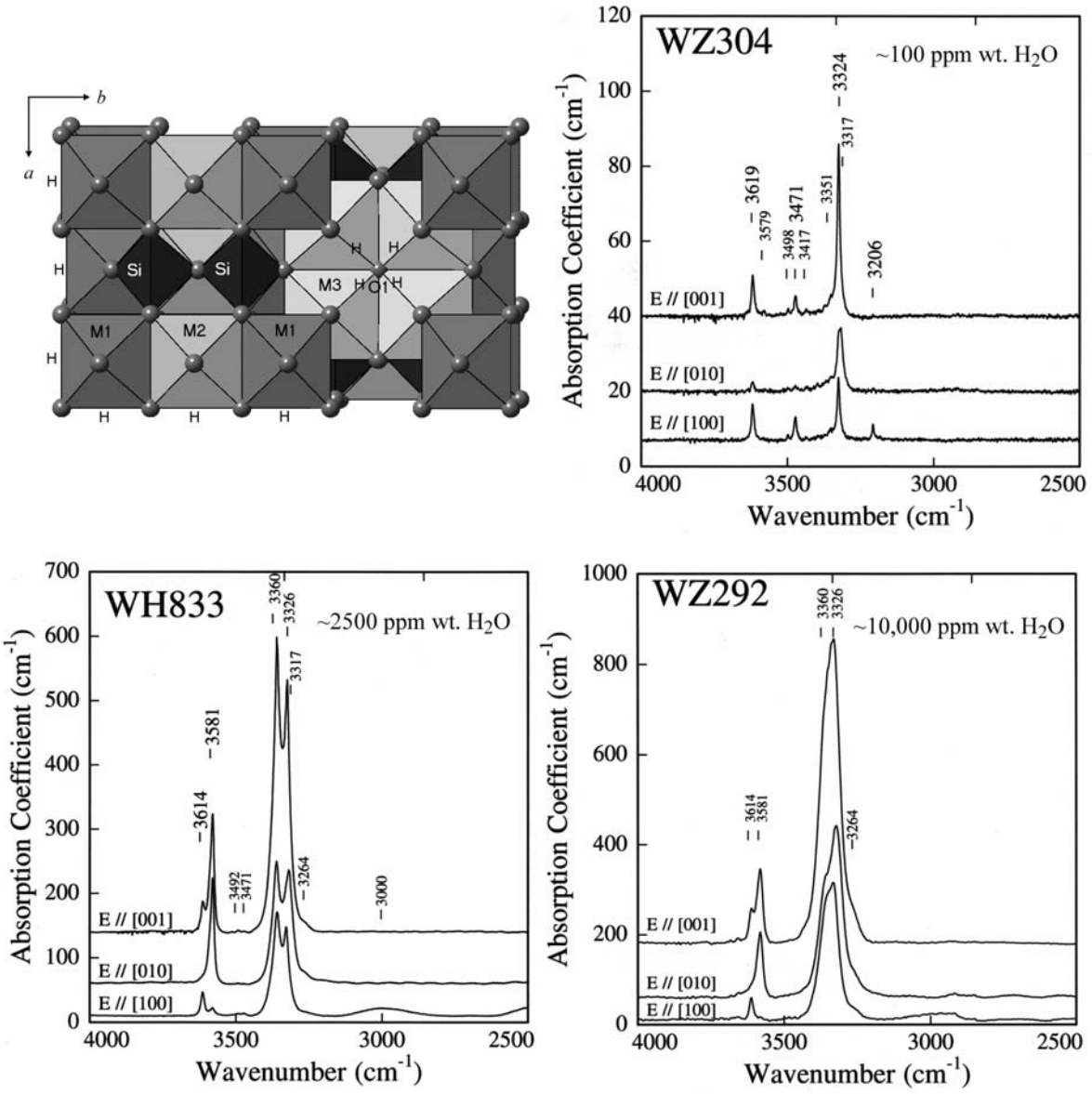

Fig. 3.6-2: The structure and polarised FTIR absorption spectra of hydrous wadsleyite.

b. *Computer simulation of hydrogen in iron-free wadsleyite (S. Demouchy, in collaboration with A. Walker and K. Wright/London)*

In this study, the General Utility Lattice Program (GULP) has been used to simulate the formation of various point defects in wadsleyite, to examine the relationship between hydrogen incorporation and vacancies and to calculate the corresponding infrared frequencies. The computer calculations were performed at The Royal Institution (Davy Faraday Research Laboratory) in London. In contrast to methods based on Density Functional Theory (DFT), GULP models solids using semi-empirical parameterized potentials. It is able to calculate various physical and chemical properties of 3-dimensional crystals and point defects using the

Mott-Littleton method (Fig. 3.6-3). An important difference between them is that a DFT calculation is extremely time-consuming compared to a GULP calculation.

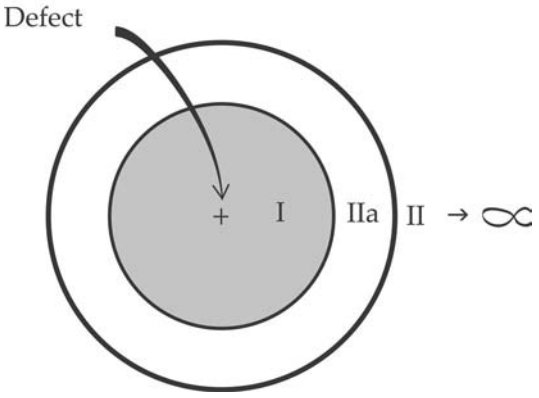

Fig. 3.6-3: The Mott-Littleton method considers that the defect is embedded in an infinite di-electric continuum, with atoms close to the defect considered explicitly. The defective crystal is therefore described using 3 spheres. The first one, close to the defect is called region I and is composed of approximately 1200 atoms where energies are calculated for a relaxed and modified lattice. The sphere a long way from the defect and extending to infinity is called region II. Finally, the intermediate sphere is called IIa and links region II and I.

The types of defect considered were vacancies on the various oxygen and magnesium sites and also vacancies on the silicon site. Furthermore defects associated with hydrogen were also considered, such as interstitial protons bonded to oxygen, hydroxyl incorporated within magnesium vacancies and also hydrated silicon vacancies. The most favourable hydroxyl related defect energies were:

Defect	Defect energy (eV)	Defect	Energy (eV)	Frequency (cm^{-1})
V''_{Mg1}	24.17	$(OH)^{\bullet}_{(01)}$	15.33	3848
V''_{Mg2}	25.15	$\left[V_{Mg1}.(OH)_{(04)}.(OH)_{(04)}\right]^{X}$	53.64	3761-3740
V''_{Mg3}	24.48	$\left[V_{Mg2}.(OH)_{(01)}.(OH)_{(02)}\right]^{X}$	53.83	3833-3743
$V^{\bullet\bullet}_{O1}$	24.44	$\left[V_{Mg3}.(OH)_{(01)}.(OH)_{(03)}\right]^{X}$	53.17	3768-3735
$V^{\bullet\bullet}_{O2}$	26.17	$\left[V_{Si}.(OH)_{(03)}\right]'''$	112.80	3983
$V^{\bullet\bullet}_{O3}$	25.35	$\left[V_{Si}.(OH)_{(04)}.(OH)_{(04)}\right]''$	123.80	3860-3809
$V^{\bullet\bullet}_{O4}$	25.11	$\left[V_{Si}.(OH)_{(04)}.(OH)_{(04)}.(OH)_{(03)}\right]'$	135.56	3864-3708-3907
V''''_{Si}	102.98	$\left[V_{Si}.(OH)_{(04)}.(OH)_{(04)}.(OH)_{(03}.(OH)_{(02)}\right]^{X}$	175.18	3519-3719-3394-2201

In the anhydrous system the V_{Mg1} is the most stable magnesium vacancy. However, because O1 is the most favourable site to fix hydrogen, Mg3 rather than Mg1 becomes the most favourable site for magnesium vacancies in the hydrous system. We have also made the first calculation of the energy required for the incorporation of hydroxyl into a silicon vacancy.

GULP permits a rapid evaluation of defect energies in dry and hydrous wadsleyite and the results are in fair agreement with DFT results. Unfortunately, simulations using either GULP or DFT do not yet provide infrared frequencies that are in good agreement with those measured for hydrous wadsleyite. Computer simulations are definitively helpful for the study of hydrous structures but are not yet powerful enough to permit simulation of complete infrared spectra. However, the continual improvement in simulation methods and computer capacity will certainly permit such calculations in the future.

c. *An experimental investigation of H and minor element incorporation in rutile (G.D. Bromiley, N. Hilairet, C.A. McCammon, in collaboration with S. Klemme/Heidelberg and H. Keppler/Tübingen)*

Rutile is the most common, naturally occurring form of titanium oxide (TiO_2), and is found as an accessory mineral in many igneous and metamorphic rocks. It is commonly found in high-pressure and ultra-high-pressure eclogites, where modal percentages may reach several weight percent. Previous investigations have demonstrated that rutile is one of the most 'hydrous' nominally anhydrous minerals (NAMs) so far described, and natural rutile can contain up to 0.8 wt.% H_2O, in the form of structurally-bound H. Rutile has a relatively simple tetragonal structure, with each Ti^{4+} ion surrounded by six oxygens at the corners of a slightly distorted, regular octahedron, and so it provides a useful model for considering some of the effects of H incorporation in NAMs. In addition, rutile is isostructural with stishovite, and investigation of H incorporation in rutile can be used to constrain the capacity of stishovite to incorporate trace amounts of H in the lower mantle.

In the present investigation, we have synthesized crystals of rutile doped with various trivalent and divalent cations to investigate the effects of composition on H incorporation. Samples were synthesized at 2.0 GPa, 1100 °C using piston-cylinder apparatus under water-saturated conditions, and have been analysed using FTIR spectroscopy, optical spectroscopy, Mössbauer spectroscopy and SIMS. Incorporation of minor oxides in rutile strongly effects the colour of the crystals. Pure TiO_2 rutile is colourless. However, rutile samples doped with Fe^{3+}, Cr^{3+} and Ti^{3+} are yellow, red-brown and blue, respectively. Figure 3.6-4a shows an electronic absorption spectrum obtained from a single crystal of rutile containing several wt.% Cr_2O_3. In the visible range, the spectrum consists of a large absorption band at 14300 cm^{-1}, and possibly another band at 19900 cm^{-1}. These absorption bands are probably due to spin allowed transitions in octahedrally coordinated Cr^{3+}, which implies that Cr^{3+} substitutes for Ti^{4+} on the octahedral site in the rutile structure. Figure 3.6-4b shows a Mössbauer

spectrum obtained from rutile containing several wt.% Fe_2O_3. The spectrum consists of a single quadrupole doublet, implying the presence of only Fe^{3+}, and with a center shift indicating an octahedral Fe^{3+} environment, again implying substitution of the trivalent cation for octrahedral Ti^{4+}.

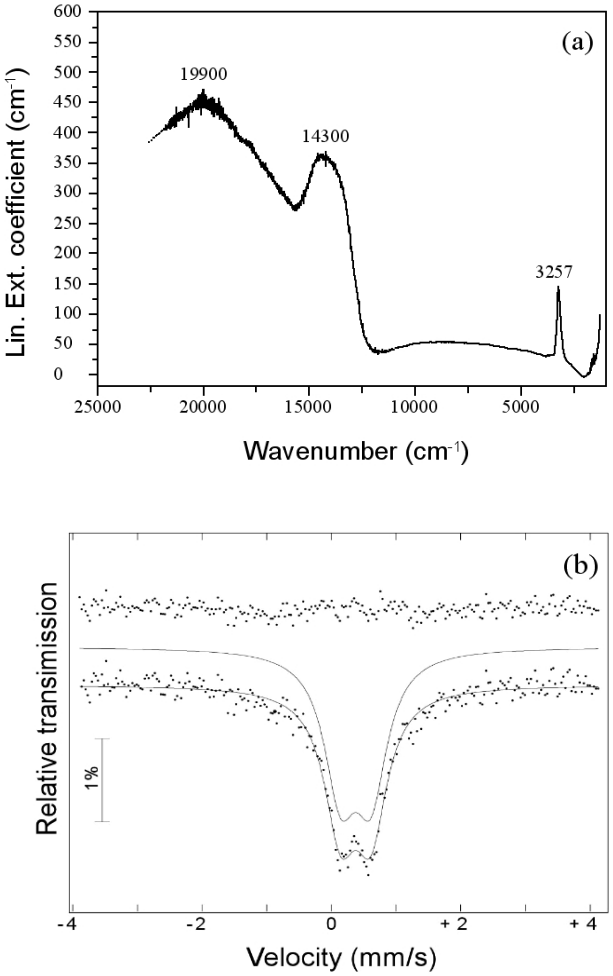

Fig. 3.6-4: (a) Electronic absorption spectrum obtained from Cr-doped rutile crystal. Absorption bands at 14300 and possibly also 19900 cm^{-1} are due to spin-allowed transitions in octahedrally-co-ordinated Cr^{3+}, accounting for the dark red-brown colour of the crystal. Absorption band at 3257 cm^{-1} is due to OH stretching (b) Mössbauer spectrum obtained from Fe^{3+}-doped rutile sample, consisting of a single quadrupole doublet due to octahedrally co-ordinated Fe^{3+}

Figure 3.5-5 shows FTIR spectra obtained from rutile doped with various minor elements. Spectra consist of a single OH stretching band. The wavenumber of this band varies significantly as a function of composition. This is consistent with a coupled substitution mechanism, where substitution of trivalent cations onto the octahedral Ti^{4+} site is locally charge-balanced by H incorporation onto one of the O sites surrounding the octahedral site (thereby forming a defect cluster). Calculated water contents for all samples are, however, at least one order of magnitude lower than minor oxide contents, implying that there must be another mechanism for charge-balancing trivalent cation substitutions. The most obvious mechanism would involve substitution of two trivalent cations on adjacent, edge-sharing octahedral sites, with an oxygen vacancy on one of the O sites on the shared edge. No evidence for the presence of cations on interstitial sites is found, which has been shown to be an important incorporation mechanism for lower valency cations in synthetic rutile grown at ambient pressure.

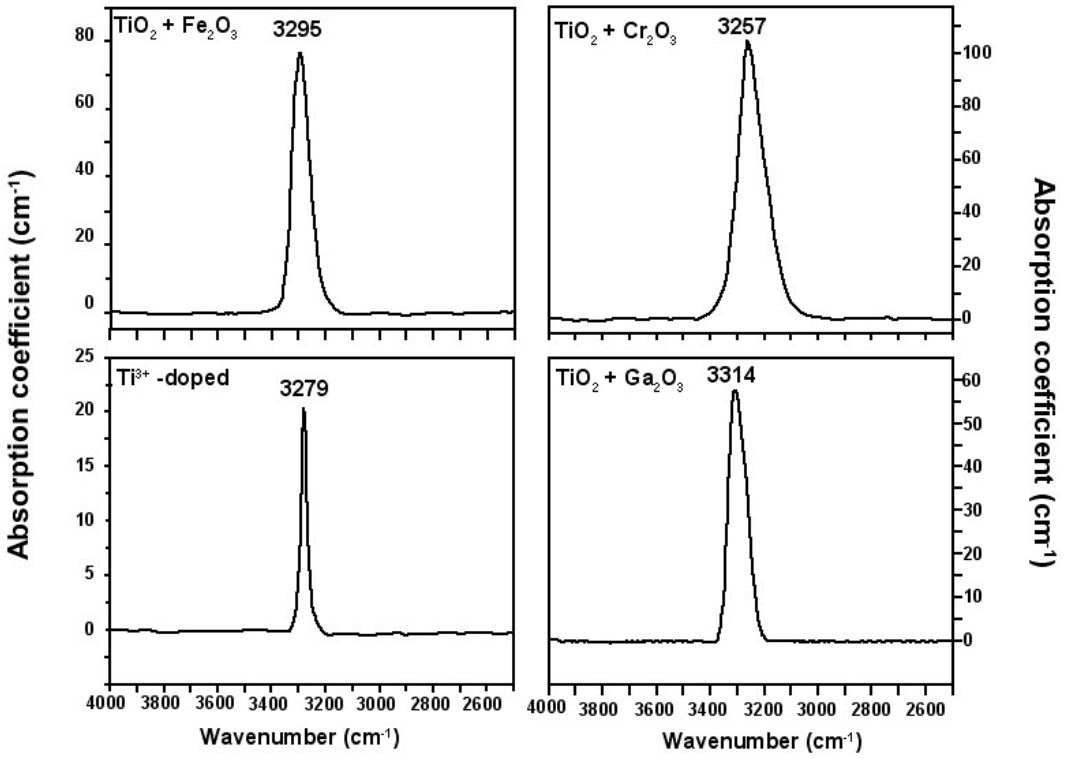

Fig. 3.6-5: Averaged FTIR spectra for synthetic, trivalent cation doped rutile synthesized at 2.0 GPa, 1100 °C under water-saturated conditions. Spectra consist of a single absorption band due to OH stretching, with the frequency of this band varying as a function of composition.

d. *H solubility in the system TiO_2 + Fe_2O_3: implications for the role of stishovite and post-stishovite phases in subducting oceanic crust in the lower mantle. (G.D. Bromiley, N. Hilairet and C.A. McCammon)*

Subduction of oceanic lithosphere provides a mechanism for transporting water deep into the Earth's interior. Beyond the stability of hydrous phases, trace amounts of water can be stored in a large number of nominally anhydrous minerals (NAMs). In subducting oceanic crust, NAMs could provide an effective mechanism for transporting water beyond the depths of sub-arc magmatism, and even into the lower mantle. Rutile is the most common naturally-occurring TiO_2 polymorph, and is an accessory mineral in many ultra-high-pressure (UHP) eclogites. H incorporation in rutile acts as a local charge-balancing mechanism for substitution of lower valency cations (*e.g.* Fe^{3+}) onto the octahedral (Ti^{4+}) site. Rutile is well-known for the great affinity which it shows towards H incorporation, and is one of the most 'hydrous' NAMs identified. With increasing pressure, rutile (tetragonal) breaks down to a phase with the α-PbO_2 structure (orthorhombic), known as TiO_2 (II). Phase transitions in TiO_2 are of considerable importance because the system may provide a lower pressure analogue for the silica system. Rutile is isostructural with stishovite, which is an important bulk mineral in

subducting oceanic crust under lower mantle conditions. Furthermore, coupled minor element and H substitution mechanisms in stishovite and rutile are probably similar; hence, investigation of rutile and TiO_2 (II) can provide information on the role of stishovite and post-stishovite phases in the lower mantle.

Samples of rutile and TiO_2 (II) doped with Fe_2O_3 were synthesized from 0.5 to 8 GPa and analysed using Raman spectroscopy, EMPA and Mössbauer spectroscopy, and H incorporation investigated using FTIR spectroscopy. All FTIR spectra from rutile consist of a single band at 3295 cm^{-1}. Absorption band anisotropy and the effect of pressure on water solubility in rutile (Fig. 3.6-6) suggests that H is incorporated in rutile as isolated OH groups, and is associated with Fe^{3+} substitution. However, FTIR spectra obtained from TiO_2 (II) contain no absorption bands over the wavenumber range 4000-2000 cm^{-1}, implying that the phase is completely anhydrous. Mössbauer spectra obtained from both rutile and TiO_2 (II) contain a single quadrupole doublet, implying the presence of only Fe^{3+}, with all iron on the octahedral (Ti^{4+}) site. In rutile, H incorporation acts as a local charge-balancing mechanism for Fe substitution. However, results suggest that the dominant mechanism for charge-balancing Fe substitution in both rutile and TiO_2 (II) involves the O vacancies. Despite the fact that it contains no H, Fe_2O_3 solubility in TiO_2 (II) is much higher than in rutile. This appears to have a marked effect on the stability of TiO_2 (II), and compared to the pure TiO_2 system, Fe-bearing TiO_2 (II) is stable to much lower pressures (Fig. 3.6-6).

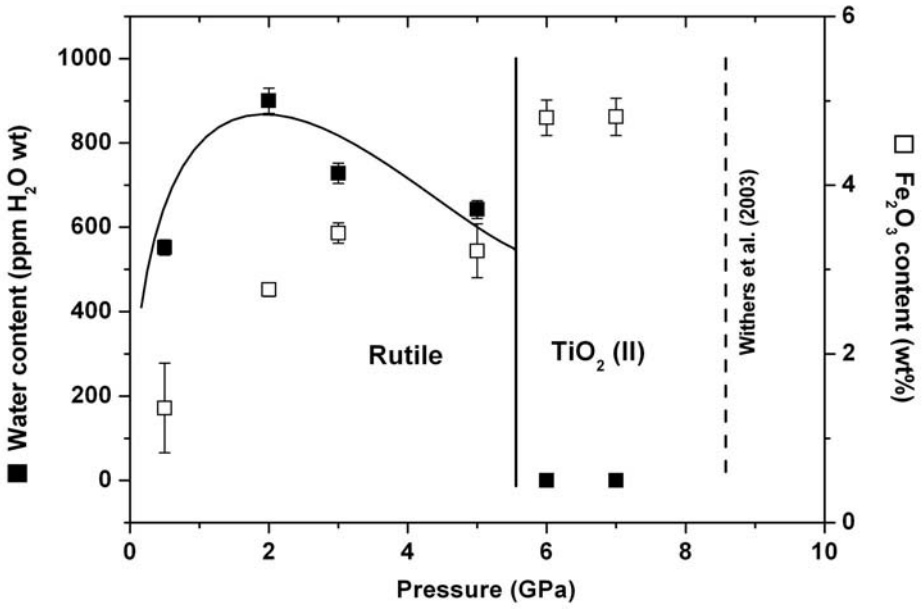

Fig. 3.6-6: Pressure dependence of water solubility (solid squares) and Fe_2O_3 content (empty squares) in rutile and TiO_2 (II). Data on water solubility in rutile is fitted to a general solubility law implying with H incorporation as isolated hydroxyl groups, consistent with a coupled substitution mechanism involving Fe^{3+} replacing Ti^{4+} on the octahedral site. Vertical lines indicate the rutile to TiO_2 (II) phase boundary in the present study (solid) and in the system TiO_2 [Withers *et al.* (2003) Contrib. Min. Pet. 145: 199-204]

In stishovite, H incorporation is charge-balanced by Al^{3+} substitution for octahedral Si^{4+}. Stishovite could act as an important repository for water in subducting oceanic crust in the lower mantle, and may provide a mechanism for water transport deep into the lower mantle. At approximately 50 GPa, stishovite undergoes a phase transition to a $CaCl_2$-type structure, and then at higher pressures, to a phase with the α-PbO_2 structure (*i.e.* isostructural with the TiO_2 (II) phase). This high-pressure phase of silica may be stable close to the core-mantle boundary. Data on water solubility in rutile and TiO_2 (II) can therefore be used to place constraints on the possible role of silica in subducting oceanic crust under lower mantle conditions. Substitution of Fe^{3+} onto octahedral Ti^{4+} sites in rutile and TiO_2 (II), charge balanced by O vacancies, has a strong effect on the stability of the two phases. By analogy, Al substitution in silica polymorphs may influence phase stability, and may make the appearance of α-PbO_2 structured silica at the base of the lower mantle more likely. This effect may be heightened in silica, because the difference in ionic radii between octahedrally co-ordinated Si^{4+} and Al^{3+} (13.5 pm) is larger than that between octahedrally co-ordinated Ti^{4+} and Fe^{3+} (9.0 pm). The phase transition from rutile to TiO_2 (II) has a marked effect on water solubility in the system. A similar effect in silica could result in a significant dehydration event in subducted oceanic crust at the base of the lower mantle, and throughout geological history, would provide an effective mechanism for hydration of the lower mantle.

e. *Hydrogen solubility and speciation in natural, gem-quality Cr-diopside (G.D. Bromiley, C.A. McCammon, F.A. Bromiley and S.D. Jacobsen, in collaboration with H. Keppler/ Tübingen)*

Determination of water solubility in minerals stable in subducting oceanic lithosphere is vital for understanding the capacity for subducting slabs to act as repositories for water, and elucidating an important part of the internal water cycle of the Earth. Examination of ultrahigh pressure (UHP) terrains can provide us with important constraints in determining which minerals may play a role in terms of water storage during subduction of oceanic lithosphere. Beyond the stability of hydrous minerals, water can be stored in nominally anhydrous minerals in the form of structurally-incorporated hydrogen. The clinopyroxene omphacite, a diagnostic mineral and one of the main constituents of UHP eclogites, has been shown to be capable of storing up to several thousand ppm H_2O at high pressures. However, despite the possible importance of water incorporation in omphacite, no experimental investigations of water solubility have been conducted. This is largely because of the complex crystal chemistry of omphacite and the difficulties involved with synthesizing large, homogeneous crack- and inclusion-free crystals. In order to provide data on water solubility in such minerals, we have developed a new technique for performing long duration (up to 300 hours) high-pressure annealing experiments under water-saturated conditions. This technique has been used to investigate water-solubility and speciation in natural, gem-quality Cr-diopside. The capsule design for the technique is a variant of the double-capsule technique, and relies on the use of a semi-permeable Pt membrane, which permits free hydrogen

diffusion into samples, but protects samples from reacting with buffer mixtures. Samples are recovered as large (up to several mm in all directions), crack- and inclusion-free crystals, and water incorporation can be investigated using polarised FTIR spectroscopy.

The investigation of a natural single crystal of Cr-diopside revealed a very unusual annealing behaviour: water contents increase sharply after short annealing times, and then decrease slowly to some metastable equilibrium value (Fig. 3.6-7). The main process that takes place during annealing experiments is hydrogen diffusion coupled with Fe^{3+} reduction.

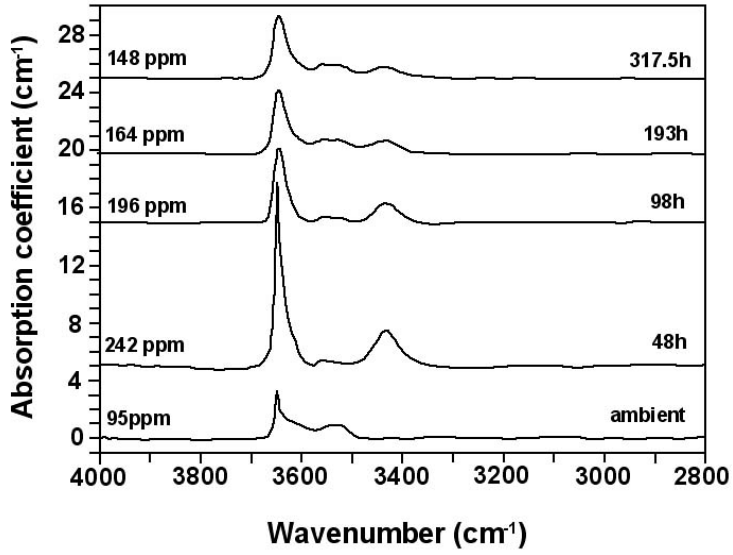

Fig. 3.6-7: Averaged fully-polarised FTIR spectra obtained from Cr-diposide samples annealed at 1.5 GPa, 1100 °C under NNO buffer conditions for increasing amounts of time (offset vertically). Run durations and calculated water contents for each annealed sample are given.

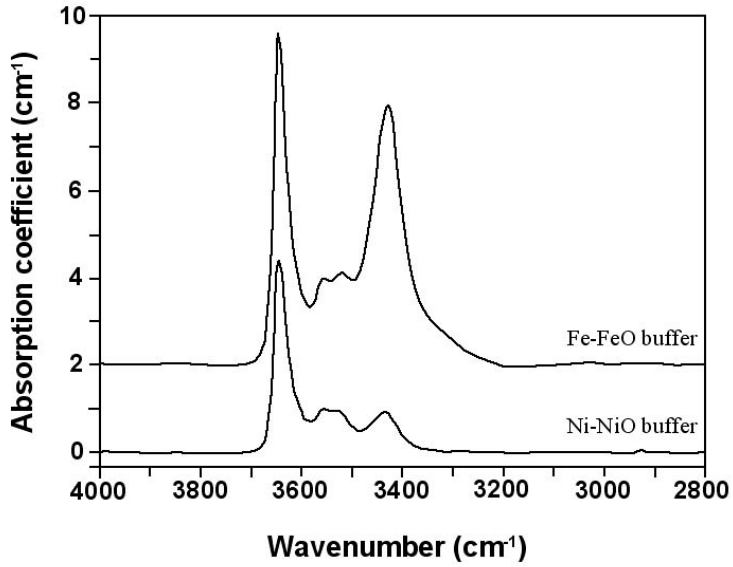

Fig. 3.6-8: Averaged, fully-polarised FTIR spectra obtained from Cr-diopside samples annealed at 1.5 GPa, 1100 °C under different buffer conditions. The ratio of peak heights for the two dominant absorption bands between the two samples changes considerably as a function of fO_2. However, this peak ratio is the same for samples annealed under the same buffer conditions but different pressures, implying that it does not vary as a function of fH_2O.

This essentially reverses the main mechanism for hydrogen loss from mantle samples during exhumation, and the technique therefore provides sample-specific information on original water contents. Absorption bands at 3646 and 3434 cm^{-1} in IR spectra from annealed samples suggest two main mechanisms for hydrogen incorporation in the diopside: [1] incorporation of hydrogen onto the O2 site, with vibration of the OH dipole in the direction of a nearby O3 site (along the edge of an M2 site), and [2] incorporation of hydrogen onto the O2 site with vibration of the OH dipole towards a nearby O1 site (along a shared M1-M2 edge) or O2 site (along the edge of an M1 site). The ratio of peak heights between the absorption bands at 3646 and 3434 cm^{-1} is independent of water fugacity but dependent on oxygen fugacity (Fig. 3.6-8), and appears to provide a measure of the redox state 'frozen' into the sample. This ratio could be used to determine whether pyroxenes from upper-mantle xenoliths had experienced concurrent hydrogen-loss and oxidation during exhumation.

f. *Dehydration profiles in oriented xenolithic olivine from Pali-Aike, Patagonia (S. Demouchy, S.D. Jacobsen, in collaboration with S.J. Mackwell/Houston and C. Stern/ Boulder)*

Hydroxyl concentration profiles in single-crystal olivine from mantle xenoliths entrained in the Pali-Aike basalt flows of southern Patagonia (Chile) were measured using polarized infrared spectroscopy. Gem-quality crystals of Fo_{90}-olivine, measuring up to several millimetres in size, were extracted from a fresh xenolith (garnet-lherzolite sample LS33) and oriented to within ± 1º using a single-crystal X-ray diffractometer. The crystals were doubly-polished perpendicular to [010], and infrared absorption profiles were measured with the electric vector (E) parallel to [100] and [001]. Figure 3.6-9 shows a three-dimension profile with E // [100] at various positions along the [100] direction. The spectra taken closest to the grain boundary show hydroxyl-depleted rims, indicating that a natural dehydration profile is preserved.

Previous work has shown that the *b*-axis or [010] direction exhibits intermediate diffusion rates, between that of the fast [001] direction and the slow [100] direction at the same temperature. Therefore, we prepared *b*-axis plates in order to measure the infrared profiles along the two most extreme directions. Calculated diffusion profile (Fig. 3.6-10) with a classical one-dimensional diffusion equation indicates that the diffusion coefficient along [001] ($2x10^{-12}$ m^2 s^{-1}) is only moderately faster than in [100] direction ($1x10^{-12}$ m^2 s^{-1}) for a calculated duration time of 19 hours. The diffusion coefficients in these natural samples are in good agreement with previous experimental results from controlled hydration and dehydration experiments at high pressures and temperatures. The results confirm the presence of water as hydroxyl in natural olivine from Earth's uppermost mantle and show that under the right conditions, evidence for natural dehydration processes can be preserved in the $(OH)^-$ concentrations and measured using FTIR spectroscopy. Further work involving the full three-dimensional diffusion equation will permit us to place tighter constraints on the dehydration history of these xenoliths, including possibly ascent rates in the host basalt.

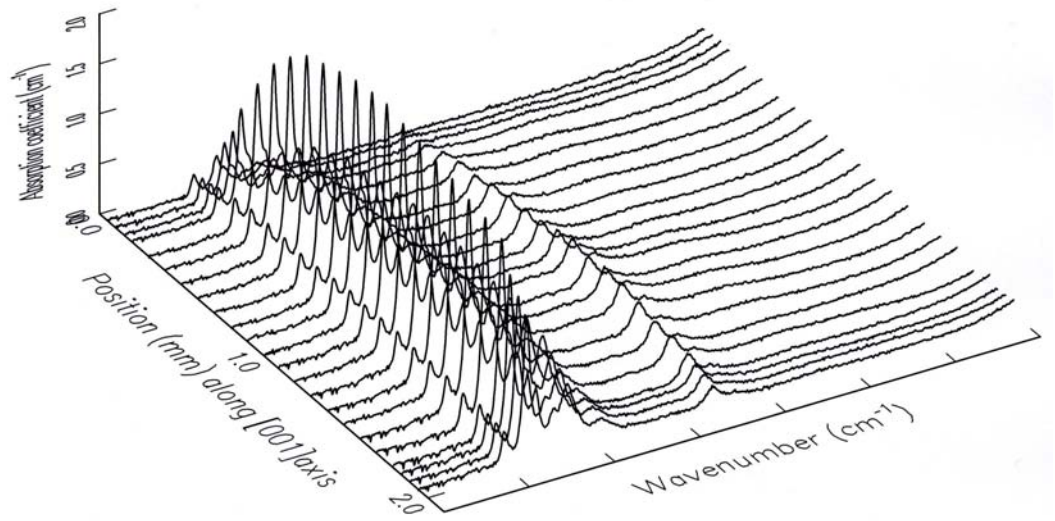

Fig. 3.6-9: Series of polarized infrared spectra with E // [100] at various positions along the [100] direction. The $(OH)^-$ concentration is most depleted at the grain boundaries, indicating the preservation of a natural dehydration process.

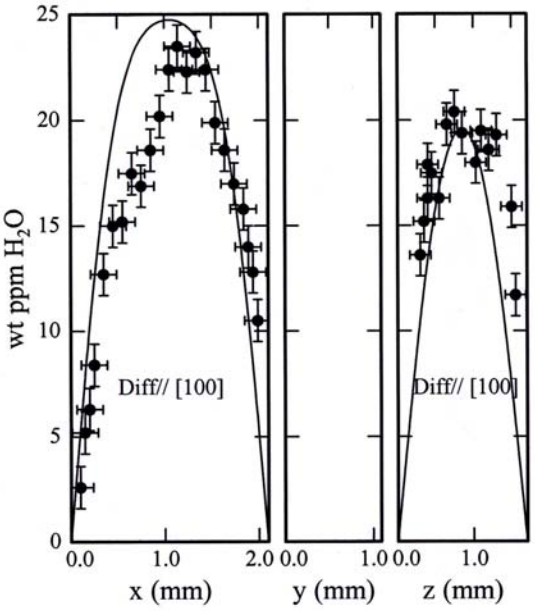

Fig. 3.6-10: Water content as a function of position along [100] and [001] directions with E // [100]. The profiles from this natural sample confirm previous experimental results indicating that diffusion is faster along [001] than [100].

g. *The influence of water and oxygen fugacity on the oxidation state of iron in a ferrobasaltic system (C.A. McCammon, in collaboration with R. Botcharnikov, J. Koepke and F. Holtz/ Hannover)*

The Skaergaard intrusion (Greenland) is a spectacular body of intrusive igneous rock. The magma crystallised slowly to produce a layered structure, which has formed the basis of numerous studies to investigate different models and mechanisms of magma differentiation.

Knowledge of the phase relations are crucial to such studies, and several laboratory investigations have been already made using the "SC1" composition, the assumed parental liquid of the intrusion. These studies were made under dry conditions, however, and since it has been suggested that the parental magmas of all plutonic bodies were wet, we were motivated to study the effect of water and oxygen fugacity on the phase relations and differentiation of hydrous magma systems.

We investigated a ferrobasaltic system with "SC1" composition. Crystallisation experiments were performed in an internally heated pressure vessel equipped with a rapid quench facility and Shaw membrane to determine the prevailing oxygen fugacity within the sample capsule. Water activity was varied by changing the H_2O/CO_2 ratio in the fluid phase. Preliminary results show that water influences not only the liquidus temperatures and temperature interval of mineral crystallisation, but also the sequence of crystallising minerals compared to the dry system. Since water solubility strongly depends on pressure in the pressure range 200-300 MPa (storage conditions of Skaergaard magma), the water activity may change significantly as a result of convection. Thus convection has the potential to produce significant differences in stability and proportions of the prevailing minerals, which may contribute to the complex layering of the Skaergaard intrusion.

The quenched glasses were mounted in epoxy and examined using Fourier Transform Infrared Spectroscopy (FTIR) and Mössbauer spectroscopy to determine the water concentration and the oxidation state of iron. Results show that $Fe^{3+}/\Sigma Fe$ is a positive function of water activity and has a non-linear dependence on water mole fraction in the fluid at 1200 °C. The influence of increasing oxygen fugacity to increase $Fe^{3+}/\Sigma Fe$ is similar in the hydrous system compared to dry melts, and suggests that existing models can be used to extract oxygen fugacities based on measured $Fe^{3+}/\Sigma Fe$ values, provided the water concentration of the melt is known.

h. *Mapping water distribution in the Earth's mantle by combining geophysical and laboratory methods (F. Gaillard, F.A. Bromiley, G.D. Bromiley, D.C. Rubie and B.T. Poe/ Rome)*

Laboratory investigations indicate that the incorporation of water into mantle minerals such as olivine strongly affects the mantle's rheology and melting temperature. Consequently, the tectonic and volcanic manifestations of the Earth are partly dominated by the water distribution in the mantle. Mapping the water content of the mantle in different tectonic settings would provide a very valuable insight into the dynamics of the Earth's interior. Recent investigations on natural mantle rocks sampled at the surface reveal that olivine contains water, but has undergone a partial dehydration during ascent to the surface. Estimating mantle water contents from analyses of natural olivine is therefore tentative. An alternative would be the use of *in situ* remote measurements of mantle properties provided by geophysical techniques, such as electrical conductivity. The electrical conductivity of olivine,

which reveals the number and the mobility of charge carriers, is likely to be strongly modified by incorporation of fast moving species such as hydrogen, the mobile form of water. Laboratory measurements of electrical conductivity of water-bearing olivine should therefore allow an interpretation of variations in the electrical properties of the mantle in terms of water distribution within the interior of the Earth.

The effect of water content on electrical conductivity of olivine can be anticipated through the Nernst-Einstein equation, here simplified as:

$$\sigma \sim \sigma^{ol}_{dry} + D_H [H]$$

σ^{ol}_{dry} is the conductivity of a dry olivine and D_H and [H] refer respectively to the self diffusion coefficient and the concentration of hydrogen in olivine. The chemical diffusion of hydrogen in olivine has been widely studied, but the self-diffusion of hydrogen is still unknown; the difference between the two migration rates might be of several orders of magnitude. This difference between chemical and self-diffusion has been ignored in previous studies, and it is very likely that previous interpretations of mantle conductivity are consequently flawed.

In this study single and polycrystalline olivine samples are being synthesised at pressure under hydrous conditions. These hydrated crystals are then inserted into a conductivity cell. Conductivity measurements are performed in the internally heated pressure vessel and piston cylinder apparatus at the BGI under low temperature conditions to avoid dehydration of the sample. The resultant Arrhenius law will allow an extrapolation of the electrical conductivity to higher temperatures.

3.7 Physics and Chemistry of Melts and Magmas

Melting and migration of magma within the Earth have been responsible for extensive mass transport and large-scale chemical differentiation during the past 4.6 billion years. Consequences of melting during the Earth's evolution include (1) formation of the Earth's core by metal-silicate segregation, (2) formation of the continental and oceanic crust by subduction-derived and mid ocean ridge magmatism respectively, and (3) formation of the atmosphere by exsolution of volatiles from magma at or close to the Earth's surface. In order to understand the role of magma transport in differentiation of the Earth requires a multi-scale experimental approach to determine the transport properties of melts and how these depend on pressure. Thus, experimental measurements are required over a broad range of pressures and temperatures, including extreme conditions.

An immediate consequence of magmatic activity is the menace associated with explosive volcanic eruptions. The potentially explosive nature of an eruption is related to volatiles, mainly water, dissolved in the magma prior to eruption and their release during the eruption. The knowledge of how much water can be dissolved in magma, how it is incorporated in the molecular structure of the liquid and how degassing of this water occurs during the ascent of the magma towards the Earth's surface are currently major scientific questions. These issues are of critical interest for human populations that are exposed to volcanic risks.

A significant proportion of the studies reported here are devoted to investigating transport properties of melts under conditions ranging from low to very high pressures. Important new measurements on diffusion and viscous flow properties of peridotite liquid at mantle pressures are presented. The results reveal the critical role of liquid composition and the importance of considering the effect of pressure on viscous flow behaviour in a deep magma ocean that likely formed during the early history of the Earth. The results have implications for large-scale global processes such as the formation of the Earth's core and early differentiation of the Earth through crystallization of a magma ocean. The effect of the component H_2O on the viscosity of melt at high pressure is also addressed. This work brings into agreement the pressure effect on the viscosity of the polymerized vs. depolymerized melts. Transport properties of magmas at crustal pressures are also investigated. The degassing rate of water from a phonolite lava from Vesuvius as a function of the magma ascent rate is elucidated. Significant disequilibrium during rapid magma ascent occurs and implies that magmas can be strongly over-saturated in volatiles at shallow levels. Explosive eruptions can thus occur through the delayed and sudden release of volatiles from the magma near the surface. The effects of water and crystal content on the electrical conductivity of silicate melts have been determined, and allow the electrical signature of molten regions, as determined by geophysical methods, to be interpreted in terms of water content and extent of crystallization in the magma chamber. The interpretation of macroscopic measurements of silicate melt properties requires also an understanding of the molecular structure of melts and how structure varies with pressure and temperature. Structural characterization requires the use of

vibrational spectroscopic methods, which are usually performed on glasses, as structural analogs of melts. The speciation of water and boron in silicate melts, addressed, below is important for understanding the products of granitic magmatism, in particular late-stage ore deposits. Finally, the molecular scale structural adjustments that occur in response to an increase in pressure are assessed in the last two contributions. Increases in the coordination number of Si and Al, the two dominant network formers of a silicate melt, are observed with increasing pressure. Such observations form the basis for explaining the effects of pressure on the density and viscosity of melts.

a. *Viscosity of a magma ocean (C. Liebske, B. Schmickler, H. Terasaki, D.C. Rubie, in collaboration with A. Suzuki and R. Ando/Sendai, K. Funakoshi/Hyogo and B.T. Poe/Rome)*

According to models for the accretion of the Earth, a deep terrestrial magma ocean formed as a result of bombardment by asteroids and planetesimals and/or due to one or more giant impact events. Therefore, many early differentiation processes, possibly including the formation of the Earth's core by metal-silicate separation, would have been strongly dependent on the viscosity of a bulk silicate Earth composition (*e.g.* pyrolite). In this study we present new experimental viscosity data on a liquid pyrolite composition up to 6.9 GPa and 2283 K. Using these data we have extrapolated the viscosity of a deep terrestrial magma ocean to around 800 km depth.

Falling sphere viscometry has been performed on beam line BL04B1 at the SPring-8 synchrotron radiation facility in Japan. This beam line combines a high-pressure 1500 tonne multianvil apparatus with an X-ray shadowgraph imaging system and enables the descent of a small metal sphere through silicate melt to be observed in real time. Knowing the falling velocity of the sphere, the viscosity of the melt at high pressures and temperatures can be calculated using Stoke's law. The main problems associated with falling sphere viscometry on pyrolite liquid are the very low viscosity of the highly depolymerised melt (NBO/T=2.5) and the broad temperature interval between solidus and liquidus (~ 400 °C at 2.5 GPa). As a consequence, even at the highest possible heating rate the sphere starts to fall before a stable temperature above the liquidus can be established. This implies that, at a given pressure, the viscosity cannot be measured as function of temperature. To circumvent these problems, a new capsule design has been developed in order to delay the descent of the sphere until the desired temperature has been reached. The pressure cell and a close-up of the sample container are shown in Fig. 3.7-1.

The goal of the stepped Mo-capsule is to initially locate one rhenium sphere outside the hotspot of the furnace and additionally to embed it in a mixture of forsterite and enstatite with the same Mg/Si ratio but a higher melting temperature than the pyrolite. The descent of this sphere is thus significantly delayed and two viscosities (for two spheres as shown in Fig. 3.7-1b) at different temperatures can be measured in a single experiment.

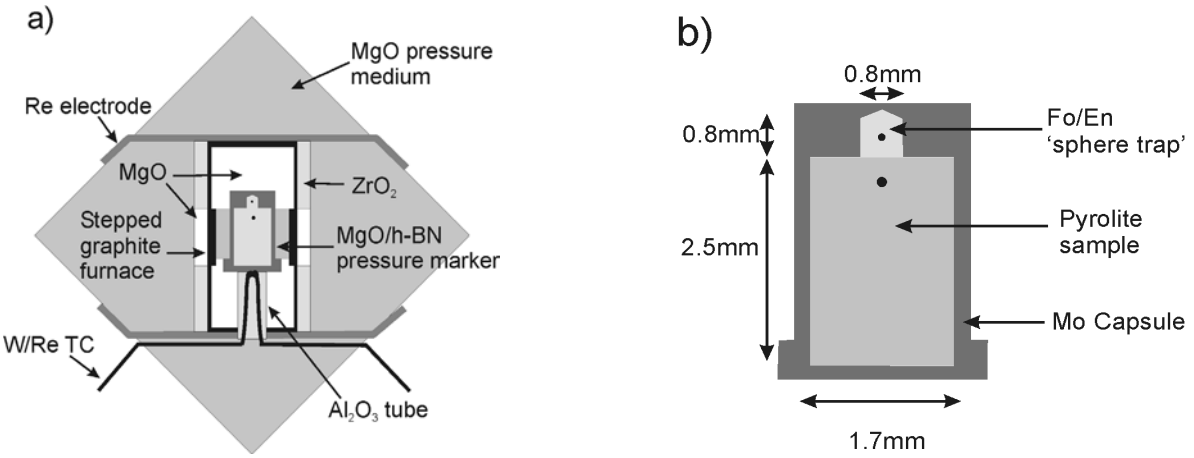

Fig. 3.7-1: a) 18 mm high-pressure multianvil viscosity cell used in falling sphere experiments. b) Close-up of the stepped Mo-capsule showing the initial location of the two rhenium spheres. The volume of the sphere trap is restricted to ~ 5 % of the total sample volume to minimize chemical contamination.

Results of the falling sphere viscometry experiments are plotted in Fig. 3.7-2. Measured viscosities range from 0.02 Pa s at 2.5 GPa, 2000 K to 0.13 Pa s at 6.0 Pa and 2243 K. To evaluate the effects of temperature and pressure on viscosity, an Arrhenius equation was fitted to the entire data set giving an activation energy E_a = 263(50) kJ/mol and an activation volume V_a = 6.7 (1.3) cm^3/mol. Compared to the more polymerised $CaMgSi_2O_6$ (diopside) liquid the viscosity of pyrolite is about one order of magnitude lower but shows a higher activation volume (V_a = 2.2 cm^3/mol for diopide) over the investigated pressure range.

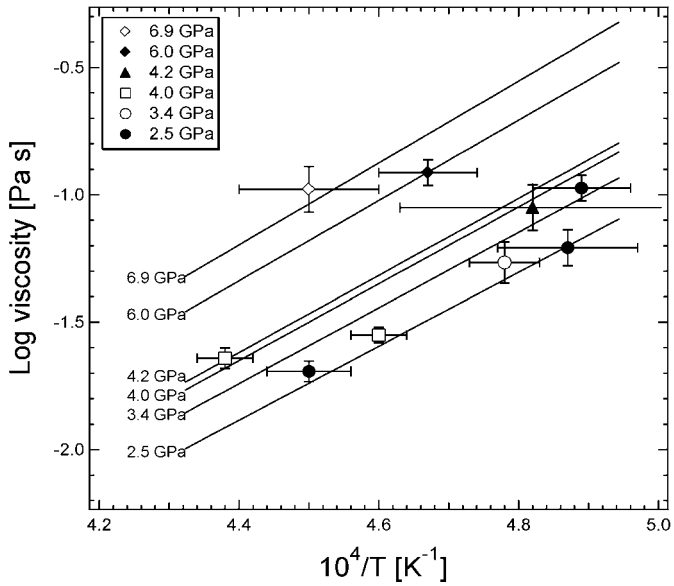

Fig. 3.7-2: Experimental viscosity data. Different symbols show results obtained at various pressures. Solid lines represent isobars calculated using the fit to the data set.

Our new experimental data have been used to estimate the effects of temperature and pressure on the viscosity of a deep terrestrial magma ocean. Assuming adiabatic behaviour, temperature has been calculated as a function of pressure up to 30 GPa (~ 800 km depth) for komatiite liquid as an analogue material (Fig. 3.7-3a). Using this temperature distribution and the fit to our data the viscosity of a deep magma ocean can be modelled. Results are given in Fig. 3.7-3b. The viscosity initially decreases to a minimum at 2-3 GPa but increases significantly at higher pressures when extrapolating our data (7-30 GPa). This is the result of the relatively flat temperature profile in this pressure range (Fig. 3.7-3a). For comparison an estimate for magma ocean viscosity given by Rubie *et al.* (2003) [EPSL, 205, 239] is also shown. This model is based on data for diopside liquid but neglects the effects of pressure on the viscosity. Depending on the activation volume calculated viscosities for both scenarios differ by more than three orders of magnitude at 30 GPa. These data indicate that the effect of pressure on the viscosity of pyrolite liquid is likely to be the most important parameter for controlling the viscous flow behaviour in a deep terrestrial magma ocean.

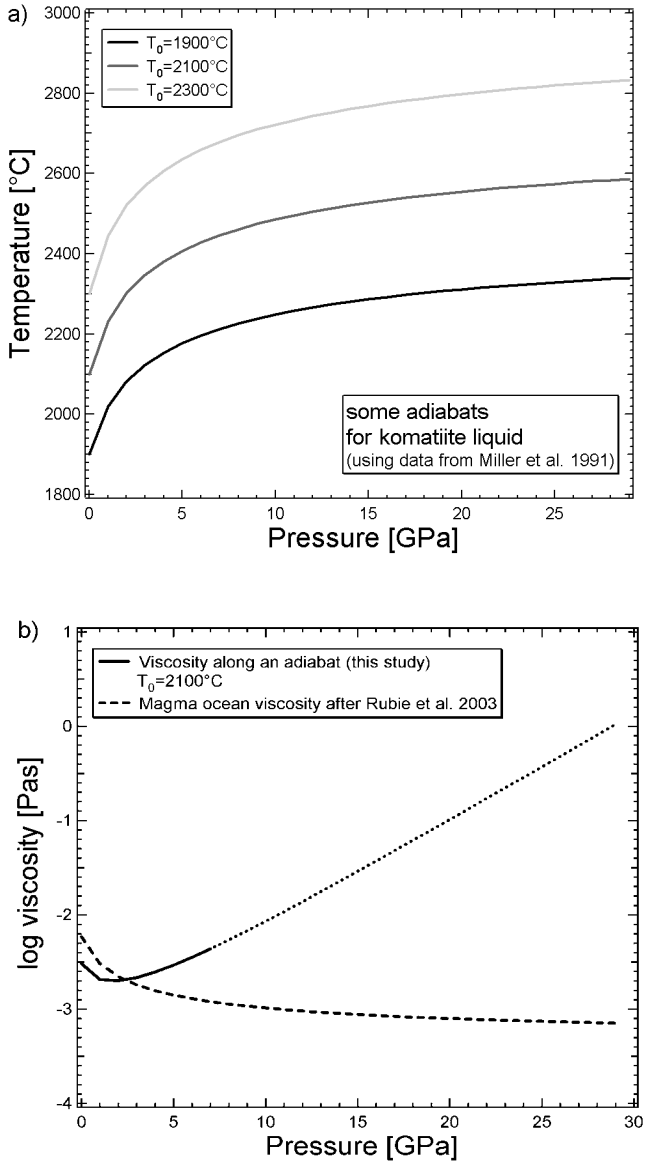

Fig. 3.7-3: a) Adiabats for komatiite liquid after Miller *et al.* (1991) [JGR, 96, 11831]. b) Viscosity of a magma ocean as function of pressure. Solid black lines (including dotted extensions) shows the viscosity along an adiabat. Dashed line represents calculations based on $CaMgSi_2O_6$ liquid.

b. *Self-diffusion in peridotite liquid at high pressure (B. Schmickler, D.C. Rubie and C. Liebske, in collaboration with B.T. Poe/Rome, J. Craven/Edinburgh and B. Patterson/Bristol)*

Knowledge of the effect of pressure on the transport properties of peridotite liquid is crucial for understanding deep Earth processes including the early physical and chemical evolution of the early Earth following formation of a deep magma ocean. For example, data on chemical diffusivities of siderophile elements (*e.g.* Ni and Co) in peridotite liquid at high pressure are required for modeling the kinetics of chemical exchange between metal and silicate liquid during core formation.

In order to investigate diffusion in peridotite liquid at high pressure, chemical and ionic self-diffusion experiments have been carried out at pressures between 4 and 15 GPa and temperatures between 1900 °C and 2300 °C using the 1200 t and 5000 t multianvil presses at the Bayerisches Geoinstitut. As starting material, powdered samples of (1) synthetic peridotite with naturally-abundant isotope contents and containing 1 wt.% Co and (2) synthetic peridotite enriched in ^{18}O (~ 15 %), ^{30}Si (~ 20 %), ^{44}Ca, ^{25}Mg and 1 wt.% Ni were used as starting materials for diffusion couples. Convection of the liquid was avoided by locating the denser, isotopically-enriched peridotite at the bottom of the capsule. To minimize diffusion during heating, a heating rate of > 40 °C/s was used. Depending on P-T conditions, the diffusion time at run temperatures was between 7 and 30 seconds. Diffusion that occurred during heating appears not to be a significant source of error for the estimated diffusion coefficients, as proved by zero-time diffusion experiments.

Quenched samples were analyzed for ^{16}O, ^{18}O, ^{28}Si, ^{29}Si, ^{30}Si, ^{44}Ca, ^{24}Mg, ^{25}Mg and ^{26}Mg using SIMS (Secondary Ion Mass Spectroscopy) at the University of Edinburgh. Co and Ni concentration profiles were determined with LA-ICP-MS (Laser ablation inductive coupled mass spectroscopy) at the University of Bristol. The initial concentrations were not preserved at the ends of the diffusion profiles in most experiments. Therefore, in order to determine the diffusion coefficients, an equation for self-diffusion between two finite bodies was fitted to the concentration profiles by a non-linear least squares routine. The self-diffusion of silicon and oxygen in peridotite liquid is slightly faster than self-diffusivities observed in $MgCaSi_2O_6$ (diopside composition) liquid. The self-diffusion coefficients of Mg^{2+} are generally slightly higher than those for Ca^{2+}, Si^{4+} and O^{2-}. Compared to ionic self-diffusion, chemical diffusion of Co and Ni is up to an order of magnitude faster. The self-diffusion coefficients for silicon and oxygen appear to decrease slightly from 4 to 10 GPa. An Arrhenius equation was fitted to the data giving an activation energy of Ea=280(50) kJ/mol and a negative activation volume of Va=-3.8 (1.3) cm^3/mol.

Viscosities were calculated from oxygen and silicon self-diffusion coefficients using the Eyring equation with a translation distance of 0.45 nm that was obtained in our earlier study of $MgCaSi_2O_6$ liquid. The Eyring-derived viscosity data are directly comparable to viscosities determined experimentally up to 7 GPa and 2280 K by *in situ* falling sphere viscometry (see contribution 3.7a by Liebske *et al.*), extrapolated to 2373K, using an activation energy of 263 kJ/mol and activation volume of 6.7×10^{-6} m^2/mol.

Though the pressure dependence of ionic diffusion for peridotite liquid appears to be slightly smaller over the range of experimental conditions, there is a good correlation between the Eyring-derived viscosities (when using a larger translation distance than the size of an oxygen anion) and results of direct viscosity measurements. These data therefore validate the use of the Eyring relation for peridotite liquid.

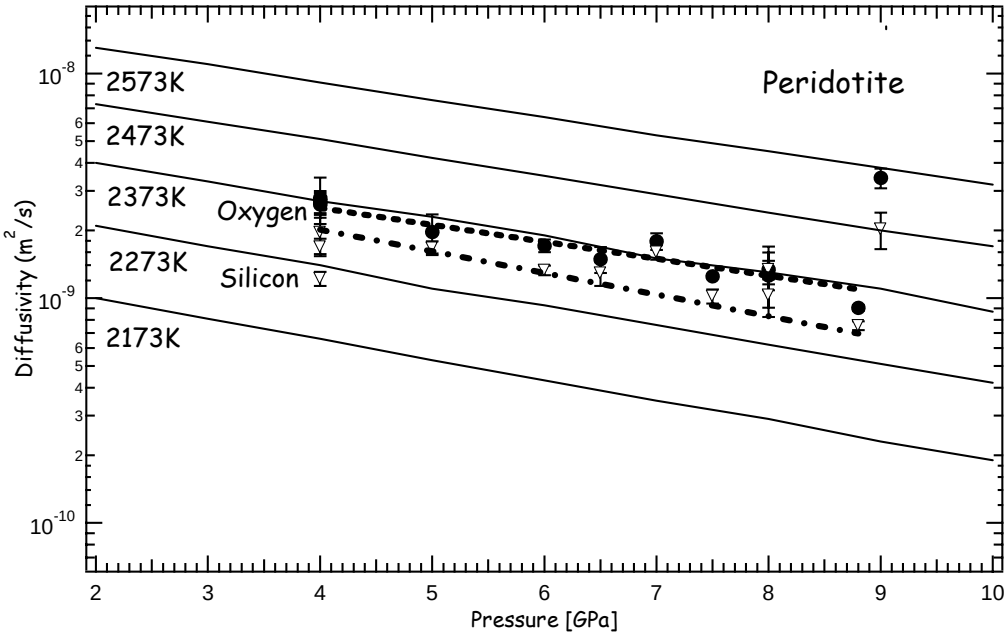

Fig. 3.7-4: Silicon and oxygen diffusion coefficients (at 2373 K) decrease slightly with pressure.

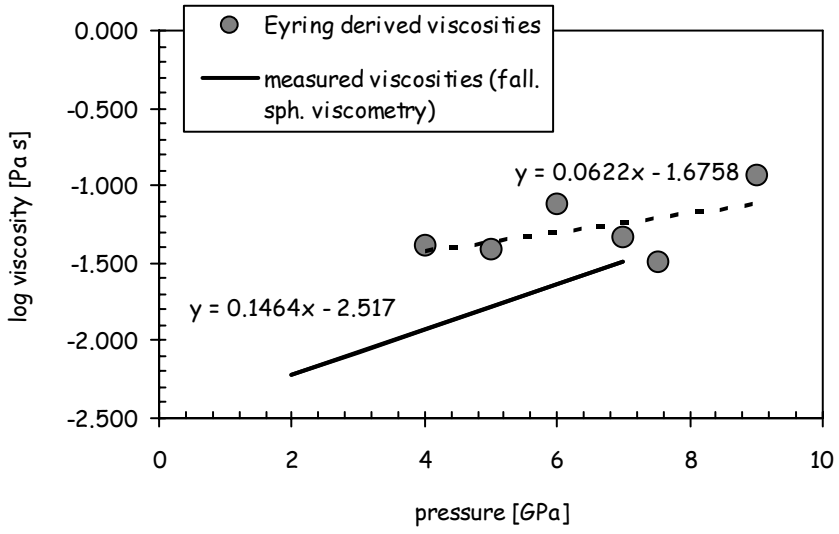

Fig. 3.7-5: Eyring derived viscosities compared to viscosities measured by *in situ* falling sphere viscometry.

c. New high-pressure viscosity determinations of $NaAlSi_3O_8$-H_2O liquids (B.T. Poe/Chieti, C. Romano/Rome, C. Liebske, H. Terasaki, D.C. Rubie, A. Suzuki/Tohoku and K. Funakoshi/ Hyogo)

Knowing the rheological properties of hydrous silicate melts is especially important with respect to understanding the potential hazards associated with volcanoes. Unfortunately, measuring viscosity of hydrous melts, at least at viscosities below about 10^8 Pa s (*i.e.* at temperatures moderately above Tg and higher), cannot be done at ambient pressure due to the rapid devolatilization of the sample. Thus, more advanced experiments are necessary which usually involve high-pressure apparatus and the method of falling sphere viscometry. With synchrotron radiation, direct images of a falling sphere through a silicate melt phase, its capsule, the graphite furnace and the solid pressure medium surrounding these components can be obtained by what is known as shadow radiography or density contrast imaging. In this study, we chose to measure viscosity of a series of samples along the $NaAlSi_3O_8$-H_2O join up to about 3 wt.% H_2O using such a method adapted for the multianvil beamline at the SPring-8 synchrotron center in Japan. One additional motive for this series of samples was to gauge the effect of depolymerization (by addition of H_2O) on the pressure effect of viscosity without changing either the Na/(Al+Si) or Al/(Al+Si) ratios. Pressure was fixed at 2.5 GPa for all experiments in order to focus our attention on the effect of composition.

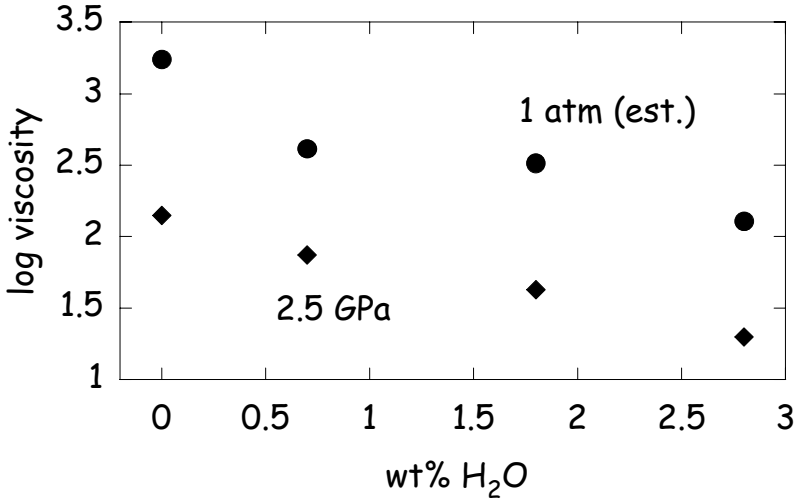

Fig. 3.7-6: Viscosities of hydrous $NaAlSi_3O_8$ liquids as a function of water content at 1 atm (dots) and 2.5 GPa (diamonds) at 1550 °C. The 1 atm viscosities are estimates based on extrapolation of data from low temperatures (micropenetration viscometry) over a viscosity range 10^8 to 10^{11} Pa s. The high-pressure viscosities were determined by in-situ falling sphere viscometry using synchrotron radiation and the shadow radiograpy technique at SPring-8.

While much work has been done in recent years regarding the pressure anomaly of highly polymerized anhydrous silicate liquids, in which viscosity is observed to decrease with

increasing pressure, little has been done on water-bearing melts due to the additional experimental challenge of maintaining a fixed concentration of H_2O. Our results show that, for all samples, viscosity decreases as a function of pressure between 1 atm and 2.5 GPa at 1550 °C, indicating that the pressure anomaly can still be observed as depolymerization of the melt increases from nominally zero (dry albite liquid) to NBO/T=0.8 (assuming water speciation entirely as hydroxyl groups at experimental conditions). Also intriguing is the observation that the magnitude of the decrease in viscosity over this pressure interval does not appear to be dependent on the amount of water in the melt (*i.e.* NBO/T).

d. *Equilibrium and disequilibrium degassing of a phonolitic melt simulated by decompression experiments (G. Iacono Marziano and B.C. Schmidt)*

The behaviour of volatiles in degassing from magmas, during their ascent to the Earth's surface, controls the explosive nature of volcanic eruptions. The aim of this study is to improve the understanding of volatile degassing by identifying possible deviations from the equilibrium regime, *i.e.* the possibility of delayed degassing during magma ascent. The investigated composition is the phonolite of the 79AD Vesuvius plinian eruption.

First, fluid-melt equilibrium relationships have been characterised as a function of pressure. The water solubility in the phonolite melt, equilibrated with a pure H_2O and a mixed H_2O+CO_2 (X_{H2O}=0.5) fluid phase, was determined up to 2.5 kbar. Experiments were performed in vertically operating TZM pressure vessels at super-liquidus conditions (1050-1100 °C) for a minimum experimental duration of 2 days, to ensure equilibrium between melt and vapour phase. Experiments were terminated by a rapid, isobaric quench of the samples.

Following the solubility experiments, decompression experiments have been performed and were compared to equilibrium relationships, in order to study the maintenance of equilibrium conditions during melt degassing. In these experiments the melt was firstly saturated with the fluid phase at 1050-1100 °C and 2 kbar, then pressure was reduced at a controlled rate to final pressures of 1, 0.75 and 0.5 kbar. Finally the samples were rapidly quenched under isobaric conditions. In order to investigate the degree of disequilibrium as a function of the depressurisation rate, different decompression velocities that simulate ascent velocities of natural magmas (m/s to hundreds m/s for explosive eruptions and cm/s for effusive eruptions) were used.

H_2O concentrations in the quenched glasses were determined by near infrared (NIR) spectroscopy on doubly polished glass chips. To relate the absorption to the water concentration, the extinctions coefficients for the 4500 and 5200 cm^{-1} bands of the phonolite glasses had to be determined. Therefore, glasses with different water contents were synthesised and then analysed by Karl Fischer Titration and NIR. The fitting of the data gave extinction coefficients of 1.14 l/mol cm for the 4500 cm^{-1} band (OH groups) and 1.18 l/mol

cm for the 5200 cm^{-1} band (molecular H_2O). For bubble-rich glasses, the water contents were determined by electron microprobe (as 100 % minus the analysis total), after having calibrated the method with IR analysed samples of different water concentrations.

Solubility and decompression results for pure water experiments are shown in Fig. 3.7-7 as wt.% water dissolved in the glasses vs. pressure. The data from the depressurisation experiments show that the degree of disequilibrium is a function of the decompression rate: the faster the decompression rate, the stronger the water over-saturation in the glass. For the highest decompression velocities the glasses show strong over-saturation and almost no degassing occurs in response to decompression. In other words, the experiments with decompression velocities of 59 and 17 bar/sec (equivalent to ascent rates of 178 and 50 m/s respectively) show almost constant water contents of 5 wt.%, which means that the water over-saturation increases from 2 wt.% at 1 kbar to 3 wt.% at 0.5 kbar. If we extrapolate the data to atmospheric pressure, over-saturation may reach 5 wt.%. The experiments with decompression velocities of 2 bar/s and 0.2 bar/s (equivalent to ascent rates of 6 and 0.6 m/s respectively) also deviate from equilibrium, but show a smaller degree of water over-saturation. The decompression experiments with the slowest velocity, 0.03 bar/s (equivalent to an ascent rate of 9 cm/s) show a near-equilibrium degassing path.

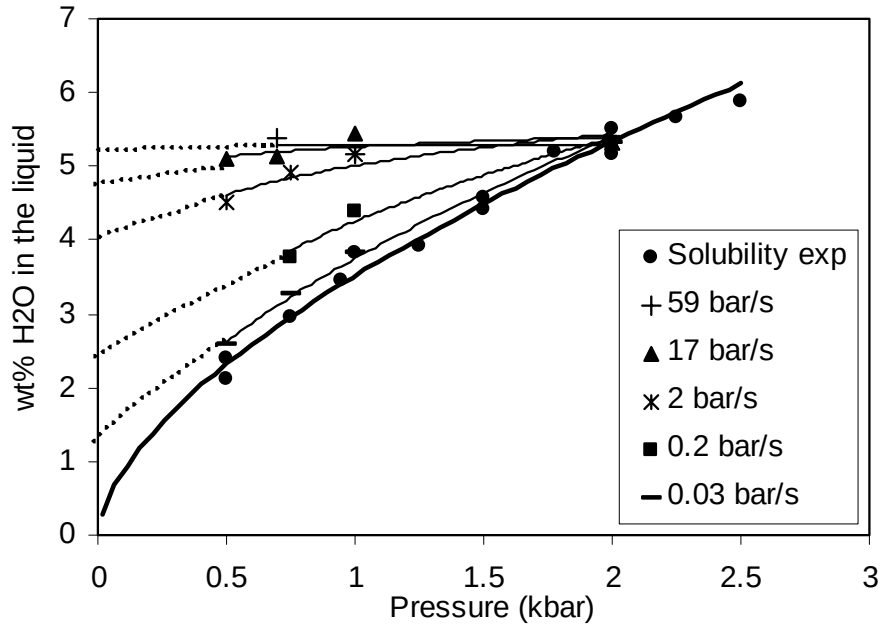

Fig. 3.7-7: Solubility and decompression results for pure water experiments. For decompression experiments, the starting pressure was always 2 kbar and the symbols show the final pressures. Solid lines show data trends and dashed lines show extrapolations to atmospheric pressure.

Figure 3.7-8 shows solubility and decompression results for the mixed H_2O-CO_2 experiments. Two decompression velocities were investigated in this case. The effect of decompression

velocity on the degassing behaviour of water is qualitatively similar to the pure H_2O experiments, even if the degree of water over-saturation in the decompressed melt is lower (because the initial water content at 2 kbar is only 2.6 wt.%). Although quantitative analysis of CO_2 was not performed, the absence of bubbles in the rapidly decompressed glasses indicates a disequilibrium degassing also for CO_2.

These results suggest that degassing of water from a rapidly ascending phonolitic magma is a non-equilibrium process, allowing that highly volatile over-saturated melts may reach the near surface. A sudden exsolution of these volatiles may then be responsible for the explosive nature of such an eruption.

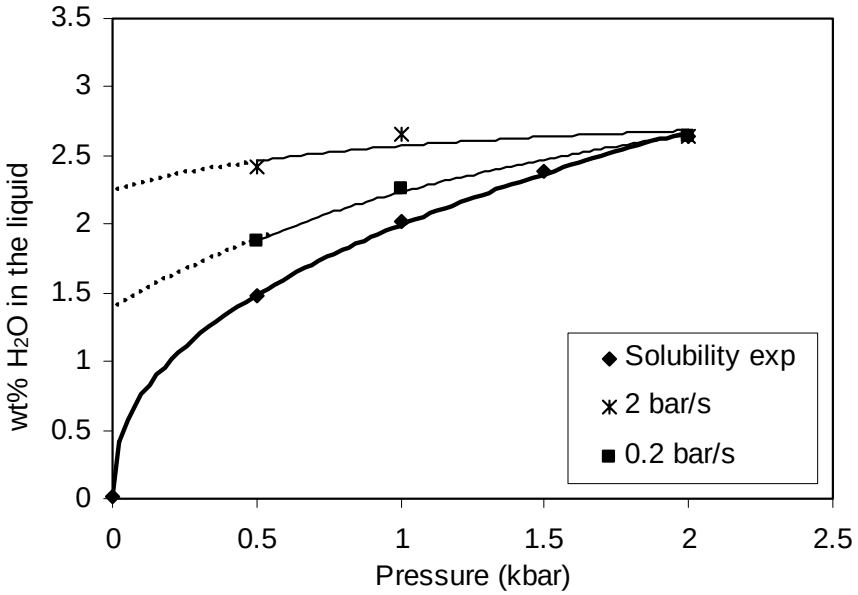

Fig. 3.7-8: Solubility and decompression results for H_2O+CO_2 experiments. For decompression experiments, the starting pressure was always 2 kbar and the symbols show the final pressures. Solid lines show data trends and dashed lines show extrapolations to atmospheric pressure.

e. *Laboratory measurements of electrical conductivity of hydrous and dry silicic melts under pressure (F. Gaillard)*

An interpretation of the electrical signature of molten rocks within the Earth's interior in terms of composition and temperature of the magma requires laboratory data on the electrical conductivity of silicate melts. The spectrum of terrestrial magma compositions is very large and is not covered by the current database of molten silicate electrical conductivity measurements. In particular, melting is often attributable or at least facilitated by the presence of water. Furthermore, during melting of rocks, water is largely partitioned into the liquid together with alkalis elements. Therefore, magma generally contains water concentrations in the range ppm to wt.%, which is likely to severely influence electrical conductivity. An

investigation of the effect of water on the electrical conductivity of silicate melts is therefore required. In addition, temperature and (to a lesser extent) pressure affect conductivity. In the absence of reliable laboratory constraints on the effects of these physico-chemical factors, estimation of magma storage conditions from electrical conductivity measurements of the Earth's interior might be tentative.

As with diffusivity and viscosity properties, the electrical conductivity (σ) of silicate melts is a property whose temperature and pressure dependence can be described, in the temperature range of natural magmas, by an Arrhenius law:

$$\sigma = \sigma_0 \exp [(-Ea + P\Delta V) / RT] \quad (1)$$

where σ_0 is the pre-exponential term, Ea is the activation energy, and ΔV is the activation volume, which describes the pressure dependence.

This contribution presents the results of measurements of the electrical impedance of dry (Fig. 3.7-9) and hydrous (Fig. 3.7-10) silicic obsidians determined in an internally heated pressure vessel, in the range 50-400 MPa and 350-1325 °C. The temperature and pressure dependences of electrical conductivity of both hydrous and dry obsidian can be fitted by an Arrhenius law both in the melt and the glass regions (Figs. 3.7-9 and 3.7-10). This suggests that a similar

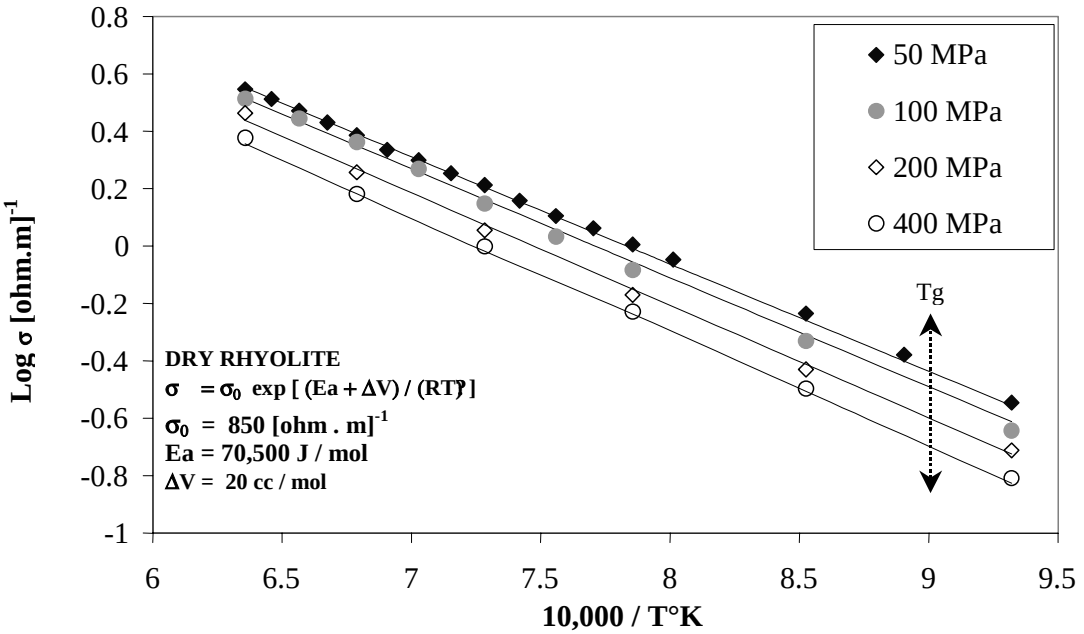

Fig. 3.7-9: Arrhenius plot of the conductivity results for the dry obsidian in the temperature range 1300-800 °C. Both temperature and pressure effects can be reproduced using an Arrhenius law whose parameters are printed in the figure. The error bars are smaller than the size of the points. Tg refers to the glass transition temperature.

transport mechanism operates in both melt and glass. The determined activation energies are 70 kJ/mol for the dry obsidian and 65 and 61 kJ/mol for the melts containing 1 and 3 wt.% H_2O respectively. The activation volume is 20 cm^3/mol. A combination of tracer diffusion and electrical conductivity investigations reveals that sodium is the dominant charge carrier in the hydrous and dry obsidians. The effects of temperature and pressure on conductivity are therefore interpreted in terms of activation energy and activation volume for Na mobility in dry and hydrous rhyolites. An increase in conductivity associated with addition of water was observed and is shown to reflect the effect of water in melts on the mobility of sodium. Consequently, it is anticipated that both the mobility and concentration of sodium could control the electrical conductivity of most terrestrial silicate melts. During cooling, magma becomes more conductive due to increasing concentrations of sodium and water associated with fractional crystallization; therefore, its electrical signature must reveal its nature and maturity. The next step is to elucidate the electrical behaviour of liquid + crystal systems.

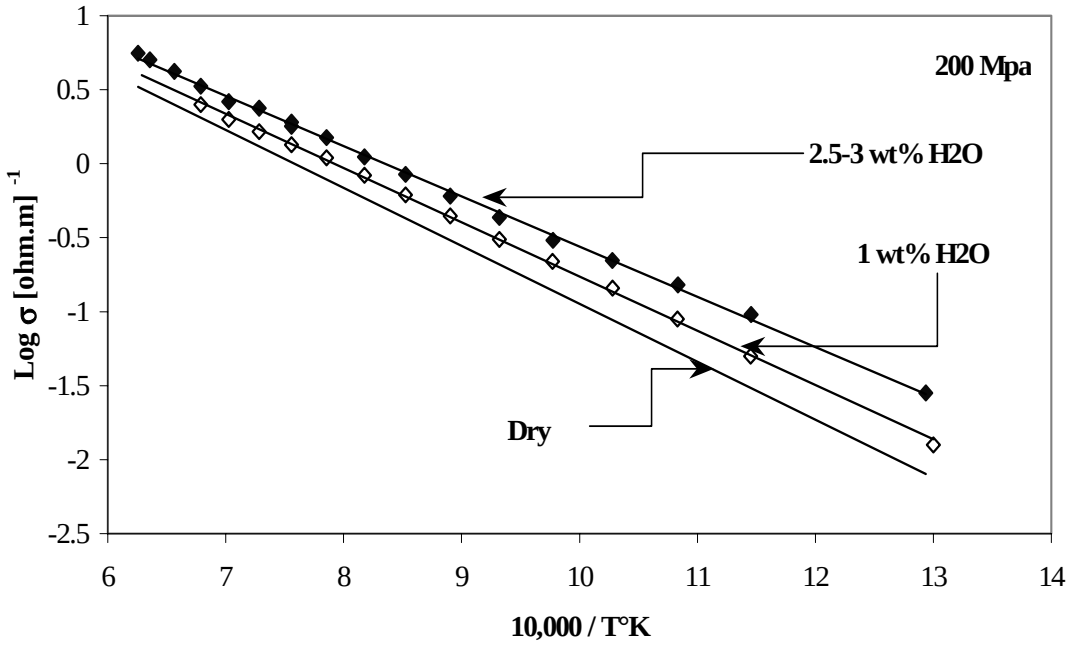

Fig. 3.7-10: Arrhenius plot of the conductivity results for hydrous obsidians in the temperature range 1325-500 °C at 200 MPa. Temperature effect can be reproduced using an Arrhenius law whose parameters are printed in Fig. 3.7-9. For comparison, the conductivity of a dry obsidian at 200 MPa calculated using the parameters in Fig. 3.7-9 is shown. The error bars are smaller than the size of the symbols.

f. *Electrical conductivity of magmas during partial crystallization (F. Gaillard)*

Recent studies at the BGI have revealed that the electrical conductivity of natural silicate melts is essentially controlled by sodium and water contents, temperature and, to a lesser extent, pressure (see 3.7e and 2002 Annual Report). The electrical signature of magma within

the Earth's interior as revealed by geophysical methods could, therefore, be interpreted in terms of magma composition and temperature conditions, but the number of variables involved is large. Furthermore, magma generally contains crystals whose contribution to the bulk electrical conductivity may be significant, depending on their abundance. Phase diagrams of magmatic rocks and multicomponent thermodynamic models tell us that temperature, crystal content and both sodium and water contents of magma are not independent parameters. Basically, as magma cools, its crystal content increases and both sodium and water contents of the liquid change in a unique, but predictable, way. Therefore, for a given bulk magma composition, there is a unique temperature-electrical conductivity path. Constraints on possible bulk compositions can be provided by petrological studies of volcanic rocks collected in the field.

The idea is illustrated here for the Merapi volcano, Java Is., probably the most active explosive volcano and therefore, an appropriate natural laboratory. The lavas recently erupted by this volcano (from the last centuries to present day) have a basalt-andesite bulk composition. The magma chamber is continuously replenished with magma of this composition, which chemically evolves by cooling prior to eruption. Using the thermodynamic model MELTS, we simulated the evolution of a basalt-andesite in a magma chamber during cooling from 1100 °C to 750 °C, at a depth of 6 km. The only unconstrained parameter is the initial water content. Calculations have been performed for initial water contents of 1, 3 and 5 wt.%, but only the 3 wt.% results are shown here. The electrical conductivity of the bulk system is calculated as a function of temperature. The conductivity of the liquid is calculated using previous results (see 3.7e) and the contribution of the crystals is estimated using an available conduction model for a two-phase system. The results are shown in Fig. 3.7-11 as electrical resistivity plotted against temperature. The resistivity value of 2 S.m corresponds to the resistivity of a region at a depth of 6 km below the Merapi Dome, determined by geophysical measurements, and is attributed to a magma chamber. Subsequently, the temperature at which the magma has a resistivity of 2 S.m should give us the storage conditions including the corresponding water content and crystal content of the melt. The values obtained are particularly consistent with what is expected from analyses of eruption products (900 °C, 35 % crystals, 6 wt.% H_2O). The approach seems therefore extremely promising for predicting volcanic eruptions. The conductivities of the liquid and the bulk liquid+crystal differ strongly for a given temperature which underlines the need for an accurate tool for predicting both crystal content and its effect on the electrical conductivity of a magma.

Experiments to test the strategy proposed here above will be carried out at the BGI. Rocks from the Merapi volcano will be partially crystallized at different temperatures in an internally pressure vessel and analyzed after the experiments to quantify the temperature dependence of key parameters such as crystal content, sodium and water content of the liquid. In addition, the electrical conductivity of these magmas will be measured and compared to the predicted values. This work should promote magnetotelluric surveys around volcanoes and open a new perspective for evaluating volcanic hazards.

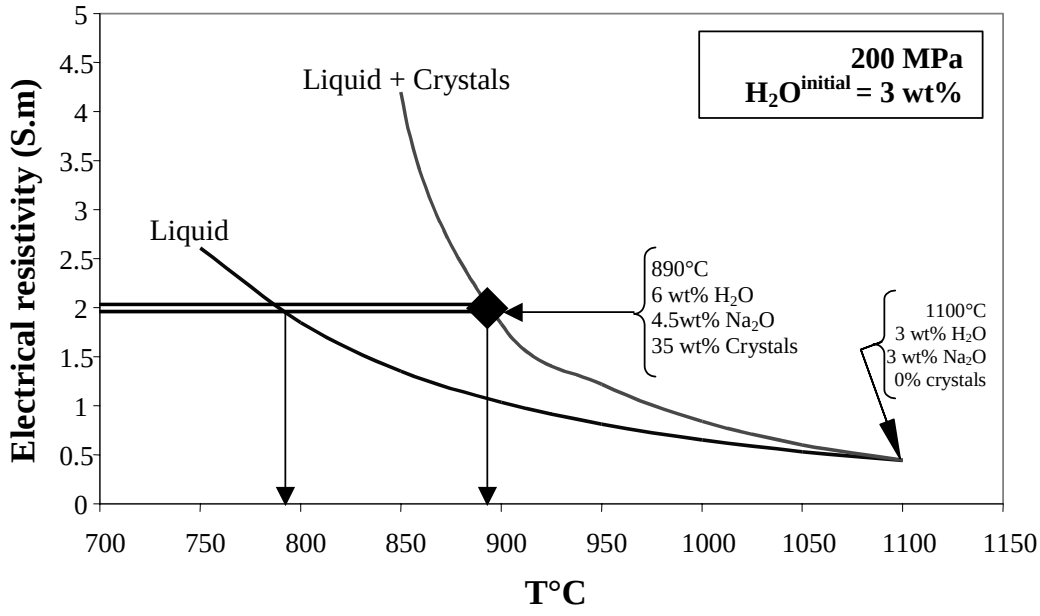

Fig. 3.7-11: Electrical conductivity calculated for a basalt-andesite undergoing partial crystallization during cooling from 1100 °C to 750 °C. The difference in conductivity between the residual liquid and the bulk magma (liquid + crystals) allows an appreciation of the effects of crystal content in terms of temperature estimated. This predicted effect, which is strongly model dependent (using MELTS and a two conductive phases model) has yet to be experimentally tested. Because pyroxene is the main crystal involved, the calculation of conductivity is done considering a liquid + pyroxene system.

g. *Temperature dependence of water and boron speciation in boro(alumino)silicate melts (B.C. Schmidt)*

Silicate glasses are often used as structural analogs of silicate melts as the glass structure corresponds to that of the melt at the glass transition temperature Tg. However, melts are very dynamic systems and their exact structures (or at least some aspects of structure) change with temperature. In order to understand melt structures at magmatic temperatures (which can be several hundred degrees centigrade higher than Tg), it is necessary to study the temperature dependence of melt structures. In previous studies it was shown that the water speciation in silicate melts has a strong temperature dependence, with the equilibrium of the reaction $H_2O_{melt} + O_{melt} = 2OH_{melt}$ shifting to the right side with increasing temperature. Also boron speciation (BO_4/BO_3) in some borosilicate melts has been shown to depend on temperature.

In our previous investigations of structures of hydrous, boron-bearing silicate glasses we observed new near infrared (NIR) absorption bands that we assigned to B-OH groups (see previous Annual Report contributions). The aim was now to study the temperature dependence of water speciation in boron-bearing silicate melts. Initially it was attempted to achieve this goal with the help of *in situ* NIR spectroscopy at high pressure and temperature using a hydrothermal diamond anvil cell. However, these experiments were plagued with

experimental difficulties, such as dissolution of melt components in the water pressure medium and subsequent crystal precipitation or problems with defining a reasonable baseline in the high temperature NIR spectra.

As an alternative approach to *in situ* NIR experiments, annealing experiments on a $NaBSi_3O_8$ glass containing 2.6 wt.% water were performed. In these experiments a hydrous glass is held for some time at a temperature in the range of the glass transition. During this heat treatment the structure of the glass adjusts to the annealing temperature. Rapid quenching of such a glass leads to the preservation of this structural configuration. Thus, using this procedure one can prepare glasses whose structures correspond to the annealing temperature. For the investigated samples, it was possible to perform successful experiments between 330 °C and 490 °C. Above 490 °C the quench rate was not fast enough to preserve the corresponding melt structure and below 330 °C structural relaxation did not occur within a reasonable experimental duration (few days). Time series experiments were performed to ensure complete structural relaxation at each temperature.

The results confirm the conversion of H_2O to OH groups with increasing T, but suggest also that B-OH groups (represented by the 4730 cm^{-1} NIR peak) seem not to participate in the conversion reaction. Only hydroxyl groups represented by the 4500 cm^{-1} peak (X-OH) are produced (Fig. 3.7-12). Assuming ideal mixing of water with the silicate network the changes in enthalpy ($\Delta H°$) and entropy ($\Delta S°$) of the reaction $H_2O_{melt} + O_{melt} = 2OH_{melt}$ were determined to be $\Delta H° = 20.5$ kJ/mol and $\Delta S° = 15.4$ J/mol·K. These values are in good agreement with data for rhyolitic melts.

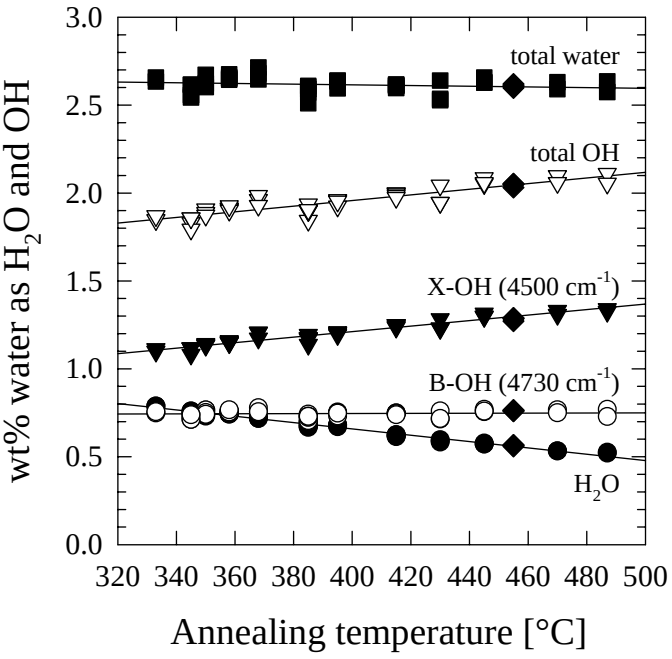

Fig. 3.7-12: Temperature dependence of water speciation in a $NaBSi_3O_8$ melt containing 2.6 wt.% water.

Annealing experiments were also used to study the temperature dependence of boron speciation in anhydrous $NaAl_{0.75}B_{0.25}Si_3O_8$ melts. Therefore samples were annealed between 720 °C and 350 °C for 24 to 48 h and subsequently analyzed with ^{11}B MAS NMR to determine the BO_4/BO_3 ratio. The data show that decreasing temperature leads to an increase of the fraction of BO_4. These results are consistent with results for Al-free Na-borosilicate glasses for which decreasing BO_4/BO_3 ratios with increasing temperature were reported.

h. *Structural mechanisms of compression and decompression in high-pressure $K_2Si_4O_9$ glasses (J. Allwardt and J.F. Stebbins/Stanford, in collaboration with B.C. Schmidt)*

Glass is typically used as a structural analog for geologic melts because the structure of glass is the same as that of the liquid at the glass transition temperature (T_g). Silicon is mostly bonded to four oxygens (four-coordinated, $^{[4]}Si$) in ambient pressure silicate glasses, where the oxygens are classified either as bridging oxygens (BO) or non-bridging oxygens (NBO). BO give glass its structural framework as it connects two silicon atoms (Si-O-Si) while NBO break up that framework because they are bonded to only one Si ($Si\text{-}O^-$) and a modifier cation such as K^+, Na^+, Mg^{2+}, etc. Previous work on high-pressure glasses has shown that the coordination number of Si increases with increasing pressure, which can be directly quantified in glasses with Silicon-29 magic-angle spinning (^{29}Si MAS) NMR, because this technique measures the local environment/coordination of Si. This increasing coordination of the Si cations has also been shown to affect macroscopic properties of melts like viscosity and density, the knowledge of which is important for accurate igneous and geophysical models.

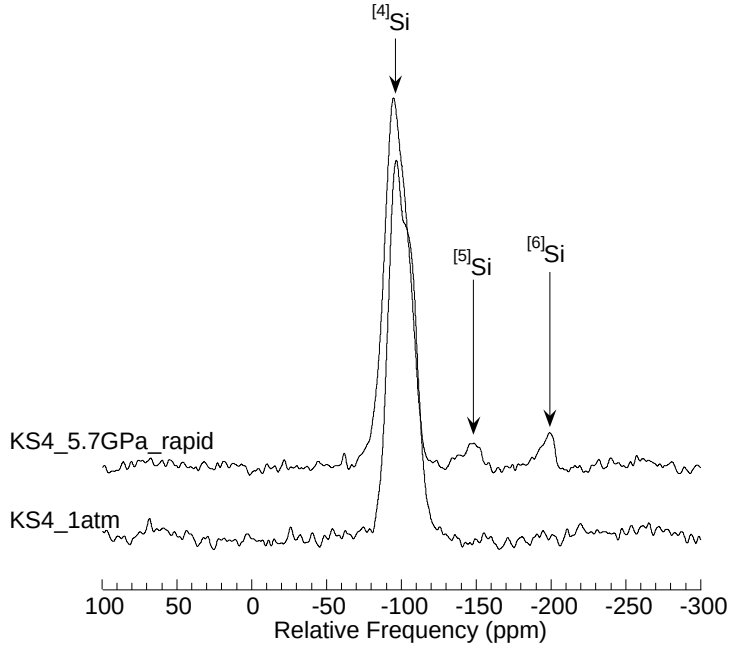

Fig. 3.7-13: Si-29 MAS spectra of 1 atm and 5.7 GPa rapidly decompressed $K_2Si_4O_9$ (KS4) glasses.

This study utilizes ^{29}Si and ^{17}O NMR and Raman spectroscopy to investigate the structure of high-pressure glasses to determine the mechanism(s) that create high-coordinated Si in high-pressure melts. To do this, high-pressure $K_2Si_4O_9$ glasses (5.7 and 8 GPa) were synthesized in the 1000 and 1200 ton multianvil press at Bayerisches Geoinstitut. The ^{29}Si and ^{17}O NMR spectra of these samples (collected at Stanford University) were compared to the NMR spectra of the ambient pressure glass. Integration of the peak areas of the ^{29}Si MAS NMR spectra (Fig. 3.7-13) clearly shows that the amount of $^{[5]}Si$ and $^{[6]}Si$ increases for both species in the high pressure glasses. In conventional ^{17}O MAS NMR spectra, the signals of different oxygen sites overlap completely which can make the evaluation of ^{17}O MAS NMR spectra quite difficult (not shown). However, a relatively new technique, ^{17}O triple-quantum (3Q) MAS NMR, produces 2-dimensional spectra where the peaks from different oxygen sites can typically be resolved. The ^{17}O 3QMAS spectra of the ambient pressure and the 5.7 GPa $K_2Si_4O_9$ glasses (Fig. 3.7-14) clearly show that a "new" oxygen species ($^{[4]}Si$-O-$^{[6]}Si$) is present in the spectrum of the high-pressure glass. However, a separate signal of $^{[4]}Si$-O-$^{[5]}Si$ is not observed. Experiments with crystalline model compounds (triclinic $CaSi_2O_5$) containing such oxygen species suggest that the resonances of $^{[4]}Si$-O-$^{[5]}Si$ overlap with those of $^{[4]}Si$-O-$^{[4]}Si$ and $^{[4]}Si$-O-$^{[6]}Si$, depending on the bonding configurations. Due to the quantitative nature of NMR, the ^{29}Si MAS and ^{17}O 3QMAS NMR spectra confirm previous suggestions that the five- and six-coordinated Si are created by the mechanisms: NBO + 4BO = 5 $^{[4]}Si$-O-$^{[5]}Si$ and 2NBO + BO = 6 $^{[4]}Si$-O-$^{[6]}Si$, when NBO are present.

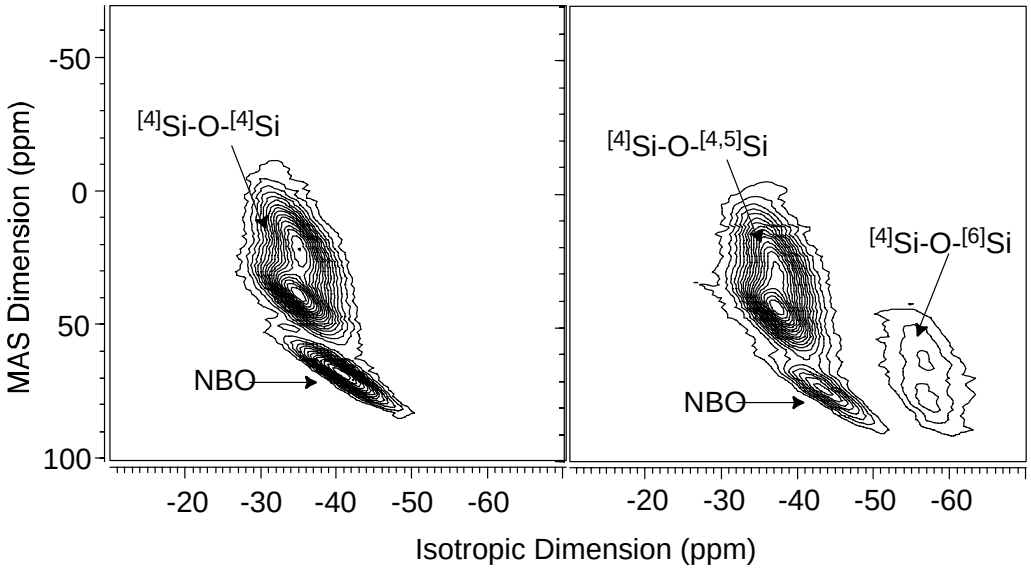

Fig. 3.7-14: O-17 3QMAS NMR spectra of the 1 atm and 5.7 GPa KS4 glasses. Contours are drawn at intervals of 5 % and range from 5 % to 95 %.

In addition to the investigation of the compression mechanisms, we studied the effect of decompression rate on the structure of high-pressure glasses. To do this, we synthesized two

glasses at 5.7 GPa, and decompressed them at different rates (over 1s vs. 14h) and compared the ^{29}Si and ^{17}O NMR spectra of the two samples. The comparison of the ^{29}Si spectra revealed that about 1 % of the total Si (*i.e.* 20 % of $^{[6]}$Si) changed from $^{[6]}$Si to $^{[5]}$Si during slow decompression. This small change has a large effect on the Raman spectra in the frequency range that is often assigned to the presence of $^{[6]}$Si species. Further work is in progress to study the effect of decompression in more detail.

i. *The effect of modifier cations on the amount of five- and six-coordinated aluminium present in high-pressure aluminosilicate glasses (J.R. Allwardt, D.J. Frost and B.C. Schmidt, in collaboration with J.F. Stebbins/Stanford)*

Previous work on high-pressure melts has shown that their macroscopic properties are highly dependent on pressure. This suggests that atomic-scale structural changes occur in the melt with increasing pressure. Glasses are typically used as a first approximation for the structure of high-pressure melts as they represent the structure present in the liquid at the glass transition temperature. In this study, we have used ^{27}Al MAS NMR to investigate how the modifier cations (Mg^{2+}, Ca^{2+}, Na^{+}, and K^{+}) present in aluminosilicates affect the distribution of different aluminium coordinations in both ambient pressure and high-pressure (to 10 GPa) glasses. High-pressure samples were synthesized using a multianvil apparatus. ^{27}Al MAS NMR spectra were collected using a high field of 18.8 Tesla (Stanford University) to minimize the peak broadening due to second-order quadrupolar effects, which causes overlapping peaks for different coordinations of Al.

Aluminium is mostly tetrahedrally coordinated ($^{[4]}$Al) in ambient-pressure aluminosilicate glasses where $M^{x+}_{(2/x)}O \geq Al_2O_3$, but ^{27}Al NMR studies have shown that small concentrations of high-coordinated Al are present in both charge balanced ($M^{x+}_{(2/x)}O = Al_2O_3$) and "depolymerized" ($M^{x+}_{(2/x)}O > Al_2O_3$) aluminosilicate glasses. The ^{27}Al NMR spectra of the ambient pressure K-, Na-, and Ca- aluminosilicate glasses contain a peak representing the presence of $^{[5]}$Al (Fig. 3.7-15). The spectrum for the ambient pressure Mg-aluminosilicate glass contains a $^{[4]}$Al peak with a large "tail" that overlaps the $^{[5]}$Al region, preventing the detection of small amounts (< 1 %) of $^{[5]}$Al in this spectrum (Fig. 3.7-15).

Previous ^{27}Al NMR studies, performed at lower magnetic fields (9.4 T), have shown that Al is more susceptible to coordination changes than Si in high-pressure aluminosilicate glasses. In the present study, ^{27}Al MAS NMR of the $M^{x+}_{(9-3x)}Al_2Si_6O_{18}$ glasses show that the alkaline-earth aluminosilicate glasses (MgAS and CAS) contain more high-coordinated species than the alkali aluminosilicate glasses (KAS and NAS) (Fig. 3.7-16). Additionally, our study clearly demonstrates that a slower decompression rate (decompression over 14 hours vs. 1 second) reduces the percentage of high-coordinated species in aluminosilicate glasses. Our recent work has also shown that high-pressure "depolymerized" aluminosilicate glasses with different fictive temperatures contain different percentages of high-coordinated species

suggesting that the amount of high-coordinated Al may increase with temperature. This likely suggests that Al-coordination results determined from high-pressure aluminosilicate glasses represent a minimum value for the melt.

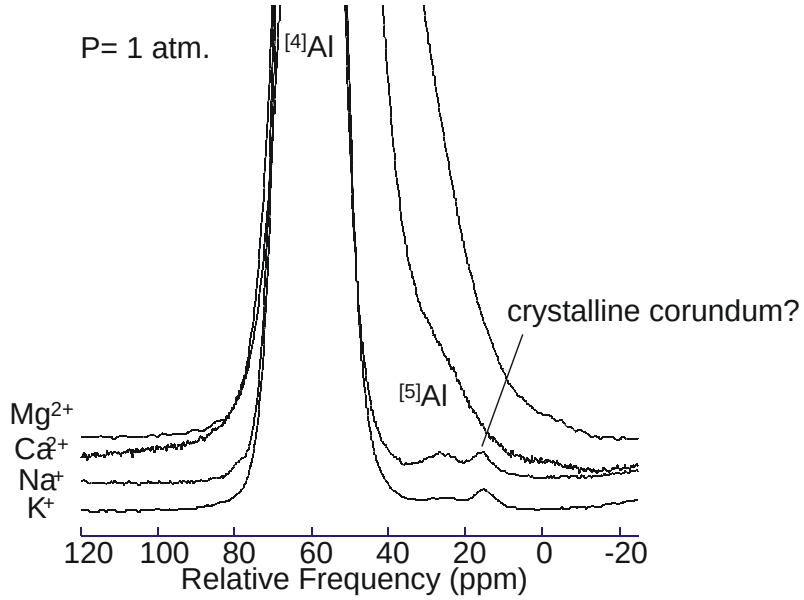

Fig. 3.7-15: Al-27 MAS NMR spectra of the ambient pressure glasses of this study. A small amount of crystalline impurity (< 1 %) is present in the sample.

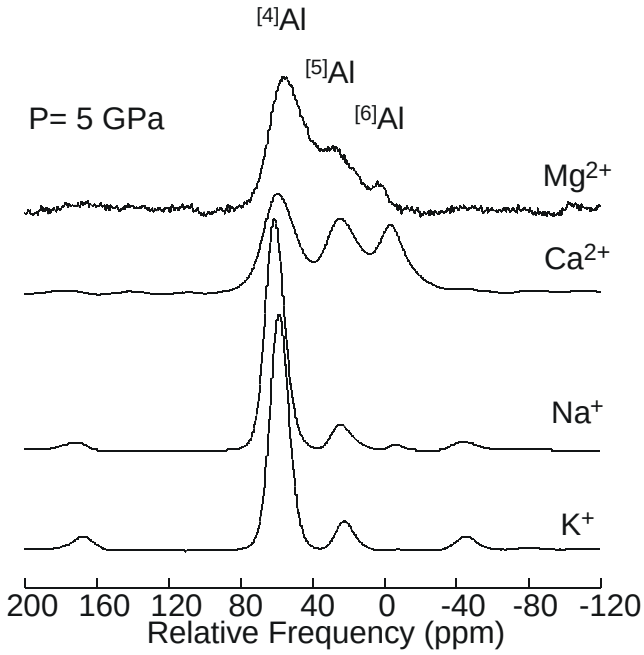

Fig. 3.7-16: Al-27 MAS NMR spectra of the 5 GPa glasses of this study.

3.8 Materials Science

Modern mineralogy and petrology, as branches of Earth science, share with materials sciences not only methodological approaches (physical and chemical methods of synthesis and characterisation of materials, the search for correlations between structures and properties, studies of the response of materials on changes of thermodynamic parameters, etc.), but also subjects of investigations. The most familiar example is diamond. While in the Earth sciences there is concern about the genesis and location of different diamond deposits, materials sciences searches for better conditions for producing synthetic diamonds. In this respect, new experiments on growth mechanisms and the catalytic effect of metal, conducted at the Bayerisches Geoinstitut, could help to optimize conditions for diamond synthesis.

Although diamond is established as the hardest material known so far, there are continuing attempts to produce even harder substances. Particularly, promising results were obtained in experiments with fullerene C_{60}, which undergoes polymerisation at high pressure and high temperature conditions. 3D-polymerized fullerite was reported to be even harder than diamond. However, there are a number of problems related to the reproducibility of the synthesis of 3D polymers. In part, these problems are related to the poorly constrained phase diagram and kinetics of metastable C_{60} polymers. *In situ* experiments demonstrate for the first time that depending on the path (pressure increase followed by heating or vice versa) different C_{60} polymers can be obtained.

Outstanding properties of titanium dioxide (TiO_2) polymorphs have not only made these materials extremely useful in many applications, but also identified them as prime materials for experimental and theoretical studies. High-pressure transformations of TiO_2 attract special attention because they are close crystal-chemical analogues of SiO_2, one of the most abundant components of the solid Earth. A new phase of titania with fluorite-type structure was found at high pressures and temperatures. According to theoretical predictions, if this phase could be stabilized at ambient conditions, it would be a very good material for photo-electrodes in photochemical energy-conversion processes.

Pressure-induced structural phase transitions in nanocrystalline materials attract significant attention as models to understand the kinetics and microscopic mechanisms of first-order solid-solid phase transitions. They are also of interest because of the possible role of nanocrystalline phases within planetary interiors and because of the potential use of dense nanometer-sized phases in shocked materials of the Earth's crust, in meteorites, and probably around presolar stars for constraining conditions of formation and evolution. Investigation of the behaviour of nanocrystalline titanium dioxide and cuprite Cu_2O under pressure demonstrates that crystal structures and chemical stability of nanocrystalline materials can be significantly different from those of their bulk counterparts.

The relations between structure and properties play a basic role in material sciences. This is illustrated again by the new studies of pressure induced high- to low-spin transformations in metal-organic compounds and chemically dependent variations in the crystal structures of zirconium phosphates.

a. *TEM study of microscopic inclusions in synthetic diamond (F. Langenhorst, J.-P. Poirier and D.J. Frost)*

Nowadays, diamonds are synthesised by various dynamic and static high-pressure techniques and by chemical vapour deposition. The conventional high-pressure technique for diamond synthesis employs metallic solvent-catalysts such as molten iron, nickel, cobalt, or mixtures of these transition metals. Despite the widespread use of this technique, the growth mechanisms of diamond and the catalytic effect of the metal are still a matter of discussion. To address this problem, we designed multianvil experiments, which allowed trapping of the solvent-catalyst at synthesis conditions as microscopic inclusions in diamond. These inclusions were small enough to be studied by transmission electron microscopy (TEM).

Two high-pressure experiments were carried out with pure iron and an iron/cobalt mixture as metallic solvent-catalysts, intermingled with graphite. Run conditions of the experiments were: 13 GPa and 2200 °C for iron/graphite; 15 GPa and 2050 °C for iron/cobalt/graphite. These pressures and temperatures are relatively high for diamond synthesis and were chosen to enhance the nucleation and growth rates of diamond, thereby improving the chances of trapping inclusions. The synthetic diamonds in both runs contained abundant microscopic inclusions with diameters being sometimes as small as 2 or 3 nm. Larger inclusions display a cubooctahedral shape. In inclusion-rich areas, we observed numerous (10^{14} m^{-2}) dislocations as well as stacking faults and microtwins on (111) planes (Fig. 3.8-1). The <110> dislocations were clearly glissile, as indicated by their curvatures. Stacking faults and microtwins were tangentially connected to octahedral faces of inclusions. These defects were absent in inclusion-free areas, suggesting that the inclusions can be regarded as the cause for the observed plastic deformation.

Energy-dispersive X-ray microanalyses on the TEM revealed that the inclusions in synthetic diamond are metallic cobalt and iron, as well as iron carbide. Metal and iron carbide inclusions were sometimes wrapped in a shell of graphite layers (Fig. 3.8-2). It is remarkable that the metal and carbide inclusions were always single crystals, in a topotactic relationship to the host diamond. The metallic cobalt inclusions possessed the hcp structure (ε-Co) and were in the following orientation relationship with diamond: $[111]_{Dia}$ // $[10\bar{1}0]_{Co}$ and $[220]_{Dia}$ // $[11\bar{2}0]_{Co}$. The metallic iron inclusions had the fcc structure (γ-Fe), like diamond, which explains the observed coincidence of *a* axes of diamond and γ-Fe. The iron carbide seems to possess a hexagonal superstructure, also in topotactic relationship to diamond.

These observations cast light on the deformation behaviour of diamond in the presence of inclusions and the role of the solvent-catalyst in diamond growth. They become understandable when the pressure-temperature path in the experiments and the different compressibilities and thermal expansivities of inclusions and diamond are taken into account. Deformation of diamond is apparently first induced, when the samples are quenched to ambient temperature at high pressure. As a consequence of the different thermal expansivities, the inclusions then shrink more than the host diamond and the pressure drops in the inclusions. Using elasticity theory we estimate a residual pressure in inclusions of only 1 GPa. This causes shear stresses in the diamond, which, while temperature is still high, can be relaxed by emission of dislocations and plastic deformation. Diamond is then deformed in a second stage, when it is decompressed to ambient pressure. Upon decompression, pressure increases again in the inclusions because the compressibility of diamond is lower than that of the inclusion. Since the diamond is now cold and cannot deform by dislocations, the resulting shear stresses are released by the formation of stacking faults and mechanical microtwins.

The decrease in internal pressure during quenching provides also an explanation for the association of the cobalt and iron carbide inclusions with graphite. For example, in the Fe-C system with 8-10 wt.% C, a molten solution of iron and carbon crystallizes at high pressure as Fe_xC_y + carbon. Since quenching leads to a drop in pressure, carbon precipitates as graphite and not as diamond. The fact that the metal and carbide inclusions crystallize as monocrystals in topotactic relation with diamond may indicate that the melt is structurally related to diamond, resulting in a good wetting of growth surfaces. It is striking that the interplanar distances between the densest planes in the hcp ($10\bar{1}0$, 0002) or fcc metals known as good catalysts (*e.g.*, Fe, Co, and Ni) are very similar to the (111) spacing of diamond. This might be an important prerequisite for a good catalyst for diamond synthesis.

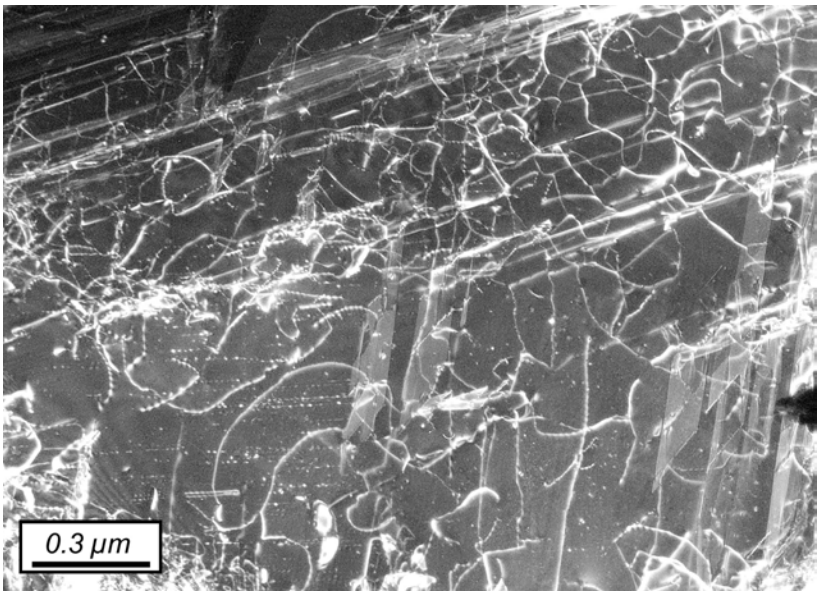

Fig. 3.8-1: Weak-beam TEM image of numerous tangled disocations and stacking faults in diamond synthesized at 13 GPa and 2200 °C.

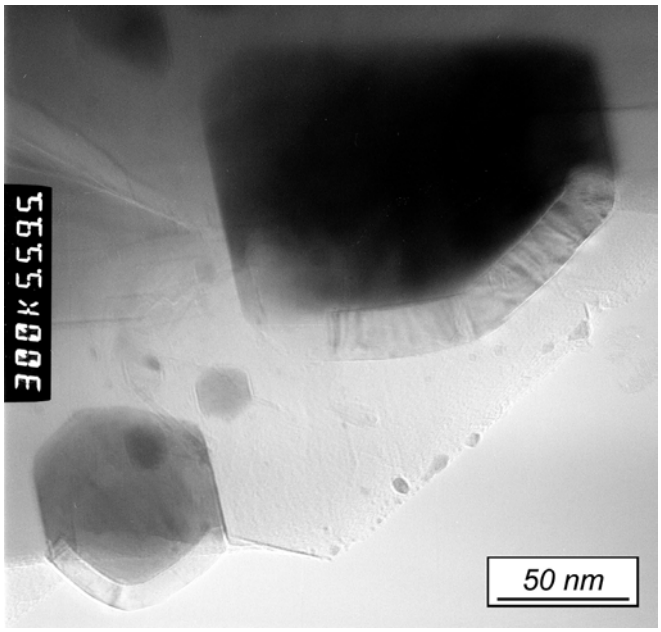

Fig. 3.8-2: Bright-field TEM image of Co inclusions in synthetic diamond rimmed by graphite.

b. *In situ Raman study of path-dependent C_{60} polymerisation: Isothermal compression up to 32 GPa at 800 K (A. Talyzin/Nice and L.S. Dubrovinsky)*

Fullerene C_{60} undergoes polymerisation at high-pressure high-temperature conditions (HPHT). Below 9 GPa and 900 K, several kinds of one- and two-dimensional polymeric phases have been obtained: orthorhombic (O), tetragonal (T) and rhombohedral (Rh). One- and two-dimensional polymeric phases are well characterized by different techniques including Raman spectroscopy and XRD. So far, most studies of C_{60} polymerization were performed *ex situ* by treatment of fullerene at HPHT and quenching the samples to ambient conditions and only very few *in situ* experiments at HPHT conditions have been reported.

Three-dimensionally polymerized superhard fullerites have been reported to exist at pressures above 12-13 GPa and temperatures above 800 K. The problem with characterization of these "superhard" phases is that they give very few lines in XRD, and Raman spectra of these phases are also typically almost featureless. One of the most interesting and controversial areas in the P-T diagram of C_{60} is at about 13 GPa and 800-830 K. Recently it became clear that not only pressure and temperature, but also some other experimental parameters such as heating time, stress and P-T history can be directly connected to physical properties of synthesized samples. It is known that two-dimensional polymerization gives different results depending on the path in P-T space. The increase of temperature followed by pressure (T-P-path) favor formation of tetragonal phase, while pressure increase followed by heating (P-T-path) applied for the same final P-T conditions (about 2.2 GPa and 870K) results in the synthesis of a mixture of tetragonal and rhombohedral polymers. It can be proposed that the

T-P-path favours to polymerization in the (001) direction of the original fcc structure of C_{60}, while the P-T-path favours polymerization in the (111) direction. So far all studies of the 3D-polymerization have been performed only using pressurizing followed by heating (P-T-path). Due to the experimental difficulties the T-P-path has never been tested for the pressure region above 6 GPa.

Two experiments were aimed an observation of 3D polymerization by isothermal compression at 800 K using 2D polymeric phases as precursors. In the first experiment rhombohedral phase was synthesized *in situ* after compression to 8 GPa and 800 K. In the second run a sample of the tetragonal phase synthesized in a piston-cylinder apparatus by heating C_{60} at 2.5 GPa and 800 K for 60 min was used.

Isothermal compression of the Rh phase from 5 to 12 GPa resulted in drastic changes of the Raman spectra (Fig. 3.8-3a). Already at 10 GPa the spectrum of the Rh phase degraded into a few broad features. At 12 GPa the Raman spectrum of this sample looks identical to the spectra of the phases reported as "superhard" ones. This spectrum can be attributed to either the 3D polymer or amorphous carbon phase that formed as a result of fullerene cage collapse.

Phase transformations of the tetragonal phase during compression from 8 GPa to 30 GPa at 800 K appeared to be different from those observed in the similar experiment on the rhombohedral phase (Fig. 3.8-3b). First of all, the sample remained as mostly tetragonal phase after heating at 8 GPa from room temperature to 800 K. We did not observed direct transformation from tetragonal to rhombohedral phase during heating. Some amount of Rh phase, which can be recognized in the Raman spectrum recorded from this sample at 800 K and 8 GPa, originates from the transformation of chain polymers, which were present in the starting material as an impurity.

It is known that the tetragonal phase forms due to polymerization of the initial *fcc* structure of C_{60} in the (001) plane, while the rhombohedral phase forms due to polymerization in the (111) direction. Due to geometrical constraints, the rhombohedral phase cannot be obtained directly from the tetragonal one without breaking some polymeric bonds. So, the possible scenarios of the behaviour of tetrahedral phase at high pressure and temperature could be: (a) depolymerization of the tetragonal polymer on chains and consequent polymerization in the (111) direction (direct transformation to rhombohedral phase); (b) the tetragonal phase remains stable even at those P-T conditions, where the rhombohedral polymer usually forms from orthorhombic chain polymers; and (c) the tetragonal phase polymerized in (111) direction of initial *fcc* C_{60} structure directly transforms into 3D polymer(s). Our experiments show that at pressures of 6 to 15 GPa and high temperature, the behaviour of the tetragonal phase follows the second scenario, and at even higher pressure the tetragonal phase starts to transform to the presumably 3D polymer (scenario (c)). Our experiments also clearly demonstrate that the kinetic P-T phase diagram (or "experimental maps") of C_{60} depends on both the starting material and the pressure-temperature path.

In fact, all P-T diagrams presented in literature were constructed using the P-T-path (isobaric heating), and the present work shows that the P-T diagram constructed using T-P-path (isothermal pressurizing) is remarkably different. This fact once more emphasizes that the true phase diagram of C_{60} polymers does not exist (because C_{60} is a metastable form of carbon), and only "experimental maps" or "kinetic P-T diagrams" can be constructed. It is clear that many more isothermal pressurizing experiments at different temperatures are required to construct a "T-P-path kinetics phase diagram". Nevertheless, at least one strong difference is clear from the presented study: in contrast to the available P-T diagrams, on the "T-P-path phase diagram" the most stable phase at 800 K and at pressure of 6-15 GPa is not rhombohedral, but the tetragonal polymeric one.

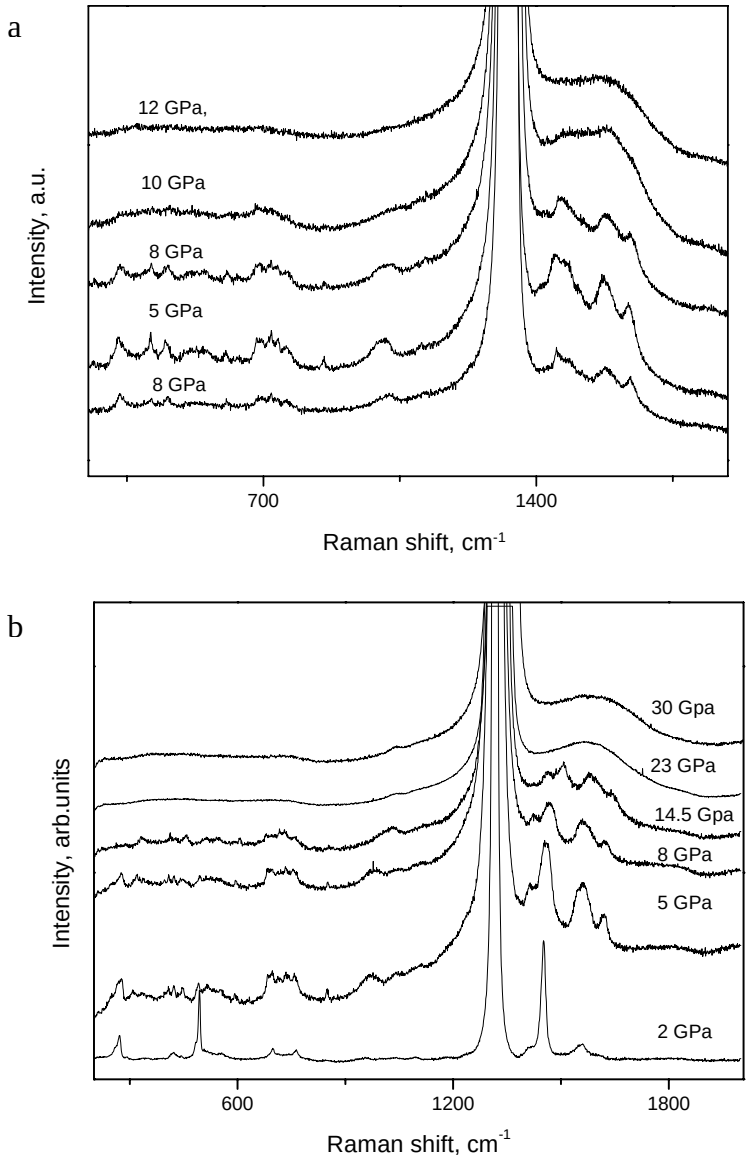

Fig. 3.8-3: Raman spectra recorded *in situ* during isothermal compression of Rh (a) and T (b) polymeric phases at 800 K.

c. *New cubic titanium dioxide polymorph (N.A. Dubrovinskaia and L.S. Dubrovinsky)*

Titanium dioxide (TiO_2) is one of the most widely used materials for commercial applications. The most abundant forms of TiO_2 (rutile and anatase) are largely used as antireflection coatings for solar cells and, more generally, in the development of photo-electrodes for photochemical energy-conversion processes. The ideal material for high-efficiency photo-electrodes must satisfy different requirements in terms of semiconducting and electrochemical properties. Among various prerequisites, the optimal band gap (E_g) and the corrosion resistance must be fulfilled. Titanium dioxide is certainly one of the best materials that can be exposed to aqueous solutions thanks to an outstanding corrosion-resistance. Nonetheless, an important drawback for its application as photo-electrodes is related to the limited ability for light absorption due to a relatively large band gap value (3.0-3.2 eV). The magnitude of the E_g makes TiO_2 absorbing only in the ultraviolet part of the solar emission spectra, thus imposing low conversion efficiency. That is, only the photons with energies equal to or larger than that of the band gap can be absorbed and used for conversion. The width between the top of the valence band and the bottom of the conduction band is therefore an important value for materials to become candidates for photo-electrodes. The optimal band gap for high-performance photo-electrodes has been fixed to ~ 2 eV. Unfortunately, high corrosion-resistant materials with such a band gap have not been identified yet. The recent discovery of novel high-pressure titania polymorphs has opened a great expectation toward the possibility to synthesize new high-pressure TiO_2 forms with smaller band gaps and to quench them at room conditions for practical applications. Particular attention is given to the high-pressure cubic phases of TiO_2.

In our experiments anatase (99.99 % TiO_2) was used as a starting material. At applied pressures of about 12 GPa or above, anatase transformed to the baddeleyite (MI, $P2_1/c$) phase, in good agreement with previous observations (Fig. 3.8-4). On further compression, reflections due to the MI phase could be followed to over 60 GPa. At pressures between 30 and 45 GPa, however, the quality of the diffraction pattern decreased drastically and at about 60 GPa, the material became translucent. We observed that at pressures of about 28 GPa, TiO_2 absorbs Nd:YAG laser radiation and the laser-heated areas of the sample became black. After laser heating at 1300-1500 K for 40 minutes at pressures between 28 and 32 GPa the material transformed to a new orthorhombic OI phase (*Pbca*) as evidenced by the X-ray diffraction spectra (Fig. 3.8-4). On further compression the OI phase could be followed to about 50 GPa.

Heating the sample at temperatures 1900 to 2100 K at 48 GPa results in complete transformation and drastic changes in the diffraction pattern (Fig. 3.8-4). A number of reflections could be interpreted as belonging to an orthorhombic OII (*Pnma*) cottunite-structured phase with lattice parameters a=5.162 Å, b=3.074 Å, c=5.942 Å (Fig. 3.8-4). The rest of the reflections were easily indexed in a framework of cubic lattice (Fig. 3.8-4) with a=4.516(1) Å. Relative intensities and positions of cubic reflections allowed us to interpret

them as those due to the CaF_2-structured TiO_2 phase. Note, that we cannot unambiguously distinguish between fluorite (*Fm3m*) and distorted fluorite (*Pa3*) structures, because relatively weak reflections expected due to the deviation of oxygen atoms from more symmetric position (0.25, 0.25, 0.25) in the *Fm3m* space group could be hidden among the reflections of the cottunite-structured phase.

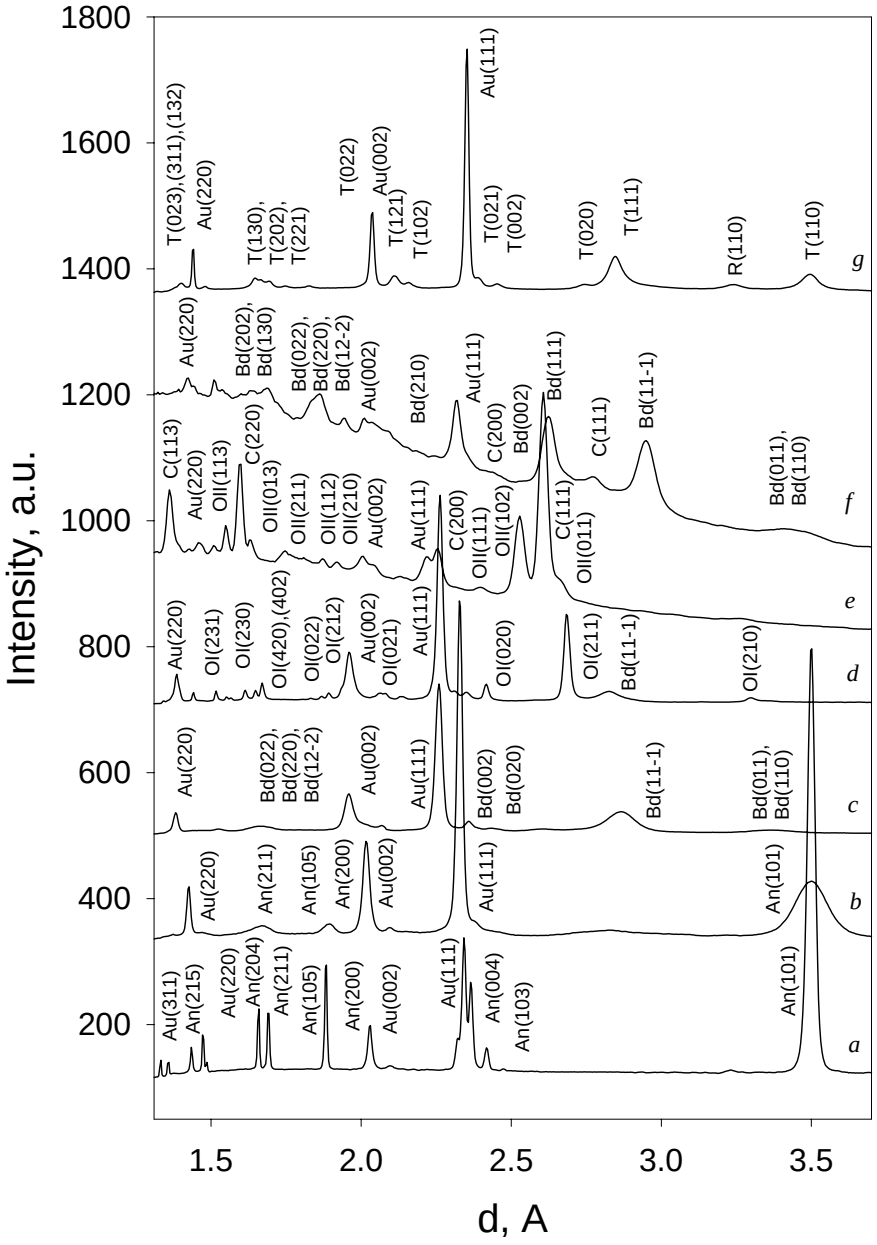

Fig. 3.8-4: Examples of X-ray diffraction patterns obtained in experiments with titanium dioxide at (a) 2.8(1) GPa, (b) 6.2(1) GPa, (c) 29(1) GPa, (d) 27(1) GPa after heating between 1300 K and 1500 K, (e) 48(1) GPa after heating between 1900 K and 2100 K, (f) on decompression at 8.9(1) GPa, and after complete release of pressure (g). (Au for gold, An for anatase, Bd for baddeleyite, OI for orthorhombic *Pbca* phase, OII for orthorhombic cottunite-type phase, C for cubic CaF_2-like phase, T for TiO_2II, and R for rutile).

On decompression at ambient temperatures at pressures below 20 GPa the OII phase transforms to the MI, while reflections of cubic phase could be followed to 9 GPa (Fig. 3.8-4). Below 7 GPa the MI transforms into a mixture of α-PbO_2-structured phase (TiO_2II) and rutile (Fig. 3.8-4).

The unit cell parameters of the cubic phase were determined in the pressure range of 10 to 55 GPa (Fig. 3.8-5). Fitting gave us the values for K_{300}=202(5) GPa, K'=1.3(1), and V_0=115.50(2) Å^3. The bulk modulus of the cubic phase is significantly lower than bulk moduli if MI (304(6) GPa), OI (318 GPa), and OII (431 GPa) phases. As a result, even V_0 of the cubic phase is relatively high and comparable with the molar volume of TiO_2II (122.2 Å^3); at pressures above ~ 40 GPa the cubic CaF_2-structured phase became the densest TiO_2 phase.

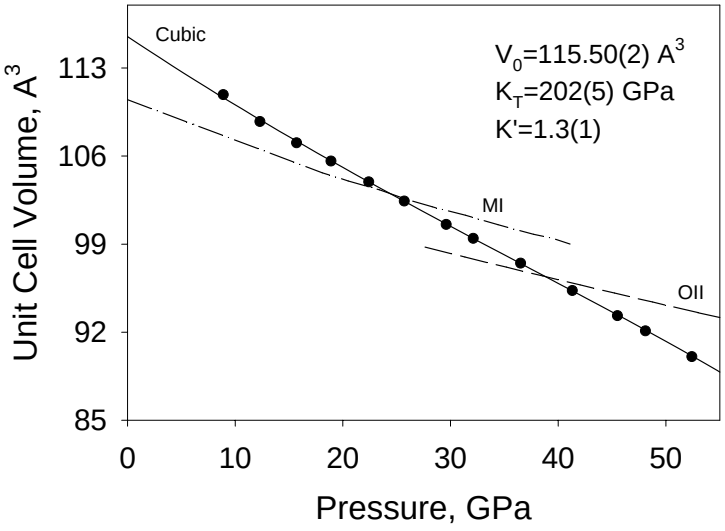

Fig. 3.8-5: Pressure dependence of the volume of the cubic fluorite-like TiO_2 phase (dots). Birch-Murnaghan equations of state (equation (1)) are plotted as solid lines with parameters K_{300}=202(5) GPa, K'=1.3(1), and V_0=115.50(1) Å^3/unit cell. Dashed and dot-dashed lines show relations for the OII and MI phases respectively.

d. *Size effects on the structure and phase transition behaviour of baddeleyite TiO_2 (V. Swamy/Victoria, N.A. Dubrovinskaia, L.S. Dubrovinsky and F. Langenhorst)*

Several high-pressure studies on nanocrystalline semiconductor systems such as CdSe and CdS have shown that these nanocrystals behave as nearly defect-free single structural domains that cycle through the transitions between four-coordinated (wurtzite and sphalerite) and six-coordinated (rock salt) structures reproducibly, with attendant simple phase transition kinetics. While considerable understanding of the microscopic mechanisms and kinetics of the pressure-induced first-order solid-solid phase transition has been achieved by investigating CdSe type nanocrystal systems, the size effects on the detailed atomic arrangements in the crystal structures and on other physical properties of the resulting high-pressure phases have

not been investigated in detail. As the crystallites' size shrinks to the nanoscale dimensions (up to a few hundred nanometers and less), a fraction of the constituent atoms placed at or near the surface in coordination environments (substantially different from the coordination environments in the bulk material) becomes significant. Such changes in the atomic arrangements may not be clearly noticed in high symmetry systems such as nanocrystalline Cd chalcogenides. We, therefore, chose to study nanocrystalline TiO_2 to understand the size-effects on the crystal structure, bulk modulus, and crystallite size evolution across the pressure-induced orthorhombic α-PbO_2 – monoclinic baddeleyite structural phase transition. TiO_2 is a particularly important model system in the study of phase transition behaviours of oxides. First, bulk (microparticle) TiO_2 has long served mineral physicists as a model system in the study of the pressure-induced phase transitions of rutile-structured stishovite SiO_2 in the depths of Earth's mantle. Second, nanocrystalline TiO_2 has been used as a prototype to investigate the size-dependent phase transition behaviour of nanoscale oxides in terrestrial environments. Furthermore, in our view, the low-symmetry structure of baddeleyite TiO_2 is an ideal case for examining size-induced changes in the crystal structure because of the extra degrees of freedom in the fractional atomic coordinates.

We investigated pressure-induced changes in nanocrystalline TiO_2 in compression-decompression cycles spanning 0-46 GPa. A comparison of the *in situ* high-pressure XRD spectra of the nanocrystalline and bulk baddeleyite structures at 34(1) GPa shown in Fig. 3.8-6 reveals distinct differences at medium to high 2Θ ranges. Additional diffraction peaks are seen in the case of nanocrystalline baddeleyite. Rietveld refinement of the data in the space group $P2_1/c$ yielded comparable good quality solutions (Fig. 3.8-6). Significantly, the *a* and *b* unit cell parameters of the nanocrystalline baddeleyite are 1.4 % and 1.7 % larger than those of the bulk phase. Similarly, the unit cell constant *c* is marginally bigger (0.4 %), whereas the cell angle β is essentially the same in comparison with the bulk structure parameters. The calculated unit cell volume for the nanocrystalline baddeleyite at 34(1) GPa, 104.20 $Å^3$, is about 3.6 % larger than that of the bulk structure, 100.60 $Å^3$, clearly demonstrating size-induced lattice expansion.

The crystallite size and shape changes accompanying the pressure-induced structural transformations in nanocrystalline TiO_2 were examined by comparative TEM observations of the starting anatase and the samples quenched to room pressure in the DAC after 50 compression-decompression cycles in the 0-40 GPa pressure range. The baddeleyite structure is not quenchable even as nanocrystals and, therefore, could not be examined under TEM. As seen in Fig. 3.8-7, the starting anatase has fairly equant crystallites with an average size of 34 nm (30-40 nm range). A recovered α-PbO_2 sample (Fig. 3.8-7) shows crystallites that are elongated with sizes in the 26-35 nm range and an average value of about 30 nm. The crystallite size reduction in the α-PbO_2 is approximately consistent with the density difference between the two phases. Crystallite coarsening as a result of sintering could not be observed in the transformed material, despite laser- and electrical-heating. This indicates that the majority of the crystallites are preserved as coherent units across multiple transitions involving 6 to 7 Ti-O coordination change amongst anatase, α-PbO_2, and baddeleyite. This is suggestive of the "single structural domain" behaviour of the nanocrystalline system.

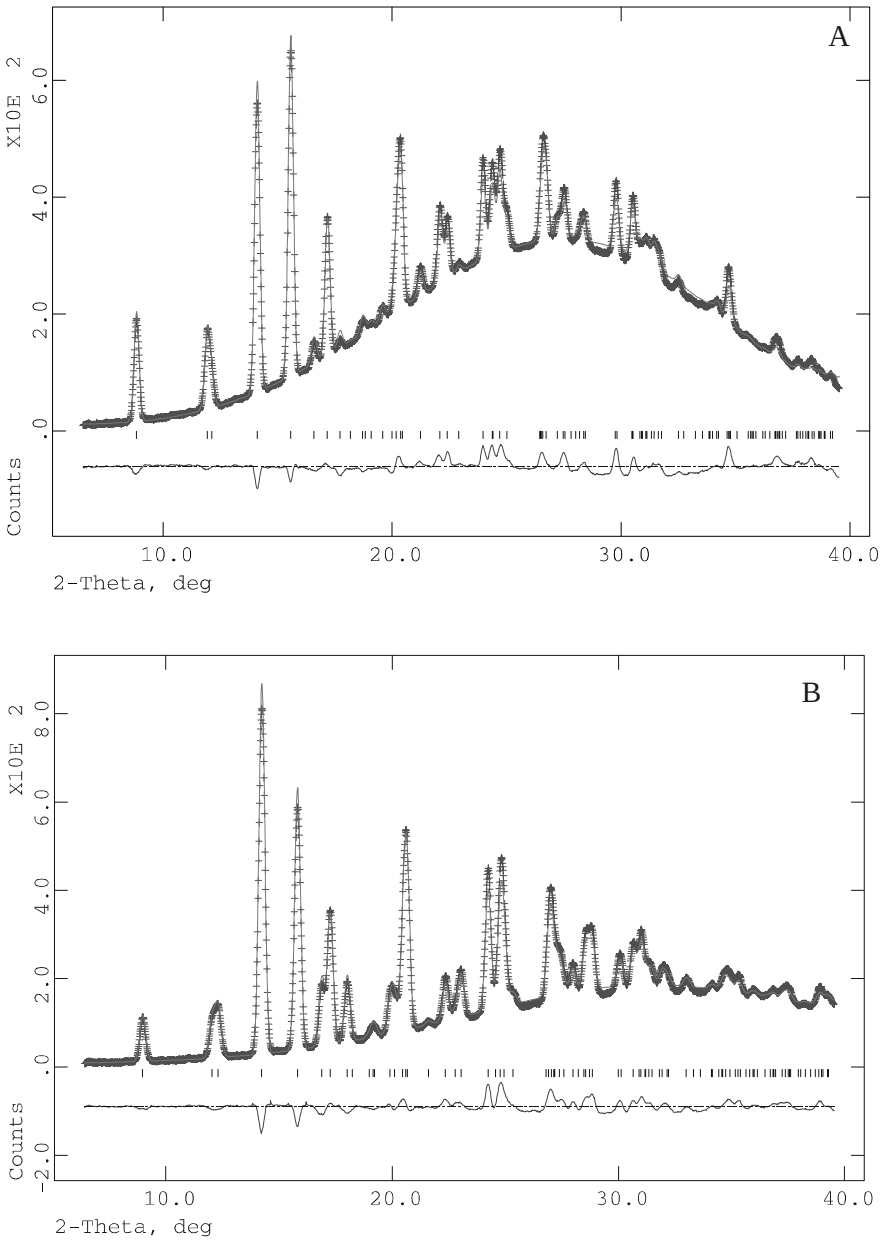

Fig. 3.8-6: Powder XRD spectra of baddeleyite structured TiO_2 recorded at room temperature and 34(1) GPa along with calculated and difference (experimental-calculated) XRD profiles obtained from Rietveld analyses. The short vertical bars indicate XRD peak positions obtained in the Rietveld refinement. **(A)** The baddeleyite synthesized from nanocrystalline anatase has the following crystal structural data: a = 4.589(1) Å, b = 4.849(1) Å, c = 4.736(1) Å, and β = 98.6(1)°. Space group $P2_1/c$. The x, y, and z fractional atomic coordinates for the titanium and two oxygen atoms in the asymmetric unit are: Ti = 0.309(1), 0.045(2), 0.218(1); $O_{(1)}$ = 0.056(1), 0.347(1), 0.282(1); and $O_{(2)}$ = 0.425(1), 0.727(1), 0.463(1). R_p = 4.6 % and R_{wp} = 5.4 %. **(B)** The baddeleyite synthesized from microcrystalline anatase has the following crystal structural data: a = 4.525(1) Å, b = 4.767(1) Å, c = 4.718(1) Å, and β = 98.7(1)°. The fractional atomic coordinates for titanium and oxygen atoms are: Ti = 0.276(2), 0.037(1), 0.212(2); $O_{(1)}$ = 0.109(1), 0.382(1), 0.261(1); and $O_{(2)}$ = 0.435(1), 0.768(1), 0.488(1). R_p = 3.0 % and R_{wp} = 3.5 %.

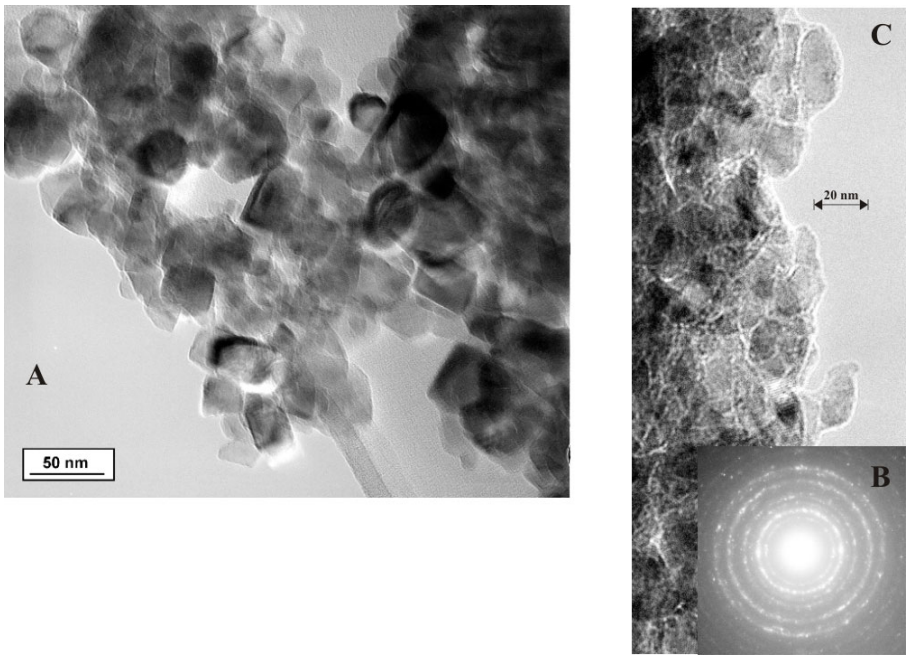

Fig. 3.8-7: **(A)** TEM image of the starting nanocrystalline anatase. The crystallites are equiaxial with an average diameter of 34 nm (size range 30-40 nm). **(B)** Electron diffraction of the α-PbO_2 structured TiO_2 recovered from the DAC after 50 compression-decompression cycles in the pressure range, where bulk α-PbO_2 and baddeleyite structures are stable (up to 40 GPa). **(C)** TEM image of the recovered α-PbO_2 sample shown in (**B**). The crystallites are elongated and have sizes in the range of 26-35 nm with an average diameter of about 30 nm.

e. *Structural transitions in Cu_2O at pressures up to 11 GPa (D. Machon, V.P. Dmitriev/ Grenoble, L.S. Dubrovinsky, V.V. Sinitsyn, I.V. Kuleshov and E.G. Ponyatovsky/ Chernogolovka)*

Copper oxide is one of the main chemical constituents of most high-temperature superconductors. The electronic properties of the Cu-O chains are believed to be responsible for their superconductivity. The study of the structural behaviour of various copper oxide forms, under different thermodynamic conditions, is therefore important for the understanding the nature of high-temperature superconductivity.

In (divalent) cupric oxide, CuO, the initial monoclinic phase is stable up to pressure of 70 GPa and temperature of 3000 K, and within this P,T range its structural behaviour is fully understood. In (monovalent) cuprous oxide, however, the situation is more complex. The semiconductor Cu_2O (called cuprite in mineralogy), exhibits sundry structural and chemical transformations in the pressure range up to 20 GPa and ambient temperature. The equilibrium phase diagram of copper oxide involves the chemical reaction, $Cu_2O \rightarrow CuO+Cu$, with, at room temperature, an equilibrium pressure value of 4 to 5 GPa. All phase transitions observed at higher pressure in this compound occur therefore between metastable phases.

At ambient conditions, Cu_2O crystallizes as a cubic phase with the space group $Pn\bar{3}m$ (Z=2) and a_0=4.627 Å. Its structure can be represented as the result of two interpenetrating face-centered F (for the Cu atoms) and body-centered I (for the O atoms) lattice complexes. At high pressure (and ambient temperature) the structural behaviour of Cu_2O has been studied at first by different groups with inconsistent results. To resolve the contradictions, detailed *in situ* study of the Cu_2O structure at pressures up to 10 GPa was called for, using more powerful tools (synchrotron radiation and area detector) than in the past.

Whether cuprite was compressed under hydrostatic or under non-hydrostatic conditions did not greatly affect the evolution of the diffraction spectra with pressure (Figs. 3.8-8 and 3.8-9). The visually most obvious difference was observed in the width of the diffraction profiles. In the hydrostatic regime diffraction lines remained sharp and narrow up to ~ 3.0 GPa, whereas in the non-hydrostatic regime the same lines dramatically increased in width, Δ, already at moderate pressures (below 1.0 GPa). Upon decompression, the reflections remained broad, *i.e.* this effect is irreversible, while the peak positions recovered their initial values (Figs. 3.8-8 and 3.8-9).

Furthermore, in the hydrostatic regime, the diffraction peaks 200, 220 and 311 of the cubic phase I started to split at pressures upward to 0.7 GPa, indicating a transition to another phase. At pressures higher than 7 GPa the peak splitting was gradually absorbed in the greater increase in the line width of the peak profiles. In the non-hydrostatic regime, it is not unlikely that similar peak splitting took place, but was masked by much larger line broadening occurring already at lower pressure.

The peak splitting, observed particular well under hydrostatic conditions (Fig. 3.8-9), can be interpreted as a slight tetragonal distortion of the cubic parent lattice. All the diffraction lines of the distorted structure can be indexed in the space group $P4_2/nnm$ (Z=2), an equitranslational subgroup of $Pn\bar{3}m$. The volume change due to the I→Ia phase transition is about 1 %. In such a *proper ferroelastic* transition, the *spontaneous* physical quantities, which are the second-rank strain tensor components, play the role of a primary order parameter. The primary order parameter for the m3m->4/mmm phase transition, according to Landau theory, is proportional to the spontaneous strain $e_t=(2e_{zz}-e_{xx}-e_{yy})$.

There are two mechanisms that can be responsible for the peak broadening observed. These are the deformational mechanism connected with the microscopic strain due to non-hydrostatic conditions and the mechanism connected with formation of the nano-sized grains. In order to distinguish between these two mechanisms, we analyzed also the diffraction patterns of the samples recovered to normal conditions after compression under different conditions (the top curve in Figs. 3.8-8 and 3.8-9). Figure 3.8-10 demonstrates a considerable increase in the microstrain induced in the sample and resulted in the diffraction peak broadening. Moreover, the material remains essentially stressed even when pressure was released (Fig. 3.8-10). This latter effect indicates indirectly onset, in course of pressure

treatment near 10 GPa, of a considerable amount of structure defects that locked up the microstrain and kept the sample in a stressed state. As the transition into the hexagonal phase, inducing an essential rearrangment of the Cu sublattice, takes place in this pressure range, the onset of defects and the corresponding microstrains can be considered as precursors of the phase transition. Particularly, the Ia-II phase transition changes the packing sequence of the Cu-containing layers from a cubic ABCABC… to a hexagonal ABAB… one. This rearrangement of the stacking sequence is known to generate a considerable amount of low-energy stacking faults. These faults can be retained after the pressure release.

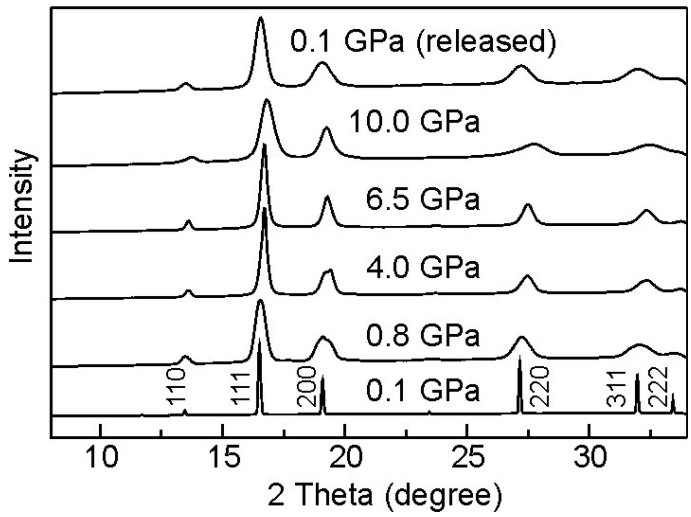

Fig. 3.8-8: Representative diffraction patterns of Cu_2O in dependence on quasi-hydrostatic pressure to 10 GPa.

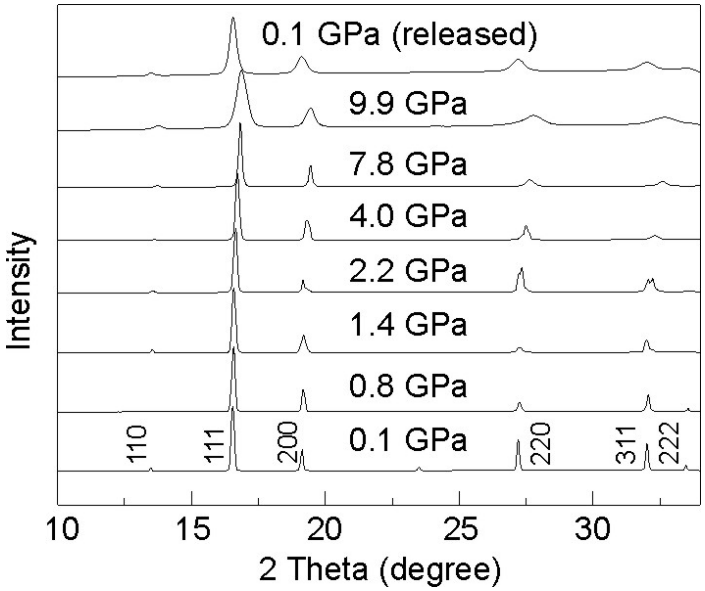

Fig. 3.8-9: Evolution of the Cu_2O diffraction pattern in dependence on hydrostatic pressure of silicon oil to 10 GPa.

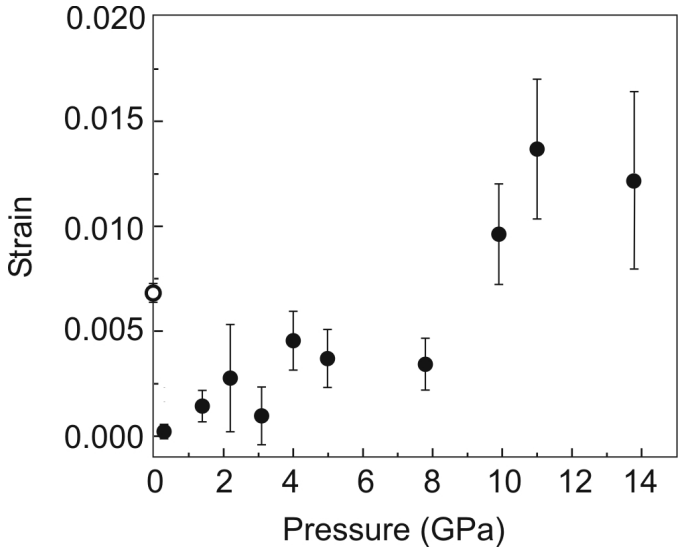

Fig. 3.8-10: Microstrain induced in Cu_2O under high pressure. Open circle corresponds to the recovered sample.

f. *Pressure tuning Raman spectroscopy of the spin crossover coordination polymer $Fe(C_5H_5N)_2[Ni(CN)_4]$ (G. Molnár/Toulouse, T. Kitazawa/Funabashi and L.S. Dubrovinsky)*

Certain (pseudo)octahedral transition metal complexes are known to display a molecular bistability of high-spin (HS) and low-spin (LS) electron configurations, which are distinguished by different occupation of antibonding e_g and non-bonding t_{2g} *d* orbitals of the central metal ion. The electronic ground state of these spin crossover complexes may be reversibly interchanged under external stimuli, such as temperature, pressure, magnetic field or light irradiation.

The molecular spin crossover phenomenon is influenced in the solid state by intermolecular interactions, which may give rise to a discontinuous, first-order phase transition accompanied by a hysteresis loop. Numerous efforts have been devoted to the design and study of such cooperative systems. One successful synthetic approach is based on the idea of replacing molecular crystals by polymers in which the active sites are linked to each other by chemical bridges allowing the propagation of strong interactions. However, the number of such systems is still rather limited and the physics governing their properties is less explored than for molecular complexes.

In order to better understand the vibrational properties of these compounds we have decided to study isotope substitution and high-pressure effects on the complex $Fe(pyridine)_2[Ni(CN)_4]$. An externally applied pressure provides a direct means to test the effects of lattice contraction on the vibrational modes. We have selected this $Fe(pyridine)_2[Ni(CN)_4]$ for the following reasons:

(i) Among the complexes of the same family it has the lowest spin transition temperature (~ 202 K). Therefore one can study both the HS and LS phases in a reasonably large pressure range without heating the sample. (The pyrazine complexes are converted to the LS form already at the onset of the pressurization at room temperature.)

(ii) The sample is well crystallized with small (~ few μm) grains, which is perfectly compatible with the diamond anvil cell (DAC) technique. The other pyridine complexes consist of large grains and we could not establish hydrostatic conditions with these samples in the DAC. The usual technique of grinding can not be applied because we have found that it destroys the spin crossover properties of these compounds.

Selected Raman spectra of $Fe(pyridine)_2[Ni(CN)_4]$ at different pressures are shown in Fig. 3.8-11. In the frequency range investigated, two main groups of Raman frequencies occur: internal modes of pyridine (600-1700 cm^{-1}) and vibrations associated with the 2D polymeric sheet around 2150 cm^{-1} and below 600 cm^{-1}. These latter involve various coupled metal-ligand stretches and bendings as well as lattice modes. Plots of wavenumber versus pressure reveal discontinuities in the slope of the graph in the pressure range between ca. 6 and 14 kbar (Fig. 3.8-12). We explain these discontinuities by a pressure induced HS↔LS spin crossover since it is accompanied by similar changes in the Raman spectra to those observed earlier for the temperature induced spin transition, *i.e.* one can observe pronounced frequency changes below 600 cm^{-1} and only small frequency shifts above 600 cm^{-1}. The vibrational entropy change upon spin-crossover can be estimated for an oscillator with frequency ω in the low-frequency approximation as: $\Delta S = R\ln(\omega^{LS}/\omega^{HS})$. It appears that the usual assumption $\Delta S_{HL}{}^{0} \cong \Delta S_{HL}{}^{p}$ (index "0" is for ambient pressure) is a good one at moderate applied pressures in the $Fe(pyridine)_2[Ni(CN)_4]$ compound.

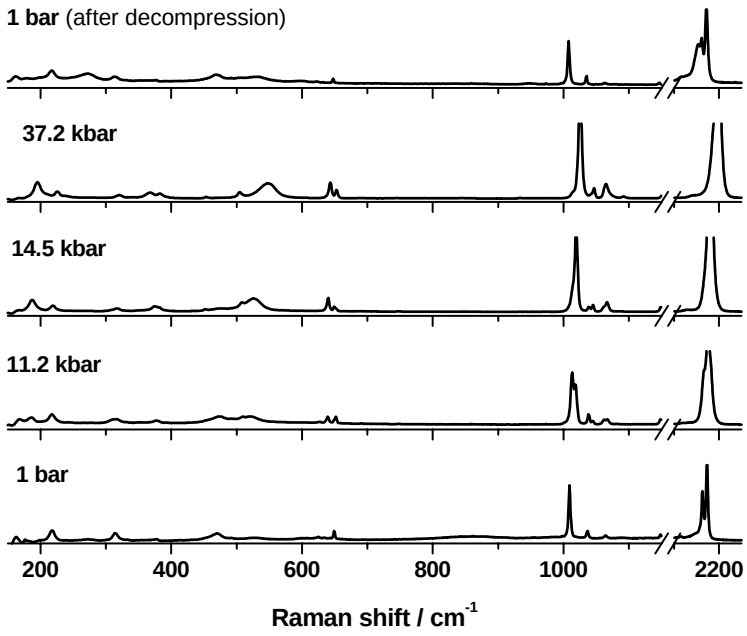

Fig. 3.8-11: Selected Raman spectra of $Fe(pyridine)_2[Ni(CN)_4]$ for different applied pressures at room temperature.

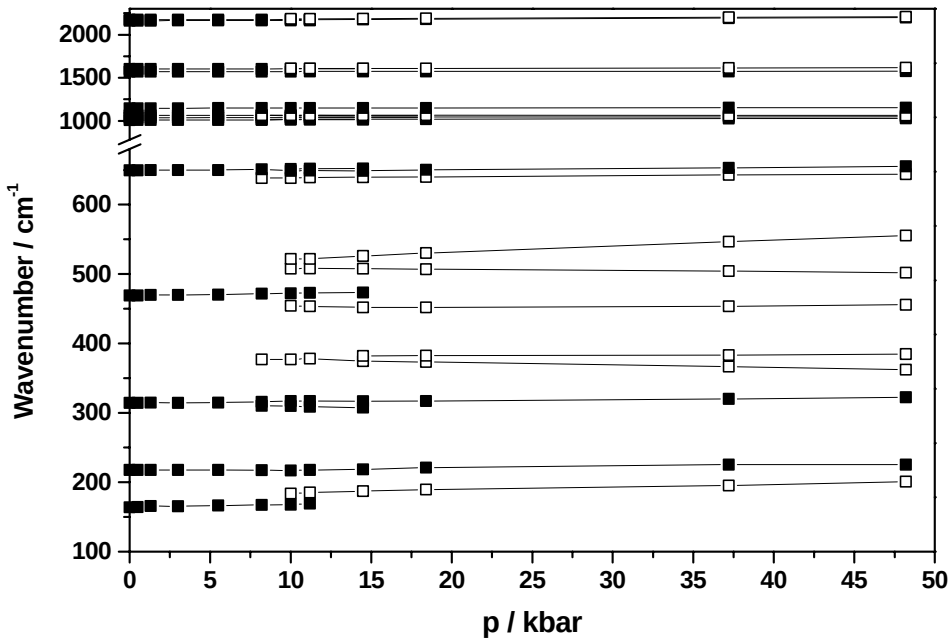

Fig. 3.8-12: The pressure dependence of Raman frequencies in Fe(pyridine)$_2$[Ni(CN)$_4$]. Closed (open) symbols represent modes assigned to the HS (LS) phase. Lines are inserted to guide the eye.

g. *Synthesis and structural characterization of new low dimensional zirconium phosphates (G.D. Gatta and R. Vivani/Perugia)*

The interest in the crystal chemistry of zirconium phosphates has grown considerably in recent years, due to the rapid development of new solid-state analytical techniques, and also because of a growing attention to new functional solids for material chemistry. A large variety of zirconium phosphate derivatives with tailor made properties can be prepared for specific applications in ion exchange, molecular intercalation and recognition, shape selective catalysis, proton conduction, non-linear optics, etc.

Most research in zirconium phosphate chemistry has been focused on layered α- and γ-phases and their derivatives. Their structure is made up of a connection of vertex sharing ZrO_6 octahedra and PO_4 tetrahedra. They are very insoluble solids, so they can be obtained as microcrystalline samples using a homogeneous precipitation method, which consists of leaving zirconium fluorocomplexes to slowly decompose in the presence of a phosphate solution. Furthermore, appropriate changes in the synthesis conditions can lead to the introduction of fluorine atoms and/or other anionic or neutral molecules into the zirconium coordination sphere, enlarging the number of accessible structures.

We have recently found that starting from the synthesis of layered zirconium phosphate of γ-type, with composition $Zr(PO_4)(H_2PO_4)\cdot 2H_2O$, changes in the pH of the reaction solution by addition of ammonia, produced the incorporation of an increasing number of fluorine atoms

coordinated to zirconium. These species, acting as terminal groups, induced a progressive reduction in the dimensionality of the solid obtained. One-dimensional single-chain and double-chain solids, with the $Zr[(NH_4)_2PO_4]_2F_2 \cdot H_2O$ (I) and $Zr(NH_4PO_4)[(NH_4)_2PO_4]F \cdot 0.5H_2O$ (II) formulae respectively, have thus been obtained. Their structure was solved "ab initio" by single crystal (I) and powder (II) X-ray diffraction data. Structure of I is monoclinic, space group $P2_1/n$, a = 10.889(3) Å, b = 10.520(3) Å, c = 12.412(3) Å, β = 115.70(2)°, while II is orthorhombic, space group $P2_12_12_1$, a = 5.351(1) Å, b = 9.247(1) Å, c = 22.644(1) Å.

These structures are topologically related to that of the γ-layered zirconium phosphate by a dimensional reduction procedure (Fig. 3.8-13). The double chain structure of II can be obtained by condensation of pairs of I single chains with NH_4F elimination, and the γ-ZrP structure can be ideally reconstructed by an iterated condensation of II chains through the replacement of fluorine atoms with triply connected phosphates coming from adjacent chains. The use of non-aqueous solvents for the synthesis can lead to new low-dimensional zirconium phosphate phases in which zirconium atoms are coordinated to different anionic and/or neutral species, such as chlorine, dimethylsulfoxide or water.

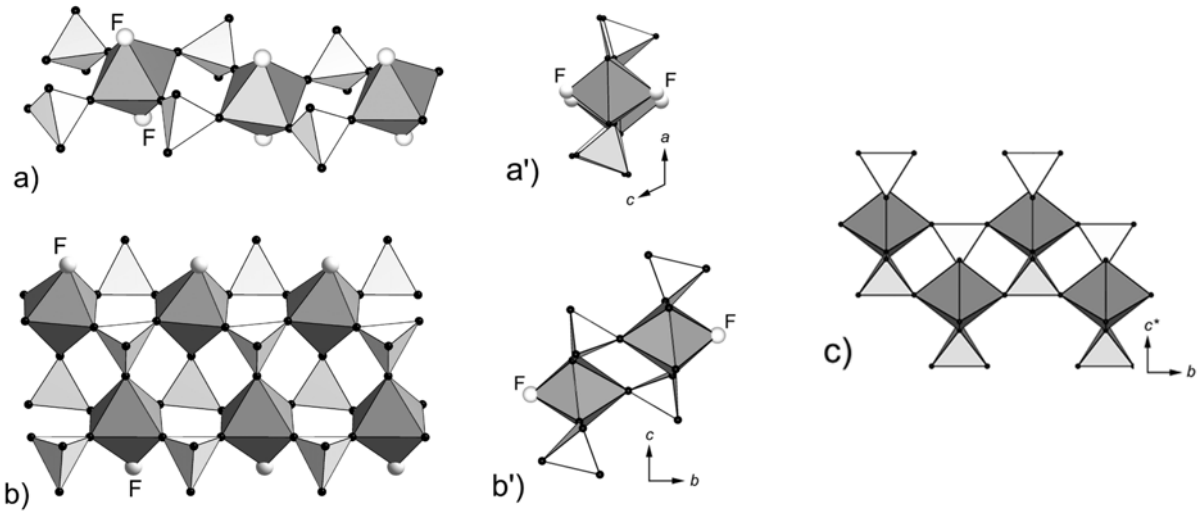

Fig. 3.8-13: Polyhedral representation of the chain structure of I (a and a'), and II (b and b') compared with that of a layer of γ-zirconium phosphate (c).

A new layered phase has recently been obtained using ethanol as a solvent, with the formula $Zr_2PO_4(NH_4PO_4)_2F(H_2O)$ (III), in which fluorine and water groups are coordinated to zirconium. This structure was solved "ab initio" by X-ray powder diffraction data by a -real space- optimization procedure using the FOX program. The structure is monoclinic, space group $P2_1/c$ and cell parameters a = 9.214(1) Å, b = 8.746(1) Å, c = 17.390(1) Å , β = 107.289(3)°. The asymmetric unit has 21 independent atoms. This beautiful "wave-like" layered structure is shown in Fig. 3.8-14.

The removal of ammonium counterions from the structure, by elution with HCl solutions, or by Na^+ ion exchange, induced the elimination of fluorine and water terminal groups, and the conversion into the 3D NASICON-type zirconium phosphate, with the formula $MZr_2(PO_4)_3$, in which M can be NH_4 or Na. Ball-and-stick models show that the ZrO_6-PO_4-framework topology of the two compounds is similar, and the dimensional change can be achieved by condensation of III sheets with the formation of Zr-O-P bridges (Fig. 3.8-14).

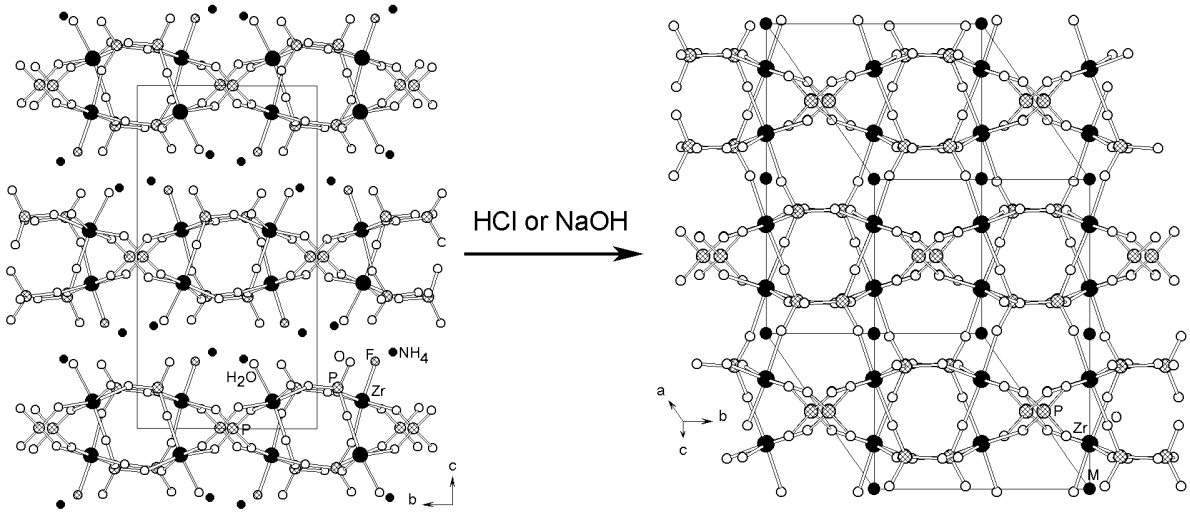

Fig. 3.8-14: Structures of $Zr_2PO_4(NH_4PO_4)_2F(H_2O)$ (III) viewed along [100] (left), and $MZr_2(PO_4)_3$, viewed along [210] (right).

3.9 Methodological Development

Modern experimental geosciences are impossible without continuing methodological development. Field-based geophysical and geochemical observations (such as depth-density profiles, elasticity, electrical conductivity, elements abundances, etc.) can only be successfully interpreted if high-quality data on Earth's materials properties can be experimentally obtained, preferably *in situ* at high pressure and high temperature simulating conditions in deep Earth's deep interior. The laser-heating system newly installed at Bayerisches Geoinstitut allows us to generate temperatures over 4000 K in diamond anvil cells (DACs). DAC is currently the only type of high-pressure apparatus capable of generating static pressures corresponding to the conditions at the center of the Earth. However, the properties of materials measured in DACs are often affected by non-hydrostatic conditions. The theory of angle-dispersive X-ray diffraction addresses this problem and proposes a way of collecting more precise data at ultra-high pressures.

Gigahertz ultrasonic interferometry is a new high-frequency acoustic method developed by collaborative efforts between Bayerisches Geoinstitut and the University of Colorado at Boulder. Using ultra-fast picosecond electronics, traditional ultrasonic travel-time experiments are extended to GHz frequencies for elasticity measurements on micrometer-sized (μm) samples. While this method was developed with high-pressure single-crystal applications in mind, here several new directions are explored by demonstrating that GHz-ultrasonics can also be applied to twinned crystals, glasses, and nanocrystalline materials.

Imperfection of natural silicate single crystals limits the areas of study for important Earth-forming minerals. The development of a new method to grow high-quality, large single crystals of silicate perovskites opens the new possibility of synthesis and characterisation of a broad class of Earth and synthetic materials.

Advances in analytical techniques are shown in new results in solid-state NMR.

a. *Laser heating in diamond anvil cells (L.S. Dubrovinsky and N.A. Dubrovinskaia)*

Experimental modelling of the conditions in deep Earth's deep interior requires simultaneous high pressures and high temperatures. The only method which currently allows one to achieve temperatures over 4000 K in the megabar pressure range is laser-heating in diamond anvil cells (DACs).

Figure 3.9-1 shows a general view and an optical scheme of the laser heating set up for experiments with diamond anvil cells installed at BGI. It consists of the three major components – laser generators, optics for the laser light delivery towards a DAC, and devices for visualization and spectroradiometry.

As a sources of laser light we use a Nd:YAG Quantronix 117 generator operating in CW TEM00 mode (light wavelength of 1074 nm) at maximum power of 15 W, and a Nd:YLF Quantronix two-head generator operating in CW TEM00 mode (light wavelength of 1064 nm) at maximum power of 70 W. All operations with lasers are computer-controlled.

We have constructed a flexible optical environment for the laser-heating system. It can operate in both one- and double-side heating modes. Exchangeable Mitutoyo long working distance objectives allow us to focus the laser beam down to 3 μm in diameter that makes possible very selective heating of only localized parts of the samples compressed in DACs. While with Mitotoyo objectives we realize so-called normal geometry (a laser beam is normal to the diamond and sample surfaces), with a lens (f.l.=75 mm) we can bring the laser light into the cells at an angle up to 45°. When the lenses are used, the spot size at the sample plane can be as large as 50 μm in diameter.

For sample visualization we have installed two digital cameras. Both of them are connected to the computer for digital recording during experiments.

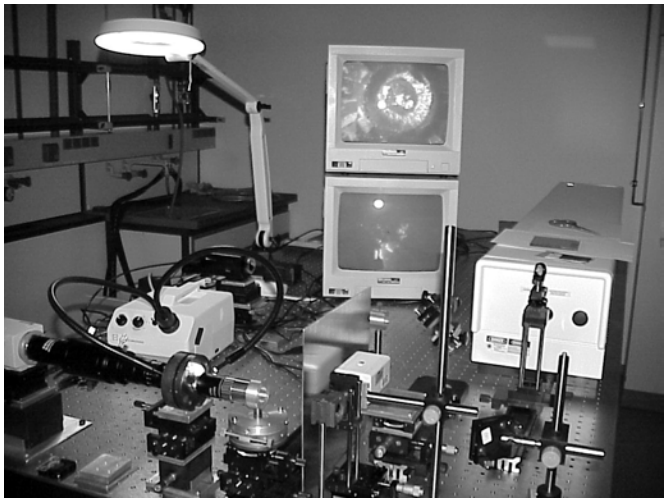

a

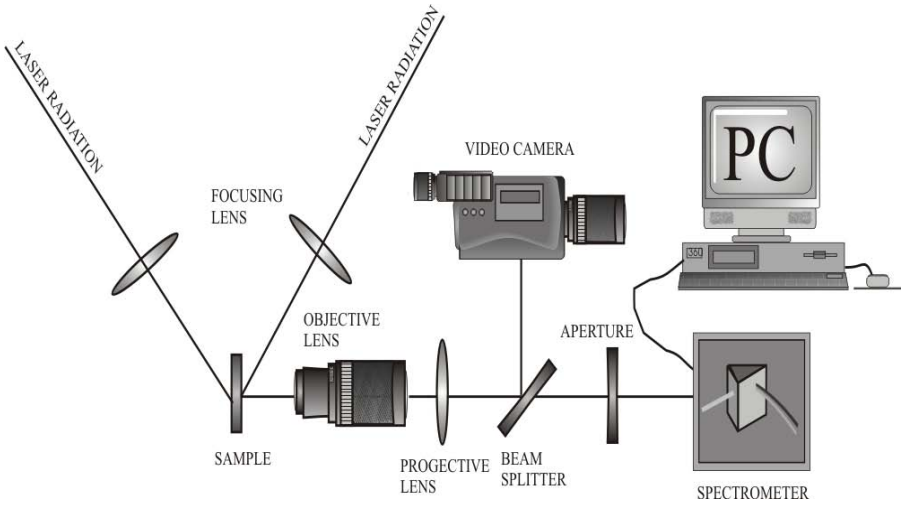

b

Fig. 3.9-1: Double-side YLF-laser heating set up for experiments with diamond anvil cells at Bayerisches Geoinstitut (a – general view, b – optical scheme)

b. *Angle dispersive diffraction under nonhydrostatic stress in diamond anvil cells (L.S. Dubrovinsky and N.A. Dubrovinskaia)*

In situ X-ray diffraction under pressure provides unique information about phase transitions, chemical reactions, and the rheological and elastic properties of materials. Progress in the diamond anvil cell (DAC) technique has made it possible to conduct static compression experiments at pressures over 400 GPa. However, X-ray diffraction data as well as the measured properties of materials are often affected by nonhydrostaticity. DAC is an opposed-anvil type high-pressure apparatus and its cylindrical symmetry causes uniaxial stress if compressed material has a non-zero yield strength. It is often assumed that the resulting stress in the DAC is deviatoric. The diffraction data obtained under non-hydrostatic stress conditions contains much more information on the elasticity and rheology of the material than data recorded in hydrostatic compression experiments. In DAC, stress σ_{33} along the loading direction is different from that in the gasket plane σ_{11} (usually $\sigma_{33} > \sigma_{11}$). Such a stress distribution should produce systematic variations in the shape of powder diffraction lines depending on the angle between the incident beam and loading direction. If the incident beam coincides with the loading direction (so called parallel diffraction geometry, PLG), the diffraction lines from the center of compressed specimen, recorded with an area detector, should be usual Debye-Scherrer rings, while, if the loading direction is normal to the incident beam (perpendicular diffraction geometry, PDG), the diffraction rings transform to ellipses. Generally, the shape of ellipse depends on the elastic properties of materials, the value of the uniaxial stress component ($t = \sigma_{33} - \sigma_{11}$), the *hkl* Miller indices of the diffraction line and the angle between the incident beam and the loading direction. By analyzing the shape of diffraction ellipses (or *d*-spacings) as a function of the angle between the incident beam and the loading direction, it is possible to extract information on single-crystal elastic moduli and the stress state of the material in DAC experiments. We analyze the effect of nonhydrostatic stress in DACs using the shape and width of the diffraction lines acquired with an area detector.

Before we can proceed with the analysis of strain in the sample, we must define the axes associated with a DAC (specimen or stress reference frame), with a detector and incident beam (measurement frame), and with a crystal frame (in which single-crystal elastic moduli are defined). We introduce an angle ω between the incident beam and the loading direction, an angle χ measured in the plane of the area detector between the projections of the loading direction and the diffracting-plane normal, and an angle ψ between the loading direction and the diffracting-plane normal (Fig. 3.9-2 (a, b)). The diffracting plane (*hkl*) in crystallographic axes of the cubic system X_i'' is shown in Fig. 3.9-2b. The diffracting-plane normal *OO*' is perpendicular to (*hkl*). The direction *OO*' coincides with X_3'; X_1' is directed from *O*' towards the point of intersection of (*hkl*) and X_1''; and X_2' is normal to both X_1' and X_3'. The set of orthogonal "stress axes" X_i is such that X_1 is in the (*hkl*) plane and makes an angle φ with X_1'; X_3 makes an angle ψ with X_3'; and X_2 (not shown on Fig. 3.9-2b) is perpendicular to both X_3 and X_1.

The data is then processed using an algorithm for lattice strain calculations in non-hydrostatically compressed sample in the DAC. In all previous studies it was assumed that the direction of the normal to the given (*hkl*)-plane does not change due to stress and considered only changes in d_{hkl}. In case of angle dispersive diffraction studies, the effect of both the length and direction of the scattering vector is important. We took this into account giving the analysis of lattice strain under deviatoric stress in DAC. Numerical simulations (Fig. 3.9-3) show that deviatoric stress changes *d*-spacings and produces broadening of all diffraction lines. Both these phenomena depend on the elastic properties of the material, the value of the uniaxial stress component, and the orientation of the cell (loading direction) with respect to the incident beam.

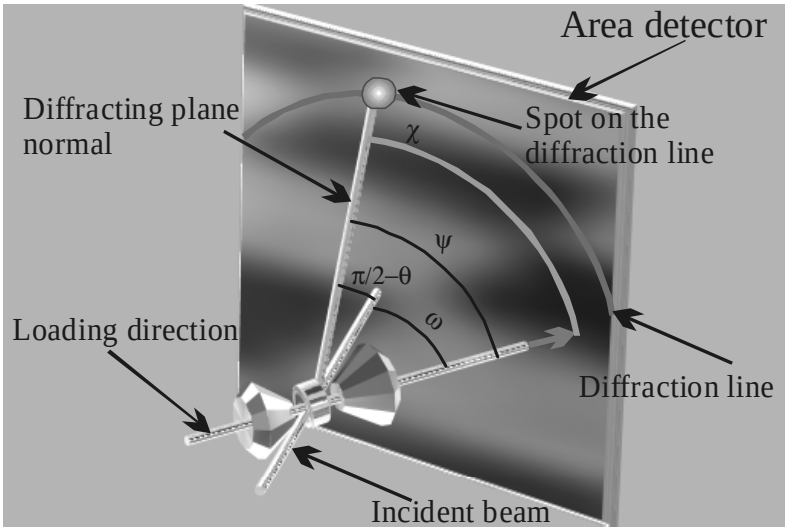

a

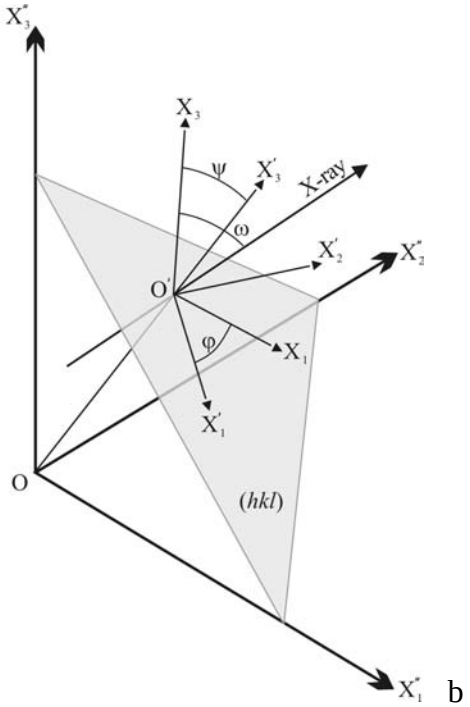

b

Fig. 3.9-2: The definition of angles (a) and axes (b) used for analysis of the stress state in the sample compressed in DAC.

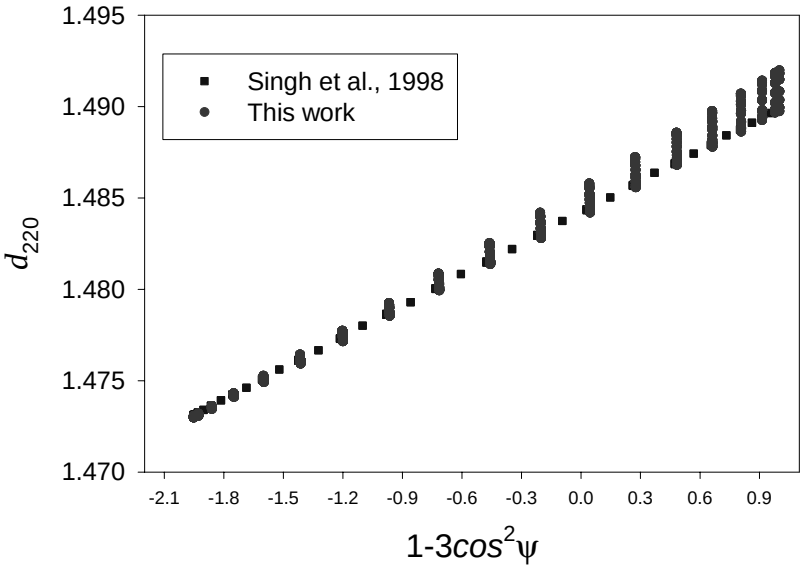

Fig. 3.9-3: Simulated variation of *d*-spacings for (220) diffraction lines of MgO as a function of $1-3\cos^2\psi$ in perpendicular diffraction geometry ($\omega=90^o$). In all calculations we used the following values of elastic compliance: S_{11}=0.00403 GPa^{-1}, S_{12}=-0.00094 GPa^{-1}, S_{44}=0.00649 GPa^{-1}, and λ=0.4 Å typical for synchrotron X-ray powder diffraction experiments in DACs. The lattice parameter of MgO is a_0=4.20 Å and the uniaxial stress component t=2 GPa, while σ_P=0.

c. *Application of gigahertz ultrasonic interferometry to twinned crystals, glasses, and nanocrystalline materials (S.D. Jacobsen, A. Kantor, G.D. Gatta and T. Boffa Ballaran, in collaboration with M. Carpenter/Cambridge and H. Spetzler/Boulder)*

Gigahertz ultrasonic interferometry is a new high-frequency acoustic method developed by collaborative efforts between Bayerisches Geoinstitut and the University of Colorado at Boulder. Using ultra-fast picosecond electronics, traditional ultrasonic travel-time experiments are extended to GHz frequencies for elasticity measurements on micrometer-sized (μm) samples. While this method was developed with high-pressure single-crystal applications in mind, here several new directions are explored by demonstrating that GHz-ultrasonics can also be applied to twinned crystals, glasses, and nanocrystalline materials.

Twinned crystals

Perovskite-type $LaAlO_3$ is the least-distorted (pseudocubic) of the rare-earth perovskites. It is widely used in various electronic devices and as a substrate for high-temperature superconductors. However, like other perovskite-type phases, $LaAlO_3$-pv crystals have a tendency to twin on quenching, making single-crystal elasticity experiments difficult or impossible. We applied GHz-ultrasonic interferometry to this problem by making use of the micro-acoustic field generated by our GHz-thin film transducers. A photomicrograph of a twinned $LaAlO_3$-pv crystal is shown in Fig. 3.9-4. The twin planes run parallel to the

pseudocubic [110] direction. We determined the elastic tensor of this phase by firing the ultrasonic P- and S-waves between the twin planes at the locations shown in Fig. 3.9-4. In the case of shear, the polarization direction was parallel to the twin-planes. When the shear polarization was perpendicular to the twin planes, we did not observe a signal. The resulting elements of the elastic tensor for $LaAlO_3$-perovskite are (in GPa), c_{11} = 307(3); c_{44} = 146(1); and c_{12} = 180(2). The calculated bulk (K_S) and shear (G) moduli are 222(2) and 105(1) GPa, respectively.

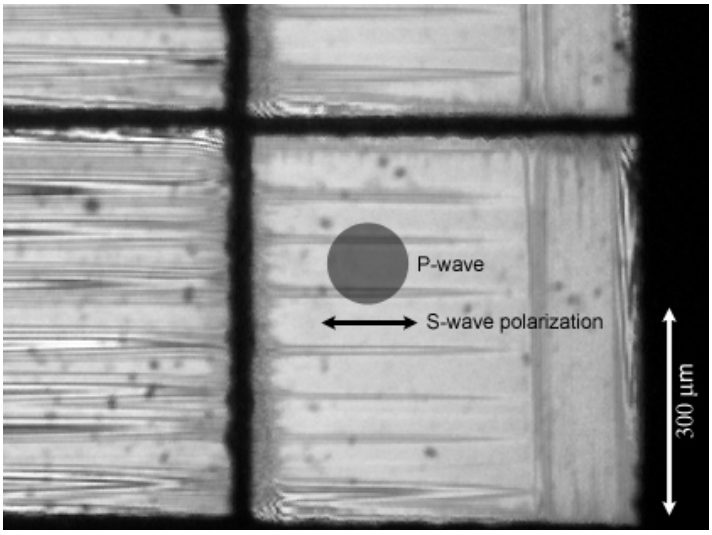

Fig. 3.9-4: Photomicrograph of twinned perovskite-type $LaAlO_3$ indicating where the micro-ultrasonic measurements were taken. P-waves were fired between the twins in an area represented by the grey circle. Shear-wave velocities were measured similarly, but with the polarization vector pointing parallel to the twin planes. In this way, the elastic tensor of this twinned crystal was determined from four pure-mode velocities.

Glasses

Glasses are elastically isotropic, requiring only the bulk sound velocities (V_P and V_S) and the density (ρ) to obtain the bulk and shear moduli. In the diamond anvil cell, we are exploring the use of GHz shear-ultrasound to observe pressure-induced liquid-glass phase transitions in the most common liquid pressure mediums used in high-pressure crystallography. In two separate experiments, we loaded a 4:1 mixture of methanol and ethanol, and then glycerol into a diamond cell along with ruby chips for pressure calibration. Shear waves were transmitted into the cell through one of the anvils, and the pressure was increased until a shear-wave reflection was detected from the opposite anvil culet. This reflection indicates that the shear waves have passed completely through the sample chamber (and back), providing the pressure of the liquid-glass phase transition, at least for these dynamic timescales (at 1-2 GHz). The observed transition pressures are 9.2 GPa for the alcohol mixture, and 4.1 GPa for glycerol (±0.5 GPa). Finally, the shear-elasticity of the glass phases was estimated by increasing the pressure further and measuring the distance between the diamond culets (d) at

each pressure. Measured shear travel-times (t_S) were converted to velocity using $V_S = 2d/t_S$, and plotted in Fig. 3.9-5.

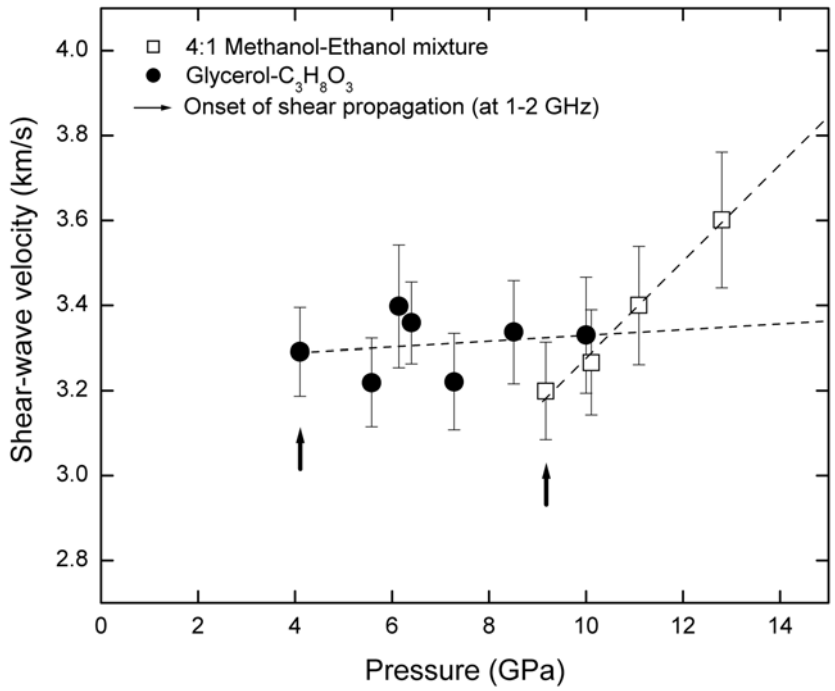

Fig. 3.9-5: Plot of shear-wave velocity with pressure in the glasses formed from a 4:1 Methanol-Ethanol mixture (open squares) and glycerol (circles). The onset of shear-wave propagation through these liquids at 9.2 and 4.1 (±0.5 GPa), respectively, determines the pressure-induced glass transition (at dynamic time scales). These liquids are widely used as hydrostatic pressure mediums in high-pressure crystallography.

Nanocrystalline materials

Many interesting high-pressure phases cannot be synthesized as quality single crystals. In addition, high-pressure reconstructive transitions often destroy single crystals under study *in situ*. The possible application of gigahertz ultrasonic interferometry to nano-polycrystalline materials is being explored. Ultrasonic measurements are routinely made at MHz-frequencies (with millimeter wavelengths) on polycrystalline samples with grain sizes of about 50 μm, resulting in a wavelength-to-grain size ratio of about 20. At 1 GHz, the acoustic wavelengths are 1-10 μm in minerals. It is therefore theoretically possible to perform acoustic elasticity experiments at GHz-frequencies on polycrystalline samples with grain sizes of ~ 50 nanometers or less.

This idea was tested by preparing a nanocrystalline sample in the diamond anvil cell. Nanocrystalline anatase-TiO_2 with ~ 30 nm grain size was compressed in a diamond cell with 800 μm culets. The sample was compressed to about 14 GPa using a hardened-steel gasket

pre-indented to 80-μm thickness with a 400-μm diameter hole. Upon decompression, Raman spectroscopy revealed that the anatase had completely transformed to the α-PbO_2-type TiO_2. The resulting dense material was placed (unpolished) on the GHz P-wave buffer rod and a good sample echo was obtained. A P-wave travel time t_P = 10.11(6) ns was measured, but requires a more quantitative thickness and grain orientation analysis for interpretation of a velocity. The test however does confirm that gigahertz ultrasonic interferometry can be used to study nanocrystalline materials synthesized at high pressure.

d. *The flux-growth of large silicate perovskite single crystals (D.P. Dobson/London and S.D. Jacobsen)*

We have developed a new method to grow high-quality, large single crystals of silicate perovskites using NaCl as a flux. Crystals grown by this method are largely un-twinned and can reach > 300 μm. X-ray diffraction of recovered flux-grown crystals shows that they are strain-free and have very narrow peak widths. The production of high-quality large perovskite single crystals opens the possibility of many new areas of study for this important Earth-forming mineral.

Starting materials consisted of fused stoichiometric mixtures of MgO, SiO_2, Al_2O_3 and Fe_2O_3. Iron bearing glasses were reduced under H_2-CO_2 mixtures at 1000 °C. These glass powders were packed to half-fill rhenium foil capsules, the remainder of the capsule being packed with NaCl. The closed capsules, which were between 2 and 2.5 mm in length, were loaded in standard 10/4 multi-anvil assemblies and compressed to 25 GPa. In order to maximise the crystal size a complex heating path was employed which minimised nucleation and increased growth on existing perovskite seeds:

1) The glass was transformed to perovskite below the $MgSiO_3$-NaCl eutectic temperature, at 1700 °C.

2) The temperature was increased to 2050 °C and maintained for 30 minutes, during which time the NaCl melted and reached saturation in perovskite.

3) The temperature was rapidly decreased to 2000 °C and maintained for 20 minutes, allowing perovskite nucleation in the melt and on the capsule walls.

4) The temperature was raised by 30 °C which re-dissolved most of the newly formed perovskite seeds, leaving relatively few seeds for subsequent growth.

5) The sample was slowly cooled at ~ 1 °C/min by 50 °C allowing slow growth of the seed crystals.

6) Steps 4 and 5 were repeated, resulting in growth of seeds and redissolution of any new nuclei, until the solidus was reached (around 1850 °C for NaCl-$MgSiO_3$ at 25 GPa) when the experiment was quenched. This *T-t* path is cartooned in Fig. 3.9-6.

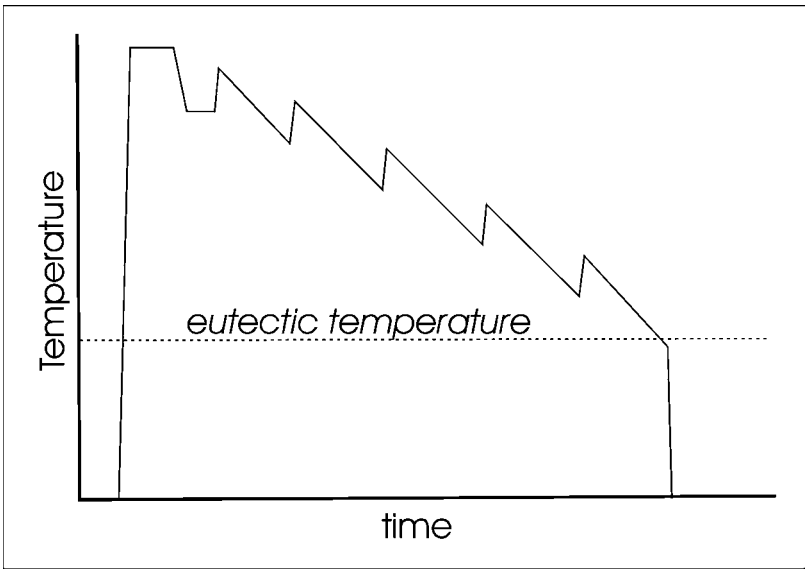

Fig. 3.9-6: Schematic T-t path for flux-growth of $MgSiO_3$ perovskites.

Recovered capsules contained euhedral perovskite crystals which were scattered through the NaCl flux and bonded onto the surface of the remaining unreacted perovskite (Fig. 3.9-7); NaCl was removed by rinsing in distilled water.

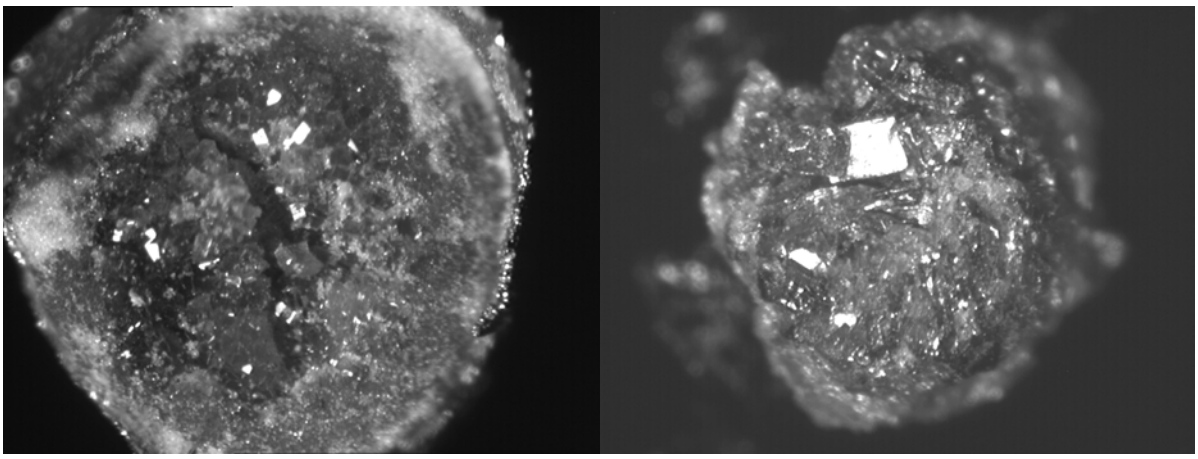

Fig. 3.9-7: Flux grown perovskite as recovered after dissolution of the flux. Left: $Mg_{0.98}Na_{0.01}Al_{0.04}Si_{0.98}O_3$. Right: $Mg_{0.94}Fe_{0.04}Na_{0.01}Al_{0.02}Si_{0.99}O_3$. The field of view is approximately 1.5 mm in both images.

Electron probe analysis of recovered perovskites is reported elsewhere and shows some contamination by Na (< 0.5 wt.% Na_2O), but no detectable Cl in the perovskites. We suggest that using KCl or $MgCl_2$ flux will reduce or entirely eliminate contamination by the flux.

The perovskite crystals grown in this study are currently being prepared for single crystal studies of their structural and elastic properties.

e. *New solid-state NMR results (M. Bechmann, X. Helluy and A. Sebald)*

Improved efficiencies in double-quantum filtration C7 MAS NMR experiments on spin systems with large chemical shielding anisotropies (M. Bechmann and A. Sebald, in collaboration with P. Tekel/Nancy and H. Foerster/Rheinstetten)

Dipolar recoupling based MAS NMR experiments are important structure-determination tools in many MAS NMR applications. A variety of dipolar recoupling schemes can be applied successfully when dealing with spin systems displaying only small chemical shielding anisotropies (CSA). In the presence of large CSA, however, almost all of the currently existing, broadbanded dipolar recoupling schemes suffer severe degradations in efficiency, sometimes to the extent that experiments become practically impossible.

Previously we demonstrated that at or near so-called rotational-resonance (R^2) n = 0,1,2... conditions, some straightforward COSY-like pulse sequences, explicitly *not* optimised for orientational properties of polycrystalline powders, perform satisfactorily even in the presence of large CSA. At or near the n = 0 R^2 condition, that is with no very little differences in isotropic chemical shielding values, also spin diffusion MAS NMR experiments may be applied successfully for spin systems with large CSA.

Whereas these approaches can cover spin systems with either very large of very small to vanishing differences in isotropic chemical shielding values in a narrowbanded selective manner, these methods are not applicable for spin sysems with intermediate differences in chemical shielding values or where, for other reasons, broadbandedness is a required feature of the dipolar recoupling pulse sequence. A pulse sequence with a reasonably broadbanded profile is the C7 sequence (Fig. 3.9-8) but in the presence of CSA the achievable C7 double-quantum filtration efficiencies are generally very poor. We were able to show that slight modifications (Fig. 3.9-8) of the original basic r.f. amplitude matching condition of the C7 sequence ($\omega_{r.f.} = 7\omega_{rot}$) lead to enormous gains in efficiency when having to deal with spin systems displaying large CSA, in some case the efficiency gains amount to nearly an order of magnitude compared to the performance of the original C7 sequence. We believe that this finding is important for many solid-state NMR applications, given the trend toward use of higher magnetic field strengths in solid-state NMR.

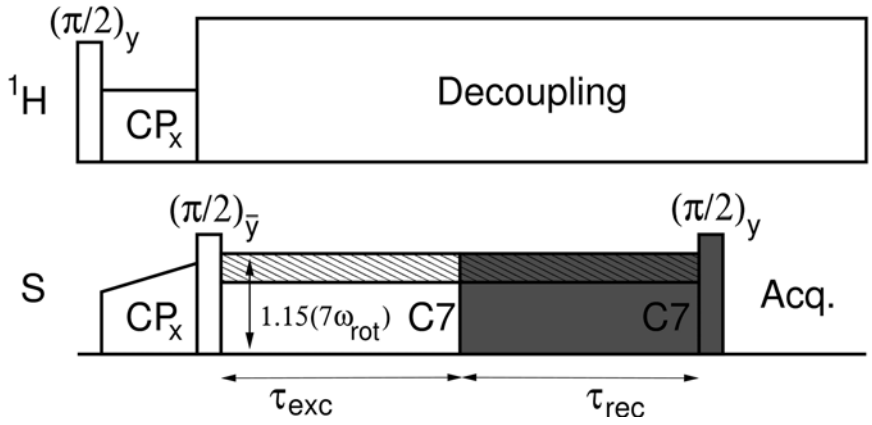

Fig. 3.9-8: Schematic drawing of the C7 pulse sequence, used for excitation 'white half') and reconversion ('grey half') of double-quantum coherences under MAS NMR conditions. The conventional C7 sequence fulfills the r.f. amplitude matching condition $\omega_{r.f.} = 7\omega_{rot}$, whereas our modified C7 sequence operates under a mismatch condition for optimum performance ($\omega_{r.f.} = 1.15 \times 7\omega_{rot;}$ indicated by the shaded part in the S-spin irradiation symbol).

Characterisation of bacterial cell-wall phosphate species by means of double-quantum filtration ^{31}P MAS NMR experiments (M. Bechmann and A. Sebald, in collaboration with N. Müller/Linz and P. Tekely/Nancy)

The cell walls of gram-negative bacteria often contain so-called secondary cell wall polymers. These units have been ascribed different roles in the cell metabolism and in transport phenomena. Phosphate moeities, most commonly phosphodiester species, constitute one of the building units of such secondary cell wall polymers. Based on some (bio)chemical and some IR-spectroscopical observations, it had been speculated that possibly in some bacterial cell walls the phosphate species present might be *pyro*-phosphate units, containing a P-O-P bonding motiv. Solution-state ^{31}P NMR spectroscopy could not provide a conclusive answer about the presence or absence of P-O-P units in these materials. In principle, it should be straightforward to resolve this ambiguity by means of solid-state ^{31}P double-quantum filtered (DQF) MAS NMR: either a ^{31}P resonance is found after DQF - in that case the phosphate species must be P-O-P units, or no ^{31}P resonance remains after DQF - in that case the phosphate species must be *ortho*-phosphate species. The challenge of this project rests with the minute amounts of sample available, as is often the case with biochemical materials. The more important it is to have efficient dipolar recoupling DQF MAS NMR techniques available (see above). Fig. 3.9-9 shows the conventional ^{31}P MAS NMR spectrum of 15 mg of the isolated cell wall material. Given the number of transients necessary to accumulate this spectrum, it is obvious that optimum experimental ^{31}P in DQF efficiency will be necessary in subsequent ^{31}P DQF MAS NMR experiments in order to clarify the nature of the phosphate species in this material - at best one can expect (theoretically) DQF MAS NMR efficiencies for a ^{31}P spin pair of this type of the order of 10 % to 15 %.

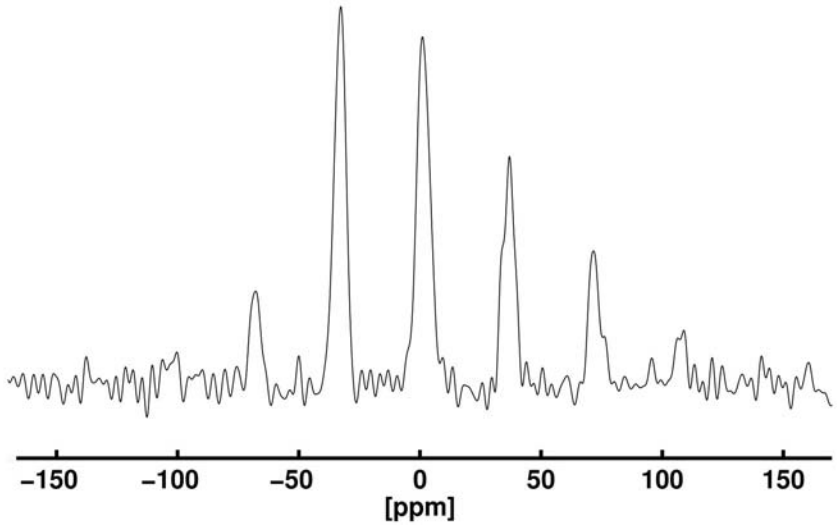

Fig. 3.9-9: ^{31}P MAS NMR spectrum of bacterial cell wall material after accumulating 24 000 transients.

Structural and dynamic properties of solid L-tyrosine-ethylester as seen by ^{13}C MAS NMR experiments (X. Helluy and A. Sebald, in collaboration with M. Baldus and K. Seidel/ Göttingen)

^{13}C MAS NMR experiments on solid L-tyrosine-ethylester with ^{13}C in (low; 1 percent) natural abundance and in fully ^{13}C enriched form were carried out at a range of temperatures. The phenyl rings were found to undergo π-flips with a rather low activation energy $E_a = 50 \pm 12$ kJmol^{-1}. In addition, the ester groups are afflicted by dynamic disorder at all temperatures accessible to MAS NMR experiments. Zero-quantum homonuclear ^{13}C recoupling experiments on fully ^{13}C enriched L-tyrosine-ethylester were carried out at low temperature. These experiments yield unambiguous spectral assignments and faithfully reproduce those molecular structural parameters, known from single-crystal X-ray diffraction, that are defined by short-range ^{13}C-^{13}C interactions but fail to uniquely characterise the complete molecular conformation defined by intermediate- and/or long-range ^{13}C-^{13}C interactions. Therefore, we recently started additional MAS NMR experiments, taking advantage of the higher gyromagnetic ratio of ^{1}H in comparison with ^{13}C. ^{1}H based NMR experiments should be able to yield the still missing intermediate- and/or long-range distance constraints in order to define the complete three-dimensional structure of the L-tyrosine-ethylester molecule in the solid state in a model-free manner, solely based on NMR data.

4. Publications, Conference Presentations, Seminars, Visiting Scientists

4.1 Publications (published)

Supplement to **2002** (papers published at the end of 2002):

MCCAMMON, C.A.; BECERRO, A.I.; LAUTERBACH, S.; BLÄß, U.W.; MARION, S.; LANGENHORST, F.; ANGEL, R.J.; VAN AKEN, P.A.; SEIFERT, F. (2002): Oxygen vacancies in perovskite and related structures: Implications for the lower mantle. Mat. Res. Soc. Symp. Proc. Vol. 718, 109-114

2003

a) Refereed international journals

BALOG, P.S.; SECCO, R.A.; RUBIE, D.C.; FROST, D.J. (2003): Equation of state of liquid Fe-10wt.% S: Implications for the metallic cores of planetary bodies. Journal of Geophysical Research 108(B2), 2124, 10.1029/2001JB001646

BECHMANN, M.; HAIN, K.; MARICHAL, C.; SEBALD, A. (2003): X-{^{1}H,^{19}F} triple resonance with a X-{^{1}H} CP MAS probe and characterisation of a ^{29}Si-^{19}F spin pair. Solid State Nuclear Magnetic Resonance 23, 50-61

BOFFA BALLARAN, T.; CARPENTER, M.A. (2003): Line broadening and enthalpy: some empirical calibrations of solid solution behaviour from IR spectra. Phase Transitions 76, 137-154

BOFFA BALLARAN, T. (2003): *Book review*: Reviews in Mineralogy and Geochemistry, 41: High-Temperature and High-Pressure Crystal Chemistry. Geochimica et Cosmochimica Acta 67, No. 3, 573

BOFFA BALLARAN, T.; ANGEL, R.J. (2003): Equation of state and high-pressure phase transitions in lawsonite. European Journal of Mineralogy 15, 241-246

BOLFAN-CASANOVA, N.; KEPPLER, H.; RUBIE, D.C. (2003): Water partitioning at 660 km depth and evidence for very low water solubility in magnesium silicate perovskite. Geophysical Research Letters 30, No. 17, 1905, 10.1029/2003GL017182

BROMILEY, G.D.; PAWLEY, A.R. (2003): The stability of antigorite in the systems MgO-SiO_2-H_2O (MSH) and MgO-Al_2O_3-SiO_2-H_2O (MASH). The effects of Al^{3+} substitution on the high-pressure stability. American Mineralogist 88, 229-234

BUREAU, H.; MÉTRICH, N. (2003): An experimental study of bromine behaviour in water-saturated silicic melts. Geochimica et Cosmochimica Acta 67, No. 9, 1689-1697

CÁMARA, F.; IEZZI, G.; OBERTI, R. (2003): HT-XRD study of synthetic ferrian magnesian spodumene: the effect of site dimension on the $P2_1/c \rightarrow C2/c$ phase transition. Physics and Chemistry of Minerals 30, 20-30

CÁMARA, F.; OBERTI, R.; IEZZI, G.; DELLA VENTURA, G. (2003): The $P2_1/m$ $C2/m$ phase transition in synthetic amphibole $NaNaMgMg_5Si_8O_{22}(OH)_2$: thermodynamic and crystal-chemical evaluation. Physics and Chemistry of Minerals 30, 570-581

COHEN, R.E.; GRAMSCH, S.; STEINLE-NEUMANN, G.; STIXRUDE, L. (2003): Importance of magnetism in phase stability, equation of state, and elasticity. – In: HEMLEY, R.J. *et al.* (Eds.): "High-Pressure Phenomena", Proceedings of the International School of Physics "Enrico Fermi" CXLVII, 215-238, IOS Press, Washington DC, USA

COMODI, P.; GATTA, G.D.; ZANAZZI, P.F. (2003): Effects of pressure on the structure of bikitaite. European Journal of Mineralogy 15, 247-255

CORNELIUS, V.J.; TITLER, P.J.; FERN, G.R.; MILLER, J.R.; SILVER, J.; SNOWDEN, M.J.; MCCAMMON, C.A. (2003): An interesting spin-state transition for [Fe(PPIX)OH] induced by high pressure in a diamond anvil cell. Hyperfine Interactions 144/145, 359-363

COVEY-CRUMP, S.J.; SCHOFIELD, P.F.; STRETTON, I.C.; KNIGHT, K.S.; BEN ISMAÏL, W. (2003): Using neutron diffraction to investigate the elastic properties of anisotropic rocks: results from an olivine + orthopyroxene mylonite. Journal of Geophysical Research 108(B2), 2092, 10.1029/2002JB001816

DELLA VENTURA, G.; HAWTHORNE, F.C.; ROBERT, J.-L.; IEZZI, G. (2003): Synthesis and infrared spectroscopy of amphibole along the tremolite-pargasite join. European Journal of Mineralogy 15, 341-348

DEMOUCHY, S.; MACKWELL, S.J. (2003): Water diffusion in synthetic iron-free forsterite. Physics and Chemistry of Minerals 30, 486-494

DOBSON, D.P.; CRICHTON, W.A.; BOUVIER, P.; VOČADLO, L.; WOOD, I.G. (2003): The equation of state of CsCl-structured FeSi to 40 GPa: Implications for silicon in the Earth's core. Geophysical Research Letters 30, No. 1, 1014, 10.1029/2002GL016228

DUBROVINSKAIA, N.A.; DUBROVINSKY, L.S. (2003): Melting curve of water studied in externally heated diamond anvil cell. High Pressure Research 23, No. 3, 307-312

DUBROVINSKAIA, N.A.; DUBROVINSKY, L.S. (2003): Whole-cell heater for the diamond anvil cell. Review of Scientific Instruments 74, 3433-3437

DUBROVINSKY, L.S.; DUBROVINSKAIA, N.A.; LANGENHORST, F.; DOBSON, D.P.; RUBIE, D.C.; GEßMANN, C.; ABRIKOSOV, I.; JOHANSSON, B.; BAYKOV, V.I.; VITOS, L.; LE BIHAN, T.; CRICHTON, W.A. (2003): Iron-silica interaction at extreme conditions and the electrically conducting layer at the base of Earth's mantle. Nature 422, 58-61

DUBROVINSKY, L.S.; DUBROVINSKAIA, N.A.; PRAKAPENKA, V.; SEIFERT, F.; LANGENHORST, F.; DMITRIEV, V.; WEBER, H.-P.; LE BIHAN, T. (2003): High-pressure and high-temperature polymorphism in silica. High Pressure Research 23, No. 1-2, 35-39

DUBROVINSKY, L.S.; DUBROVINSKAIA, N.A.; MCCAMMON, C.A.; ROZENBERG, G.K.; AHUJA, R.; OSORIO-GUILLEN, J.M.; DMITRIEV, V.; WEBER, H.-P.; LE BIHAN, T.; JOHANSSON, B. (2003): The structure of the metallic high-pressure Fe_3O_4 polymorph: experimental and theoretical study. Journal of Physics: Condensed Matter 15, 7697-7706

DUPAS-BRUZEK, C.; LAUDE, L.D.; LANGENHORST, F.; KOLEV, K. (2003): Surface structural transformation of sintered alumina induced by excimer laser. Journal of Applied Physics 93, No. 8, 4489-4496

EL GORESY, A.; DUBROVINSKY, L.S.; GILLET, P.; MOSTEFAOUI, S.; GRAUP, G.; DRAKOPOULOS, M.; SIMIONOVICI, A.S.; SWAMY, V.; MASAITIS, V.L. (2003): A new natural, super-hard, transparent polymorph of carbon from the Popigai impact crater, Russia. Journal d'Academie de Science Francaise 335, 889-898

FORTENFANT, S.S.; RUBIE, D.C.; REID, J.; DALPÉ, C.; CAPMAS, F.; GESSMANN, C.K. (2003): Partitioning of Re and Os between liquid metal and magnesiowüstite at high pressure. Physics of the Earth and Planetary Interiors 139, 77-91

FORTENFANT, S.S.; GÜNTHER, D.; DINGWELL, D.B.; RUBIE, D.C. (2003): Temperature dependence of Pt and Rh solubilities in a haplobasaltic melt. Geochimica et Cosmochimica Acta 67, 123-131

FREI, D.; LIEBSCHER, A.; WITTENBERG, A.; SHAW, C.S.J. (2003): Crystal chemical controls on rare earth element partitioning between epidote-group minerals and melts: an experimental and theoretical study. Contributions to Mineralogy and Petrology 146, 192-204

FROST, D.J. (2003): Fe^{2+}-Mg partitioning between garnet, magnesiowüstite and $(Mg,Fe)_2SiO_4$ phases of the transition zone. American Mineralogist 88, 387-397

FROST, D.J. (2003): The structure and sharpness of $(Mg,Fe)_2SiO_4$ phase transformations in the transition zone. Earth and Planetary Science Letters 216(3), 313-318

GAILLARD, F.; PICHAVANT, M.; SCAILLET, B. (2003): Experimental determination of activities of FeO and Fe_2O_3 components in hydrous silicic melts under oxidizing conditions. Geochimica et Cosmochimica Acta 67, 4389-4409

GAILLARD, F.; SCHMIDT, B.C.; MACKWELL, S.J.; MCCAMMON, C.A. (2003): Rate of hydrogen-iron redox exchange in silicate melts and glasses. Geochimica et Cosmochimica Acta 67, No. 13, 2427-2441

GAILLARD, F.; PICHAVANT, M.; MACKWELL, S.J.; CHAMPALLIER, R.; SCAILLET, B.; MCCAMMON, C.A. (2003): Chemical transfer during redox exchange between H_2 and Fe-bearing silicate melts. American Mineralogist 88, 308-315

GALLARDO, M.C.; BECERRO, A.I.; ROMERO, F.J.; DEL CERRO, J.; SEIFERT, F.; REDFERN, S.A.T. (2003): Cubic-tetragonal phase transition in $Ca_{0.04}Sr_{0.96}TiO_3$: a combined specific heat and neutron driffraction study. Journal of Physics: Condensed Matter 15, 91-100

GATTA, G.D.; MASCI, S.; VIVANI, R. (2003): Dimensional reduction in zirconium phosphate; from layer to ribbons to chains. Journal of Materials Chemistry 13, 1215-1222

GATTA, G.D.; COMODI, P.; ZANAZZI, P.F. (2003): New insights on high-pressure behaviour of microporous materials from X-ray single crystal data. Microporous and Mesoporous Materials 61, 105-115

HEIDELBACH, F.; STRETTON, I.C.; LANGENHORST, F.; MACKWELL, S.J. (2003): Fabric evolution during high shear-strain deformation of magnesiowüstite. Journal of Geophysical Research 108(B3), 2154, 10.1029/2001/JB001632

HELLUY, X.; SEBALD, A. (2003): Order/Disorder phenomena in crystalline phases of compounds $E(XMe_3)_4$ where E = C,Si,Ge and X = Si,Sn. Applied Organometallic Chemistry 17, 42-51

HELLUY, X.; SEBALD, A. (2003): Structure and dynamic properties of solid L-tyrosine-ethylester as seen by ^{13}C MAS NMR. Journal of Physical Chemistry B 107, 3290-3296

HELLUY, X.; PIETSCHNIG, R.; SEBALD, A. (2003): ^{29}Si and ^{19}F MAS NMR spectra of isolated $^{29}Si(^{19}F)_2$ and $^{29}Si(^{19}F)_3$ spin systems: Experiments and simulations. Solid State Nuclear Magnetic Resonance 24, 286-300

HOLTZMAN, B.K.; KOHLSTEDT, D.L.; ZIMMERMAN, M.E.; HEIDELBACH, F.; HIRAGA, T.; HUSTOFT, J. (2003): Melt segregation and strain partitioning: implications for seismic anisotropy and mantle flow. Science 301, 1227-1230

HOLZAPFEL, C.; RUBIE, D.C.; MACKWELL, S.J.; FROST, D.J. (2003): Effect of pressure on Fe-Mg interdiffusion in $(Fe_xMg_{1-x})O$, ferropericlase. Physics of the Earth and Planetary Interiors 139, 21-34

IEZZI, G.; DELLA VENTURA, G.; PEDRAZZI, G.; ROBERT, J.-L.; OBERTI, R. (2003): Synthesis and characterisation of ferri-clinoferroholmquistite, $Li_2(Fe^{2+}_3Fe^{3+}_2)Si_8O_{22}(OH)_2$. European Journal of Mineralogy 15, 321-328

IEZZI, G.; DELLA VENTURA, G.; CÁMARA, F.; PEDRAZZI, G.; ROBERT, J.-L. (2003): ^{B}Na-^{B}Li solid solution in A-site-vacant amphiboles: synthesis and cation ordering along the ferri-clinoferroholmquistite-riebeckite join. American Mineralogist 88, 955-961

JACOBSEN, S.D.; SMYTH, J.R.; SWOPE, R.J. (2003): Thermal expansion of hydrated six-coordinate silicon in thaumasite, $Ca_3Si(OH)_6(CO_3)\ (SO_4)\cdot 12\ H_2O$. Physics and Chemistry of Minerals 30, 321-329

KOGISO, T.; HIRSCHMANN, M.M.; FROST, D.J. (2003): High-pressure partial melting of garnet pyroxenite: possible mafic lithologies in the source of ocean island basalts. Earth and Planetary Science Letters 216(4), 603-617

KOZLOV, E.A.; SAZONOVA, L.V.; FEL'DMAN, V.I.; DUBROVINSKAYA, N.A.; DUBROVINSKII, L.S. (2003): Formation of ringwoodite during shock-wave loading of two-mica quartz schist: Experimental Data. Doklady Earth Sciences 390, No. 4, 571-573. Translated from Doklady Akademii Nauk 390, No. 3, 379- 381

LANGENHORST, F. (2003): Nanostructures in ultra-high pressure metamorphic coesite and diamond: a genetic fingerprint. Mitteilungen der Österreichischen Mineralogischen Gesellschaft 148, 401-412

LIEBSKE, C.; BEHRENS, H.; HOLTZ, F.; LANGE, R.A. (2003): The influence of pressure and composition on the viscosity of andesitic melts. Geochimica et Cosmochimica Acta 67, 473-485

LITASOV, K.; OHTANI, E.; LANGENHORST, F.; YURIMOTO, H.; KUBO, T.; KONDO, T. (2003): Water solubility in Mg-perovskites and water storage capacity in the lower mantle. Earth and Planetary Science Letters 211, 189-203

MACHON, D.; SINITSYN, V.V.; DMITRIEV, V.P.; BDIKIN, I.K.; DUBROVINSKY, L.S.; KULESHOV, I.V.; PONYATOVSKY, E.G.; WEBER, H.P. (2003): Structural transitions in Cu_2O at pressures up to 11 GPa. Journal of Physics: Condensed Matter 15, 7227-7235

MACKWELL, S.J.; PATERSON, M.S. (2003): New developments in deformation studies: High-strain deformation. Reviews in Mineralogy and Geochemistry 51, 1-19

MCCAMMON, C.A. (2003): Mössbauer spectroscopy in the geosciences: Highlights and perspectives. Hyperfine Interactions 144/145, 289-296

MCCAMMON, C.A.; ROSS, N.L. (2003): Crystal chemistry of ferric iron in (Mg,Fe)(Si,Al)O_3 majorite with implications for the transition zone. Physics and Chemistry of Minerals 30, 206-216

MOLNÁR, G.; NIEL, V.; REAL, J.-A.; DUBROVINSKY, L.S.; BOUSSEKSOU, A.; MCGARVEY, J.J. (2003): Raman spectroscopic study of pressure effects on the spin-crossover coordination polymers Fe(pyrazine)[$M(CN)_4$]·$2H_2O$ (M = Ni, Pd, Pt). First observation of a piezo-hysteresis loop at room temperature. Journal of Physical Chemistry B 107, 3149-3155

PADRO, D.; SCHMIDT, B.C.; DUPREE, R. (2003): On the water solubility mechanism in hydrous aluminosilicate glasses: Information from ^{27}Al MAS and MQMAS NMR. Geochimica Cosmochimica Acta 67, No. 8, 1543-1551

PRAKAPENKA, V.B.; DUBROVINSKY, L.S.; SHEN, G.; RIVERS, M.L.; SUTTON, S.R.; DMITRIEV, V.; WEBER, H.-P.; LE BIHAN, T. (2003): α-PbO_2-type high-pressure polymorph of GeO_2. Physical Review B 67, 132101

RAKIC, S.; KAHLENBERG, V.; SCHMIDT, B.C. (2003): Hydrothermal synthesis and structural characterization of κ-$Na_2Si_2O_5$ and $Na_{1.84}K_{0.16}Si_2O_5$. Solid State Sciences 5, 473-480

RAKIC, S.; KAHLENBERG, V.; SCHMIDT, B.C.; IDE, S.; DEPMEIER, W. (2003): High pressure mixed alkali disilicates in the system $Na_{2-x}K_xSi_2O_5$: hydrothermal synthesis and crystal structures of $NaKSi_2O_5$-II and $Na_{0.5}K_{1.5}Si_2O_5$. Zeitschrift für Kristallographie 218, 413-420

REID, J.E.; SUZUKI, A.; FUNAKOSHI, K.-I.; TERASAKI, H.; POE, B.T.; RUBIE, D.C.; OHTANI, E. (2003): The viscosity of $CaMgSi_2O_6$ liquid at pressures up to 13 GPa. Physics of the Earth and Planetary Interiors 139, 45-54

RIOS, S.; BOFFA BALLARAN, T. (2003): Microstructure of radiation-damaged zircon under pressure. Journal of Applied Crystallography 36, 1006-1012

ROZENBERG, G.K.; PASTERNAK, M.P.; XU, W.M.; DUBROVINSKY, L.S.; OSORIO GUILLÉN, J.M.; AHUJA, R.; JOHANSSON, B. (2003): Pressure-induced structural transformations in the Mott insulator FeI_2. Physical Review B 68, 064105

RUBIE, D.C.; MELOSH, H.J.; REID, J.E.; LIEBSKE, C.; RIGHTER, K. (2003): Mechanisms of metal-silicate equilibration in the terrestrial magma ocean. Earth and Planetary Science Letters 205, 239-255

SCHOFIELD, P.F.; COVEY-CRUMP, S.J.; STRETTON, I.C.; DAYMOND, M.R.; KNIGHT, K.S.; HOLLOWAY, R.F. (2003): Using neutron diffraction measurements to characterize the mechanical properties of polymineralic rocks. Mineralogical Magazine 67, 967-987

SMYTH, J.R.; HOLL, C.M.; FROST, D.J.; JACOBSEN, S.D.; LANGENHORST, F.; MCCAMMON, C.A. (2003): Structural systematics of hydrous ringwoodite and water in Earth's interior. American Mineralogist 88, 1402-1407

STEINLE-NEUMANN, G.; STIXRUDE, L.; COHEN, R.E. (2003): Physical properties of iron in the inner core. – In: DEHANT, V. *et al*. (Eds.): Core dynamics, structure, and rotation. Geodynamics Series 31, 137-162, American Geophysical Union, Washington DC, USA

STOYANOVA, R.; ZHECHEVA, E.; ALCÁNTARA, R.; TIRADO, J.L.; BROMILEY, G.D.; BROMILEY, F.A.; BOFFA BALLARAN, T. (2003): Lithium/nickel mixing in the transition metal layers of lithium nickelate: High-pressure synthesis of layered $Li[Li_xNi_{1-x}]O_2$ oxides as cathode materials for lithium-ion batteries. Solid State Ionics 161 (3-4), 197-204

SWAMY, V.; DUBROVINSKAIA, N.A.; DUBROVINSKY, L.S.; SIMIONOVICI, A.S.; DRAKOPOULOS, M.; DMITRIEV, V.; WEBER, H. (2003): Compression behavior of nanocrystalline anatase TiO_2. Solid State Communications 125, 11-115

TALYZIN, A.V.; DUBROVINSKY, L.S. (2003): Pressure-induced phase transformations in tetragonal and rhombohedral C_{60} polymers. High Pressure High Temperature 37/36, 47-53

TERRY, M.P.; ROBINSON, P. (2003): Evolution of amphibolite-facies structural features and boundary conditions for deformation during exhumation of high- and ultrahigh-pressure rocks, Nordøyane, Western Gneiss Region, Norway. Tectonics 22, No. 4, 1036, 10.1029/2001TC001349

THUREL, E.; CORDIER, P. (2003): Plastic deformation of wadsleyite: I. High-pressure deformation in compression. Physics and Chemistry of Minerals 30, 256-266

THUREL, E.; CORDIER, P.; FROST, D.J.; KARATO, S.-I. (2003): Plastic deformation of wadsleyite II. High-pressure deformation in shear. Physics and Chemistry of Minerals 30, 267-270

THUREL, E.; DOUIN, J.; CORDIER, P. (2003): Plastic deformation of wadsleyite: III. Interpretation of dislocations and slip systems. Physics and Chemistry of Minerals 30, 271-279

TRIBAUDINO, M.; NESTOLA, F.; MENEGHINI, C.; BROMILEY, G.D. (2003): The high-temperature $P2_1/c$-$C2/c$ phase transition in Fe-free Ca-rich $P2_1/c$ clinopyroxenes. Physics and Chemistry of Minerals 30, 527-535

WILKINS, C.J.; TENNANT, W.C.; WILLIAMSON, B.E.; MCCAMMON, C.A. (2003): New Zealand jade: Colouring and constitution. Chem NZ 90, 16-23

WILKINS, C.J.; TENNANT, W.C.; WILLIAMSON, B.E.; MCCAMMON, C.A. (2003): Spectroscopic and related evidence on the colouring and nature of New Zealand jade. American Mineralogist 88, 1336-1344

b) Conference proceedings

DUBROVINSKY, L.S.; DUBROVINSKAIA, N.A. (2003): High-pressure crystallography at elevated temperatures. Lecture Notes of 34th International School of Crystallography on High Pressure Crystallography, Erice, Italy, 187- 206

DUBROVINSKY, L.S.; DUBROVINSKAIA, N.A. (2003): Synthesis, structures and properties of high-pressure modifications of the group IV metals dioxides. Proceedings of International Symposium on Advanced Materials (ISAM), 33-35

LANGENHORST, F. (2003): Applications of transmission electron microscopy in geoscience. Proceedings Book Scandem 2003, 13-14

KOONS, P.O.; UPTON, P.; TERRY, M.P. (2003): Three-dimensional mechanics of UHPM terrains and resultant P-T-t paths. EMU Notes in Mineralogy 5, Chapter 9, 27

ROBINSON, P.; TERRY, M.P.; CARSWELL, D.A.; VAN ROERMUND, H.; KROGH, T.E.; ROOT, D.; TUCKER, R.D.; SOLLE, A. (2003): Tectono-stratigraphic setting, structure, and petrology of HP and UHP metamorphic rocks and garnet peridotites in the Western Gneiss Region. Møre and Romsdal, Norway: Trondheim, Norges geologiske undersøkelse, 142

4.2 Publications (submitted, in press)

ALLWARDT, J.R.; SCHMIDT, B.C.; STEBBINS, J.F.: Structural mechanisms of compression and decompression in high-pressure $K_2Si_4O_9$ glasses: An investigation utilizing Raman and NMR spectroscopy of high-pressure glasses and crystals. Chemical Geology (submitted)

ANANDAN, S.; SILVER, J.; FERN, G.R.; TITLER, P.J.; MCCAMMON, C.A.: A high pressure Mössbauer spectroscopy study of [^{57}FeOEPCl]. Hyperfine Interactions (in press)

BECHMANN, M; SEBALD A.: Double-quantum filtration at and near the $n = 0$ rotational-resonance condition. Solid State Nuclear Magnetic Resonance (submitted)

BLÄß, U.W.; LANGENHORST, F.; BOFFA BALLARAN, T.; SEIFERT, F.; FROST, D.J.; MCCAMMON, C.A.: A new oxygen deficient perovskite phase $Ca(Fe_{0.4}Si_{0.6})O_{2.8}$ and phase relations along the join $CaSiO_3$-$CaFeO_{2.5}$ at transition zone conditions. Physics and Chemistry of Minerals (in press)

BOFFA BALLARAN, T.; CARPENTER, M.A.; DOMENEGHETTI, M.C.: Local and macroscopic order parameter variations through the C2/m-$P2_1$/m phase transition in cummingtonite. American Mineralogist (submitted)

BROMILEY, G.D.; HILARET, N.; MCCAMMON, C.A.: H solubility in rutile and TiO_2 (II): Implications for the role of stishovite and post-stishovite phases in subducting oceanic crust in the lower mantle. Geophysical Research Letters (in press)

BROMILEY, G.D.; KEPPLER, H.: An experimental investigation of hydroxyl solubility in jadeite and Na-rich clinopyroxenes. Contributions to Mineralogy and Petrology (in press)

BROMILEY, G.D.; KEPPLER, H.; MCCAMMON, C.A.; BROMILEY, F.A.; JACOBSEN, S.D.: Hydrogen solubility and speciation in natural, gem-quality Cr-diposide. American Mineralogist (in press)

COMODI, P.; BERNARDI, M.; BENTIVOGLIO, A.; GATTA, G.D.; ZANAZZI, P.F.: Production and technology of Middle Age glazed ceramic from Saepinum territory (Italy): a multi-methodical approach. Archeometry (submitted)

COUVY, H.; FROST, D.J.; HEIDELBACH, F.; NYILAS, K.; UNGÁR, T.; MACKWELL, S.J.; CORDIER, P.: Shear deformation experiments of forsterite at 11 GPa – 1400 °C in the multianvil apparatus. European Journal of Mineralogy (submitted)

DAHL, P.S.; HAMILTON, M.A.; TERRY, M.P.; JERCINOVIC, M.J.; WILLIAMS, M.L.; FREI, R.: Comparative geochronometry of metamorphic monazite in the eastern Wyoming province (USA), with implications for electron microprobe dating of Proterozoic thermotectonism. American Mineralogist (submitted)

DOBSON, D.P.; JACOBSEN, S.D.: The flux growth of magnesium silicate perovskite single crystals. American Mineralogist (in press)

DU, L.-S.; ALLWARDT, J.R.; SCHMIDT, B.C.; STEBBINS J.F.: Pressure-induced structural changes in a borosilicate glass-forming liquid: reorganization of a complex network system. Nature Materials (submitted)

DUBROVINSKAIA, N.A.; DUBROVINSKY, L.S.; MCCAMMON, C.A.: Iron-magnesium alloying at high pressures and temperatures. Journal of Physics: Condensed Matter (in press)

DUBROVINSKY, L.S.; DUBROVINSKAIA, N.A.; PRAKAPENKA, V.; SEIFERT, F.; LANGENHORST, F.; DMITRIEV, V.; WEBER, H.-P.; LE BIHAN, T.: A class of new high-pressure silica polymorphs. Physics of the Earth and Planetary Interiors (in press)

DUBROVINSKY, L.S.; DUBROVINSKAIA, N.A.; LANGENHORST, F.; DOBSON, D.P.; RUBIE, D.C.; GEßMANN, C.; LE BIHAN, T.; CRICHTON, W.A.: Iron-silica interaction at core-mantle boundary conditions. Physics of the Earth and Planetary Interiors (in press)

DUBROVINSKY, L.S.; DUBROVINSKAIA, N.A.: Angle dispersive diffraction under nonhydrostatic stress in diamond anvil cells. Journal of Alloys and Compounds (in press)

DUBROVINSKY, L.S.; DUBROVINSKAIA, N.A.: High-pressure crystallography at elevated temperatures: experimental approach. NATO Meeting/NATO ASI Series , NATO Publishing Unit, Vol. High-pressure crystallography (in press)

FROST, D.J.; LIEBSKE, C.; LANGENHORST, F.; MCCAMMON, C.A.; TRØNNES, R.G.; RUBIE, D.C.: Experimental evidence for the existence of Fe-rich metal in the Earth's lower mantle. Nature (in press)

FROST, D.J.; POE, B.T.; TRØNNES, R.G.; LIEBSKE, C.; DUBA, A.; RUBIE, D.C.: A new large-volume multianvil system. Physics of the Earth and Planetary Interiors (in press)

GAILLARD, F.: Real time assessment of magma storage conditions by geophysical, petrological and laboratory constraints. Nature (submitted)

GAILLARD, F.: Laboratory measurements of electrical conductivity of hydrous and dry silicic melts under pressure. Earth and Planetary Science Letters (in press)

GATTA, G.D.; BOFFA BALLARAN, T.; COMODI, P.; ZANAZZI, P.F.: Isothermal equation of state and compressional behavior of tetragonal edingtonite. American Mineralogist (in press)

GATTA, G.D.; BOFFA BALLARAN, T.: New insight into the crystal structure of orthorhombic edingtonite. Mineralogical Magazine (in press)

GATTA, G.D.; BOFFA BALLARAN, T.; COMODI, P.; ZANAZZI, P.F.: Comparative compressibility and equation of state of orthorhombic and tetragonal edingtonite. Physics and Chemistry of Minerals (in press)

HUBER, A.; HEUER, M.; FEHR, K.T.; BENTE, K.; SCHMIDBAUER, E.; BROMILEY, G.D.: Characterisation of synthetic hedenbergite ($CaFeSi_2O_6$) - petedunnite ($CAZnSi_2O_6$) solid solution series by X-ray powder diffraction and ^{57}Fe Mössbauer spectroscopy. European Journal of Mineralogy (in press)

IEZZI, G.; DELLA VENTURA, G.; OBERTI, R.; CÁMARA, F.; HOLTZ, F.: Synthesis and crystal-chemistry of $Na(NaMg)Mg_5Si_8O_{22}(OH)_2$, a $P2_1/m$ amphibole. American Mineralogist (in press)

IEZZI, G.; CÁMARA, F.; DELLA VENTURA, G.; OBERTI, R.; PEDRAZZI, G.; ROBERT, J.-L.: Synthesis, crystal structure and crystal-chemistry of ferri-clinoholmquistite: $\square Li_2Mg_2Fe_3Si_8O_{22}(OH)_2$. Physics and Chemistry of Minerals (submitted)

IEZZI, G.; DELLA VENTURA, G.; PEDRAZZI, G.; HAWTHORNE, F.C.; NOVEMBRE, D.; ROBERT, J.-L.: The (Mg-Fe^{2+}) substituion in ferri-clinoholmquistite: an infrared study in the OH-stretching region. Canadian Mineralogist (submitted)

JACOBSEN, S.D.; SMYTH, J.R.; SPETZLER, H.A.; HOLL, C.M.; FROST, D.J.: Sound velocities and elastic constants of iron-bearing hydrous ringwoodite. Physics of the Earth and Planetary Interiors (in press)

KANTOR, I.Yu.; MCCAMMON, C.A.; DUBROVINSKY, L.S.: Mössbauer spectroscopic study of pressure induced magnetization in wüstite (FeO). Journal of Alloys and Compounds (in press)

KAWAMOTO, T.: Hydrous phase stability and partial melt chemistry in H_2O-saturated KLB-1 peridotite up to the uppermost lower mantle conditions (in press)

LANGENHORST, F.; POIRIER, J.-P.; FROST, D.J.: TEM observations of microscopic inclusions in synthetic diamond. Journal of Materials Science (in press)

LEPORA, A.; GROBETY, B.; MCCAMMON, C.A.: Dehydroxylation of a 3T phengite under reducing and oxidising conditions. European Journal of Mineralogy (submitted)

MARTON, F.C.; RUBIE, D.C.; SHANKLAND, T.J.; XU, Y.: Effects of variable thermal conductivity on the mineralogy of subducting slabs and implications for mechanisms of deep earthquakes. Physics of the Earth and Planetary Interiors (submitted)

MASHKINA, E.; MCCAMMON, C.A.; SEIFERT, F.: A Mössbauer study of oxygen vacancy and cation distribution in 6H-$BaTi_{1-x}Fe_xO_{3-x/2}$. Journal of Solid State Chemistry (in press)

MCCAMMON, C.A.; LAUTERBACH, S.; SEIFERT, F.; LANGENHORST, F.; VAN AKEN, P.A.: Iron oxidation state in lower mantle mineral assemblages I. Experimental synthesis at high pressure. Earth and Planetary Science Letters (submitted)

MCCAMMON, C.A.: Mössbauer spectroscopy: Applications. In: BERAN, A.; LIBOWITSKY, E. (Eds.): "Spectroscopic Methods in Mineralogy" – Eötvös University Press, Budapest (submitted)

MCCAMMON, C.A.; FROST, D.J.; SMYTH, J.R.; LAUSTSEN, H.M.; KAWAMOTO, T.; ROSS, N.L.; VAN AKEN, P.A.: Oxidation state of iron in hydrous mantle phases: Implications for subduction and mantle oxygen fugacity. Physics of the Earth and Planetary Interiors (in press)

MCCAMMON, C.A.; KOPYLOVA, M.G.: A redox profile of the Slave mantle and oxygen fugacity control in the cratonic mantle. Contributions to Mineralogy and Petrology (submitted)

MCCAMMON, C.A.; STACHEL, T.; HARRIS, J.W.: Iron oxidation state in lower mantle mineral assemblages II. Inclusions in diamonds from Kankan, Guinea. Earth and Planetary Science Letters (submitted)

MCENROE, S.A.; LANGENHORST, F.; ROBINSON, P.; BROMILEY, G.D.: What's magnetic in the lower crust? Earth and Planetary Science Letters (submitted)

MIYAJIMA, N.; LANGENHORST, F.; FROST, D.J.; YAGI, T.: Electron channeling spectroscopy of iron in majoritic garnet and silicate perovskite by using a transmission electron microscope. Physics of the Earth and Planetary Interior (in press)

NESTOLA, F.; BOFFA BALLARAN, T.; BENNA, P.; TRIBAUDINO, M.; BRUNO, E.: High-pressure phase transitions in $Ca_{0.2}Sr_{0.8}Al_2Si_2O_8$ feldspar. American Mineralogist (submitted)

NESTOLA, F.; TRIBAUDINO, M.; BOFFA BALLARAN, T.: High pressure behavior, transformation and crystal structure in synthetic iron-free pigeonite. American Mineralogist (in press)

O'NEILL, H.S.C.; POWNCEBY, M.; MCCAMMON, C.A.: The magnesiowüstite – iron equilibrium and its implications for the activity-composition relations of $(Mg,Fe)_2SiO_4$ olivine solid solutions. Contributions to Mineralogy and Petrology (in press)

PARTZSCH, G.M.; LATTARD, D.; MCCAMMON, C.A.: Mössbauer spectroscopic determination of Fe^{3+}/Fe^{2+} in synthetic basaltic glass: A test of empirical fO_2 equations under superliquidous and subliquidous conditions. Contributions to Mineralogy and Petrology (submitted)

PROYER, A.; DACHS, E.; MCCAMMON, C.A.: Pitfalls in geothermometry of eclogites: Fe^{3+} and changes in the mineral chemistry of omphacite at ultrahigh pressures. Contributions to Mineralogy and Petrology (submitted)

RAVNA, E.J.K.; TERRY, M.P.: Geothermobarometry of HP and UHP eclogites and schists – an evaluation of equilibria between clinopyroxene-kyanite-phengite-garnet-coesite/quartz. Journal of Metamorphic Geology (submitted)

REICHMANN, H.-J.; JACOBSEN, S.D.: High-pressure elasticity of a natural magnetite. American Mineralogist (in press)

RUBIE, D.C.; GESSMANN, C.K.; FROST, D.J.: Partitioning of oxygen during core formation on Earth and Mars. Nature (in press)

SCHMIDT, B.C.; ZOTOV, N.; DUPREE, R.: Structural implications of water and boron dissolution in albite glass. Journal of Non-Crystalline Solids (submitted)

SILVER, J.; MCCAMMON, C.A.; DAVIES, D.A.; ANANDAN, S.; TITLER, P.J.; FERN, G.R.; MARSH, P.J.: High pressure Mössbauer spectroscopic studies on two low spin iron porhyrins [Fe(PPIX)(HIm)$_2$]Cl and [Fe(OEP)(4-NH$_2$Py)$_2$]Cl. Journal of the American Chemical Society (submitted)

SMYTH, J.R.; HOLL, C.M.; FROST, D.J.; JACOBSEN, S.D.: High-pressure crystal chemistry of hydrous ringwoodite and water in the Earth's interior. Physics of the Earth and Planetary Interiors (in press)

SMYTH, J.R.; HOLL, C.M.; LANGENHORST, F.; LAUSTSEN, H.M.; ROSSMAN, G.R.; KLEPPE, A.; MCCAMMON, C.A.; KAWAMOTO, T.: Crystal chemistry of wadsleyite II and water in the Earth's interior. American Mineralogist (submitted)

STEINLE-NEUMANN, G.; COHEN, R.E.; STIXRUDE, L.: Magnetism in iron as a function of pressure. Journal of Physics: Condensed Matter (submitted)

STEINLE-NEUMANN, G.; STIXRUDE, L.; COHEN, R.E.: Magnetism in dense hexagonal iron. Proceedings of the National Academy of Sciences (in press)

STOYANOVA, R.; ZHECHEVA, E.; ALCÁNTARA, R.; TIRADO, J.L.; BROMILEY, G.D.; BROMILEY, F.A.; BOFFA BALLARAN, T.: Layered solid solutions of $LiCo_{1-x}Ni_xO_2$ with alpha-$LiGaO_2$ obtained under high oxygen pressure. Journal of materials Chemistry (submitted)

SUZUKI, A.; OHTANI, E.; TERASAKI, H.; FUNAKOSHI, K.-I.: Viscosity of silicate melts in $CaMgSi_2O_6$-$NaAlSi_2O_6$ system at high pressure. Physics and Chemistry of Minerals (submitted)

TERASAKI, H.; KATO, T.; FUNAKOSHI, K.-I.; SUZUKI, A.; URAKAWA, S.: Viscosity of liquid sulphur under high pressure. Journal of Physics: Condensed Matter (submitted)

TERRY, M.P.; ROBINSON, P.: Geometry of eclogite-facies structural features: Implications for production and exhumation of UHP and HP rocks, Western Gneiss Region, Norway. Tectonics (in press)

TERRY M.P.; HEIDELBACH, F.: Superplasticity in garnet from eclogite-facies shear zones in the Haram Gabbro, Haramsøya, Norway. Geology (in press)

TOMMASI, A.; CORDIER, P.; MAINPRICE, D.; COUVY, H.; THORAVAL, C.: Dominant horizontal flow in the transition zone of the Earth's mantle. Nature (submitted)

URAKAWA, S.; SOMEYA, K.; TERASAKI, H.; KATSURA, T.; YOKOSHI, S.; FUNAKOSHI, K.-I.; UTSUMI, W.; KATAYAMA, Y.; SUEDA, Y.; IRIFUNE, T.: Phase relations and equations of state for FeS at high pressures and high temperatures and implications to the internal structure of Mars. Physics of the Earth and Planetary Interiors (in press)

WILLIAMS, H.M.; MCCAMMON, C.A.; PESLIER, A.H.; HALLIDAY, A.N.; TEUTSCH, N.; LEVASSEUR, S.; BURG, J.-P.: Iron isotope variations in mantle spinels and the influence of oxygen fugacity. Nature (submitted)

XU, Y.; SHANKLAND, T.J.; LINHARDT, S.; RUBIE, D.C.; LANGENHORST, F.; KLASINSKI, K.: Thermal diffusivity measurements of olivine, wadsleyite and ringwoodite to 20 GPa and 1100 °C. Physics of the Earth and Planetary Interior (submitted)

4.3 Presentations at scientific institutions and at congresses

ALLWARDT, J.R.; POE, B.T.; SCHMIDT, B.C.; STEBBINS, J.F.: 06.-11.04.2003, EGS-AGU-EUG Joint Assembly, Nice, France[*1]: "Compression mechanisms and temperature effects in high pressure glasses investigated by ^{27}Al MAS and ^{17}O 3QMAS NMR", Geophysical Research Abstracts 5, Abstract 07757, 2003

ANDO, R.; OHTANI, E.; SUZUKI, A.; RUBIE, D.C.; FUNAKOSHI, K.-I.: 08.-12.12.2003, AGU Fall Meeting, San Francisco, USA[*3]: "Pressure dependency of viscosities of MORB melts", EOS Trans. AGU, 84(47), Fall Meet. Suppl., Abstract V31D-0958, 2003

BECHMANN, M.; SEBALD, A.: 14.-18.09.2003, 3rd Alpine Conference on Solid-State NMR, Chamonix, France: "Improved C7 DQF efficiencies in the presence of large shielding anisotropies"

BECHMANN, M.; SEBALD, A.: 30.09.-02.10.2003, 25th Meeting of the Magnetic Resonance Discussion Group of GDCh, Leipzig, Germany: "Improved C7 DQF efficiencies in the presence of large shielding anisotropies"

BLÄß, U.W.; BOFFA BALLARAN, T.; FROST, D.J.; LANGENHORST, F.; MCCAMMON, C.A., SEIFERT, F.; VAN AKEN, P.A.: 06.-11.04.2003, EGS-AGU-EUG Joint Assembly, Nice, France[*1]: "Exchange of silicon by trivalent cations of iron or aluminium in calcium silicate perovskite", Geophysical Research Abstracts 5, Abstract 04066, 2003

BLÄß, U.W.; BOFFA BALLARAN, T.; FROST, D.J.; LANGENHORST, F.; MCCAMMON, C.A.; SEIFERT, F.; VAN AKEN, P.A.: 22.-25.09.2003, 81. Jahrestagung der DMG, Bochum, Germany[*2]: "Incorporation of trivalent cations (Fe^{3+}, Al) in calcium silicate perovskite", Beihefte zum European Journal of Mineralogy 15, 21

BOFFA BALLARAN, T.; NESTOLA, F.; BENNA, P.; TRIBAUDINO, M.; BRUNO, E.: 02.-05.11.2003, GSA Annual Meeting – Geoscience Horizons, Seattle, USA: "High-pressure behavior of $Ca_{0.2}Sr_{0.8}Al_2Si_2O_8$ feldspar", Geological Society of America Abstracts with Programs 35(6), 219-8

BOLFAN-CASANOVA, N.; MCCAMMON, C.A.: 06.-11.04.2003, EGS-AGU-EUG Joint Assembly, Nice, France[*1]: "Effect of trivalent cation substitutions on H solubility in MgO at high pressures", Geophysical Research Abstracts 5, Abstract 10488, 2003

BOTCHARNIKOV, R.; KOEPKE, J.; HOLTZ, F.; MCCAMMON, C.A.: 06.-11.04.2003, EGS-AGU-EUG Joint Assembly, Nice, France[*1]: "The effect of water activity and oxygen fugacity on the phase relations and oxidation state of Fe in a parental ferrobasaltic magma of Skaergaard", Geophysical Research Abstracts 5, Abstract 08436, 2003

BOTCHARNIKOV, R.; KOEPKE, J.; HOLTZ, F.; MCCAMMON, C.A.: 22.-25.09.2003, 81. Jahrestagung der DMG, Bochum, Germany[*2]: "The effect of aH_2O and fO_2 on the phase relations and oxidation state of Fe in a parental ferrobasaltic magma of Skaergaard: An experimental study", Beihefte zum European Journal of Mineralogy 15, 29

BROMILEY, F.A., BOFFA BALLARAN, T.; LANGENHORST, F.: 06.-11.04.2003, EGS-AGU-EUG Joint Assembly, Nice, France[*1]: "Mixing behaviour in the $MgCO_3$-$CdCO_3$ solid solution", Geophysical Research Abstracts 5, Abstract 02139, 2003

BROMILEY, G.D.; KEPPLER, H.: 06.-11.04.2003, EGS-AGU-EUG Joint Assembly, Nice, France[*1]: "Solubility and speciation in jadeite and Na-rich pyroxenes under upper-mantle conditions", Geophysical Research Abstracts 5, Abstract 03211, 2003

BROMILEY, G.D.; KEPPLER, H.; BROMILEY, F.A.; JACOBSEN, S.D.: 06.-11.04.2003, EGS-AGU-EUG Joint Assembly, Nice, France[*1]: "A novel method for high-pressure annealing experiments in a water-rich environment: hydrogen solubility and speciation in natural, gem-quality diopside", Geophysical Research Abstracts 5, Abstract 03721, 2003

BROMILEY, G.D.: 06.-11.04.2003, EGS-AGU-EUG Joint Assembly, Nice, France[*1]: "Structurally-incorporated hydrogen as an internal probe to phase transitions in minerals: a proof-of-concept investigation of enstatite", Geophysical Research Abstracts 5, Abstract 05152, 2003

BROMILEY, G.D.; KEPPLER, H.; MCCAMMON, C.A.; BROMILEY, F.A.; JACOBSEN, S.D.: 21.-28.06.2003, Alice Wain Memorial Western Norway Eclogites Field Symposium, Selje, Norway: "An experimental investigation of water contents in UHP pyroxenes: insights into the role of omphacite as a repository for water during subduction"

CÁMARA, F.; OBERTI, R.; IEZZI, G.; DELLA VENTURA, G.: 16.-18.09.2003, FIST Geoitalia 2003, 4° Forum Italiano di Scienze della Terra, Bellaria, Italy: "The $P2_1/m$-$C2/m$ phase transition in the synthetic amphibole $Na(NaMg)Mg_5Si_8$. Thermodynamic and crystal-chemical evaluation", 614-615

COHEN, R.E.; SHOOK, D.; STEINLE-NEUMANN, G.; STIXRUDE, L.: 02.-05.11.2003, GSA Annual Meeting – Geoscience Horizons, Seattle, USA: "Effects of magnetism on the thermal equation of state of iron", Geological Society of America Abstracts with Programs 35(6), 49-6

CORNELIUS, V.J.; FERN, G.R.; MILLER, J.R.; SILVER, J.; SNOWDEN, M.J.; MCCAMMON, C.A.: 04.11.2003, RSC Mössbauer Spectroscopy Discussion Group 44th Meeting, London, U.K.: "Iron protoporphyrin IX hydroxide – A high pressure Mössbauer spectroscopy study"

COUVY, H.; CORDIER, P.; MACKWELL, S.J.; FROST, D.J; HEIDELBACH, F.; UNGAR, T.: 24.-26.03.2003, Colloque Plasticité 2003, Villeneuve d'Ascq, France: "Déformation plastique en cisaillement de la forstérite: étude expérimentale sous haute pression"

COUVY, H.; CORDIER, P.; MACKWELL, S.J.; FROST, D.J; HEIDELBACH, F.; UNGAR, T.: 06.-11.04.2003, EGS-AGU-EUG Joint Assembly, Nice, France[*1]: "Multi-anvil study of plastic deformation of forsterite at high pressure and temperature", Geophysical Research Abstracts 5, Abstract 00552, 2003

DELLA VENTURA, G.; REDHAMMER, G.; IEZZI, G.; PAPIN, A.; ROBERT, J-L.: 06.-11.04.2003, EGS-AGU-EUG Joint Assembly, Nice, France[*1]: "A Mössbauer and FTIR study of synthetic amphiboles along the magnesio-riebeckite – ferri-clinoholmquistite join", Geophysical Research Abstracts 5, Abstract 11886, 2003

DELLA VENTURA, G.; IEZZI, G.; PEDRAZZI, G.; NOVEMBRE, D.; ROBERT, J.-L.: 16.-18.09.2003, FIST Geoitalia 2003, 4° Forum Italiano di Scienze della Terra, Bellaria, Italy: "The (Mg-Fe^{2+}) substitution in ferri-clinoholmquistite: an infrared study in the OH-stretching region", 622-623

DELLA VENTURA, G.; PICCININI, M.; MARCELLI, A.; MARESCH, W.V.; OBERTI, R.; CÁMARA, F.; IEZZI, G.: 22.-25.09.2003, 81. Jahrestagung der DMG, Bochum, Germany[*2]: "High-*T* FTIR spectroscopy of $NaNa_2Mg_5Si_8O_{21}(OH)_3$", Beihefte zum European Journal of Mineralogy 15, 40

DEMOUCHY, S.; MACKWELL, S.J.; KEPPLER, H.: 04.04.2003, "Hydrospec" mid-term Meeting, Nice, France: "Hydrogen Diffusion in synthetic Forsterite"

DEMOUCHY, S.; GAILLARD, F.; STERN, C.R.; MACKWELL, S.J.: 06.-11.04.2003, EGS-AGU-EUG Joint Assembly, Nice, France[*1]: "Water diffusion as a natural process in olivine crystal from garnet-peridotite xenoliths in basalts", Geophysical Research Abstracts 5, Abstract 03216, 2003

DEMOUCHY, S.; GAILLARD, F.; JACOBSEN, S.D.; STERN, C.R.; MACKWELL, S.J.: 17.06.2003, Universität Tübingen, Institut für Geowissenschaften, Tübingen, Germany: "Hydrogen diffusion in olivine"

DEMOUCHY, S.; JACOBSEN, S.D.; STERN, C.R.; MACKWELL, S.J.: 16.07.03, University College London, Department of Earth Sciences, London, U.K.: "Hydrogen diffusion in olivine"

DEUTSCH, A.; LANGENHORST, F.; HORNEMANN, U.; IVANOV, B.A.: 06.-11.04.2003, EGS-AGU-EUG Joint Assembly, Nice, France[*1]: "The Chicxulub crater – impact metamorphism of sulphate and carbonate lithologies", Geophysical Research Abstracts 5, Abstract 04908, 2003

DEUTSCH, A.; LANGENHORST, F.; HORNEMANN, U.; IVANOV, B.A.: 05.-07.08.2003, 3rd International Conference on Large Meteorite Impacts, Nördlingen, Germany: "On the shock behavior of anhydrite and carbonates – is post-shock melting the most important effect?", Abstract Volume, No. 4080

DUBROVINSKAIA, N.A.; DUBROVINSKY, L.S.: 04.-15.06.2003, 34th International School of Crystallography on High Pressure Crystallography, Erice, Italy: "High-pressure, high-temperature polymorphs of titanium dioxide"

DUBROVINSKAIA, N.A.; DUBROVINSKY, L.S.; MCCAMMON, C.A.: 07.-11.07.2003, Joint 19th AIRAPT International Conference & 41st EHPRG meeting on High Pressure Science and Technology, Bordeaux, France: "Iron-magnesium alloying at high pressures and temperatures"

DUBROVINSKAIA, N.A.; DUBROVINSKY, L.S.; LANGENHORST, F.; JACOBSEN, S.D.; LIEBSKE, C.: 07.-11.07.2003, Joint 19th AIRAPT International Conference & 41st EHPRG meeting on High Pressure Science and Technology, Bordeaux, France: "Nanocrystalline diamond and 6H diamond polytype from C_{60}"

DUBROVINSKAIA, N.A.: 10.-12.12.2003, 1st International Workshop on Advanced Superhard Materials, Villetaneuse, France *(invited)*: "Nanocrystalline superdiamond synthesised from C_{60}"

DUBROVINSKY, L.S.; DUBROVINSKAIA, N.A.: 10.-13.03.2003, The 10th International Symposium on Advanced Materials, Tsukuba, Japan *(invited)*: "Synthesis, structures and properties of high-pressure modifications of the group IV metals dioxides"

DUBROVINSKY, L.S.: 24.-27.03.2003, The SMEC (Study of Matter at Extreme Conditions) 2003 Conference, Miami, USA *(invited)*: "New class of high-pressure silica polymorphs"

DUBROVINSKY, L.S.; DUBROVINSKAIA, N.A.; PRAKAPENKA, V.; SHEN, G.: 06.-11.04.2003, EGS-AGU-EUG Joint Assembly, Nice, France[*1]: "Carbon diffusion in diamond anvil cells at high pressures and temperatures", Geophysical Research Abstracts 5, Abstract 09935, 2003

DUBROVINSKY, L.S.; DUBROVINSKAIA, N.A.: 04.-15.06.2003, 34th International School of Crystallography on High Pressure Crystallography, Erice, Italy *(invited)*: "High-pressure crystallography at elevated temperature"

DUBROVINSKY, L.S.; DUBROVINSKAIA, N.A.; MCCAMMON, C.A.; ROZENBERG, G.Kh.; AHUJA, R.; OSORIO-GUILLÉN, J.M.; DMITRIEV, V.; WEBER, H.-P.; LE BIHAN, T.; JOHANSSON, B.: 07.-11.07.2003, Joint 19th AIRAPT International Conference & 41st EHPRG meeting on High Pressure Science and Technology, Bordeaux, France *(invited)*: "Structure of metallic and magnetic high-pressure Fe_3O_4 polymorph: experimental and theoretical study"

DUBROVINSKY, L.S.; DUBROVINSKAIA, N.A.; LANGENHORST, F.; MCCAMMON, C.A.: 07.-11.07.2003, Joint 19th AIRAPT International Conference & 41st EHPRG meeting on High Pressure Science and Technology, Bordeaux, France: "Phase relations and equations of state in Fe-Ni and Fe-Si alloys: implications for Earth's core"

DUBROVINSKY, L.S.: 10.-12.12.2003, 1st International Workshop on Advanced Superhard Materials, Villetaneuse, France *(invited)*: "Synthesis, structure and properties of superhard high-pressure modifications of the group IV metals oxides"

EL GORESY, A.; DUBROVINSKY, L.S.: 24.-27.03.2003, The SMEC (Study of Matter at Extreme Conditions) 2003 Conference, Miami, USA: "Phases in Earth's interior"

EL GORESY, A.; DUBROVINSKY, L.S.; GILLET, P.; CHEN, M.; GRAUP, G.: 22.-25.09.2003, 81. Jahrestagung der DMG, Bochum, Germany[*2]: "Two new natural shock-induced dense and ultradense polymorphs of rutile in the Ries Crater, Germany: Mechanisms of phase transition and petrographic settings", Beihefte zum European Journal of Mineralogy 15, 45

FROST, D.J.: 06.-11.04.2003, EGS-AGU-EUG Joint Assembly, Nice, France[*1]: "Experimental calibration of factors affecting the width of the 410 km seismic discontinuity", Geophysical Research Abstracts 5, Abstract 06864, 2003

FROST, D.J.: 07.11.2003, Universität München, Germany: "The oxidation state of iron in the Earth's lower mantle"

FROST, D.J.; LIEBSKE, C.; MCCAMMON, C.A.; LANGENHORST, F.; TRØNNES, R.G.; RUBIE, D.C.: 08.-12.12.2003, AGU Fall Meeting, San Francisco, USA[*3]: "Experimental evidence for the existence of metallic Fe-rich alloy in the Earth's lower mantle", EOS Trans. AGU, 84(47), Fall Meet. Suppl., Abstract T22D-05, 2003

FUNAKOSHI, K.-I.; TERASAKI, H.: 07.-11.07.2003, Joint 19th AIRAPT International Conference & 41st EHPRG meeting on High Pressure Science and Technology, Bordeaux, France: "High-pressure viscosity measurements of the Fe-FeS melts using an X-ray radiograph technique"

GAILLARD, F.; SCAILLET, B.; PICHAVANT, M.: 06.-11.04.2003, EGS-AGU-EUG Joint Assembly, Nice, France[*1]: "Oxidation of magmas by redox exchanges of hydrogen with mantle peridotite", Geophysical Research Abstracts 5, Abstract 11473, 2003

GAILLARD, F.: 06.-11.04.2003, EGS-AGU-EUG Joint Assembly, Nice, France[*1]: "Electrical conductivity of water-bearing magmas", Geophysical Research Abstracts 5, Abstract 11621, 2003

GAILLARD, F.: 07.-11.10.2003, 7th Silicate Melt Workshop, La Petite Pierre, France: "Laboratory measurements of electrical conductivity of hydrous and dry silicic melts"

GATTA, G.D.; BOFFA BALLARAN, T.; COMODI, P.; ZANAZZI, P.F.: 06.-11.04.2003, EGS-AGU-EUG Joint Assembly, Nice, France[*1]: "Equation of state and compressional behaviour of edingtonite: preliminary results", Geophysical Research Abstracts 5, Abstract 05215, 2003

GATTA, G.D.; BOFFA BALLARAN, T.; COMODI, P.; ZANAZZI, P.F.: 04.-15.06.2003, 34th International School of Crystallography on High Pressure Crystallography, Erice, Italy: "Microporous framework silicates under high-pressure conditions: the case of natural zeolites"

GATTA, G.D.; BOFFA BALLARAN, T.; COMODI, P.; ZANAZZI, P.F.: 21.-25.07.2003, Joint Congress AIC-SILS, The XXXIII National Congress of the Italian Crystallographic Association, Trieste, Italy: "Topological effects on microporous materials under pressure conditions: framework and extra-framework behaviour of Ca- and Ba-fibrous zeolites"

GATTA, G.D.; COSTANTINO, F.; MASCI, S.; VIVANI, R.: 21.-25.07.2003, Joint Congress AIC-SILS, The XXXIII National Congress of the Italian Crystallographic Association, Trieste, Italy: "Dimensional changes in zirconium phosphates"

GATTA, G.D.; COMODI, P.; ZANAZZI, P.F.; BOFFA BALLARAN, T.: 16.-18.09.2003, FIST Geoitalia 2003, 4° Forum Italiano di Scienze della Terra, Bellaria, Italy: "Compressional behaviour of tetragonal edingtonite: equation of state and high-pressure crystal structure"

GATTA, G.D.; BOFFA BALLARAN, T.: 02.-05.11.2003, 2003 GSA Annual Meeting – Geoscience Horizons, Seattle, USA: "Comparative high-pressure study of orthorhombic and tetragonal edingtonite: equations of state and crystal structures", Geological Society of America Abstracts with Programs 35(6), 254-7

HEIDELBACH, F.: 11.02.2003, Universität Freiberg, Geologisches Institut, Freiberg, Germany: "Texture analysis with synchrotron radiation"

HEIDELBACH, F.: 13.02.2003, Universität Freiberg, Geologisches Institut, Freiberg, Germany: "Texture analysis in experimentally deformed rocks"

HEIDELBACH, F.: 14.02.2003, Universität Erlangen, Geologisches Institut, Erlangen, Germany: "Texturanalyse mit EBSD"

HEIDELBACH, F.; STRETTON, I.C.; MACKWELL, S.J.: 22.-25.09.2003, 81. Jahrestagung der DMG, Bochum, Germany[*2]: "The effect of iron content on the deformation behaviour of magnesiowüstite (Mg,Fe)O", Beihefte zum European Journal of Mineralogy 15, 77

HOLL, C.M.; SMYTH, J.R.; JACOBSEN, S.D.: 08.-12.12.2003, AGU Fall Meeting, San Francisco, USA[*3]: "The effect of water on the compressibility of wadsleyite", EOS Trans. AGU, 84(47), Fall Meet. Suppl., Abstract T11C-0414, 2003

HOLZAPFEL, C.; RUBIE, D.C.; FROST, D.J.: 06.-11.04.2003, EGS-AGU-EUG Joint Assembly, Nice, France[*1]: "Kinetic constraints on core formation", Geophysical Research Abstracts 5, Abstract 02709, 2003

HOLZHEID, A.; BALOG, P.; RUBIE, D.C.: 06.-11.04.2003, EGS-AGU-EUG Joint Assembly, Nice, France[*1]: "Metal-silicate separation processes in terrestrial planets: insights from sulphide melt distribution in partially molten silicate aggregates", Geophysical Research Abstracts 5, Abstract 04350, 2003

HOLZHEID, A.; BALOG, P.; RUBIE, D.C.: 22.-25.09.2003, 81. Jahrestagung der DMG, Bochum, Germany[*2]: "Benetzungsverhaltensstudien von flüssigem Metall in einer Silikatmatrix: Implikationen für Kern-Mantel-Differentiationsprozesse?", Beihefte zum European Journal of Mineralogy 15, 85

HYDE, R.; STEINLE-NEUMANN, G.; DERA, P.: 08.-12.12.2003, AGU Fall Meeting, San Francisco, USA[*3]: "Layer shift phase transition in kaolins by computer", EOS Trans. AGU, 84(47), Fall Meet. Suppl., Abstract V11D-0522, 2003

IEZZI, G.; CÀMARA, F.; DELLA VENTURA, G.; OBERTI, R.; HOLTZ, F.: 06.-11.04.2003, EGS-AGU-EUG Joint Assembly, Nice, France[*1]: "Crystal-structure and FTIR spectroscopy of synthetic $Na(NaMg)Mg_5Si_8O_{22}(OH)_2$, a $P2_1/m$ amphibole", Geophysical Research Abstracts 5, Abstract 11801, 2003

IEZZI, G.; CÀMARA, F.; DELLA VENTURA, G.; OBERTI, R.; BENY, J.-M.: 20.-25.06.2003, LERM 2003, International Symposium on Light Elements in Rock-forming Minerals, Nové Město na Moravě, Czech Republik: "Long-range and short-range order in synthetic leakeite, $NaNa_2Mg_2Fe^{3+}{}_2LiSi_8O_{22}(OH)_2$. at different P, T, FO_2 conditions", LERM 2003 Book of Abstracts, 33-34

IEZZI, G.; CÀMARA, F.; DELLA VENTURA, G.; OBERTI, R.; PEDRAZZI, G.; ROBERT, J.L.: 20.-25.06.2003, LERM 2003, International Symposium on Light Elements in Rock-forming Minerals, Nové Město na Moravě, Czech Republik: "Synthesis, crystal structure and crystal-chemistry of ferri-clinoholmquistites, $\square Li_2Mg_3Fe^{3+}{}_2Si_8O_{22}(OH)_2$." LERM 2003 Book of Abstracts, 35-36

IEZZI, G.; DELLA VENTURA, G.; CÁMARA, F.; OBERTI, R.: 16.-18.09.2003, FIST Geoitalia 2003, 4° Forum Italiano di Scienze della Terra, Bellaria, Italy: "Synthesis and crystal-chemistry of leakeite, $NaNa_2(Mg_2Fe^{3+}{}_2Li)Si_8O_{22}(OH)_2$", 630-631

IEZZI, G.; DELLA VENTURA, G.; CÁMARA, F.; OBERTI, R.: 16.-18.09.2003, FIST Geoitalia 2003, 4° Forum Italiano di Scienze della Terra, Bellaria, Italy: "Synthesis, crystal-structure and FTIR spectroscopy of $Na(NaMg)Mg_5Si_8O_{22}(OH)_2$, a $P2_1/m$ amphibole", 631-632

JACKSON, J.M.; BASS, J.D.; SINOGEIKIN, S.V.; JACOBSEN, S.D.; REICHMANN, H.-J.; MACKWELL, S.J.: 08.-12.12.2003, AGU Fall Meeting, San Francisco, USA[*3]: "High-pressure Brillouin measurements on single-crystal ferropericlase, $(Mg_{0.94}Fe_{0.06})O$: implications for Earth's lower mantle", EOS Trans. AGU, 84(47), Fall Meet. Suppl., Abstract T21A-07, 2003

JACOBSEN, S.D.: 14.04.2003, California Institute of Technology, Seismological Laboratory, Pasadena, USA: "High-pressure elasticity of minerals in the ultrasonic diamond anvil cell"

JACOBSEN, S.D.: 18.04.2003, Mineral Physics Seminar, Carnegie Institution of Washington, Geophysical Laboratory, Washington, USA: "Ultrasonic interferometry in the diamond anvil cell: where acoustic and optical wavelengths meet"

JACOBSEN, S.D.; SPETZLER, H.A.; REICHMANN, H.-J.; SMYTH, J.R.: 07.-10.09.2003, World Congress on Ultrasonics, Paris, France: "Ultrasonic velocities in single-crystal (Mg,Fe)O to 10 Gigapascals", Abstract WCU2003/75

JACOBSEN, S.D.; SPETZLER, H.A.; REICHMANN, H.-J.; SMYTH, J.R.; KANTOR, A.; DUBROVINSKY, L.S.; HEMLEY, R.J.; MAO, H.-K.: 08.-12.12.2003, AGU Fall Meeting, San Francisco, USA[*3]: "Ultrasonic shear waves in the diamond anvil cell and shear-mode softening in (Mg,Fe)O", EOS Trans. AGU, 84(47), Fall Meet. Suppl., Abstract V31D-0965, 2003

KOPYLOVA, M.G.; MCCAMMON, C.A.: 22.-27.06.2003, 8th International Kimberlite Conference, Victoria, Canada: "Composition and the redox state of the Slave peridotitic mantle"

KOPYLOVA, M.G.; JONES, A.; MCCAMMON, C.A.: 08.-12.12.2003, AGU Fall Meeting, San Francisco, USA[*3]: "Geophysical signatures of chemical depletion in Slave cratonic peridotite", EOS Trans. AGU, 84(47), Fall Meet. Suppl., Abstract T32B-0921, 2003

KROGH, T.E.; ROBINSON, P.; TERRY, M.P.: 21.-28.06.2003, Alice Wain Memorial Western Norway Eclogites Field Symposium, Selje, Norway: "Precise U-Pb zircon ages define 18 and 19 m.y. subduction to uplift intervals in the Averøya-Nordøyane area, Western Gneiss Region"

LANGENHORST, F.: 04.02.2003, Geowissenschaftliches Kolloquium, Universität Karlsruhe (TH), Germany: "Schockmetamorphose von Karbonaten und Sulfaten: Beobachtungen in Experiment und Natur"

LANGENHORST, F.: 17.02.2003, Georg-August-Universität Göttingen, Germany: "Perspektiven der Nanogeowissenschaften – Einblicke in einen neuen Forschungszweig am Beispiel des Diamanten"

LANGENHORST, F.: 24.03.2003, Universität Wien, Austria: "Nanostrukturen in UHP-metamorphem Coesit und Diamant: Ein genetischer Fingerabdruck"

LANGENHORST, F.: 25.03.2003, Universität Graz, Austria: "Nanostrukturen in UHP-metamorphem Coesit und Diamant: "Ein genetischer Fingerabdruck"

LANGENHORST, F.: 27.03.2003, Universität Innsbruck, Austria: "Nanostrukturen in UHP-metamorphem Coesit und Diamant: Ein genetischer Fingerabdruck"

LANGENHORST, F.; POIRIER, J.-P.: 06.-11.04.2003, EGS-AGU-EUG Joint Assembly, Nice, France[*1]: "Defect microstructure of coesite from the ultra-high pressure metamorphic Dora Maira Massif, Alps", Geophysical Research Abstracts 5, Abstract 08281, 2003

LANGENHORST, F.: 06.06.2003, Geowissenschaftliches Kolloquium, Ruhr-Universität Bochum, Germany: "TEM-Untersuchungen zur Ultrahochdruck-Metamorphose: Auf Spurensuche im Nanomaßstab"

LANGENHORST, F.: 10.-13.06.2003, SCANDEM 2003, The 54th Annual Meeting of SCANDEM, Nordic Microscopy Society, University of Oslo, Norway: "Applications of transmission electron microscopy in geoscience"

LANGENHORST, F.: 27.06.2003, Friedrich-Schiller-Universität Jena, Germany: "Minerale im Zustand des Schocks – über diaplektische Gläser und Impaktdiamanten"

LANGENHORST, F.: 27.10.2003, Geowissenschaftliches Kolloquium, Friedrich-Alexander-Universität Erlangen, Germany: "Genese und Eigenschaften metamorpher Diamanten: Auf Spurensuche im Nanomaßstab"

LANGENHORST, F.; SOLOZHENKO, V.: 10.-12.12.2003, Université Paris Nord, France: "ATEM-EELS studies of novel superhard phases of the B-C-N system"

LANGENHORST, F.; DEUTSCH, A.; HORNEMANN, U.; IVANOV, B.A.; LOUNEJEVA, E.: 17.-21.03.2003, 34th Lunar and Planetary Science Conference, Houston, Texas: "On the Shock behaviour of anhydrite: Experimental results and natural observations", Abstract No. 1638

LANGENHORST, F.; TERRY, M.P.; ROBINSON, P.: 21.-28.06.2003, Alice Wain Memorial Western Norway Eclogites Field Symposium, Selje, Norway: "Microstructure of rutile inclusions in a kyanite-garnet gneiss from Fjørtoft, Western Norway: hints to the metamorphic evolution"

LANGENHORST, F.; DRESSLER, B.: 05.-07.08.2003, 3rd International Conference on Large Meteorite Impacts, Nördlingen, Germany: "First observation of silicate hollandite in a terrestrial rock", Abstract Volume, No. 4046

LANGENHORST, F.; TERRY, M.P.; ROBINSON, P.: 22.-25.09.2003, 81. Jahrestagung der DMG, Bochum, Germany[*2]: "Defect microstructure of rutile in ultra-high pressure metamorphic kyanite-garnet gneiss, Fjørtoft, Western Norway", Beihefte zum European Journal of Mineralogy 15, 115

LEE, K.K.M.; JEANLOZ, R.; STEINLE-NEUMANN, G.: 06.-11.07.2003, Gordon Research Conference on the Origin of Solar Systems, Bristol, USA: "High-pressure alloying of potassium and iron: Radioactivity in planetary cores?"

LEE, K.K.M.; STEINLE-NEUMANN, G.; JEANLOZ, R.: 08.-12.12.2003, AGU Fall Meeting, San Francisco, USA[*3] *(invited)*: "Quantum theory and high pressure experiments on iron-potassium alloying: Radioactivity in the Earth's core?", EOS Trans. AGU, 84(47), Fall Meet. Suppl., Abstract T31G-03, 2003

LEPORA, A.; GROBÉTY, B.; MÉTRAUX, C.; MCCAMMON, C.A.: 06.-11.04.2003, EGS-AGU-EUG Joint Assembly, Nice, France[*1]: "Dehydroxylation of phengite under reducing and oxidizing conditions", Geophysical Research Abstracts 5, Abstract 13192, 2003

LIEBSKE, C.; FROST, D.J., TRØNNES, R.G.; LANGENHORST, F.; MCCAMMON, C.A.; RUBIE, D.C.: 06.-11.04.2003, EGS-AGU-EUG Joint Assembly, Nice, France[*1]: "The oxidation state of iron in the hadean lower mantle", Geophysical Research Abstracts 5, Abstract 06808, 2003

LIEBSKE, C.; FROST, D.J.; LANGENHORST, F.; MCCAMMON, C.A.; RUBIE, D.C.: 12.-13.06.2003, Workshop on Basaltic Melts, Hannover, Germany: "The oxidation state of iron the early lower mantle"

LIEBSKE, C.; SCHMICKLER, B.; TERASAKI, H.; SUZUKI, A.; FUNAKOSHI, K.-I.; POE, B.T.; RUBIE, D.C.: 07.-11.10.2003, 7th Silicate Melt Workshop, La Petite Pierre, France: "The viscosity of peridotite liquid up to 6.9 GPa measured by *in situ* falling sphere viscometry"

LIEBSKE, C.; CORGNE, A.; FROST, D.J.; WOOD, B.J.; RUBIE, D.C.: 07.-11.10.2003, 7th Silicate Melt Workshop, La Petite Pierre, France: "Compositional effects on trace element partitioning between Mg-silicate perovskite and silicate melt"

LIEBSKE, C.; CORGNE, A.; FROST, D.J.; RUBIE, D.C.; WOOD, B.J.: 08.-12.12.2003, AGU Fall Meeting, San Francisco, USA[*3]: "Compositional effects on trace element partitioning between Mg-silicate perovskite and silicate melt", EOS Trans. AGU, 84(47), Fall Meet. Suppl., Abstract T21A-08, 2003

MARTON, F.C.; RUBIE, D.C.; SHANKLAND; T.J.; YU, X.: 06.-11.09.2003, EURESCO Conference 'The Deep Earth: Theory, Experiment and Observation', Acquafredda di Maratea, Italy: "Thermal properties, temperature, and metastable olivine in subducting slabs"

MARTON, F.C.; RUBIE, D.C.; SHANKLAND; T.J.; YU, X.: 13.-18.09.2003, 8th European Workshop on Numerical Modeling of Mantle Convection and Lithospheric Dynamics, Castle of Hrubá Skála, Czech Republic: "Variable thermal conductivity in subducting slabs: olivine metastability and the mechanisms of deep earthquakes"

MARTON, F.C.; FROST, D.J.: 08.-12.12.2003, AGU Fall Meeting, San Francisco, USA[*3]: "Latent heat release and temperature changes as a result of metastable $(Mg,Fe)_2SiO_4$ phase transitions", EOS Trans. AGU, 84(47), Fall Meet. Suppl., Abstract V41C-0304, 2003

MCCAMMON, C.A.: 06.-11.04.2003, EGS-AGU-EUG Joint Assembly, Nice, France[*1]: "Oxygen fugacity, diamonds and mantle dynamics", Geophysical Research Abstracts 5, Abstract 05443, 2003

MCCAMMON, C.A.: 07.-12.09.2003, 13th V.M. Goldschmidt Conference, Kurashiki, Japan: "Deep diamonds: Geochemical constraints on mantle dynamics"

MCCAMMON, C.A.: 14.-16.09.2003, International Workshop in High-Pressure Mineral Physics and Geochemistry, Harima (SPring-8), Japan: "Mantle oxidation state and its influence on mantle properties and dynamics"

MCCAMMON, C.A.; KOPYLOVA, M.G.: 22.-27.06.2003, 8th International Kimberlite Conference, Victoria, Canada: "Mantle oxygen fugacity and diamond formation"

NOVEMBRE, D.; DI SABATINO, M.; PASCULLI, A.; IEZZI, G.; BALIVA, A.: 23.01.2003, 1° Congresso AIGA 2003, Chieti, Italy: "Valorizzazione dei caolini di Romana (Sassari)", Abstract volume, 543-549

REICHMANN, H.-J.; JACOBSEN, S.D.: 07.-10.09.2003, World Congress on Ultrasonics, Paris, France: "High-pressure elasticity of magnetite by ultrasonic interferometry", Abstract WCU2003/83

RUBIE, D.C.; GESSMANN, C.K.; FROST, D.J.: 06.-11.04.2003, EGS-AGU-EUG Joint Assembly, Nice, France[*1]: "A new model for early differentiation and chemical stratification of the Earth's mantle", Geophysical Research Abstracts 5, Abstract 05353, 2003

RUBIE, D.C.; GESSMANN, C.K.; FROST, D.J.: 06.-11.04.2003, EGS-AGU-EUG Joint Assembly, Nice, France[*1]: "Solubility of oxygen in liquid Fe at high pressure and consequences for the early differentiation of Earth and Mars", Geophysical Research Abstracts 5, Abstract 03517, 2003

RUBIE, D.C.; GESSMANN, C.K.; FROST, D.J.: 06.-11.09.2003, EURESCO Conference 'The Deep Earth: Theory, Experiment and Observation', Acquafredda di Maratea, Italy: "Early differentiation of the Earth's mantle"

RUBIE, D.C.: 08.-10.10.2003, Wissenschaftliches Kolloquium zum DFG Schwerpunkt-programm 'Mars und die terrestrischen Planeten', Münster, Germany: "Partitioning of oxygen during core formation on Earth and Mars"

RUBIE, D.C.: 14.11.2003, Sitzung der Kommission für Geowissenschaftliche Hoch-druckforschung der Bayerischen Akademie der Wissenschaften, München, Germany: "Partitioning of oxygen during core formation on Earth and Mars"

RUBIE, D.C.; GESSMANN, C.K.; FROST, D.J.: 08.-12.12.2003, AGU Fall Meeting, San Francisco, USA[*3]: "Partitioning of oxygen during core formation on Earth and Mars", EOS Trans. AGU, 84(46), Fall Meet. Suppl., Abstract S12D-04, 2003

SCHMICKLER, B.; LIEBSKE, C.; TERASAKI, H.; SUZUKI, A.; POE, B.T.; FUNAKOSHI, K.-I.; ANDO, R.; RUBIE, D.C.: 08.-12.12.2003, AGU Fall Meeting, San Francisco, USA[*3]: "The viscosity of peridotite liquid up to 6.9 GPa measured by *in situ* falling sphere viscometry", EOS Trans. AGU, 84(46), Fall Meet. Suppl., Abstract T11C-0408, 2003

SCHMIDT, B.C.: 13.06.2003, University of Warwick, Department of Physics, Coventry, U.K.: "Effect of water on the structure of boro(alumino)silicate melts and glasses"

SCHMIDT, B.C.: 17.09.2003, Universität Göttingen, Geowissenschaftliches Zentrum, Göttingen, Germany: "Löslichkeit von Volatilen in Silikatschmelzen: zwei Fallbeispiele"

SCHMIDT, B.C.: 07.-11.10.2003, 7th Silicate Melt Workshop, La Petite Pierre, France: "Effect of boron on the water speciation in (alumino)silicate melts and glasses"

SEBALD, A.: 24.02.2003, Max-Planck-Institut für Biophysikalische Chemie, Göttingen, Germany: "At and around rotational-resonance conditions"

SEBALD, A.: 04.-05.07.2003, Solid-State NMR Symposium, University of Durham, Department of Chemistry, Durham, U.K.: "Does it spin?"

SEBALD, A.: 15.07.2003, University of Exeter, Department of Chemistry, Exeter, U.K.: "Virtual + real NMR spectrometer = quantitative structural information about solids"

SEIFERT, F.: 24.-27.03.2003, The SMEC (Study of Matter at Extreme Conditions) 2003 Conference, Miami, USA: "Oxygen defects in Si- and Ti-bearing perovskites"

SHCHEKA, S.; WIEDENBECK, M.; FROST, D.J.; KEPPLER, H.: 22.-25.09.2003, 81. Jahrestagung der DMG, Bochum, Germany[*2]: "Carbon solubility in nominally volatile-free mantle minerals", Beihefte zum European Journal of Mineralogy 15, 189

SKÁLA, R.; HÖRZ, F.; LANGENHORST, F.: 05.-07.08.2003, 3rd International Conference on Large Meteorite Impacts, Nördlingen, Germany: "Diaplectic glass content in experimentally shock-loaded quartz determined by X-ray powder diffraction", Abstract Volume, No. 4033

SMYTH, J.R.; HOLL, C.M.; FROST, D.J.; JACOBSEN, S.D.: 06.-11.04.2003, EGS-AGU-EUG Joint Assembly, Nice, France[*1]: "Geophysical and mineralogical constraints on H cycling in the deep interior", Geophysical Research Abstracts 5, Abstract 07719, 2003

SMYTH, J.R.; HOLL, C.M.; FROST, D.J.; JACOBSEN, S.D.; MANGHNANI, M.; AMULELE, G.; CHEN, G.: 02.-05.11.2003, GSA Annual Meeting – Geoscience Horizons, Seattle, USA: "Searching for Earth's lost oceans: an expedition in mineral crystal chemistry", Geological Society of America Abstracts with Programs 35(6), 219-3

SMYTH, J.R.; HOLL, C.M.; JACOBSEN, S.D.; MANGHNANI, M.H.; AMULELE, G.: 08.-12.12.2003, AGU Fall Meeting, San Francisco, USA[*3]: "Hydration and velocity heterogeneity in the mantle", EOS Trans. AGU, 84(47), Fall Meet. Suppl., Abstract T32B-0931, 2003

SPETZLER, H.A.; JACOBSEN, S.D.; REICHMANN, H.-J.; SMYTH, J.R.; BASSETT, W.A.; HEMLEY, R.; MAO, H.-K.: 07.-10.09.2003, World Congress on Ultrasonics, Paris, France: "A GHz-ultrasonic interferometer for measurements in a diamond anvil cell", Abstract WCU2003/129

STEINLE-NEUMANN, G.: 27.02.2003, New Mexico State University, Department of Physics, Las Cruces, USA: "Solid state physics underground: Computing deep Earth structure"

STEINLE-NEUMANN, G.: 03.-07.03.2003, Annual APS March Meeting 2003, Austin, USA *(invited)*: "Magnetism and elasticity of iron at high pressures", Bulletin of the American Physical Society 48, S34.001, 2003

STEINLE-NEUMANN, G.; STIXRUDE, L.; COHEN, R.E.: 26.03.2003 Frühjahrstagung des Arbeitskreises Festkörperphysik der Deutschen Physikalischen Gesellschaft, Dresden, Germany: "Magnetoelastic effects in cobalt under compression", Abstract: Verhandl. DPG (VI) 38, SYEC 3.1, 2003

STEINLE-NEUMANN, G.; COHEN, R.E.; STIXRUDE, L.: 23.-26.04.2003, WIEN2k workshop, Wien, Österreich: "Magnetism in dense hexagonal iron?"

STEINLE-NEUMANN, G.: 02.06.2003, Northwestern University, Department of Geology, Evanston, USA: "From electronic charge density to deep Earth structure"

STEINLE-NEUMANN, G.: 03.06.2003, Northwestern University, Department of Geology, Evanston, USA: "Magnetism in dense hexagonal iron?!"

STEINLE-NEUMANN, G: 24.06.2003, Universität Bayreuth, Fakultät für Angewandte Naturwissenschaften, Bayreuth, Germany: "Reise zum Mittelpunkt der Erde"

STEINLE-NEUMANN, G.; COHEN, R.E.; STIXRUDE, L.: 07.-11.07.2003, Joint 19th AIRAPT International Conference & 41st EHPRG meeting on High Pressure Science and Technology, Bordeaux, France: "Magnetism in iron under pressure"

STEINLE-NEUMANN, G.: 22.09.2003, Princeton University, Department of Geosciences, Princeton, USA: "Hot core to cold subduction: Computational mineralogy under pressure"

STEINLE-NEUMANN, G.: 24.10.2003, Ludwig-Maximilians Universität München, Department für Geo- und Umweltwissenschaften, München, Germany: "From electronic charge density to deep Earth structure"

STEINLE-NEUMANN, G.: 21.11.2003, University of Chicago, Department of Geophysical Sciences, Chicago, USA: "Hot core to cold subduction: Computational mineralogy under pressure"

STEINLE-NEUMANN, G.; LEE, K.K.M.; JEANLOZ, R.: 08.-12.12.2003, AGU Fall Meeting, San Francisco, USA[*3]: "Understanding Fe-K alloying at high pressure using density functional theory", EOS Trans. AGU, 84(47), Fall Meet. Suppl., Abstract V11D-0525, 2003

SUZUKI, A.; RUBIE, D.C.: 06.-11.04.2003, EGS-AGU-EUG Joint Assembly, Nice, France[*1]: "Thermal diffusivity of diopside-composition glass at high pressure", Geophysical Research Abstracts 5, Abstract 11695, 2003

TERASAKI, H.; RUBIE, D.C.; HOLZHEID, A.; FROST, D.J.; LANGENHORST, F.: 20.-21.08.2003, Deutsche Forschungsgemeinschaft Kolloquium 'Mars and the terrestrial planets', Münster, Germany: "Mechanisms of metal-silicate segregation during formation of the Martian core"

TERASAKI, H.; RUBIE, D.C.; FROST, D.J.; LANGENHORST, F.: 09.-10.10.2003, 1st Workshop of the Interior – Early Evolution – Core Formation Group on DFG Priority Program 'Mars and the terrestrial planets', Münster, Germany: "Effect of FeO content in silicate phase on dihedral angle between Fe-S liquid and silicate crystals"

TERASAKI, H.; RUBIE, D.C.; FROST, D.J.; LANGENHORST, F.: 08.-12.12.2003, AGU Fall Meeting, San Francisco, USA[*3]: "Compositional effect on the dihedral angle between olivine and Fe-S liquid up to 20 GPa: Possibility of percolative core formation", EOS Trans. AGU, 84(47), Fall Meet. Suppl., Abstract T42A-0273, 2003

TERRY, M.P.; BROMILEY, G.D.; ROBINSON, P.: 06.-11.04.2003, EGS-AGU-EUG Joint Assembly, Nice, France[*1]: "Determination of equilibrium water content and composition of omphacitic pyroxene in a UHP kyanite-eclogite, Western Norway", Geophysical Research Abstracts 5, Abstract 08698, 2003

TERRY, M.P.; HEIDELBACH, F.: 06.-11.04.2003, EGS-AGU-EUG Joint Assembly, Nice, France[*1]: "Microstructures and textures in eclogite-facies shear zones and deformation mechanisms in garnet, Western Norway", Geophysical Research Abstracts 5, Abstract 08847, 2003

TERRY, M.P.; DAHL, P.S.; FREI, R.: 06.-11.04.2003, EGS-AGU-EUG Joint Assembly, Nice, France[*1]: "Isotopic and geothermometric constraints on the structural and metamorphic evolution of Homestake Gold Deposit, Black Hills, South Dakota (USA)", Geophysical Research Abstracts 5, Abstract 13191, 2003

TERRY, M.P.; ROBINSON, P.: 21.-28.06.2003, Alice Wain Memorial Western Norway Eclogites Field Symposium, Selje, Norway: "Boundary conditions deformation of related to the production and exhumation of HP and UHP rocks in hinterland of the Scandinavian Caledonides, Western Gneiss Region, Norway"

TERRY, M.P.; HEIDELBACH, F.: 21.-28.06.2003, Alice Wain Memorial Western Norway Eclogites Field Symposium, Selje, Norway: "Microstructures and textures in synkinematic garnet from eclogite-facies shear zones in the Haram Gabbro, Haramsøya, Norway"

TERRY, M.P.; HEIDELBACH, F.: 22.-25.09.2003, 81. Jahrestagung der DMG, Bochum, Germany[*2]: "Linking deformation and metamorphism eclogite-facies shear zones in the Haram Gabbro, Haramsøya, Norway", Beihefte zum European Journal of Mineralogy 15, 203

TERRY, M.P.; HEIDELBACH, F.: 02.-05.11.2003, GSA Annual Meeting – Geoscience Horizons, Seattle, USA: "Evidence for superplasticity in garnet and the role of deformation in enhancing reaction progress in a high-pressure shear zone, Haramsøya, Norway", Geological Society of America Abstracts with Programs 35(6), 32-9

WILLIAMS, H.M.; PESLIER, A.H.; MCCAMMON, C.A.; TEUTSCH, N.; LEVASSEUR, S.; BURG, J.; HALLIDAY, A.N.: 08.-12.12.2003, AGU Fall Meeting, San Francisco, USA[*3]: "Large iron isotope variations in mantle minerals: The influence of oxidation state and the implications for the iron isotope heterogeneity of the upper mantle", EOS Trans. AGU, 84(47), Fall Meet. Suppl., Abstract V52A-0422, 2003

[*1] **EGS-AGU-EUG: European Geophysical Society – American Geophysical Union – European Union of Geosciences Joint Assembly, 06.-11.04.2002, Nice, France – Geophysical Research Abstracts 5**

[*2] **DMG: 81. Jahrestagung der Deutschen Mineralogischen Gesellschaft, 22.-25.09.2003, Bochum, Germany – Beihefte zum European Journal of Mineralogy 15**

[*3] **AGU: American Geophysical Union Fall Meeting, 08.-12.12.2002, San Francisco, DC, USA – EOS Transactions, American Geophysical Union, 84(47), AGU Fall Meeting 2003 Supplement**

4.4 Lectures and seminars at Bayerisches Geoinstitut

ALLWARDT, J.: 23.10.2003 "The structure of high-pressure silicate and aluminosilicate glasses: a perspective from solid-state NMR"

AUDETAT, A.: 10.04.2003 "Insights into the formation of magmatic-hydrothermal ore deposits"

BOUHIFD, M.A.: 17.09.2003 "Ni and Co partitioning between Cl-chondrite and iron-rich metal liquids up to 50 GPa"

BROMILEY, F.A.: 16.01.2003 "Mixing behaviour in the magnesite-otavite solid solution"

BROMILEY, G.D.: 22.05.2003 "Hydrogen incorporation in pyroxenes: new experimental approaches and results"

CASTRO, J.M.: 12.11.2003 "Natural and experimental observations on ascent-driven crystallization of the inyo rhyolite"

CORGNE, A.: 11.02.2003 "Trace elements incorporation into deep mantle minerals and implications for the differentiation and deep structure of the Earth"

CONNOLLY, J.: 25.06.2003 "Compaction-driven fluid flow revisted: From sediment fluid expulsion to asthenospheric melt extraction"

COUVY, H.: 10.07.2003 "Shear deformation experiments of forsterite in the multianvil apparatus"

CUI, X.: 30.09.2003 "Photoisomerization, magnetism, phonons, and structural transitions by computer: first principles calculations in the material sciences"

DEGTYAREVA, O.: 04.03.2003 "Crystal structure of elements under high pressure: Recent findings and surprises"

DEMOUCHY, S.: 05.06.2003 "Water diffusion in olivine?"

DEN BROK, B.: 25.06.2003 "Water-weakening of minerals and rocks"

DOBSON, D.P.: 28.11.2003 "Constraining convection: electrical conductivity, temperature and rheology"

DUBROVINSKAIA, N.A.: 04.12.2003 "Nanocrystalline diamond: synthesis and properties"

FAUL, U.: 15.07.2003 "Structure of the upper mantle and origin of the low velocity zone"

GAILLARD, F.: 21.05.2003 "Thermodynamic modeling of iron properties in silicate melts"

GAILLARD, F.: 21.05.2003 "Electrical conductivity of magmas and minerals"

GATTA, G.D.: 29.09.2003 "HP-crystallography of natural microporous materials: experimental setup and comparative crystal physics"

GREEN, D.: 03.06.2003 "Primary magmas at Hawaii and mid-ocean ridges: Implications for mantle potential temperatures, source compositions and plumes"

HERWEGH, M.: 26.06.2003 "Evolution of rocks under static and deformational conditions: What can we learn from experiments and nature?"

IACONO MARZIANO, G.: 03.12.2003 "Degassing behaviour of a phonolitic melt. An experimental study on the pumice of the 79 A.D. Vesuvius eruption"

IEZZI, G.: 08.12.2003 "Germanate garnets in the CaO-Fe_2O_3-GeO_2 system"

JACOBSEN, S.D.: 26.06.2003 "High-pressure elasticity of minerals in the diamond anvil cell: where acoustic and optical wavelengths meet"

KEPPLER, H.: 28.11.2003 "Defekte in Mineralen und der globale Wasserkreislauf"

KOMABAYASHI, T.: 23.01.2003 "Petrogenetic grid in the system MgO-SiO_2-H_2O up to 30 GPa, 1600 °C: applications to hydrous slab peridotite subducting into Earth's deep interior"

KUZNETSOV, A.: 03.11.2003 "Experimental and theoretical study of phase transitions between close-packed structures in 'elemental' crystals: La, Ce, Pr, Nd as examples"

LEE, K.K.M.: 03.04.2003 "Equation of state of an upper-mantle rock at conditions of the Earth's lower mantle"

LIEBSKE, C.: 20.03.2003 "Mantle melting at high pressure"

MARTON, F.: 02.10.2003 "Variable thermal conductivity in subducting slabs: olivine metastability and the mechanisms of deep earthquakes"

NEUFELD, K.: 16.01.2003 "Deformation and dehydration interactions in serpentinite under orogenic conditions"

POIRIER, J.-P.: 15.05.2003 "Crystallization at the inner core boundary"

RENNER, J.: 26.06.2003 "State, stress, scale: An experimentalist's view"

SCHMIDT, B.C.: 02.04.2003 "How does water affect the structure of boro(alumino)silicate melts and glasses"

SKÁLA, R.: 30.10.2003 "Assessing the role of anhydrite in the KT mass extinction: Hints from shock-loading experiments"

SPIELER, O.: 08.05.2003 "Experimental fragmentation of magma – the developement of an idea born in BGI"

STOYANOV, E.: 14.05.2003 "Morphology of natural, cosmic and synthetic diamond crystals and metastable diamond synthesis"

TERASAKI, H.: 09.01.2003 "The effect of time and melt fraction on connectivity of liquid FeS-alloy under high pressure"

TRAMPERT, J.A.: 06.11.2003 "The quest for compositional heterogeneity deep in the Earth"

ULRICH, S.: 16.06.2003 "Influence of initial grain size on microstructural stability of dynamically recrystallized polycrystalline rocks"

VAN DER LEE, S.: 30.07.2003 "Seismic constraints on the Andean mantle wedge and the Mediterranean 410-km discontinuity"

WANG, D.: 27.11.2003 "Electrical conductivities of quartz and olivine from complex impedance measurements"

YOSHIASA, A.: 30.06.2003 "Detailed structure, properties and transition mechanism of hexagonal diamond and wurtzite-type BN"

4.5 Scientific conferences organized by/with assistance of Bayerisches Geoinstitut

16.-20.02.2003 DMG-Short Course "High-Pressure Experimental Techniques and Applications to the Earth's Interior", Bayerisches Geoinstitut, Universität Bayreuth, Germany (D.C. RUBIE)

05.-07.08.2003 3rd International Conference on Large Meteorite Impacts, Nördlingen, Germany (G. PÖSGES, T. KENKMANN, M. SCHIEBER, J. POHL, F. LANGENHORST, P. SCHIELE)

07.-12.09.2003 2nd International Summer School 'Solid-State NMR', Niederöblarn, Austria (M. BECHMANN and A. SEBALD, with N. MÜLLER/Linz, M. ERNST/Zürich, M.H. LEVITT/Southampton, A. JERSCHOW/New York, S. STEUERNAGEL/Rheinstetten)

08.-12.12.2002 American Geophysical Union Fall Meeting, San Francisco, DC, USA: Special session "Heat Sources in the Core" (G. STEINLE-NEUMANN, B. BUFFETT)

08.-12.12.2002 American Geophysical Union Fall Meeting, San Francisco, DC, USA: Special session "State of the Art in Theory of Materials: Methods and Applications II" (G. STEINLE-NEUMANN, R.E. COHEN, B. WINKLER)

4.6 Visiting scientists

a) Visiting scientists funded by the Bayerisches Geoinstitut

ALLWARDT, J., Stanford University, Department of Geological and Environmental Sciences, Stanford, USA: 01.09.-31.10.2003

BOUHIFD, M.A., Institut de Physique du Globe de Paris, Laboratoire des Geomateriaux, Paris, France: 16.-18.09.2003

CASTRO, J.M., Oberlin College, Geology Department, Oberlin, USA: 12.-13.11.2003

CONNOLLY, J., ETH Zürich, Institut für Mineralogie und Petrographie, Zürich, Switzerland: 24.-27.06.2003

CUI, X., University of Salford, U.K.: 27.09.-02.10.2003

DEGTYAREVA, O., University of Edinburgh, School of Physics, Edinburgh, U.K.: 03.-06.03.2003

DEN BROOK, B., ETH Zürich, Geologisches Institut, Zürich, Switzerland: 24.-27.06.2003

DOBSON, D.P., University College London, Department of Geological Science, London, U.K.: 26.-30.11.2003

FAUL, U., Australian National University, Research School of Earth Sciences, Canberra, Australia: 15.-16.07.2003

GILPIN, L.A., University of Bristol, U.K.: 20.05.-19.06.2003

GREEN, D., Australian National University, Research School of Earth Sciences, Canberra, Australia: 03.-04.06.2003

HERWEGH, M., Universität Bern, Institut für Geologie, Bern, Switzerland: 24.-26.06.2003

HILAIRET, N., ENS Lyon, France: 05.05.-04.07.2003

IVANOV, B., Russian Academy of Science, Institute for Dynamics of Geospheres, Moscow, Russia: 06.-12.09.2003, 29.09.-04.10.2003

KEPPLER, H., Universität Tübingen, Mineralogisches Institut, Tübingen, Germany: 28.-29.11.2003

KUZNETSOV, A., Swiss-Norwegian Beam Lines at European Synchrotron Radiation Facility, Grenoble, France: 01.-04.11.2003

LEE, K.K.M., University of California at Berkeley, Department of Earth and Planetary Science, Berkeley, USA: 30.03.-19.04.2003

MELOSH, H.J., University of Arizona, Lunar and Planetary Laboratory, Tucson, USA: 03.-04.08.2003

PALME, H., Universität zu Köln, Institut für Mineralogie und Geochemie, Köln, Germany: 25.-26.06.2003, 24.10.2003, 28.11.2003

RENNER, J., Ruhr-Universität Bochum, Institut für Geologie, Mineralogie und Geophysik, Bochum, Germany: 24.-26.06.2003

SHELDON, R., Washington University, St. Louis, USA: 19.-23.05.2003

SMYTH, J.R., University of Colorado at Boulder, Department of Geological Sciences, Boulder, USA: 14.-25.04.2003

SOFFEL, H., Ludwig-Maximilians-Universität München, Institut für Allgemeine und Angewandte Physik, München, Germany: 25.-26.06.2003, 15.07.2003, 24.10.2003, 28.11.2003

SOLOZHENKO, V.L., Universite Pierre et Marie Curie, Paris, France: 20.-27.07.2003

SPETZLER, H., University of Colorado at Boulder, CIRES, Boulder, USA: 13.-26.04.2003

SPICAK, A., Czech Academy of Science, Geophysical Institute, Prague, Czech Republik: 16.-17.06.2003

SCHERTL, H.-P., Ruhr-Universität Bochum, Institut für Geologie, Bochum, Germany: 26.-28.11.2003

SCHWARZ, J.-O., Technische Universität Darmstadt, Germany: 24.-25.03.2003

STOYANOV, E., Friedrich-Schiller-Universität Jena, Institut für Geowissenschaften, Jena, Germany: 14.-15.05.2003

TRAMPERT, J.A., Utrecht University, Faculty of Earth Sciences, Seismological Department, Utrecht, The Netherlands: 06.-07.11.2003

ULRICH, S., Czech Academy of Science, Geophysical Institute, Prague, Czech Republik: 16.-17.06.2003

VAN DER LEE, S., ETH Hönggerberg, Zürich, Switzerland: 29.-30.07.2003

WANG, D., Chinese Academy of Sciences, Institute of Geochemistry, Guiyang, China: 22.-29.11.2003

YOSHIASA, A., Osaka University, Department of Earth and Space Science, Osaka, Japan: 29.06.-01.07.2003

ZÖLLNER, C., Berlin, Germany: 20.-22.01.2003

b) Visiting scientists funded by EU Programme "Access to Large-Scale Facilities"

The Bayerisches Geoinstitut is funded by the European Union under the "Access to Research Infrastructure" Programme. Visiting scientists from EU countries who wish to use the experimental (especially high pressure) facilities of the Institute are funded through this programme. Projects and visiting scientists funded during 2003 are as follows (titles of research projects in *italics*):

BENNA, P., Università degli Studi di Torino, Dipartimento di Scienze Mineralogiche e Petrologiche, Torino, Italy: *"High pressure behaviour and phase transitions in monoclinic and triclinic feldspars of along the join $SrAl_2Si_2O_8$-$CaAl_2Si_2O_8$"*, 22.-26.01.2003

BOLFAN-CASANOVA, N., Université Blaise Pascal CNRS, Laboratoire Magmas et Volcans, Clermont-Ferrand, France: 23.07.-05.08.2003

CONTE, A.M., Università degli Studi di Roma "La Sapienza", Dipartimento di Scienze della Terra, Roma, Italy: *"Microstructural and chemical analyses on experimental products from Stromboli lavas (Aeolian arc Islands, Italy)"*, 20.-24.01.2003

CORDIER, P., Université des Sciences et Technologies de Lille, Laboratoire de Structure et Propriétés de l'Etat Solide, Villeneuve d'Ascq, France: 21.07.-02.08.2003

CORGNE, A., University of Bristol, Department of Earth Sciences, Bristol, U.K.: *"Metal silicate partitioning during core formation"*, 07.-17.02.2003

GILIOLI, E., Istituto dei Materiali per l'Elettronica ed il Magnetismo, IMEM-CNR, Parma, Italy: *"High pressure synthesis of perovskite-like AA´3Mn4O12 for the investigation of novel quantum phenomena in transition metal oxides"*, 19.-30.01.2003

MALAVERGNE, V., Université de Marne la Vallée, Laboratoire des Geomateriaux, Marne la Vallée, France: *"High pressure and high temperature metal-silicate interactions in the metal Fe-Si-S and Fe-Si-C systems"*, 23.04.-27.04.2003

NESTOLA, F., Università degli Studi di Torino, Dipartimento di Scienze Mineralogiche e Petrologiche, Torino, Italy: *"High pressure behaviour and phase transitions in monoclinic and triclinic feldspars of along the join $SrAl_2Si_2O_8$-$CaAl_2Si_2O_8$"*, 04.01.-05.02.2003

OKUBE, M., Osaka University, Department of Earth and Space Science, Osaka, Japan: 29.06.-04.07.2003

PERINELLI, C., Università degli Studi di Roma "La Sapienza", Dipartimento di Scienze della Terra, Roma, Italy: *"Microstructural and chemical analyses on experimental products from Stromboli lavas (Aeolian arc Islands, Italy)"*, 20.-24.01.2003

PRODI, A., Istituto dei Materiali per l'Elettronica ed il Magnetismo, IMEM-CNR, Parma, Italy: *"High pressure synthesis of perovskite-like AA´3Mn4O12 for the investigation of novel quantum phenomena in transition metal oxides"*, 21.-31.01.2003

SCHOFIELD, P.F., The Natural History Museum, Department of Mineralogy, London, U.K.: *"Preparation and characterization of synthetic pyroxenes"*, 14.-19.07.2003

SIEBERT, J., Université de Marne la Vallée, Laboratoire des Geomateriaux, Marne la Vallée, France: *"High pressure and high temperature metal-silicate interactions in the metal Fe-Si-S and Fe-Si-C systems"*, 23.04.-04.05.2003

SKÁLA, R., Czech Geological Survey, Prague, Czech Republic: *"Experimentally shock-loaded quartz: Comparison of two different experimental setups through TEM and X-ray powder diffraction data"*, 26.01.-15.02.2003

TRIBAUDINO, M., Università degli Studi di Torino, Dipartimento di Scienze Mineralogiche e Petrologiche, Torino, Italy: *"High pressure behaviour and phase transitions in monoclinic and triclinic feldspars of along the join $SrAl_2Si_2O_8$-$CaAl_2Si_2O_8$"*, 26.-29.01.2003

c) Visiting scientists supported by other externally funded BGI projects

DI CARLO, I., Università degli Studi di Palermo, Italy: *"The role of amphibole in trace elements partitioning in island arc tectonic settings (the case of Ustica Island)"*, 17.11.-31.12.2003 (EU Marie Curie Training Site)

IACONO MARZIANO, G., Università degli Studi di Palermo, Italy: *"Water solubility in a phonolitic melt and disequilibrium degassing simulated by decompression experiments"*, 15.04.-25.07.2003 (EU Marie Curie Training Site)

LIU, J., Peking University, Department of Geology, Beijing, China: 16.-20.07.2003 (AvH Sofja Kovalevskaja-Programm)

MISITI, V., Università di Roma "La Sapienza", Roma, Italy: *"Formation of low pressure migmatites of Gennargentu Igneous Complex (central-eastern Sardinia)*", 01.01.-28.02.2003 (EU Marie Curie Training Site)

NESTOLA, F., Universitá degli Studi di Torino, Dipartimento di Scienze Mineralogiche e Petrologiche, Torino, Italy: 06.-20.09.2003, 10.06.-09.07.2003, 17.03.-16.04.2003 (AvH Sofja Kovalevskaja-Programm)

SKÁLA, R., Czech Geological Survey, Prague, Czech Republic: *"Deformation phenomena in experimentally shock-loaded anhydrite"*, 01.07.-31.10.2003 (EU Marie Curie Training Site)

d) Visitors (externally funded)

ALLETTI, M., Università degli Studi di Palermo, Italy: 17.11.-31.12.2003

AUDETAT, A., Universität Tübingen, Institut für Mineralogie, Tübingen, Germany: 09.-11.04.2003

BESTMANN, M., Universität Wien, Austria: 07.-21.07.2003, 06.-12.10.2003

BUREAU, H., Laboratoire Pierre Sue, CEA/CNRS, CE Saclay, Gif sur Yvette, France: 16.-22.02.2003

CARPENTER, M., University of Cambridge, Department of Earth Sciences, Cambridge, U.K.: 13.-14.02.2003

CORDIER, P., Université des Sciences et Technologies de Lille, Laboratoire de Structure et Propriétés de l'Etat Solide, Villeneuve d'Ascq, France: 14.-26.04.2003

DEUTSCH, A., Westfälische Wilhelms-Universität Münster, Institut für Planetologie, Münster, Germany: 12.-14.03.2003

DOBMEIER, C., Freie Universität Berlin, Institut für Geologische Wissenschaften, Fachrichtung Geologie, Berlin, Germany: 19.-23.05.2003

DOBSON, D.P., University College London, Department of Geological Science, London, U.K.: 25.06.-04.07.2003

DOLLASE, W., University of California, Department of Earth and Space Sciences, Los Angeles, USA: 05.09.-11.11.2003

DURHAM, W.B., Lawrence Livermore National Laboratory, Livermore, USA: 14.-18.04.2003

EL GORESY, A., Max-Planck-Institut für Chemie, Mainz, Germany: 19.-21.02.2003

HAZEN, B., Carnegie Institution of Washington, Geophysical Laboratory, Washington, USA: 24.-25.05.2003

HEJNY, C., University of Edinburgh, Department of Physics and Astronomy, Edinburgh, U.K.: 15.-22.08.2003

HOLZHEID, A., Westfälische Wilhelms-Universität Münster, Institut für Mineralogie, Münster, Germany: 17.-18.11.2003

KAHLE, A., Johann Wolfgang Goethe-Universität Frankfurt am Main, Institut für Mineralogie, Abteilung Kristallographie, Frankfurt/M., Germany: 14.01.2003

KEGLER, P., Universität Köln, Geologisches Institut, Paläontologische Arbeitsgruppe, Köln, Germany: 17.-29.11.2003

KOMABAYASHI. T., Tokyo Institute of Technology, Department of Earth & Planetary Sciences, Maruyama & Hirose Laboratory, Tokyo, Japan: 01.01.-05.03.2003

MARIANI, E., University of Liverpool, U.K.: 09.-18.05.2003, 29.11.-08.12.2003

MECKLENBURGH, J., University of Manchester, Department of Earth Sciences, Manchester, U.K.: 29.11.-08.12.2003

NEUFELD, K., Universität Mainz, Institut für Geowissenschaften, Mainz, Germany: 18.-21.11.2003, 09.-12.12.2003

QIN, S., Peking University, Department of Geology, Beijing, China: 01.08.-15.09.2003

REICHMANN, H.-J., GeoForschungsZentrum Potsdam, Germany: 07.-11.04.2003

SHCHEKA, S., Universität Tübingen, Institut für Mineralogie, Tübingen, Germany: 09.-13.02.2003, 30.11.-10.12.2003

SHEN, G., University of Chicago, CARS, Argonne, USA: 14.-15.07.2003

TALYZINE, A., IMRA, Nice, France: 25.01.-01.02.2003, 19.-25.05.2003, 22.-27.09.2003

ZÖLLNER, C., Max-Planck-Institut für Chemie, Mainz, Germany: 21.-22.01.2003

ZUMBULYADIS, N., Eastman Kodak Company, Research Laboratories, Rochester, USA: 18.03.2003

4.7 Honours and awards

Giacomo Diego GATTA	received the award for the best scientific contribution during High Pressure Crystallography – 34th crystallographic course sponsored by N.A.T.O. – I.U.Cr., Erice, Italy, 04.-15.06.2003
Falko LANGENHORST	received in September 2003 the Victor-Moritz-Goldschmidt price of the Deutsche Mineralogische Gesellschaft
Christian LIEBSKE	received an "Outstanding Student Paper Award" from the Tectonophysics Section of the American Geophysical Union (AGU) for a presentation at the 2003 AGU Fall Meeting (San Francisco, USA)

4.8 Editorship of scientific journals

MCCAMMON, C.A.	Editorial Advisory Board of "Physics and Chemistry of Minerals" Advisory Board of "Mössbauer Information Exchange"
SEBALD, A.	Editorial Board of "Solid State Nuclear Magnetic Resonance"
RUBIE, D.C.	Editor-in-Chief, Physics of the Earth and Planetary Interiors
SEIFERT, F.	Editorial Advisory Board of "Physics and Chemistry of Minerals"

4.9 Membership of scientific advisory bodies

MCCAMMON, C.A.	Nominating committee for Officers of the Mineralogical Society of America
	Advisory Board of "Mössbauer Information Exchange"
	International Advisory Board of the Mössbauer Effect Data Center
RUBIE, D.C.	Member of AGU Mineral and Rock Physics Executive Committee
	Member of Geochemical Society Fellows Committee
	Member of Roebling Medal Committee, Mineralogical Society of America
	Member of SPring-8 Beamline Review Committee (BL04B1)
SEBALD, A.	Chairperson of the German Magnetic Resonance Discussion Group, 2001-2004
SEIFERT, F.	Senate and Hauptausschuß of German Science Foundation (DFG) (until July 2003)
	Senats-Kommission für geowissenschaftliche Gemeinschaftsforschung (DFG) (until July 2003)
	DFG-Senatskommission Perspektiven der Forschung (until July 2003)
	Committee for Glaciology, Bavarian Academy of Sciences
	Forschungskollegium Mineralogie
	Mitglied des Kuratoriums des Geo-Zentrums an der KTB e. V.
	Academia Europaea, London
	Deutsche Akademie der Naturforscher Leopoldina, Halle (Senate 2003-2006)
	Bayerische Akademie der Wissenschaften, München
	Akademie der Wissenschaften, Göttingen

4.10 Public relations and press reports

LANGENHORST F. (2003): Einschlagskrater auf der Erde – Zeugen kosmischer Katastrophen. In: "Die Erde – Der Planet, auf dem wir leben", Sterne und Weltraum Dossier 2003, 58-69

POIRIER J.-P., LANGENHORST, F. (2003): Der innere Aufbau unseres Planeten. In: "Die Erde – Der Planet, auf dem wir leben", Sterne und Weltraum Dossier 2003, 10-20

5. Scientific and Technical Personnel

Name		Position	Duration in 2003	Funding source
BECHMANN, Matthias	Dipl.-Phys.	Wiss. Angestellter		DFG[1]
BLÄß, Ulrich	Dipl.-Min.	Wiss. Angestellter		DFG
BÖHM, Ulrich		Mechaniker		BGI
BÖSS, Wolfgang	RAR	Verwalt. Beamter		BGI
BOFFA BALLARAN, Tiziana	Dr.	Sofia Kovalevskaja-Preisträgerin		AvH
BROMILEY, Fiona	B.Sc.	Stipendiatin	to 28.02	AvH[2]
	M.Phil.	Wiss. Angestellte	from 01.03.	AvH[2]
BROMILEY, Geoffrey	Dr.	Wiss. Angestellter	to 31.03.	EU
			from 01.04.	BGI/VP
COUVY, Hélène	Dipl.-Geol.	Stipendiatin	to 16.11.	EU
		Wiss. Angestellte	from 17.11.	BGI/VP
DEMOUCHY, Sylvie	Dipl.-Geol.	Wiss. Angestellte	to 14.06.	EU
			from 15.06.	TÜB[3]
DUBROVINSKAIA, Natalia	Dr.	Wiss. Angestellte		BGI
DUBROVINSKY, Leonid	PD Dr.	Akad. Oberrat		BGI
FISCHER, Heinz		Mechaniker		BGI
FROST, Daniel	Dr.	Akad. Rat		BGI
GAILLARD, Fabrice	Dr.	Wiss. Angestellter		BGI/VP
GATTA, Giacomo Diego	Dr.	Wiss. Angestellter		AvH[2]
GOLLNER, Gertrud		Chem.-Techn. Assistentin		BGI
HEIDELBACH, Florian	Ph.D.	Wiss. Assistent		BGI
HELLUY, Xavier	Dr.	Wiss. Angestellter	to 28.02.	DFG[1]
HERRMANNSDÖRFER, Georg		Mechaniker		BGI
HOLZAPFEL, Christian	Dipl.-Min.	Wiss. Angestellter	to 31.08.	EU
IEZZI, Gianluca	Dr.	Wiss. Angestellter		AvH[2]
JACOBSEN, Steven	Dr.	Forschungsstipendiat	to 31.03.	AvH
		Wiss. Angestellter	from 01.04.	BGI/VP
KANTOR, Anastasia	Dipl.-Geol.	Wiss. Angestellte	from 18.08.	BGI/VP
KANTOR, Innokenty	Dipl.-Geol.	Wiss. Angestellter	from 18.08.	BGI/VP
KEYSSNER, Stefan	Dr.	Akad. Oberrat		BGI
KISON-HERZING, Lydia		Sekretärin		BGI
KLASINSKI, Kurt	Dipl.-Ing. (FH)	Techn. Angestellter		BGI
KRAUßE, Detlef	Dipl.-Inform. (FH)	Techn. Angestellter		BGI

KRIEGL, Holger		Haustechniker		BGI
LANGENHORST, Falko	PD Dr.	Akad. Oberrat		BGI
LEITNER, Oskar		Präparator		BGI
LIEBSKE, Christian	Dipl.-Min.	Wiss. Angestellter		DFG
LINHARDT, Sven		Elektroniker		BGI
LIU, Jun	Dipl.-Min.	Stipendiatin	from 01.10.	AvH[2]
MARKERT, Anke		Techn. Angestellte	to 14.03.	EU
MARTON, Fred	Dr.	Wiss. Angestellter		BGI/VP
MCCAMMON, Catherine	Dr.	Akad. Oberrätin		BGI
MECKLENBURGH, Julian	Dr.	Wiss. Angestellter	to 30.06.	BGI/VP
NEUFELD, Kai	Dipl.-Geol.	Wiss. Angestellter	to 31.07.	BGI/VP
NING, Jie Yuan	Dr.	Stipendiat	to 03.09.	UBT
POIRIER, Jean-Paul	Prof. Dr.	Forschungs-preisträger	from 06.03. to 31.05.	AvH
RAMMING, Gerd		Elektroniker		BGI
RAUSCH, Oliver		Mechaniker		BGI
RUBIE, David C.	Prof. Dr.	Stellvertr. Leiter		BGI
SCHMICKLER, Bettina	Dr.	Wiss. Angestellte		DFG, EU
SCHMIDT, Burkhard	Dr.	Wiss. Angestellter		BGI/VP
SCHULZE, Hubert		Präparator		BGI
SEBALD, Angelika	PD Dr.	Wiss. Angestellte		
SEIFERT, Friedrich	Prof. Dr.	Stellvertr. Leiter		BGI
SHIRYAEV, Andrei	Dr.	Forschungsstipendiat	from 01.12.	AvH
STÄNDNER, Petra		Fremdsprachen-Sekretärin		BGI
STEINLE-NEUMANN, Gerd	Dr.	Juniorprofessor		BGI
STOYANOV, Emil	Dipl.-Chem.	Wiss. Angestellter	from 01.10.	BGI/VP
STRETTON, Iona	Dr.	Wiss. Assistentin		BGI
SUZUKI, Akio	Dr.	Forschungsstipendiat	to 30.04.	AvH
TERASAKI, Hidenori	Dr.	Wiss. Angestellter		DFG, BGI/VP
TERRY, Michael	Dr.	Wiss. Angestellter		BGI/VP

Abbreviations/explanations:

BGI	Staff Position of Bayerisches Geoinstitut
BGI/VP	Visiting Scientists' Program of Bayerisches Geoinstitut
DFG	German Science Foundation
EU	European Union
AvH	Alexander von Humboldt Foundation
UBT	University of Bayreuth, Germany

[1] project granted to Prof. B. Wrackmeyer, Bayreuth

[2] Sofia Kovalevskaja-Preis

[3] H. Keppler, Tübingen

Index